

# Optoelectronic Properties of Graphene: Light Interaction and Emission

by

Angela Melina Beltaos

A thesis submitted in partial fulfillment of the requirements for the degree of

Doctor of Philosophy

Department of Physics

University of Alberta

©Angela Melina Beltaos, 2018

# ABSTRACT

Graphene has created much excitement in the scientific community since 2004, when Novoselov and Geim developed a method to exfoliate atomic layers from graphite, earning them the 2010 Nobel prize. The great interest in graphene stems from its outstanding material properties such as atomic thickness, high mechanical strength and good electrical conductivity, making it potentially useful for a variety of applications. The combination of such properties is particularly attractive in the field of optoelectronics, and research in this area will likely increase in the future. In this thesis, the optoelectronic properties of graphene were investigated experimentally through studies of light interaction and light emission. Light interaction with graphene was performed by a femtosecond laser and the resulting damage effects and induced periodic surface structures were investigated. Light emission was excited by applying voltage to graphene devices and measured by spectroscopy and imaging techniques. Graphene samples were fabricated by mechanical exfoliation, and incorporated into field effect transistors by electron beam vapor deposition of patterned electrodes. Characterization techniques included Raman spectroscopy, optical microscopy, scanning electron microscopy, atomic force microscopy, and electronic measurements. Key results included the demonstration of patterning graphene by ultrafast laser interaction, determination of the laser ablation threshold, the first observation of laser induced periodic surface structures on graphene, and the characterization of visible light emission from graphene field effect transistors. The results supported a light emission mechanism based on a recent theory; the quantum Čerenkov effect.

## PREFACE

This thesis is based on the research summarized in three lead-authored publications/chapters (Chapters 4, 5, and 6). All three works were conducted as research collaborations and have been published. The other chapters; namely the Introduction (Chapter 1), Background (Chapter 2), Mechanisms (Chapter 3) and Conclusions (Chapter 7), are my original work.

Chapter 4 was published as Beltaos, A., Kovačević, A., Matković, A., Ralević, U., Jovanović, D., and Jelenković, B. (2014). “Damage effects on multi-layer graphene from femtosecond laser interaction”. *Physica Scripta*, 2014 (T162), 014015. I was responsible for leading this work in terms of the concept, experiment set-up, fabrication, data collection, analysis, and manuscript preparation. A. Kovačević contributed to research ideas, experiment set-up, data collection, artwork (experiment schematic drawing), and was the main coauthor editing the manuscript. A. Matković contributed to sample fabrication and data collection. U. Ralević and D. Jovanović contributed to data collection. B. Jelenković contributed to lab resources and project leadership. The experimental work was carried out at Institute of Physics, University of Belgrade, Belgrade, Serbia.

Chapter 5 was published as Beltaos, A., Kovačević, A. G., Matković, A., Ralević, U., Savić-Šević, S., Jovanović, D., Jelenković, B. M., and Gajić, R. (2014). “Femtosecond laser induced periodic surface structures on multi-layer graphene”. *Journal of Applied Physics*, 116(20), 204306. I was responsible for leading this work in terms of the concept, experiment set-up, fabrication, data collection, analysis, and manuscript preparation. A. G. Kovačević contributed to research ideas, experiment set-up, data collection, and was the main coauthor editing the manuscript. A. Matković contributed to sample fabrication, data collection, and artwork (experiment schematic drawing). U. Ralević, S. Savić-Šević, and D. Jovanović contributed to data collection. B. M. Jelenković and R. Gajić contributed to lab resources and project leadership. The exper-

imental work was carried out at Institute of Physics, University of Belgrade, Belgrade, Serbia.

Chapter 6 was published as Beltaos, A., Bergren, A. J., Bosnick, K., Pekas, N., Lane, S., Cui, K., Matković, A., and Meldrum, A. (2017). “Visible light emission in graphene field effect transistors”. *Nano Futures*, 1(2), 025004. I was responsible for leading this work in terms of the concept, experiment set-up, fabrication, data collection, analysis, and manuscript preparation. A. J. Bergren contributed to concept, research ideas, experiment set-up, lab resources, project leadership, and was one of the main coauthors editing the manuscript. K. Bosnick contributed to experiment set-up, lab resources, and project leadership. N. Pekas contributed to device design, device fabrication, experiment set-up, and lab resources. S. Lane contributed to device modification and data collection. K. Cui contributed to data collection. A. Matković contributed to sample fabrication and artwork (experiment schematic drawing). A. Meldrum contributed to concept, research ideas, experiment set-up, lab resources, and was one of the main coauthors editing the manuscript. The experimental work was carried out mainly at the National Institute for Nanotechnology and partially at the University of Alberta, Edmonton, Alberta.

*Dedicated to my parents Spyros and Ljilja, my siblings Terry, Elaine, and Andrew, and my nephew little Andrew.*

## ACKNOWLEDGEMENTS

I am very grateful to those who have supported, contributed to, and assisted in this work. Many thanks to all!

Institutions that have supported this research and my studies: Department of Physics, University of Alberta (U of A); National Institute for Nanotechnology (NINT), which operates as a partnership between U of A, National Research Council of Canada (NRC), and the Government of Alberta; Faculty of Physics and Institute of Physics, University of Belgrade (U of B).

My supervisors, Dr. Adam Bergren (NINT) and Dr. Al Meldrum (U of A), for their ongoing support and guidance. Each has inspired me immensely, and their combined leadership, curiosity and enthusiasm has been invaluable. I wish to thank both for sharing their wisdom and insights and always taking the time to discuss my research with me. It has been a pleasure to work on this team.

Committee members for their time commitment, review of this work, and guidance - Supervisory committee: Dr. Adam Bergren (NINT), Dr. Al Meldrum (U of A), Dr. Frank Hegmann (U of A); Candidacy committee: Dr. Adam Bergren (NINT), Dr. Al Meldrum (U of A), Dr. Frank Hegmann (U of A), Dr. Sharon Morsink, chair (U of A), and Dr. Lindsay LeBlanc (U of A); Defense committee: Dr. Adam Bergren (NINT), Dr. Al Meldrum (U of A), Dr. Frank Hegmann (U of A), Dr. Sharon Morsink, chair (U of A), Dr. Lindsay LeBlanc (U of A), and Dr. Johannes Barth, external (Technical University of Munich).

Professors and technical officers who have assisted with the research: Dr. Richard L. McCreery (NINT and U of A) for lab resources and helpful discussion, Mr. Bryan Szeto (NINT) for technical assistance, Dr. Frank Hegmann

(U of A) for helpful discussion, Mr. Rob Indoe (NINT) for technical assistance, Mr. Miloš Bokorov (University of Novi Sad) for preliminary SEM measurements, and Dr. Dejan Pantelić (U of B) for helpful discussion.

Academic and support staff who have assisted with the logistics of my study program - From U of A: Dr. Richard Marchand, Ms. Sarah MacKinnon; From NINT: Ms. Zarina Ashraf, Ms. Salome Asea; From U of B: Ms. Mirjana Vasiljev, Dr. Maja Burić, Ms. Mirzeta Savić, and Mr. Miomir Erdeljanović.

My colleagues and fellow group members for sharing in my grad studies experience and learning together.

My family, friends, and former professors for their encouragement, advice, and inspiration.

Hongtao Yang who created the  $\text{\LaTeX}$  style file `mathesis.sty` that was used in the preparation of this thesis.

Funding of this work was provided by the National Institute for Nanotechnology (in partnership with U of A, NRC, and the Government of Alberta), and the Institute of Physics, University of Belgrade (Ministry of Science, Republic of Serbia (MPNTR)). Project funding was provided by NINT projects A1-009201 and A1-004914, and MPNTR projects OI171005, III45016, and III45018.

# Table of Contents

List of Tables	xi
List of Figures	xxiii
<b>1 Introduction</b>	<b>1</b>
1.1 History of Graphene . . . . .	1
1.2 Applications . . . . .	3
1.3 Thesis Overview . . . . .	4
1.4 References . . . . .	6
<b>2 Background</b>	<b>10</b>
2.1 Electronic Properties . . . . .	10
2.1.1 Crystal Structure . . . . .	10
2.1.2 Dispersion Relation . . . . .	12
2.1.3 Electric Field Effect . . . . .	16
2.2 Optical Properties . . . . .	19
2.2.1 Absorption and Transmission . . . . .	19
2.2.2 Visualization . . . . .	21
2.2.3 Raman Spectrum . . . . .	23
2.3 Optoelectronic Properties . . . . .	27
2.3.1 Plasmons . . . . .	27
2.4 Closing Remarks . . . . .	39
2.5 References . . . . .	40

<b>3</b>	<b>Mechanisms</b>	<b>44</b>
3.1	Laser Ablation and Patterning . . . . .	44
3.1.1	Ablation Process . . . . .	44
3.1.2	Ablation of Graphite . . . . .	45
3.1.3	Laser surface structuring . . . . .	47
3.1.4	Patterning . . . . .	49
3.2	Laser Induced Periodic Surface Structures . . . . .	50
3.2.1	Experimental Observations . . . . .	50
3.2.2	Formation process . . . . .	51
3.2.3	Surface Plasmon Polariton Model . . . . .	53
3.3	Light Emission from Graphene . . . . .	56
3.3.1	Photoluminescence . . . . .	57
3.3.2	Electroluminescence . . . . .	59
3.3.3	Thermal Emission . . . . .	63
3.3.4	Surface plasmon-electron interaction . . . . .	67
3.3.5	Čerenkov Effect . . . . .	69
3.4	References . . . . .	76
<b>4</b>	<b>Damage effects on multi-layer graphene from femtosecond laser interaction</b>	<b>84</b>
4.1	Abstract . . . . .	84
4.2	Introduction . . . . .	85
4.3	Experiment . . . . .	86
4.4	Results and discussion . . . . .	87
4.5	Conclusion . . . . .	90
4.6	Acknowledgements . . . . .	92
4.7	References . . . . .	92
<b>5</b>	<b>Femtosecond laser induced periodic surface structures on multi-layer graphene</b>	<b>94</b>
5.1	Abstract . . . . .	94
5.2	Introduction and background . . . . .	95

5.3	Experiment . . . . .	98
5.4	Results and discussion . . . . .	99
5.5	Conclusion . . . . .	109
5.6	Acknowledgements . . . . .	110
5.7	References . . . . .	110
<b>6</b>	<b>Visible light emission in graphene field effect transistors</b>	<b>114</b>
6.1	Abstract . . . . .	114
6.2	Introduction . . . . .	115
6.3	Methods . . . . .	117
6.4	Results . . . . .	119
6.5	Discussion . . . . .	128
6.6	Conclusion . . . . .	132
6.7	Acknowledgements . . . . .	133
6.8	References . . . . .	133
6.9	Supporting information . . . . .	137
6.10	References for Supporting Information . . . . .	148
<b>7</b>	<b>Conclusions</b>	<b>149</b>
7.1	Summary . . . . .	149
7.2	Future Work . . . . .	151
7.3	Outlook . . . . .	152
	<b>Bibliography</b>	<b>155</b>
	<b>Appendix</b>	<b>178</b>
<b>A</b>	<b>Fabrication Methods</b>	<b>178</b>
A.1	Sample Fabrication . . . . .	178
A.2	Device Fabrication . . . . .	183
A.3	References . . . . .	187

# List of Tables

6.1	Atomic percent (%) of the EDX spectra for the points indicated in Figure 6.17 (b). All points show the presence of C, O, and Si due to the graphene and backing Si/SiO <sub>2</sub> substrate, while points 7 and 9 (interacted by the e-beam) show increased values of C due to the EBID C nano-deposits, as well as a lack of Au distinguishing them from the gold nanoparticles known to form near the electrodes (eg. point 6). . . . .	146
-----	---	-----

# List of Figures

2.1	TEM image of single-layer suspended graphene (K. Cui, National Institute for Nanotechnology) . . . . .	11
2.2	Electronic properties of graphene: (a) Crystal lattice in real space, showing $A$ (white) and $B$ (black) atoms, primitive lattice vectors $\vec{a}_1$ and $\vec{a}_2$ , and distance between neighbouring atoms $a_0$ ; (b) Reciprocal lattice in $\vec{k}$ -space, showing primitive lattice vectors $\vec{b}_1$ and $\vec{b}_2$ , the first Brillouin zone (defined by black hexagon) with high symmetry points along the zone boundary (crossed circles) $\vec{K}'$ , $\vec{M}$ , and $\vec{K}$ , and center $\vec{\Gamma}$ ; (c) Dispersion relation (equation 2.4 for $-\frac{2\pi}{a} < k_x < \frac{2\pi}{a}$ , $k_y = 0$ , and $t = 1$ eV); (d) Enlarged view of the dispersion relation near the $\vec{K}$ and $\vec{K}'$ points showing the conduction band ( $CB$ ) and valence band ( $VB$ ), i.e. the “Dirac cone” . . . . .	13
2.3	Electric field effect in graphene: (a) graphene field effect transistor device schematic, showing source (S), drain (D), gate (G) electrodes, and voltages applied to the source-drain ( $V_{SD}$ ) and source-gate ( $V_G$ ); (b) transfer characteristics of graphene (resistance vs gate voltage), showing the Dirac point ( $DP$ ), Dirac voltage ( $V_D$ ), and doping; (c) p-doped graphene as represented by the field effect transistor device schematic (left), showing the applied electric field ( $\vec{E}$ ) and the graphene dispersion relation (right), showing the Fermi energy ( $E_F$ ); and (d) the same as (c) for n-doped graphene. . . . .	17

2.4	Visualizing graphene: (a) Optical microscope image of an exfoliated graphene sample on an Si/SiO <sub>2</sub> substrate, collected by reflected white light, in which single-layer (SLG), bi-layer (BLG), and few-layer (FLG) graphene regions are marked; (b) Schematic cross-section of a graphene (G) sample (dark grey) on an Si (yellow)/SiO <sub>2</sub> (light grey) substrate viewed by an inverted microscope objective (red). Refractive indices $n$ and thicknesses $d$ are marked for the various layers. The incoming ( $E_{in}$ ) and reflected fields ( $E_G$ , $E_{SiO_2}$ , $E_{Si}$ ) are marked for the various surfaces. The schematic in (b) was reprinted with permission from [17], <a href="http://dx.doi.org/10.1021/nl071168m">http://dx.doi.org/10.1021/nl071168m</a> . Copyright (2007) American Chemical Society. . . . .	22
2.5	Raman spectra of (a) exfoliated single-layer graphene (SLG); (b) exfoliated bilayer graphene (BLG); (c) exfoliated trilayer graphene (TLG); (d) CVD trilayer graphene (TLG). Insets: optical microscope images of the corresponding samples. . . . .	25
2.6	Schematic illustration of a surface plasmon at the interface of two media $\epsilon_1$ (plasma), and $\epsilon_2$ (dielectric or vacuum), showing the electric field ( $\vec{E}$ ), magnetic field ( $\vec{B}_y$ ) and wave vector $\vec{k}$ . This illustration was modeled after several references [1,7,28,29].	30
2.7	Example surface plasmon polariton dispersion relation of graphene (black solid curve) compared to the light line (red dashed line). Republished (adapted) with permission of World Scientific Publishing Co., Inc., from <a href="http://dx.doi.org/10.1142/S0217979213410014">http://dx.doi.org/10.1142/S0217979213410014</a> [30], copyright (2013); permission conveyed through Copyright Clearance Center, Inc.. . . . .	33
2.8	Wave vector matching for (a) coupling and (b) decoupling light to/from SPPs using a graphene sheet (purple) atop a patterned grating structure in a dielectric (orange). This illustration was modeled after several references [7,25,38]. . . . .	37

3.1	Femtosecond laser surface structuring of metals: schematics of the process (top), and images of typical nanostructures and deposits (bottom). This figure was reproduced by permission from John Wiley and Sons: Laser & Photonics Reviews, copyright (2012), <a href="http://dx.doi.org/10.1002/lpor.201200017">http://dx.doi.org/10.1002/lpor.201200017</a> [7]. . . . .	48
3.2	Summary of the FLIPSS formation process (left) and images of a titanium surface during the formation of FLIPSS in air: (a) before laser interaction; (b) after 2 laser shots; (c) after 10 laser shots; (d) after 40 laser shots. This figure was reproduced by permission from John Wiley and Sons: Laser & Photonics Reviews <a href="http://dx.doi.org/10.1002/lpor.201200017">http://dx.doi.org/10.1002/lpor.201200017</a> [7], copyright (2012). . . . .	54
3.3	Schematic diagrams illustrating (a) the excitation of surface plasmons ( $\vec{k}_{s1}, \vec{k}_{s2}$ ) during the interaction of normally incident linearly polarized laser radiation with a metal surface and (b) the law of quasi-momentum conservation and the formation of nanorelief lattices on the metal surface due to the interference of the incident wave with surface plasmons ( $\vec{g}_1$ lattice) and the mutual interference of the laser-excited surface plasmons ( $\vec{g}_2$ lattice). This figure and caption were reproduced by permission of Springer: Technical Physics Letters, copyright (2008), <a href="https://doi.org/10.1134/S1063785008050088">https://doi.org/10.1134/S1063785008050088</a> [32]. . . . .	55
3.4	Two types of light emission from graphene, schematically represented on the dispersion relation: (a) photoluminescence (PL); (b) electroluminescence (EL). The schematic in (a) was adapted by permission from Macmillan Publishers Ltd: Nature, copyright (2011), <a href="http://dx.doi.org/10.1038/nature09866">http://dx.doi.org/10.1038/nature09866</a> [44]. The schematic in (b) was adapted by permission from IOP Publishing: Nanotechnology, copyright (2014), <a href="http://dx.doi.org/10.1088/0957-4484/25/5/055206">http://dx.doi.org/10.1088/0957-4484/25/5/055206</a> [48]. . . . .	58

3.5	Phonon-assisted electroluminescence spectra at varying voltages for devices based on (a) single-wall carbon nanotubes, and (b) few-layer graphene. Reprinted with permission from <a href="http://dx.doi.org/10.1021/nl9039795">http://dx.doi.org/10.1021/nl9039795</a> [49]. Copyright (2010) American Chemical Society. . . . .	62
3.6	Visible thermal emission from suspended graphene devices: (a) schematic of the device structure showing interference effects between the light emission (solid arrow) and reflected light (dashed arrow) in the trench below graphene; (b) simulated emission intensity for various trench depths, showing constructive (solid curves) and destructive (dashed curves) interference conditions; (c) simulated emission spectra for various trench depths. This figure was reprinted by permission from Macmillan Publishers Ltd: Nature Nanotechnology, <a href="http://dx.doi.org/10.1038/NNANO.2015.118">http://dx.doi.org/10.1038/NNANO.2015.118</a> [63], copyright (2015). . . . .	65
3.7	Light emission from graphene due to electron-plasmon interaction: (a) schematic diagram of the scattering process; (b) illustration of the graphene device and the emission mechanism. This figure was reprinted (adapted) by permission from Macmillan Publishers Ltd: Nature Photonics, copyright (2015), <a href="http://dx.doi.org/10.1038/NPHOTON.2015.223">http://dx.doi.org/10.1038/NPHOTON.2015.223</a> [68]. . . . .	68
3.8	The conventional Čerenkov radiation process schematically illustrated. This figure was reprinted (with adaption) from Scientific Reports <a href="http://dx.doi.org/10.1038/s41598-017-08705-4">http://dx.doi.org/10.1038/s41598-017-08705-4</a> [75], copyright (2017), under the Creative Commons Attribution 4.0 International License <a href="http://creativecommons.org/licenses/by/4.0/">http://creativecommons.org/licenses/by/4.0/</a> . . . . .	70

3.9	The quantum Čerenkov effect: (a) schematic of the graphene plasmon emission process from hot carrier excitation; (b) diagram of the excitation-emission process. This figure was reprinted (without adaption) from Nature Communications, copyright (2016), <a href="http://dx.doi.org/10.1038/ncomms11880">http://dx.doi.org/10.1038/ncomms11880</a> [71], under the Creative Commons Attribution 4.0 International License, which can be found at <a href="https://creativecommons.org/licenses/by/4.0/">https://creativecommons.org/licenses/by/4.0/</a> .	73
4.1	Schematic diagram of the femtosecond laser interaction setup.	86
4.2	Optical microscope images of SLG with nearby graphite before (a) and after (b) laser interaction. . . . .	89
4.3	(a), (b) AFM images of the areas of laser interaction in 10-15-layer samples showing ablation and degradation, respectively; (c), (d) corresponding optical images of the samples, with white squares indicating positions of AFM measurement above. . . . .	89
4.4	Raman spectra of top, a five-layer sample before (a) and after (b) laser interaction; bottom, the same sample from figure 4.3(c) in three different areas—completely ablated (c); damaged (d); undamaged (e); Insets: optical microscope images of the samples showing positions of measurement in the Raman spectrometer. . . . .	91
4.5	Optical microscope images of areas of interaction on 10-15-layer samples at different exposure times and laser powers in reflection mode (a) and transmission mode (b). . . . .	91
5.1	Schematic of the femtosecond laser interaction set-up. . . . .	99
5.2	Optical microscope images of (a) and (b) 15-layer graphene, and (c) and (d) 5-layer graphene samples before (left) and after (right) laser interaction. The green dots mark regions ablated for $t=4$ min ( $N \approx 1.8 \times 10^{10}$ ) of irradiation by a beam of $F \approx 4.3 - 4.4$ mJ/cm <sup>2</sup> . . . . .	100

5.3	(a) Micro-Raman spectrum of a 14-layer graphene sample. Inset: Optical microscope image, where the red dot indicates the position of the Raman measurement on a non-interacted area of the sample. (b) Transmission optical image of a 5-layer graphene (5 LG) sample, adjacent to a 24-layer flake (24 LG). The intensity of transmitted light for profile lines 1, 2, and 3 is shown in (c) in blue, red, and green, respectively. . . . .	101
5.4	SEM images of LIPSS observed on multi-layer graphene coated with a gold layer of $\sim 5$ nm: (a) ablated region due to laser interaction marked by orange dashed line. The white square shows where LIPSS were found, with a zoomed in image shown in part (b); (c) typical obtained LIPSS, showing width $w$ and period $\Lambda$ of the nanostructures and the polarization direction ( $\mathbf{P}$ ) of the laser used in the interaction. . . . .	102
5.5	Comparison SEM images of 15-layer graphene (left panel) and 5-layer graphene (right panel) samples. Ablated regions are shown in (a) and (b), where the white squares indicate the area examined in the corresponding larger image below in (c) and (d). The SEM images were taken without gold on the sample. . . . .	103
5.6	AFM analysis of LIPSS on multi-layer graphene: (a) Ablated region of the sample. Inset: optical image of the sample where the ablated region can be seen as a black dot (scale bar of inset is $40 \mu\text{m}$ ). White squares represent areas where structures were found, corresponding to (b) and (c), respectively; (d) phase image of the structures, zoomed in from the white square in (b); (e) height profile corresponding to the profile line “1” in (b); (f) 3D height map of structures, with inset showing corresponding 2D image. . . . .	105

5.7	SEM images showing the lateral dimensions of the LIPSS on multilayer graphene coated with a gold layer of $\sim 5$ nm: (a) range and length; (b) variations in length, marked by the yellow dashed curve. Black squares are due to SEM charging, while black dots are due to ambient contamination. . . . .	106
5.8	AFM analysis of LIPSS on multi-layer graphene with reduced laser exposure time: (a) ablated region; structures are seen around the peripheral area; (b) phase image of structures; (c) height profile corresponding to the profile line “1” in (a). . . . .	107
6.1	Schematics of (a) graphene FET device (NOT to scale the graphene channel length is $\sim 15\text{-}25 \mu\text{m}$ , and the gate dielectric thickness is $\sim 300$ nm); (b) light emission spectroscopy and imaging setup. The sample is located inside a vacuum chamber with a top window (schematically represented in the inset) and connected to a source meter for the application of voltages $V_{sd}$ and $V_g$ . . . . .	118
6.2	Images of a graphene FET: (a) SEM image of the graphene channel area; (b) optical microscope color image of the same area as in (a), showing light emission excited by applied voltage ( $V_g = 0$ V, $V_{sd} = -27$ V). The inset shows the relative intensity on the corresponding black and white emission image; (c) schematic representation of light emission from a graphene FET based on the quantum ČE effect. . . . .	120
6.3	Typical light emission spectra, showing spectral intensity versus wavelength, of three different graphene FET light sources excited by applied voltage; devices A (green) ( $V_g = 30$ V, $V_{sd} = 7$ V), B (red) ( $V_g = 0$ V, $V_{sd} = -30$ V), and C (blue) ( $V_g = 40$ V, $V_{sd} = 18$ V), fitted to two-term Gaussian functions (black curves). 121	

6.4	Effects of varying (a) source-drain and (b) gate voltage on light emission spectra, and corresponding effects on the spectral parameters for positive (blue) and negative (red) $V_{sd}$ (left plot) and $V_g$ (right plot); (c) peak spectral intensity (Int.) versus $ I_{sd} $ by varying $V_{sd}$ , plotted on a log scale and fitted to exponential functions (black lines); (d) peak spectral intensity (Int.) versus $ I_{sd} $ by varying $V_g$ , plotted on a log scale and fitted to exponential functions (black lines). . . . .	123
6.5	Effects of varying $V_{sd}$ and $V_g$ on the light emission location of a graphene FET, as observed in color light emission images (left) and corresponding overlays of light emission and brightfield images (right) for (a) positive $V_{sd}$ ; (b) negative $V_{sd}$ ; (c) positive $V_{sd}$ ; (d) negative $V_{sd}$ ; (e) positive $V_g$ ; (f) negative $V_g$ ; (g) positive $V_g$ ; (h) negative $V_g$ . The light emission appears as a bright spot in the upper left corner of the graphene channel. The horizontal scanning lines are artifacts for the particular camera/software used here. . . . .	125
6.6	(a) and (d) typical optical microscope color images of light emission corresponding to devices A (a) ( $V_g=0$ V, $V_{sd}= 7$ V) and B (d) ( $V_g=0$ V, $V_{sd}= -30$ V) of figure 6.3, respectively. (b) and (e) the same images of light emission overlaid with brightfield images, corresponding to (a) and (d), respectively. (c) and (f) typical SEM images of devices after light emission, corresponding to the devices in (b) and (e), respectively. White rectangles indicate selected areas of light emission enlarged in the insets. The additional left inset in (d) is a brightfield optical image of the device. The dashed blue lines in (e) and (f) mark the edges of the graphene channel. . . . .	126

6.7	Various images showing the same channel area of a patterned device (“device C”): (a) SEM image of the device before light emission experiments; patterned defects are seen as white points; (b) color light emission image of the device ( $V_g=0$ V, $V_{sd}= -28$ V); (c) SEM image of the device after light emission experiments; the white rectangle indicates a selected area of emission with an enlarged view in the inset; the green circles indicate defects associated with light emission locations; (d) corresponding emission and brightfield image overlay of (b). . . . .	127
6.8	Typical Characterization of graphene FETs: (a) Raman spectra before (blue) and after (red) light emission, (b) $I-V$ curves ( $I_{sd}$ vs $V_{sd}$ ) before (blue) and after (red) light emission, (c) transfer characteristics ( $I_{sd}$ vs $V_g$ ) during a light emission experiment at a fixed $V_{sd}$ . . . . .	138
6.9	Experimental spectrum (red) of a graphene FET ( $V_g= 0$ V, $V_{sd}= -25$ V) with a two-term Gaussian fit (black) using coefficients: $a_1 = 10200$ , $b_1 = 997.2$ , $c_1 = 135$ , $a_2 = 4701$ , $b_2 = 713.7$ , $c_2 = 123.8$ as defined below. . . . .	140
6.10	Light emission spectrum from a graphene FET ( $V_g= -40$ V, $V_{sd}= 12$ V) displaying light in the NIR range only, without the characteristic peak in the VIS range as observed on other devices.	141
6.11	Light emission spectrum of a graphene FET ( $V_g= 30$ V, $V_{sd}= 7$ V, $R = 2.49 \times 10^4 \Omega$ ) used to calculate an order-of-magnitude estimate of the power conversion efficiency $\eta = 10^{-7}$ . . . . .	141

- 6.12 Threshold behaviour of the peak spectral intensity (*Int.*) of the VIS light emission for two different graphene FETs: device C (blue) and device B (green). The peak spectral intensity is plotted in terms of (a) the source-drain voltage  $|V_{sd}|$  and (b) the electric field  $|E| = |V_{sd}|/L$ , where  $L$  is the channel length. The threshold for observable light emission in terms of source-drain voltage is different for each device as seen in (a), but becomes apparent as a single value in (b) as the minimum of the curves for the two devices converge at a value on the order of  $1 \times 10^6$  V/m (i.e. the threshold electric field for observable light emission). All fits (black curves) are polynomials of a second order. . . . . 143
- 6.13 Effects of varying source-drain (top row) and gate voltage (bottom row) on light emission spectral parameters for positive (blue) and negative (red)  $V_{sd}$  and  $V_g$ , corresponding to the spectra shown in Figure 6.3 of the main text: (a) peak spectral intensity (*Int.*) vs  $|V_{sd}|$ , plotted on a logarithmic scale and fitted to exponential functions (black lines); (b) peak wavelength ( $\lambda$ ) vs  $|V_{sd}|$ ; (c) full-width-at-half-maximum (*FWHM*) vs  $|V_{sd}|$ ; (d) *Int.* vs  $|V_g|$ ; (e) peak  $\lambda$  vs  $|V_g|$ , fitted to linear functions (black lines); (f) *FWHM* vs  $|V_g|$ . All fits (black curves) except in (a) and (e) are polynomials of a second order. . . . . 143
- 6.14 Effects of current on spectral peak wavelength corresponding to the spectra in Figure 6.4 (a) and (b): (a) peak wavelength ( $\lambda$ ) vs  $|I_{sd}|$  by varying  $V_{sd}$  and (b) peak wavelength ( $\lambda$ ) vs  $|I_{sd}|$  by varying  $V_g$ . Error bars representing 2% (a) and 1% (b) were determined from the 95% confidence bounds of the Matlab Gaussian fits to the data. In (a) and (b) a downward trend was observed corresponding to a blue-shift in emitted light with increasing current. . . . . 144

6.15	SEM and EDX characterization of graphene FETS after applying voltage in light emission experiments showing gold nanoparticles. (a) and (d): SEM images of two different graphene FETs in which nanoparticles were observed near the gold electrodes (white rectangles); (b) and (e) corresponding enlarged SEM images from the white rectangles in (a) and (d), respectively; (c) and (f) corresponding EDX maps of gold (Au) from the SEM images in (b) and (e), respectively showing that the nanoparticles consisted of gold. . . . .	144
6.16	SEM images of a graphene FET before (a) and after (b) applying voltage in light emission experiments. Nanoparticles were observed after experiments (b) near the gold electrode (white rectangle and corresponding enlarged view in inset). Before experiments (a), no such nanoparticles were observed, confirming that the nanoparticles formed due to applied voltage, likely by electromigration of gold. The dark shaded circles centered by light-contrast points in (a) and (b) are due to focused e-beam interaction for patterning defects on the graphene channel as described in the main text. . . . .	145
6.17	SEM and EDX characterization of defects patterned onto a graphene FET by e-beam interaction: (a) SEM image of a graphene channel where the e-beam was used to pattern defects (white oval); (b) Enlarged view of the area, showing points of EDX analysis (green numbered crosses) given in Table 6.1 below. Points 7 and 9 (white oval) are the e-beam interacted spots, while the others are used as reference points. . . . .	145

6.18	Raman spectra of a graphene FET channel before (blue) and after (red) focused e-beam interaction in an SEM for the purpose of patterning defects as described in the main text. The D-peak (marked “D”) in the spectrum after SEM e-beam interaction indicates the presence of defects in the crystal lattice of the graphene channel. . . . .	146
6.19	Blackbody spectra based on Plancks law (black) compared to experimental light emission spectra (blue) of two different graphene FETs excited by applied voltage: (a) graphene FET at $V_g = 0$ V, $V_{sd} = -25$ V with peak emission of $\sim 700$ nm compared to a blackbody at 4000K ; (b) graphene FET at $V_g = 30$ V, $V_{sd} = 7$ V with peak emission at $\sim 600$ nm compared to a blackbody at 4600 K. . . . .	147
A.1	Optical microscope image of an Si/SiO <sub>2</sub> substrate with exfoliated graphite flakes and graphene flakes (enlarged in inset). . .	183
A.2	Schematic illustrations of (a) device structure; (b) shadow mask (not to scale). . . . .	185
A.3	Optical microscope images of (a) graphene sample aligned with wire mask above; (b) the same sample with gold deposited; (c) an enlarged view of (b). . . . .	185

# Chapter 1

## Introduction

### 1.1 History of Graphene

Graphene is known as the world's first two-dimensional (2D) material [1]. It consists of a single atomic layer of graphite approximately 0.3 nm thick. Due to its 2D crystal structure and nanoscale thinness, graphene has extraordinary material properties which are quite different from bulk materials [1]. The discovery of graphene has led to the study of other 2D materials fabricated by similar methods, which are now a large research topic in their own right. Some of these have a similar 2D honeycomb lattice structure like graphene, such as silicene (a silicon allotrope), germanene (a germanium allotrope) and hexagonal boron nitride (alternating boron and nitrogen atoms) [2,3].

Graphene was studied from a theory perspective for decades before a method of fabrication was discovered. In 1947, J. C Wallace postulated the graphene structure in order to calculate the band structure of graphite [4], and it was studied as a hypothetical material that might allow interesting physics to be discovered. However, it was thought that graphene would be a thermally unstable material that could not exist in nature. This was in part due the common misinterpretation, based on the Mermin-Wagner theorem, that finite 2D crystals could not exist [5]. Many of the properties of graphene were eventually predicted over the years and a tremendous body of literature on

the theory of graphene was developed [6].

Finally, in 2004, Konstantin Novoselov and Andre Geim of the University of Manchester discovered a reliable method for fabricating graphene [7], leading to them being awarded the 2010 Nobel Prize in Physics. This groundbreaking result made graphene a real and practical material for the first time, and together with the known theory, it sparked an explosion of experimental research and interest in graphene applications. In their first work on graphene, which was published in *Science*, Novoselov and Geim demonstrated the electric field effect in graphene by fabricating field effect transistors and conducting electrical experiments [7].

Novoselov and Geim's method of fabricating graphene is known as "micro-mechanical exfoliation" (or the "scotch tape" method). In this method, tape is used to successively peel graphite and isolate individual atomic layers. The exfoliation method relies on the fact that weak Van der Waals forces hold graphite layers together as compared to the strong covalent bonds within the plane of the layers. As a result of this process, flakes of micrometer scale area and nanometer scale thickness (single-layer up to multi-layers of graphene) can be randomly distributed on a substrate after removal from the adhesive tape. The graphene flakes are typically identified by optical contrast using an optical microscope [8] and characterized by Raman spectroscopy [9]. Other imaging/characterization methods include electron microscopy and atomic force microscopy [7]. Several additional methods of graphene fabrication have now been developed, such as chemical vapour deposition (CVD), liquid phase exfoliation, or thermal exfoliation [1]. These methods can be simpler, less time consuming, cheaper, or produce larger samples than mechanical exfoliation; nevertheless the original exfoliation method is still often used by researchers because it provides clean and high quality samples (i.e. few defects) allowing for easier interpretation of experimental results [1].

Now, over a decade since the Nobel prize discovery and 70 years since the first theoretical work of Wallace, graphene is a hot research topic, with a dramatic rise of the number of publications occurring each year [10]. Many of the

predicted extraordinary properties of graphene have now been experimentally verified, with some properties even surpassing theoretical limits [1], and it has proven to be stable under ambient conditions [7]. As a relatively new material, graphene continues to be studied for its fundamental properties and potential applications.

## 1.2 Applications

The combined exceptional properties of graphene make it attractive for a variety of applications, from health to electronics. For example, in addition to being the thinnest possible carbon network, it is also highly flexible [11], transparent [8], and stronger than any other known material (Young's modulus of 1 TPa [12]), and it has low toxicity [13]. The electronic properties of graphene are particularly attractive; it is highly conductive, with an electron mobility at room temperature of  $\sim 2.5 \times 10^5$  cm<sup>2</sup>/Vs [14] and can sustain high current densities [15]. For example, a current density on the order of  $10^8$  A/cm<sup>2</sup> was found for a graphene sample of 4  $\mu$ m width and 0.35 nm thickness with a current on the order of a few mA [15]. Graphene is reported to have near-ballistic transport at room temperature [14] and in the limit of zero carrier concentration it still has a minimal conductivity value of  $\sim 4e^2/h$ , where  $e$  is the electronic charge and  $h$  is Planck's constant [6]. Finally, the optical and optoelectronic properties of graphene are also interesting. For example, it can emit light through optical or electronic excitation [16], and it supports surface plasmons with high confinement [17].

A variety of applications are emerging which make use of the various material properties of graphene. Many of them take advantage of the high strength and light weight of graphene. Recent products or conceptual demonstrations include: a car with graphene in its bodywork, made by Briggs Automotive Company [18], graphene-containing bicycle tires by Vittoria [19], graphene headphones by ORA [20] and by Zolo [21], graphene transistors by IBM [22], graphene-based sensors by Biolin Scientific and by Nanomedical Diagnostics

[21], security smart packaging by Siren Technology [21], graphene-based ink by Vorbeck Materials [21], thermal paste by Thermene [21], graphene-based supercapacitors by Urbix Resources [21], graphene-enhanced cycling helmets and shoes by Catlike [21], graphene-enhanced skis by HEAD [21] and a graphene speed tennis racquet by HEAD which has been used by tennis star Novak Djoković [23].

Of particular interest to this work are the electronic, optical, and optoelectronic applications. Many of the electronic applications rely on graphene field effect transistors for on-chip devices, or make use of graphene as transparent electrodes [24,25]. Photonics and optoelectronics applications in development include solar cells, touch screens, displays, lighting, photodetectors, and bio-imaging and labeling [16]. Due to their small size and low toxicity, luminescent graphene quantum dots may become useful for cellular imaging and drug delivery to treat cancer [13].

Due to the ability of graphene to support surface plasmons, there is also potential for applications in plasmonics. Plasmonics uses surface waves confined at the interface between a conductor and an insulator to transmit electrical and optical signals. Topics such as optical sensing and metamaterials have been researched on graphene using plasmonic principles [26,27]. As will be seen in the next chapter (2.3.1), graphene plasmonics and light emission are also connected, leading to new photonic possibilities. For example, researchers have theorized that a compact electrically-controlled graphene light source would have directional, monochromatic, and tunable emission from infrared to X-ray wavelengths, and would be integrable in on-chip devices [28].

### **1.3 Thesis Overview**

Graphene continues to be an exciting research topic which may lead to useful new technologies. The future possibilities are numerous and promising, but in order to fully exploit the potential, we need a broad and thorough understanding of the properties and capabilities of graphene. This is where the current

thesis research fits in. This work is an investigation of the optoelectronic properties of graphene through three experimental studies of light interaction with graphene and light emission from graphene.

The first study used ultrafast pulsed lasers as a way to modify graphene. A femtosecond laser beam was exposed to graphene, and the areas of interaction were characterized using techniques including scanning electron microscopy and atomic force microscopy. The damage effects of this type of interaction were explored and the damage threshold was determined. This work demonstrated the feasibility of patterning multi-layer graphene with a pulsed laser.

The second study used ultrafast laser interaction with graphene to form surface structures. Using a pulsed laser beam with power slightly above the damage threshold of the material, we demonstrated a process that led to the synthesis of parallel periodic structures in the material, with nanometer-scale periodicity. Laser induced periodic surface structures had been observed in various other materials for nearly 50 years before this study, but this was the first demonstration that such structures could be fabricated in graphene. Their dimensions were controllable with the laser parameters and the resulting period of the structures was as small as 70 nm ( $\sim 1/12$  of the laser wavelength), which was amongst the smallest period observed in any material.

In the third study, the light emitting properties of a graphene device were explored through spectroscopy and imaging techniques. A field effect transistor was used to control the flow of carriers through a graphene channel by gate and source-drain voltages. Light emission from the fabricated devices was demonstrated in the visible spectral range. The intensity of the light was controllable through the applied voltages, and the location of the light emission was determined by features such as defects and nanoparticles on the graphene. The goal of this work was to understand the mechanism of the light emission and demonstrate how to control it. In summary, this thesis aims to demonstrate and understand the optoelectronic processes in graphene in order to unlock a greater potential for graphene nanotechnology.

The thesis is outlined as follows: First the background material is covered

in Chapter 2, with a review of the known and relevant optical, electrical, and optoelectronic properties of graphene. Next, Chapter 3 thoroughly describes the physical mechanisms that are related to the three research studies. The three studies resulting from the thesis research are then presented as published (re-formatted to the style of the thesis): “Damage effects on multi-layer graphene from femtosecond laser interaction” [29] in Chapter 4, “Femtosecond laser induced periodic surface structures on multi-layer graphene” [30] in Chapter 5), and “Visible light emission in graphene field effect transistors” [31] in Chapter 6). Finally, conclusions are presented in (Chapter 7), with a summary, future work, and outlook. A bibliography of all literature cited in the thesis is provided at the end. Appendix A follows, describing details of the methods used to fabricate samples and devices. Each chapter includes its own reference section, and the publication chapters (4, 5, 6) also each include their own abstract, introduction, experimental methods, results and discussion, conclusion, and acknowledgements sections. In addition, Chapter 6 includes a supporting information section corresponding to the published paper.

## 1.4 References

- [1] Novoselov K S, Fal’ko V I, Colombo L, Gellert P R, Schwab M G and Kim K 2012 A roadmap for graphene *Nature* **490** 192-200
- [2] Cahangirov S, Topsakal M, Aktürk E, Şahin H and Ciraci S 2009 Two- and One-Dimensional Honeycomb Structures of Silicon and Germanium *Phys. Rev. Lett.* **102**
- [3] Lin Y and Connell J W 2012 Advances in 2D boron nitride nanostructures: nanosheets, nanoribbons, nanomeshes, and hybrids with graphene *Nanoscale* **4** 6908
- [4] Wallace P R 1947 The Band Theory of Graphite *Physical Review* **71** 622-34
- [5] Andrei E Y, Li G and Du X 2012 Electronic properties of graphene: a perspective from scanning tunneling microscopy and magnetotransport *Rep.*

*Prog. Phys.* **75** 056501

- [6] Geim A K and Novoselov K S 2007 The rise of graphene *Nat. Mater.* **6** 183-91
- [7] Novoselov K S, Geim A K, Morozov S V, Jiang D, Zhang Y, Dubonos S V, Grigorieva I V and Firsov A A 2004 Electric Field Effect in Atomically Thin Carbon Films *Science* **306** 666-9
- [8] Nair R R, Blake P, Grigorenko A N, Novoselov K S, Booth T J, Stauber T, Peres N M R and Geim A K 2008 Fine Structure Constant Defines Visual Transparency of Graphene *Science* **320** 1308-1308
- [9] Ferrari A C, Meyer J C, Scardaci V, Casiraghi C, Lazzeri M, Mauri F, Piscanec S, Jiang D, Novoselov K S, Roth S and Geim A K 2006 Raman Spectrum of Graphene and Graphene Layers *Phys. Rev. Lett.* **97**
- [10] Wang J, Chen Y, Li R, Dong H, Zhang L, Lotya M, Jonathan N and Werner J 2011 Nonlinear Optical Properties of Graphene and Carbon Nanotube Composites *Carbon Nanotubes - Synthesis, Characterization, Applications*
- [11] Pei S, Zhao J, Du J, Ren W and Cheng H-M 2010 Direct reduction of graphene oxide films into highly conductive and flexible graphene films by hydrohalic acids *Carbon N. Y.* **48** 4466-74
- [12] Lee C, Wei X, Kysar J W and Hone J 2008 Measurement of the Elastic Properties and Intrinsic Strength of Monolayer Graphene *Science* **321** 385-8
- [13] Shen J, Zhu Y, Yang X and Li C 2012 Graphene quantum dots: emergent nanolights for bioimaging, sensors, catalysis and photovoltaic devices *Chem. Commun.* **48** 3686
- [14] Mayorov A S, Gorbachev R V, Morozov S V, Britnell L, Jalil R, Ponomarenko L A, Blake P, Novoselov K S, Watanabe K, Taniguchi T and Geim A K 2011 Micrometer-Scale Ballistic Transport in Encapsulated Graphene at Room Temperature *Nano Lett.* **11** 2396-9
- [15] Moser J, Barreiro A and Bachtold A 2007 Current-induced cleaning of graphene *Appl. Phys. Lett.* **91** 163513
- [16] Bonaccorso F, Sun Z, Hasan T and Ferrari A C 2010 Graphene photonics

- and optoelectronics *Nat. Photonics* **4** 611-22
- [17] Grigorenko A N, Polini M and Novoselov K S 2012 Graphene plasmonics *Nat. Photonics* **6** 749-58
- [18] News B 2016 The worlds first graphene car is unveiled in Manchester - BBC News *BBC News*
- [19] Anon 2015 Vittorias 2016 Graphene tire range - Vittoria.com *Vittoria.com*
- [20] Anon 2017 ORA introduce the worlds first graphene headphones - News *soundonsound.com*
- [21] Anon 2017 Graphene products: introduction and market status - The graphene experts *graphene-info.com*
- [22] Wu Y, Lin Y-M, Bol A A, Jenkins K A, Xia F, Farmer D B, Zhu Y and Avouris P 2011 High-frequency, scaled graphene transistors on diamond-like carbon *Nature* **472** 74-8
- [23] Anon World premiere of the new HEAD Graphene<sup>TM</sup> Speed racquet — Novak Djokovic *Novak Djokovic*
- [24] Hong J-Y and Jang J 2012 Micropatterning of graphene sheets: recent advances in techniques and applications *J. Mater. Chem.* **22** 8179
- [25] Feng J, Li W, Qian X, Qi J, Qi L and Li J 2012 Patterning of graphene *Nanoscale* **4** 4883
- [26] Bao Q and Loh K P 2012 Graphene Photonics, Plasmonics, and Broad-band Optoelectronic Devices *ACS Nano* **6** 3677-94
- [27] Maier S A 2012 Graphene plasmonics: All eyes on flatland *Nat. Phys.* **8** 581-2
- [28] Wong L J, Kaminer I, Ilic O, Joannopoulos J D and Soljačić M 2015 Towards graphene plasmon-based free-electron infrared to X-ray sources *Nat. Photonics* **10** 46-52
- [29] Beltaos A, Kovačević A, Matković A, Ralević U, Jovanović D and Jelenković B 2014 Damage effects on multi-layer graphene from femtosecond laser interaction *Phys. Scr.* **T162** 014015
- [30] Beltaos A, Kovačević A G, Matković A, Ralević U, Savić-Šević S, Jovanović D, Jelenković B M and Gajić R 2014 Femtosecond laser induced peri-

odic surface structures on multi-layer graphene *J. Appl. Phys.* **116** 204306  
[31] Beltaos A, Bergren A J, Bosnick K, Pekas N, Lane S, Cui K, Matković A  
and Meldrum A 2017 Visible light emission in graphene field effect transistors  
*Nano Futures* **1** 025004

# Chapter 2

## Background

In this chapter we review some of the fundamental properties of graphene relevant to the thesis work, namely the electronic, optical, and optoelectronic properties. This chapter aims to provide the background for the mechanisms and publications that follow in Chapters 3, 4, 5, and 6.

### 2.1 Electronic Properties

#### 2.1.1 Crystal Structure

The crystal structure of graphene consists of a 2D hexagonal array (honeycomb lattice) of carbon (C) atoms, as shown in Figure 2.1. In this transmission electron microscopy (TEM) image, a single layer of suspended graphene is shown in which the higher intensity (brighter) regions correspond to the carbon atoms of the hexagonal lattice.

Graphene is classified as a semimetal (or a zero band gap semiconductor) due to its band structure, which differs from metals or semiconductors [1,2]. It is an allotrope of carbon that forms the basic structure of some other allotropes including graphite, carbon nanotubes and C60 molecules [1]. Graphite is a semimetal consisting of hundreds of thousands of stacked graphene layers that are held together by Van der Waals forces [3]. Electrons moving in delocalized  $\pi$  orbitals parallel to the layers lead to electrical conduction. Carbon

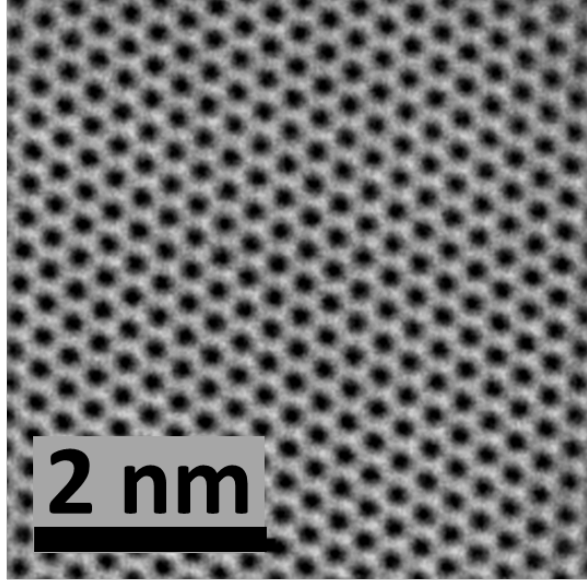


Figure 2.1: TEM image of single-layer suspended graphene (K. Cui, National Institute for Nanotechnology)

nanotubes are a one dimensional (1D) material, formed from rolls of graphene sheets. Electrons moving in the direction of the tube axis leads to electrical conduction. The C<sub>60</sub> molecule, also known as buckminster fullerene or “bucky ball” is a truncated icosahedron cage formed from 20 hexagons and 12 pentagons with a carbon atom at each vertex, analogous to a soccer ball structure. The molecular structure of the bucky ball is like that of wrapped graphene with added pentagons in the hexagonal lattice [4].

The graphene honeycomb lattice structure can be represented as two interpenetrating triangular Bravais lattices in the  $x - y$  plane with two carbon atoms per site, “A” and “B” as shown in Figure 2.2 (a), with primitive lattice vectors  $\vec{a}_1$  and  $\vec{a}_2$ :

$$(2.1) \quad \begin{aligned} \vec{a}_1 &= a\hat{x}, \\ \vec{a}_2 &= \frac{a}{2}\hat{x} + \frac{\sqrt{3}}{2}a\hat{y}, \end{aligned}$$

where  $a = \sqrt{3}a_0 \approx 2.46 \text{ \AA}$  is the lattice constant of the triangular lattice and

$a_0 = 1.42 \text{ \AA}$  is the C-C bond length [5,6].

The electronic structure of carbon is  $1s^2 2s^2 2p^2$  such that four valence electrons are in the  $n = 2$  atomic shell. In graphene, the valence shell orbitals hybridize to form  $sp^2$  hybrid orbitals, so that the electronic structure is  $1s^2 2s 2p_x 2p_y 2p_z$  [5]. For each carbon atom, there are three valence electrons in the  $sp^2$  orbitals ( $2s$ ,  $2p_x$ , and  $2p_y$ ) forming covalent  $\sigma$  bonds with nearest neighbours in the lattice plane angled at  $120^\circ$  from each other and one delocalized electron along the plane in the  $2p_z$  orbital [2]. These  $2p_z$  orbitals hybridize to form  $\pi$  bonds above and below the lattice plane [7]. The  $\sigma$  bonds hold the graphene sheet together and affect the mechanical properties of graphene while the  $\pi$  bonds ( $2p_z$  electrons) are responsible for conduction and are related to the electronic and optical properties. Only the  $\pi$  energy bands are relevant near the Fermi level, while the  $\sigma$  bands are separated in energy by  $> 10 \text{ eV}$  and thus can be neglected in considering the electronic properties [2].

### 2.1.2 Dispersion Relation

The reciprocal lattice of graphene in  $\vec{k}$ -space can be represented as simple hexagonal, as shown in Figure 2.2 (b). The primitive lattice vectors  $\vec{b}_1$  and  $\vec{b}_2$  in this case are defined by [4,5]:

$$(2.2) \quad \begin{aligned} \vec{b}_1 &= \left( \frac{2\pi}{a}, -\frac{2\pi}{\sqrt{3}a} \right), \\ \vec{b}_2 &= \left( 0, \frac{4\pi}{\sqrt{3}a} \right). \end{aligned}$$

The first Brillouin zone is a hexagon, with high symmetry points  $\vec{\Gamma}$ ,  $\vec{M}$ , and  $\vec{K}$ .

At two inequivalent corners of the first Brillouin zone, i.e. the  $\vec{K}$  and  $\vec{K}'$  points, the top of the valence band and bottom of the valence band touch, i.e., there is no energy gap between them, and the dispersion relation (energy  $E$  vs momentum vector  $\vec{k}$ ) becomes linear, as shown in Figure 2.2 (c). An

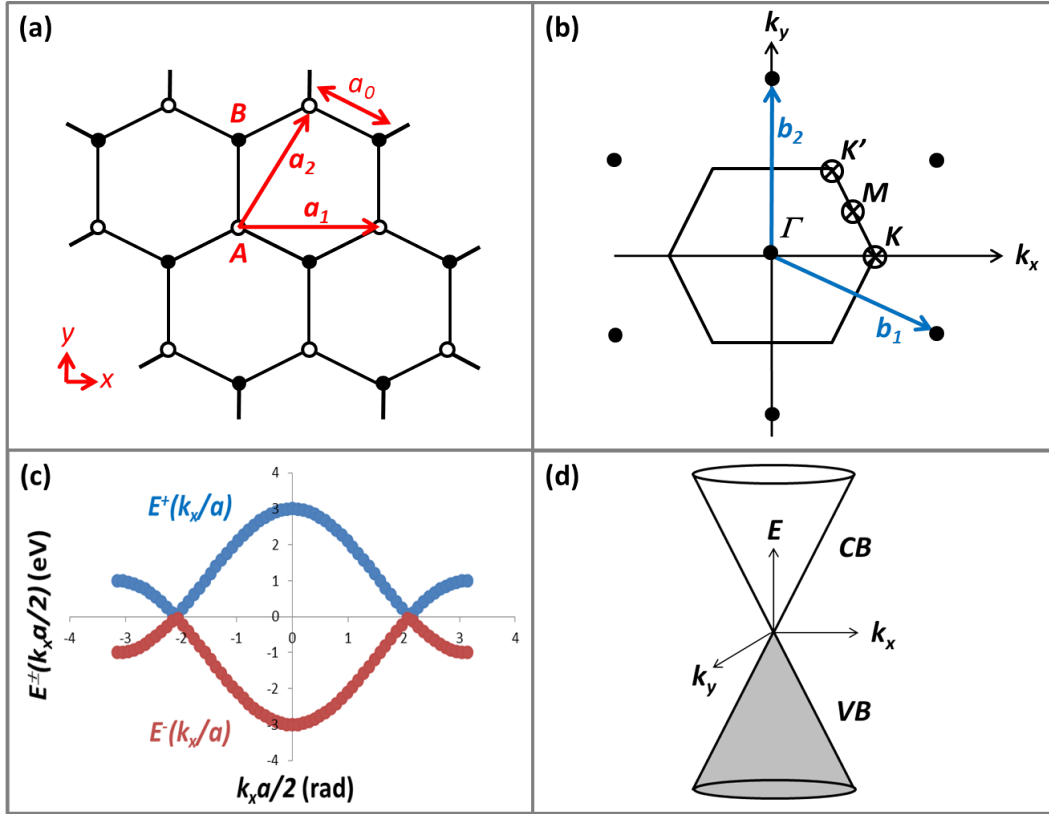


Figure 2.2: Electronic properties of graphene: (a) Crystal lattice in real space, showing A (white) and B (black) atoms, primitive lattice vectors  $\vec{a}_1$  and  $\vec{a}_2$ , and distance between neighbouring atoms  $a_0$ ; (b) Reciprocal lattice in  $\vec{k}$ -space, showing primitive lattice vectors  $\vec{b}_1$  and  $\vec{b}_2$ , the first Brillouin zone (defined by black hexagon) with high symmetry points along the zone boundary (crossed circles)  $\vec{K}'$ ,  $\vec{M}$ , and  $\vec{K}$ , and center  $\vec{\Gamma}$ ; (c) Dispersion relation (equation 2.4 for  $-\frac{2\pi}{a} < k_x < \frac{2\pi}{a}$ ,  $k_y = 0$ , and  $t = 1$  eV); (d) Enlarged view of the dispersion relation near the  $\vec{K}$  and  $\vec{K}'$  points showing the conduction band (CB) and valence band (VB), i.e. the “Dirac cone”

enlarged view of the band structure near the  $\vec{K}$  or  $\vec{K}'$  point (“Dirac points”) plotted vs  $k_x$  and  $k_y$  is shown in Figure 2.2 (d), in which the valence band and conduction band form conical structures known as “Dirac cones”. As shown in Figure 2.2 (c), the linearity of the dispersion relation remains near the Dirac points, extending out to  $E/t \approx \pm 0.5$  before becoming curved [7].

The tight-binding approximation is used to find the electronic band structure of graphene [8]. A superposition of the orbital wavefunctions for  $A$  and  $B$  atoms is considered at each lattice site. The relation between the 2x2 tight-binding Hamiltonian matrix  $H_{TB}(\vec{k})$  and energy  $E(\vec{k})$  can be used to determine the coefficients  $a_k$  and  $b_k$  according to:

$$(2.3) \quad H_{TB}(\vec{k}) \begin{bmatrix} a_k \\ b_k \end{bmatrix} = E(\vec{k}) \begin{bmatrix} a_k \\ b_k \end{bmatrix}.$$

The eigenvalues of  $H_{TB}(\vec{k})$  give the energy levels [2]:

$$(2.4) \quad E^\pm(\vec{k}) = \pm t \sqrt{1 + 4\cos\left(\frac{k_x a}{2}\right) \cos\left(\frac{\sqrt{3}k_y a}{2}\right) + 4\cos^2\left(\frac{k_x a}{2}\right)},$$

where  $t$  is an energy constant related to nearest neighbour hopping. To illustrate, equation 2.4 is plotted in Figure 2.2 (c) for  $-\frac{2\pi}{a} < k_x < \frac{2\pi}{a}$ ,  $k_y = 0$ , and taking  $t = 1$  eV as an arbitrary constant for the sake of calculation. The negative energy branch corresponds to occupied levels (valence band), while the positive branch is empty (conduction band) and the zero energy reference  $E(\vec{k}) = 0$  is the Fermi energy  $E_F$  [2]. Energy levels near the fermi level are related to electron transport.

This “zero band gap” and linear dispersion relation are uncommon in other materials and are responsible for many of the interesting properties of graphene [1,4]. If we consider the group velocity of electrons given by [9]:

$$(2.5) \quad v_g = \frac{1}{\hbar} \frac{dE}{dk},$$

we see that a linear  $E$  vs  $k$  relation will lead to a constant electronic group velocity  $v_g$  since  $dE/dk$  will be constant. This constant velocity has been calculated as  $v_F \approx c/300$ , where  $c$  is the speed of light, which all conduction electrons have regardless of their energy [1]. In comparison, for a typical semiconductor, the dispersion relation is parabolic ( $E$  is proportional to  $k^2$ ), so that  $dE/dk > 0$  and the velocity increases with energy.

The linear dispersion also implies that the conduction electrons in graphene behave as massless relativistic particles, analogous to photons [1,6]. This is apparent from Einstein's energy equation [1]:

$$(2.6) \quad E^2 = m^2 c^4 + c^2 p^2,$$

where  $m$  is the rest mass of electrons and  $p$  is their linear momentum. If  $m = 0$  in this equation, then  $E^2 = c^2 p^2$  or  $E = cp = c\hbar k$ , i.e.  $E$  is proportional to  $k$ , so that the dispersion relation is linear. Hence the electrons in graphene are treated relativistically by the Dirac equation as opposed to the non-relativistic Schrödinger equation.

At the Dirac points  $\vec{K}$  and  $\vec{K}'$ , the Dirac Hamiltonian for massless fermions from relativistic quantum mechanics is applied, with the speed of light being replaced by the Fermi velocity of carriers  $v_F$  [2,6]:

$$(2.7) \quad H_{TB}(\vec{k}) \approx \hbar v_F \vec{\sigma} \cdot \vec{p},$$

where  $\vec{p} = \vec{k} - \vec{K}$ , and the components of  $\vec{\sigma} = (\sigma_x, \sigma_y)$  are the first two Pauli matrices. The corresponding band structure is approximated by the linear dispersion relation for relativistic massless particles [2]:

$$(2.8) \quad E^\pm(\vec{k}) \approx \pm \hbar v_F |\vec{p}|,$$

where

$$(2.9) \quad v_F \approx \frac{\sqrt{3} a t}{2 \hbar}.$$

Using equation 2.9 and experimentally determined values of  $t = 2.575$  eV [10] and  $a = 2.46$  Å [5], the Fermi velocity (electronic group velocity) is found to be  $v_F \approx 1 \times 10^6$  m/s.

### 2.1.3 Electric Field Effect

The electric field effect in graphene was the first effect to be experimentally verified by Novoselov et al. when they fabricated graphene in 2004 [11]. This effect refers to the use of an applied electric field to control the electronic behaviour of a conducting material. The electric field modifies the conductivity (or equivalently the resistivity, resistance, or current) of the material by controlling the quantity of carriers carrying current. It is this controllability of the electronic behaviour of graphene that is behind its potential in electronics and optoelectronics applications.

A typical device that takes advantage of the electric field effect is a field effect transistor (FET), as shown in Figure 2.3 (a). The device consists of three electrodes or terminals known as the source (S), drain (D), and gate (G). A conducting channel (e.g. graphene) atop a substrate is connected to the source and drain. The substrate is typically a semiconductor (e.g. Si) that acts as the gate electrode, and is coated by an insulating layer (e.g. SiO<sub>2</sub>). An applied voltage across two of the terminals (e.g. source to drain) produces an electric field that causes the flow of current through the conducting channel, and an applied voltage across two other terminals (e.g. source to gate, or gate

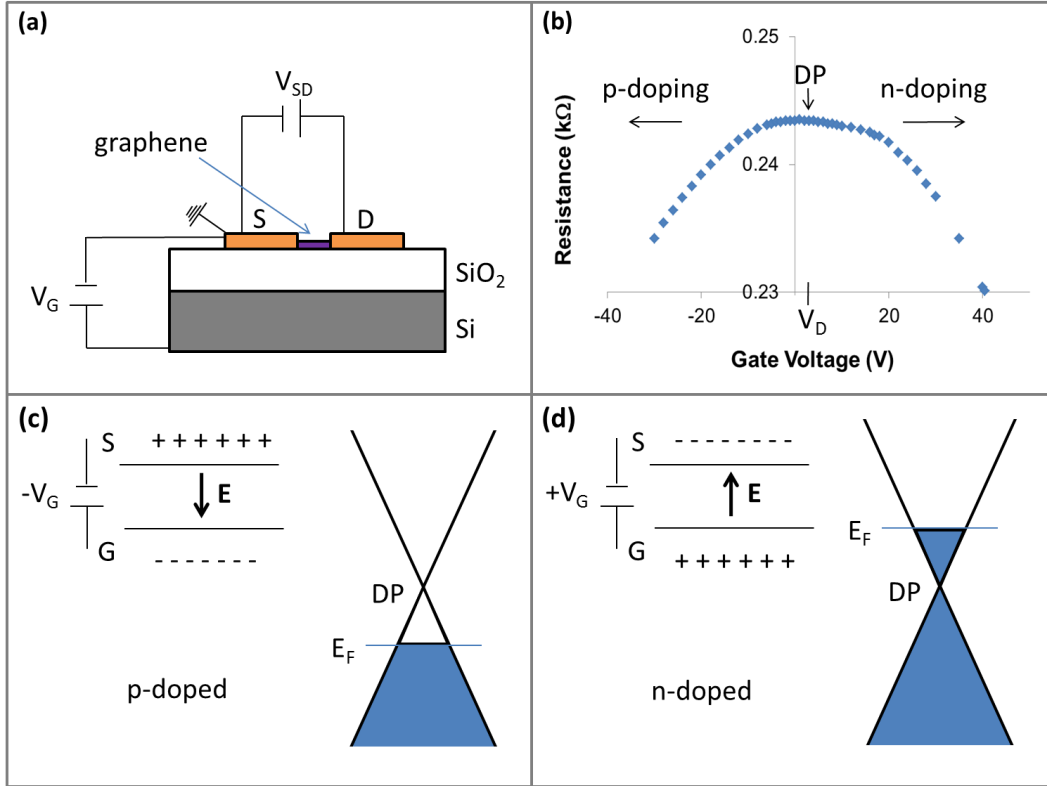


Figure 2.3: Electric field effect in graphene: (a) graphene field effect transistor device schematic, showing source (S), drain (D), gate (G) electrodes, and voltages applied to the source-drain ( $V_{SD}$ ) and source-gate ( $V_G$ ); (b) transfer characteristics of graphene (resistance vs gate voltage), showing the Dirac point ( $DP$ ), Dirac voltage ( $V_D$ ), and doping; (c) p-doped graphene as represented by the field effect transistor device schematic (left), showing the applied electric field ( $\vec{E}$ ) and the graphene dispersion relation (right), showing the Fermi energy ( $E_F$ ); and (d) the same as (c) for n-doped graphene.

voltage ( $V_G$ ) produces an electric field that further controls the flow of current in the channel. The source-drain voltage ( $V_{SD}$ ) controls the current  $I$  linearly for small  $V_{SD}$ , such that the resistance is found from Ohm's Law  $R = V_{SD}/I$  [12].

By varying  $V_G$  in a graphene field effect transistor, the resistance ( $R$ ) of the graphene is modulated, as shown by the transfer characteristics plotted in Figure 2.3 (b). The transfer characteristics form a curve of  $R$  vs  $V_G$  peaking at a maximum resistance value (minimum current) corresponding to the Dirac point ( $DP$ ) (i.e. the charge neutrality point) at the “Dirac voltage” ( $V_D$ ). The

changes in resistance are due to changes in the carrier concentration and type of majority carrier via shifting of the Fermi energy with respect to the  $DP$ , an effect known as the “electronic doping” of graphene [6,1215]. In undoped graphene, the Fermi level is at the Dirac point ( $E_F = DP$ ), and there are an equal number of holes and electrons. With the application of a negative gate voltage ( $V_G < V_D$ ), holes are added so that the Fermi energy shifts down ( $E_F < DP$ ) and the graphene is p-doped, as shown in Figure 2.3 (c). With the application of a positive gate voltage ( $V_G > V_D$ ), electrons are added so that the Fermi energy shifts up ( $E_F > DP$ ) and the graphene is n-doped (Figure 2.3 (d)). In this way, the majority carriers can be controlled through  $V_G$ .

In the field effect transistor device, the graphene and the gate act as capacitors, and the electric field  $E$  across the insulating layer can thus be calculated [6]:

$$(2.10) \quad E = \frac{en}{\epsilon_0\epsilon},$$

where  $n$  is the surface charge carrier density,  $e$  is the electronic charge,  $\epsilon_0$  is the permittivity of space and  $\epsilon$  is the relative permittivity of the insulator. The electric field is controlled by the thickness of the insulator  $d$  and the gate voltage  $V_G$ , such that [6]:

$$(2.11) \quad E = \frac{V_G}{d}.$$

Comparing Equations 2.10 and 2.11, we see that the charge density is directly proportional to the gate voltage as  $n = (\epsilon_0\epsilon V_G)/(ed) = \alpha V_G$ , where  $\alpha$  is a constant.

In neutral graphene, when  $V_G = 0$  V, the residual charge is  $n_0 = 0$ , so that  $V_D = 0$  V. It is possible for a residual charge to exist on the graphene when  $V_G = 0$  V due to substrate doping or doping due to interaction with the ambient environment. In that case  $V_D \neq 0$  V and the amount of shifting of

$V_D$  depends on the residual charge on the graphene  $n_0$  when  $V_G = 0$  V [13]:

$$(2.12) \quad V_D = -\frac{n_0 e}{C_G},$$

where  $C_G$  is the gate capacitance per unit area. The charge carrier density of the graphene in this case is given by [13]:

$$(2.13) \quad n = \frac{C_G}{e}(V_G - V_D).$$

## 2.2 Optical Properties

The relativistic character of electrons in graphene is also responsible for its interesting optical properties [1]. These properties come from optical transitions at the Dirac point between the valence and conduction bands, which can occur for any photon energy due to the zero band gap.

### 2.2.1 Absorption and Transmission

The high frequency conductivity in graphene  $G$  is theoretically constant, and given by [16]:

$$(2.14) \quad G = \frac{e^2}{4\hbar} = \frac{c}{4}\alpha,$$

where  $\alpha$  is the fine structure constant, given in turn by [2,16]:

$$(2.15) \quad \alpha = \frac{e^2}{\hbar c} \approx \frac{1}{137}.$$

Because of this universality, the transmittance  $T$  and the reflectance  $R$  in graphene are also universal quantities [16]:

$$(2.16) \quad T = (1 + 2\pi G/c)^{-2} = (1 + \pi\alpha/2)^{-2},$$

and

$$(2.17) \quad R = \frac{1}{4}\pi^2\alpha^2T.$$

At visible wavelengths ( $\sim 400 - 700$  nm), less than 0.1% of light is reflected from single-layer graphene [16], reaching nearly 2% for 10-layer graphene [17]. In this wavelength region, the absorption is independent of the photon energy [1]. The absorbance per layer (for suspended graphene) has a value of [2,16]:

$$(2.18) \quad A = 1 - T \approx \pi\alpha = 2.3\%.$$

This absorbance is considered to be quite high for such a thin material. The transmittance  $T$  is thus 97.7% for single-layer graphene.

For few-layer graphene, the transmittance in the visible range has been shown to be [16]:

$$(2.19) \quad T = 1 - \pi\alpha N,$$

where  $N$  is the number of layers, for up to 5 layers. As with the absorbance, the transmittance of few-layer graphene displays a linear scaling behaviour with the number of layers. On the other hand, for multi-layer graphene of up to 65 layers, the transmittance in the visible range can be well described by [18]:

$$(2.20) \quad T = (1 + 1.13\pi\alpha N/2)^2.$$

### 2.2.2 Visualization

It is possible to visualize single-layer and multi-layer graphene samples and deduce the number of layers using an optical microscope [2,11,16]. By measuring the transmitted light through multi-layer graphene of varying numbers of layers, the 2.3% absorbance per layer leads to varying transmittance that appears as contrast between the background and each additional layer in an optical microscope image [16]. By comparing the intensity of the transmitted light to the background, the number of layers can be determined.

Using reflected light with multi-layer graphene samples on a silicon (Si) substrate coated with a layer of silicon dioxide ( $\text{SiO}_2$ ), interference effects within the  $\text{SiO}_2$  layer lead to optical contrast that scales linearly with the number of graphene layers (up to six layers) [11,17]. The thickness of the  $\text{SiO}_2$  and the wavelength of the light source determine the amount of contrast. The maximum contrast was achieved using either  $\sim 300$  nm or  $\sim 100$  nm of  $\text{SiO}_2$  for a typical optical microscope setup using white light [2,11,17]. This technique relies on the Rayleigh (elastic) scattering of photons from the sample [17], as opposed to the Raman (inelastic) scattering technique described in the next section.

An example optical microscope image of an exfoliated sample including single-layer, bi-layer, and few-layer graphene on an Si/ $\text{SiO}_2$  substrate is shown in Figure 2.4 (a). This image was collected by reflecting light off the sample, using a typical microscope white light source. The graphene sample appears a darker shade than the surrounding substrate. Areas of different numbers of layers (single-layer, bi-layer, and few-layer) are apparent by the varied contrast, where the darker regions correspond to more graphene layers.

The image contrast is given by the difference between the intensity of reflected light from the bare substrate and from the sample on the substrate. A

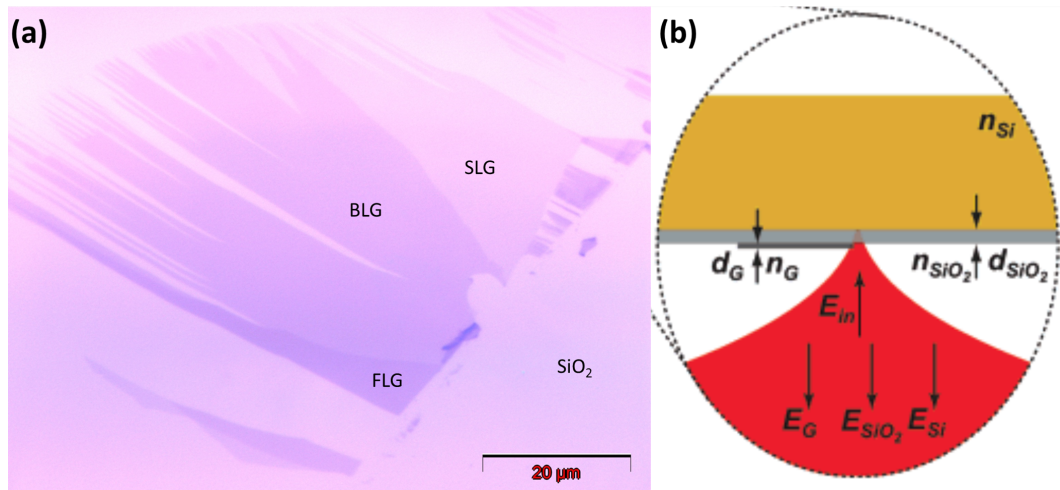


Figure 2.4: Visualizing graphene: (a) Optical microscope image of an exfoliated graphene sample on an Si/SiO<sub>2</sub> substrate, collected by reflected white light, in which single-layer (SLG), bi-layer (BLG), and few-layer (FLG) graphene regions are marked; (b) Schematic cross-section of a graphene (G) sample (dark grey) on an Si (yellow)/SiO<sub>2</sub> (light grey) substrate viewed by an inverted microscope objective (red). Refractive indices  $n$  and thicknesses  $d$  are marked for the various layers. The incoming ( $E_{in}$ ) and reflected fields ( $E_G$ ,  $E_{SiO_2}$ ,  $E_{Si}$ ) are marked for the various surfaces. The schematic in (b) was reprinted with permission from [17], <http://dx.doi.org/10.1021/nl071168m>. Copyright (2007) American Chemical Society.

schematic cross-section of a graphene sample on an Si/SiO<sub>2</sub> substrate viewed by an inverted microscope is shown in Figure 2.4 (b) [17]. The total detected intensity from the sample is a superposition of the reflected light at multiple interfaces; air-graphene, graphene-SiO<sub>2</sub>, and SiO<sub>2</sub>-Si, while that from the substrate is a superposition of reflected light from the air-SiO<sub>2</sub> and the Si. The detected intensity from the sample is dominated by the light reflected by the graphene and that reflected from the Si that has been transmitted through the graphene and the SiO<sub>2</sub>. The SiO<sub>2</sub> layer acts as a spacer, and the contrast from the sample is due to the phase variation of the reflected light.

For the general case of a multi-layer graphene sample, spacer, and substrate, the total electric and magnetic fields in each layer can be calculated using boundary conditions at each interface [17]. A multi-layer graphene sample of less than six layers is assumed to be optically equivalent to a superposition of individual graphene layers. Interference from multiple reflections lead to the scaling behaviour of the contrast with the number of layers.

### 2.2.3 Raman Spectrum

Raman spectroscopy is a common optical technique for material characterization, as each material has a unique Raman spectrum that is sensitive to the material atomic structure and bonding [19]. The technique consists of the inelastic scattering of light from optical phonons of a material, as originally discovered by C. V. Raman who won a Nobel prize for his work in 1930. The change of frequency of the scattered light is measured to produce the spectrum and characterize the material [1]. Raman spectroscopy was first used to characterize graphene in 2006 by Andrea C. Ferrari et al. [20], and is now generally the primary method in use. Raman spectra are used not only to identify the graphene, but also to determine the quality and the number of layers in the sample.

In an inelastic scattering process, an incoming photon of frequency  $\omega_1$  is scattered by a material, causing the emission or absorption of a phonon of

frequency  $\Omega$  and a change in the frequency of the scattered photon to  $\omega_2$ . Due to conservation of energy, the following relation holds:

$$(2.21) \quad \omega_1 = \omega_2 \pm \Omega,$$

where the “+” corresponds to the emission of a phonon, known as a “Stokes” scattering, and the “-” corresponds to the absorption of a phonon, known as “Anti-Stokes” scattering. Thus the frequency shift of the photon  $\Delta\omega$  is used to measure the phonon frequency.

Raman scattering is a Stokes process, meaning that the scattered photon has a downshift in frequency, i.e.  $\omega_2 < \omega_1$ . Stokes scattering is likely to occur at any temperature, as the material does not have an existing phonon already before the light scattering. Anti-Stokes scattering, on the other hand, corresponds to an up-shift in photon frequency, such that  $\omega_2 > \omega_1$  and therefore occurs at higher temperatures [1].

Example Raman spectra are shown in Figure 2.5 for single-layer (SLG), bilayer (BLG) and trilayer (TLG) exfoliated graphene samples ((a), (b), and (c), respectively) and a trilayer CVD graphene sample (d). Optical images of the corresponding samples are shown in the insets. The prominent peaks used to identify the graphene material are the G peak at  $\sim 1580 \text{ cm}^{-1}$  and 2D peak (also known as G') at  $\sim 2700 \text{ cm}^{-1}$  [2022]. The G peak corresponds to an in-plane vibrational mode relating to the  $\text{sp}^2$  hybridized atoms forming the graphene lattice [19]. The 2D peak is a vibrational mode that has approximately twice the frequency of the D peak at  $\sim 1350 \text{ cm}^{-1}$ . The D peak is an in-plane vibrational mode that is induced by disorder (symmetry breaking) in the graphene crystal lattice, caused by scattering from defects. Hence, it does not appear in the spectrum of pristine (high quality) graphene, but appears only when defects are present (lower quality graphene). For example, in Figure 2.5, the mechanically exfoliated graphene samples ((a), (b), and (c)) are of high crystalline quality and hence the Raman spectra do not have D peaks,

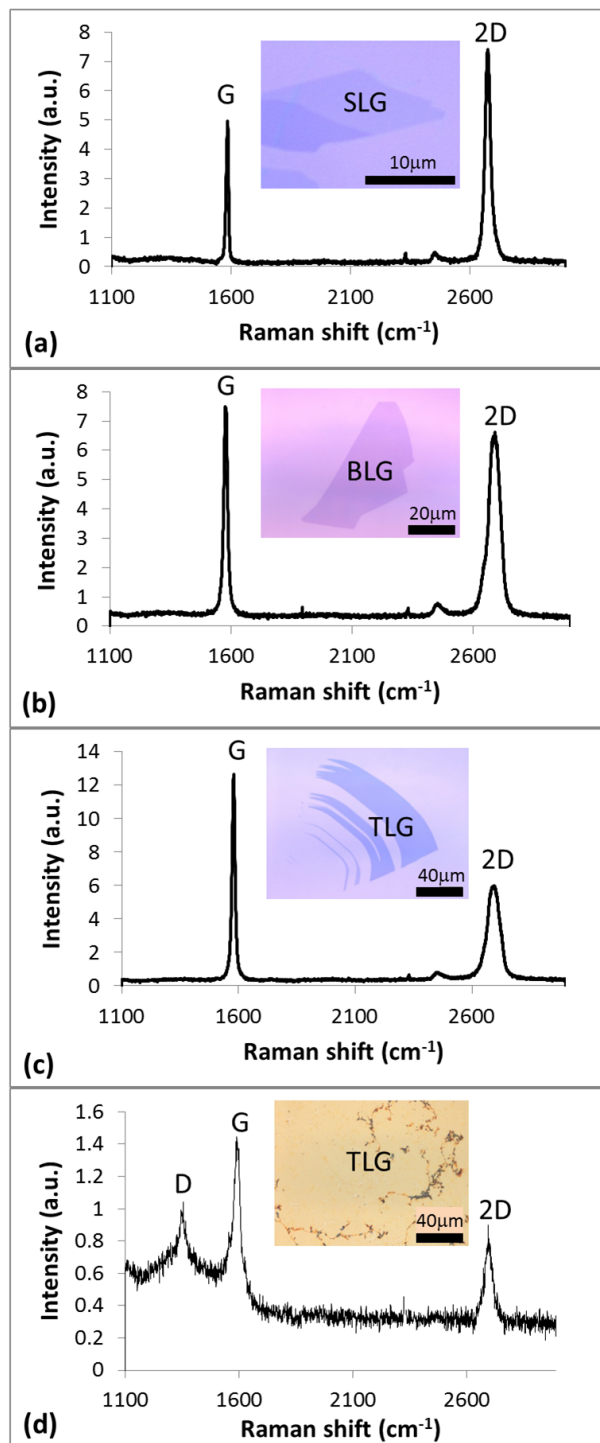


Figure 2.5: Raman spectra of (a) exfoliated single-layer graphene (SLG); (b) exfoliated bilayer graphene (BLG); (c) exfoliated trilayer graphene (TLG); (d) CVD trilayer graphene (TLG). Insets: optical microscope images of the corresponding samples.

whereas the CVD sample (d) has a large D peak due to disorder. The ratio of the intensity of the D peak ( $I_D$ ) to the G peak ( $I_G$ ) indicates the level of disorder, where an increased  $I_D/I_G$  means increased scattering due to greater disorder [22]. In the regime of extremely high defect densities where the carbon structure is mainly amorphous, this ratio method is not applicable as all the peaks are significantly attenuated [22].

The Raman spectrum is useful for determining the number of graphene layers, up to  $\sim 10$  layers. As the number of layers changes, the G and 2D peaks change their shape, position, and relative intensity [19,23], as shown in Figure 2.5 (a) and (b) for differences between bilayer and trilayer samples. Single-layer graphene can be identified by an intensity ratio between the 2D and G peaks of  $I_G/I_{2D} \approx 1/4 - 1/2$  and a sharp symmetric 2D peak [19,20,22,23]. As the number of layers increases, the ratio  $I_G/I_{2D}$  increases while the 2D mode splits into multiple overlapping modes due to interactions between the layers. The 2D peak also becomes wider, shorter, and shifts to a higher frequency. The G peak slightly decreases in frequency and increases intensity linearly with increasing number of layers [19].

A formula relating the number of layers  $N$  to the position of the G peak  $\omega_G$  (in wavenumbers) is given by [19]:

$$(2.22) \quad \omega_G = 1581.6 + 11/(1 + N^{1.6}),$$

for Raman spectra of graphene using laser excitation of 532 nm wavelength. The Raman spectra of graphene for varying numbers of layers from 1-10 are available in the literature as a reference for determining the number of layers of measured samples [20,23]. Temperature, doping level, and strain may also affect the Raman spectrum [19].

## 2.3 Optoelectronic Properties

We have now seen some of the important electronic and optical properties that are responsible for the interesting nature of graphene. By combining the two, even more interesting phenomena arise such as photocurrent, electroluminescence, and surface plasmons [2,24]. Electroluminescence and other electrically-driven light emission will be discussed in the next chapter (Mechanisms). This section is devoted to the properties of plasmons and graphene plasmons, which are fundamental concepts that take part in several of the mechanisms discussed in the next chapter and the thesis research.

### 2.3.1 Plasmons

#### Plasma Oscillations in a Bulk Medium

A plasma oscillation is a coherent oscillation of conduction electrons with respect to a fixed lattice of positive ions excited in an electrically neutral medium, i.e. the “plasma” (usually a metal or doped semiconductor) [1,25]. These oscillations can occur when charge fluctuations in the plasma lead to accumulation of charge in a region where the local density of electrons exceeds the density of positive charge carriers [1,26]. The repulsive forces between electrons create an electric field which works to restore the equilibrium by moving the electrons away from the region. With this motion, the electrons go further than their original position, creating an electric field in the opposite direction. The cycle continues leading to the harmonic oscillation of the electrons, corresponding to a charge density wave [26].

The resonant frequency of the plasma oscillation is calculated using Maxwell’s equations for the case of a collective motion of electrons, and solving the equation of motion of the electrons as functions of the electric field [1]. In a bulk medium, the plasma oscillation is longitudinal, such that the electric field is parallel to the direction of wave propagation (i.e. direction of the oscillation). The equation of motion for the longitudinal component of the electric field  $\vec{E}_l$

is given by [1]:

$$(2.23) \quad \frac{\partial^2 \vec{E}_l}{\partial t^2} + \omega_p^2 \vec{E}_l = 0.$$

Here,  $\omega_p$  is the plasma frequency that represents the critical frequency of transparency for electromagnetic waves in a plasma [26], given by [1]:

$$(2.24) \quad \omega_p = \left( \frac{Ne^2}{\epsilon_0 m_0} \right)^{1/2},$$

where  $N$  is the number of electrons per unit volume,  $e$  is the electron charge,  $\epsilon_0$  is the permittivity of free space, and  $m_0$  is the electron mass. The wave-like solutions of Equation 2.23 determine the frequency of the plasma oscillation to be  $\omega = \omega_p$ , which is a dispersionless relation (independent of wave vector). Equation 2.23 shows that the plasma oscillations behave as harmonic oscillators with frequency  $\omega_p$  defined in Equation 2.24.

In the quantum mechanical picture, harmonic oscillators have quantized energies, and hence so do plasma oscillations [1]. The quantized energies are in units of  $\hbar\omega_p$ , where  $\hbar$  is Planck's constant. The quantized oscillation corresponds to a quasi-particle (or wave), known as the "plasmon", with a corresponding frequency and wavelength.

Excitation of plasmons in a bulk medium can be achieved by inelastic scattering of electrons or photons incident on the plasma [1]. Typically, excitation with electrons in the keV energy range is used for metals, and excitation with photons in the optical frequency range (visible light) is used for doped semiconductors. The incoming energy of the particle  $E_{in}$  must be greater than the plasmon energy  $\hbar\omega$  for the excitation to occur. The energy of the outgoing particle  $E_{out}$  is related to the plasmon energy through the conservation of energy [1]:

$$(2.25) \quad E_{out} = E_{in} - n\hbar\omega,$$

where  $n$  is the number of plasmons excited in the plasma.

## Surface Plasmons

A plasmon may be of three different types: the “volume plasmon” (also known as “bulk plasmon”); “surface plasmon” (SP) or “nanoparticle plasmon” (also known as “localized plasmon”), depending on whether the plasmon occurs in a bulk material, at a surface, or within a nanoparticle. For graphene (a flat, thin, conductive surface), surface plasmons are of particular interest. In this section we discuss some important properties of surface plasmons and graphene surface plasmons (“graphene plasmons”).

Surface plasmons are plasmons that are confined at the interface of a conductor and a medium with different optical properties, such as a metal/dielectric or metal/vacuum interface [1,25,27,28]. The plasmon travels along the interface with a wave vector  $\vec{k}$ , as shown in Figure 2.6 [29]. The oscillating charges create an electromagnetic field extending into both media with both transverse and longitudinal components [29]. Using the axis system defined in Figure 2.6, the electric field has components in the  $x$  and  $z$  directions, while the magnetic field has a component in the  $y$  direction. The fields have a maximum intensity at the surface, and disappear far from the surface [29]. The transverse component of the electric field has an amplitude that decays exponentially with distance from the interface [1].

Because of the associated electromagnetic field with the oscillating charges, some authors refer to surface plasmons as electromagnetic surface waves [29]. Another term used for an evanescent electromagnetic surface wave coupled to plasma oscillations is a “surface plasmon polariton” (SPP) [7,30]. Other authors define a surface plasmon polariton as a coupled system (or combined excitation) of a photon and surface plasmon, in which the word “polariton”

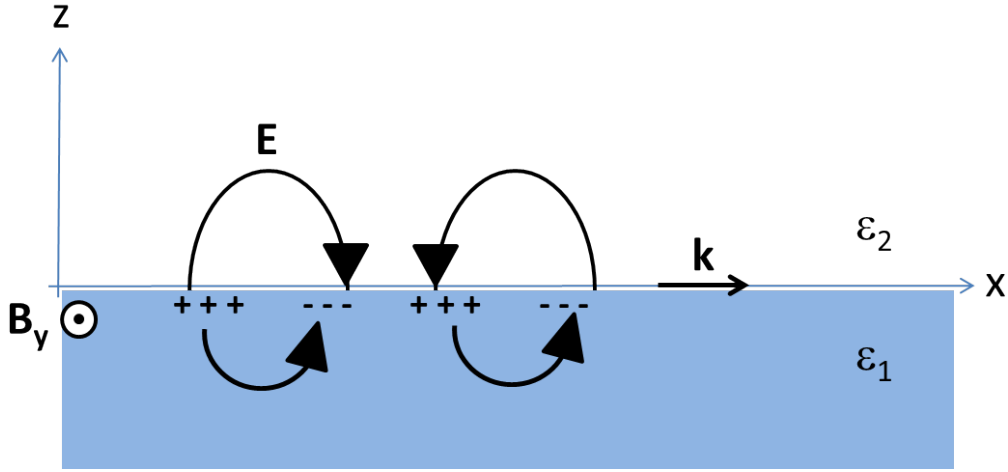


Figure 2.6: Schematic illustration of a surface plasmon at the interface of two media  $\epsilon_1$  (plasma), and  $\epsilon_2$  (dielectric or vacuum), showing the electric field ( $\vec{E}$ ), magnetic field ( $\vec{B}_y$ ) and wave vector  $\vec{k}$ . This illustration was modeled after several references [1,7,28,29].

abbreviates a coupled electric *polarization-photon* wave [1,31,32]. While some authors use the two terms, surface plasmon and surface plasmon polariton, interchangeably [25], the latter term typically refers to a surface plasmon (or electron oscillations) coupled with an electromagnetic field [28]. In this thesis both terms are used according to the literature cited.

Using Maxwell's equations and applying boundary conditions for the electric and magnetic fields at the interface, the allowable surface-bound modes are determined leading to the dispersion relation of the plasmons. We use as a commonly known example an interface between a metal and a dielectric, and compare it to a graphene/dielectric interface [1,7,25].

The derivation for the allowable surface-bound modes at a metal/dielectric interface leads to an important relation between the dielectric constants and wave vectors [1,7]:

$$(2.26) \quad \frac{\epsilon_d}{k_d} + \frac{\epsilon_m}{k_m} = 0,$$

where  $k_m$  and  $k_d$  are the wave vector magnitudes in the metal and dielectric, respectively, and  $\epsilon_m$  and  $\epsilon_d$  are the dielectric constants of the metal and dielectric, respectively. For the electromagnetic wave to be confined to the interface, the real part of  $k_m$  and  $k_d$  must be positive. Hence, considering Equation 2.26, the dielectric constants  $\epsilon_m$  and  $\epsilon_d$  must have opposite signs for surface plasmons to exist.

The derivation for a metal/dielectric interface relates to the configuration shown in Figure 2.6, i.e. a transverse magnetic (TM or p-polarized) wave, in which the surface-bound modes exist. Using a similar derivation, solutions for transverse electric (TE or s-polarized) surface waves (with the electric field in the  $y$ -direction of the figure) are not possible for a metal/dielectric interface [1,7]. However, in graphene both TM and TE SPP modes could be supported depending on the chemical potential  $\mu$  (or Fermi level) [32]. Higher chemical potentials ( $|\mu| > \hbar\omega/2$ ) are associated with the usual TM modes, while lower chemical potentials are associated with TE modes.

The dispersion relation for the in-plane wave vector  $k_{\parallel}$  of an SP or SPP at a metal/dielectric interface is given by [1,7,25]:

$$(2.27) \quad k_{\parallel} = \frac{\omega}{c} \sqrt{\frac{\epsilon_m \epsilon_d}{\epsilon_m + \epsilon_d}},$$

where  $\omega$  is the plasmon frequency and  $c$  is the speed of light. In Equation 2.27, the dielectric constant of the dielectric is assumed to be real and independent of frequency, while that of the metal (assuming it has zero damping) is complex and a function of frequency, given by [1,7]:

$$(2.28) \quad \epsilon_m = 1 - \frac{\omega_p^2}{\omega^2},$$

where  $\omega_p$  is defined in Equation 2.24. We can see from Equations 2.27 and 2.28 that  $k$  depends on  $\omega$ , and vice versa. So for surface plasmons (unlike bulk

plasmons), there is dispersion and the frequency depends on the wave vector (as well as the dielectric constants of the two media).

For doped graphene atop a substrate, TM surface plasmon modes are sustained, and the dispersion relation is given by [33]:

$$(2.29) \quad k \approx \frac{\hbar^2}{4e^2 E_F} (\epsilon + 1) \omega (\omega + i/\tau),$$

where  $\epsilon$  is the permittivity of the substrate that the graphene is atop, and  $\tau$  is the relaxation time of excited carriers. An example SPP dispersion relation for a graphene/dielectric interface is shown in Figure 2.7 (solid curve) [30]. The dispersion of light in the dielectric is also shown for comparison (straight dashed line), given by [25,30]:

$$(2.30) \quad k_{light} = \omega \frac{\sqrt{\epsilon_d}}{c},$$

where the light has wave vector  $k_{light}$  and frequency  $\omega$ . These plots are similar to those for a metal/dielectric interface [1,7,25], in which the SPP curve lies to the right of (or below) the light line.

At small wave vector values, the metal/dielectric SPP dispersion curve approaches that of the light line. The SPP in this regime resembles a Sommerfeld-Zenneck surface wave, i.e. a light wave propagating parallel to the surface [7]. At large wave vector values, the group velocity  $v_g = \partial\omega/\partial k$  approaches zero. In this regime, the SPP dispersion curve levels off and approaches an asymptote called the surface plasmon frequency  $\omega_{sp}$ , given by [7]:

$$(2.31) \quad \omega_{sp} = \frac{\omega_p}{\sqrt{1 + \epsilon_d}}.$$

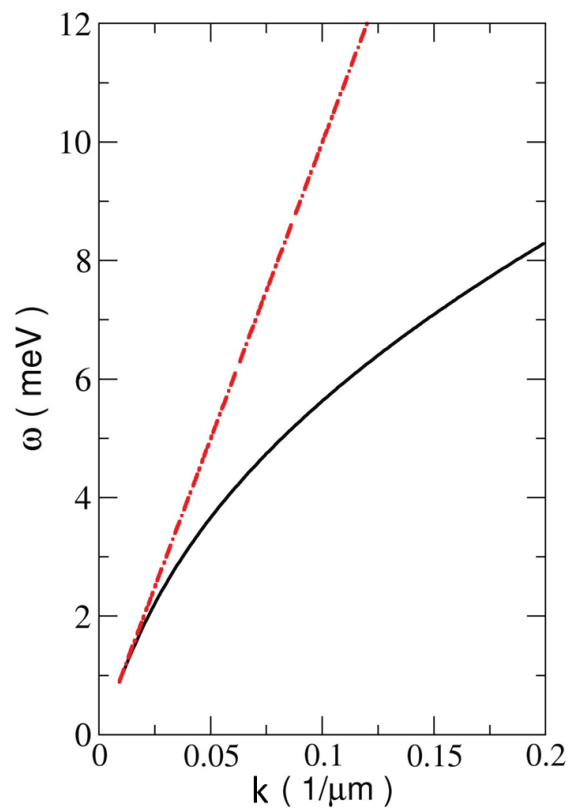


Figure 2.7: Example surface plasmon polariton dispersion relation of graphene (black solid curve) compared to the light line (red dashed line). Republished (adapted) with permission of World Scientific Publishing Co., Inc., from <http://dx.doi.org/10.1142/S0217979213410014> [30], copyright (2013); permission conveyed through Copyright Clearance Center, Inc..

## Excitation

The excitation of SPPs (or SPs) can be achieved using incident electrons or photons. In a typical electrical excitation scenario, plasmons can be excited by the transmission of electrons through a thin film [29]. The incoming electrons transfer energy and momentum to the solid and also scatter from the film. The energy loss of the scattered electrons is determined to obtain information about the excited plasmons. Optical excitation is, however, more common than the electrical type. The electromagnetic field of incoming photons induces the displacement of electrons with respect to the ion lattice thus exciting the plasmon oscillation [25].

To optically excite surface plasmon polaritons, there needs to be a momentum and frequency match between the incident wave and the SPP due to the conservation of momentum. For the SPP dispersion relation (of a graphene/dielectric or metal/dielectric interface), the SPP modes lie below the light line [30]. This means that it is not possible to couple light directly into SPPs (on a smooth surface), because the wave vectors do not match for the same frequency [1,30]. The wave vector (or momentum) of the surface plasmon is greater than that of a photon with the same frequency (or energy). This can be observed by comparing the SPP dispersion curve to the light line in the example of Figure 2.7. The same is true for the opposite scenario, i.e. light cannot be directly decoupled (emitted) from an SPP due to the momentum mismatch.

In order to couple/decouple light to/from SPPs, a structural modification must be done in order to overcome this mismatch. Typically, this is achieved by scattering using diffraction gratings, scattering from defects at the conductor surface, or by placing a prism directly above or below a thin metallic film [1,30]. In the latter scenario, light incident on the prism experiences total internal reflection inside the prism and produces an evanescent wave at the surface of the metal that can excite surface plasmons [34].

Surface plasmons in graphene can be excited in a variety of ways including

prism coupling, grating-coupling, or excitation by a moving line of charge parallel to the graphene [1,7,30]. A primary example of electrical excitation of graphene plasmons is the quantum Čerenkov effect, which is described in detail in Section 3.3.5. Typically, graphene plasmons have been optically excited, utilizing incident light of infrared or terahertz wavelengths [30,32,33,35].

## Radiation

Two types of surface plasmon modes exist: those which can couple directly with light (i.e. be optically excited) and decay by light emission (radiative modes), and those which generally do not couple directly with light or decay by light emission (non-radiative modes) [34]. In this section we discuss these two modes, and in particular ways in which surface plasmons can lead to light emission.

The two types of modes are classified by the relation of their phase velocity  $v_p$  to the speed of light  $c$ . The phase velocity is given by:

$$(2.32) \quad v_p = \frac{\omega}{k}.$$

Radiative modes occur when the surface plasmon phase velocity is greater than the speed of light:

$$(2.33) \quad v_p > c.$$

Non-radiative modes occur when the surface plasmon phase velocity is less than the speed of light:

$$(2.34) \quad v_p < c.$$

For example, on thin silver films, the radiative surface plasmon modes have

been shown to radiate as light in almost all directions and the peak intensity of the radiation occurs at the plasmon frequency [36]. Non-radiative modes on thin or thick films can be made to radiate by reducing the wave vector of the plasmon, so that the condition for radiative modes  $v_p > c$  is satisfied [28,34]. For example, radiation has been achieved when using electron excitation of SPs at grazing incidence on a rough surface or normal incidence on a grating surface [34].

In an ideal semi-infinite medium, SPP modes are non-radiative [28]. However, in thin films, the SPP modes can be non-radiative or radiative leading to the possibility of light emission [28]. Due to the interaction of electric fields of both surfaces involved with the thin film there are both tangential and normal charge oscillations. The tangential oscillations always satisfy  $v_p < c$ , so that they are non-radiative. The normal oscillations, on the other hand, might satisfy  $v_p > c$ , so that they are radiative. Hence, the normal oscillations are responsible for light emission from the thin film.

Surface plasmons (both radiative and non-radiative) can also radiate light when they interact with surface roughness or interior inhomogeneities in the conductor [37]. Kretschmann applied electromagnetic scattering theory to a rough metal/air interface and described the mechanism of light emission from this process [37]. In addition to the currents on a smooth surface involved with an SP, the incident electromagnetic wave generates polarization currents on the rough boundary. It is these additional polarization currents that are the sources of light emission.

### **Coupling/Decoupling with Gratings**

We use here as an example one of the most common methods for coupling or decoupling light to or from SPPs in a graphene/dielectric or metal/dielectric interface – by the incorporation of a grating structure, patterned into the conductor or the dielectric [7,25]. The coupling/decoupling process is illustrated in Figure 2.8 (a) and (b), respectively, for the case of a graphene sheet on a patterned dielectric grating structure.

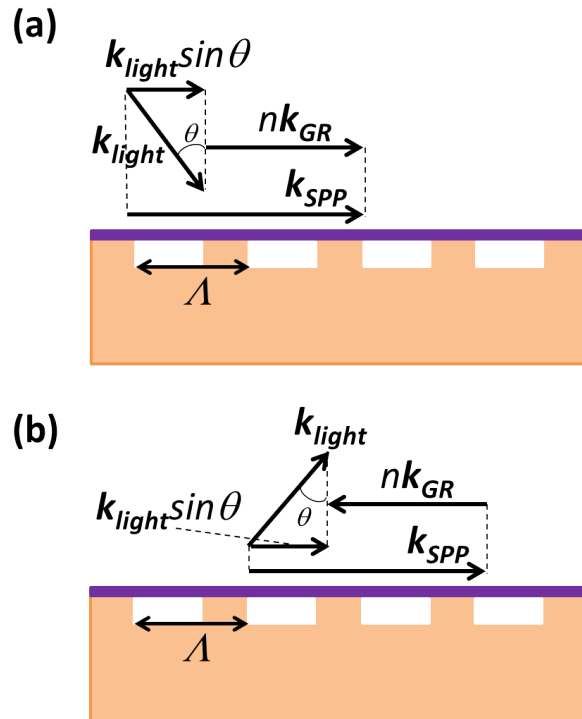


Figure 2.8: Wave vector matching for (a) coupling and (b) decoupling light to/from SPPs using a graphene sheet (purple) atop a patterned grating structure in a dielectric (orange). This illustration was modeled after several references [7,25,38].

In this scenario, light is incident on the grating leading to a set of diffraction orders that provide additional wave vector contributions in multiples of the grating wave vector. Excitation of an SPP (i.e. coupling light to an SPP as shown in Figure 2.8 (a)) occurs when the wave vectors are balanced to satisfy momentum conservation. The opposite effect also can occur when the wave vectors are balanced (i.e. decoupling light from an SPP as shown in Figure 2.8 (b)). In this case, there will be an outgoing light wave from the interface after a previously excited SPP is incident on the grating.

The phase-matching equation using a grating with a metal/dielectric or graphene/dielectric interface is [7,25]:

$$(2.35) \quad k_{SPP} = k_{light} \sin(\theta) \pm nk_{GR},$$

where  $k_{SPP}$  is the SPP wave vector,  $k_{light} = 2\pi/\lambda$  is the wave vector of the light (also as in Equation 2.30),  $\theta$  is the angle of incidence (or decoupling) of the light,  $n$  is an integer,  $k_{GR} = 2\pi/\Lambda$  is the grating wave vector,  $\lambda$  is the wavelength of light in the dielectric and  $\Lambda$  is the grating period. Hence, a relation is established between the wave vector (or wavelength) of the SPP, the wavelength of incident light, the angle of incidence (or decoupling) and the grating period. The “+” in Equation 2.35 corresponds to the coupling of light to SPPs (Figure 2.8 (a)), and the “-” corresponds to decoupling light from SPPs (Figure 2.8 (b)).

### **Graphene Plasmon Advantages**

Finally, we conclude this section by discussing some of the advantages of graphene plasmonics. These include low loss through long propagation lengths, dynamic tunability of the spectrum by electrical gate control of the charge carrier density, extremely high electromagnetic field confinement, and low phase velocity (down to a few hundred times smaller than the speed of light) [32,3941].

The long propagation lengths are due to the long lifetime of graphene plasmons [32]. The distances are given by  $1/Im(k)$ , approximately proportional to  $1/\tau$  [33]. Typical propagation lengths can reach above 100 times the graphene plasmon wavelength [33]. The degree of field confinement is defined by the ratio (unitless) of the graphene plasmon wavelength  $\lambda_{GP}$  to the free-space-light wavelength  $\lambda_0$  [30,32,33,35], given by [33]:

$$(2.36) \quad \frac{\lambda_{GP}}{\lambda_0} \approx \frac{4\alpha}{(\epsilon + 1)} \frac{E_F}{\hbar\omega},$$

where  $\alpha$  is the fine structure constant.

From Equations 2.29 and 2.36, we can see that the properties of graphene plasmons can be controlled by various factors including the permittivity of the substrate, the Fermi energy of graphene and the free-space-light wavelength. For example, Bao *et al.* [32] calculated some values for graphene plasmons excited by light of 10  $\mu\text{m}$  wavelength, with graphene having a Fermi energy of 0.15 eV and relaxation time of excited carriers of  $\sim 10^{-13}$  s. The graphene plasmons in this case would have a wavelength of 144 nm, demonstrating significant upconversion as compared to the excitation wavelength. The confinement of the plasmons would be 69.34, and the in-plane propagation distance would be 2.25  $\mu\text{m}$  (15.6 times the plasmon wavelength).

## 2.4 Closing Remarks

In closing, this chapter has reviewed the background material for the works presented in Chapters 4, 5, and 6. We have now seen some of the fundamental electronic, optical, and optoelectronic properties of graphene necessary for understanding the experimental research that will be presented. Further details of the mechanisms and theoretical basis of the studies follows in Chapter 3. Each of Chapters 4, 5, and 6 includes its own specific introduction and experiment section. Hence, a broader background, in terms of the properties

of graphene, has been presented here.

The properties covered are relevant to the experimental work that was conducted and the corresponding analysis of the results. For example, the crystal properties of graphene as reviewed in Section 2.1.1 are relevant to the technique of mechanical exfoliation, which was applied throughout this thesis work (details of the “recipe” used can be found in references [11] and [42] and in Appendix A). The optical absorption in Section 2.1.9 and methods to image graphene in an optical microscope as discussed in Section 2.2.2 were applied in Chapters 4, 5, and 6. The Raman spectrum described in Section 2.2.3 was also a common theme, applied in Chapters 4, 5, and 6 to characterizing graphene samples, and determining the amount of damage or defects in the crystal lattice. The electronic properties, particularly the electric field effect in graphene were reviewed in Section 2.1.3 and applied in Chapter 6 to the work on graphene devices. Finally, Section 2.3.1 reviews surface plasmons, which come into play in the proposed mechanisms of periodic structure formation on graphene in Chapter 5 and the electrically-driven light emission from graphene in Chapter 6. These mechanisms will be described in detail in the next chapter (Chapter 3).

## 2.5 References

- [1] Fox M 2010 *Optical Properties of Solids* (Oxford University Press)
- [2] Bonaccorso F, Sun Z, Hasan T and Ferrari A C 2010 Graphene photonics and optoelectronics *Nat. Photonics* **4** 611-22
- [3] Andrei E Y, Li G and Du X 2012 Electronic properties of graphene: a perspective from scanning tunneling microscopy and magnetotransport *Rep. Prog. Phys.* **75** 056501
- [4] Castro Neto A H, Guinea F, Peres N M R, Novoselov K S and Geim A K 2009 The electronic properties of graphene *Rev. Mod. Phys.* **81** 109-62
- [5] Reddy D, Register L F, Carpenter G D and Banerjee S K 2011 Graphene field-effect transistors *J. Phys. D Appl. Phys.* **44** 313001

- [6] Peres N M R 2010 Colloquium: The transport properties of graphene: An introduction *Rev. Mod. Phys.* **82** 2673-700
- [7] Gonçalves P A D and Peres N M R 2015 *An Introduction to Graphene Plasmonics* (World Scientific)
- [8] Wallace P R 1947 The Band Theory of Graphite *Physical Review* **71** 622-34
- [9] Ashcroft N W and David Mermin N 1976 *Solid state physics* (Harcourt School)
- [10] Yang L, Deslippe J, Park C-H, Cohen M L and Louie S G 2009 Excitonic Effects on the Optical Response of Graphene and Bilayer Graphene *Phys. Rev. Lett.* **103**
- [11] Novoselov K S, Geim A K, Morozov S V, Jiang D, Zhang Y, Dubonos S V, Grigorieva I V and Firsov A A 2004 Electric Field Effect in Atomically Thin Carbon Films *Science* **306** 666-9
- [12] Schwierz F 2010 Graphene transistors *Nat. Nanotechnol.* **5** 487-96
- [13] Joshi P, Romero H E, Neal A T, Toutam V K and Tadigadapa S A 2010 Intrinsic doping and gate hysteresis in graphene field effect devices fabricated on SiO<sub>2</sub> substrates *J. Phys. Condens. Matter* **22** 334214
- [14] Novoselov K S, Falko V I, Colombo L, Gellert P R, Schwab M G and Kim K 2012 A roadmap for graphene *Nature* **490** 192-200
- [15] Ponomarenko L A, Belle B D, Jalil R, Britnell L, Gorbachev R V, Geim A K, Novoselov K S, Castro Neto A H, Eaves L and Katsnelson M I 2013 Field-effect control of tunneling barrier height by exploiting graphenes low density of states *J. Appl. Phys.* **113** 136502
- [16] Nair R R, Blake P, Grigorenko A N, Novoselov K S, Booth T J, Stauber T, Peres N M R and Geim A K 2008 Fine Structure Constant Defines Visual Transparency of Graphene *Science* **320** 1308-1308
- [17] Casiraghi C, Hartschuh A, Lidorikis E, Qian H, Harutyunyan H, Gokus T, Novoselov K S and Ferrari A C 2007 Rayleigh Imaging of Graphene and Graphene Layers *Nano Lett.* **7** 2711-7
- [18] Zhu S-E, Yuan S and G C A 2014 Optical transmittance of multilayer graphene *EPL* **108** 17007

- [19] Wall M 2011 *The Raman spectroscopy of graphene and the determination of layer thickness* ( Madison, WI Thermo Fisher Scientific)
- [20] Ferrari A C, Meyer J C, Scardaci V, Casiraghi C, Lazzeri M, Mauri F, Piscanec S, Jiang D, Novoselov K S, Roth S and Geim A K 2006 Raman Spectrum of Graphene and Graphene Layers *Phys. Rev. Lett.* **97**
- [21] Malard L M, Pimenta M A, Dresselhaus G and Dresselhaus M S 2009 Raman spectroscopy in graphene *Phys. Rep.* **473** 51-87
- [22] Childres I, Jauregui L A, Park W, Cao H and Chen Y P 2013 Raman spectroscopy of graphene and related materials *New developments in photon and materials research*
- [23] Graf D, Molitor F, Ensslin K, Stampfer C, Jungen A, Hierold C and Wirtz L 2007 Spatially Resolved Raman Spectroscopy of Single- and Few-Layer Graphene *Nano Lett.* **7** 238-42
- [24] Grigorenko A N, Polini M and Novoselov K S 2012 Graphene plasmonics *Nat. Photonics* **6** 749-58
- [25] Shalaev V M and Kawata S 2007 *Nanophotonics with surface plasmons* (Elsevier)
- [26] Solymar L, Walsh D and Syms R R A 2014 *Electrical Properties of Materials* (OUP Oxford)
- [27] Heinrichs J 1973 Surface plasmons at metal-vacuum and metal-dielectric interfaces *Solid State Commun.* **12** 167-70
- [28] Pitarke J M, Silkin V M, Chulkov E V and Echenique P M 2007 Theory of surface plasmons and surface-plasmon polaritons *Rep. Prog. Phys.* **70** 1-87
- [29] Raether H 1988 *Surface Plasmons on Smooth and Rough Surfaces and on Gratings* (Springer-Verlag)
- [30] Bludov Y U V, Ferreira A, Peres N M R and Vasilevskiy M I 2013 A primer on surface plasmon-polaritons in graphene *Int. J. Mod. Phys. B* **27** 1341001
- [31] Zayats A V and Smolyaninov I I 2003 Near-field photonics: surface plasmon polaritons and localized surface plasmons *J. Opt. A: Pure Appl. Opt.* **5** S16-50

- [32] Bao Q and Loh K P 2012 Graphene Photonics, Plasmonics, and Broadband Optoelectronic Devices *ACS Nano* **6** 3677-94
- [33] Koppens F H L, Chang D E and de Abajo F J G 2011 Graphene Plasmonics: A Platform for Strong Light-Matter Interactions *Nano Lett.* **11** 3370-7
- [34] Kretschmann E and Raether H 1968 Notizen: Radiative Decay of Non Radiative Surface Plasmons Excited by Light *Zeitschrift für Naturforschung A* **23**
- [35] Maier S A 2012 Graphene plasmonics: All eyes on flatland *Nat. Phys.* **8** 581-2
- [36] Brambring J and Raether H 1965 Plasma Radiation from Thin Silver Foils Excited by Light *Phys. Rev. Lett.* **15** 882-3
- [37] Kretschmann E 1972 The angular dependence and the polarisation of light emitted by surface plasmons on metals due to roughness *Opt. Commun.* **5** 331-6
- [38] Peres N M R, Bludov Y V, Ferreira A and Vasilevskiy M I 2013 Exact solution for square-wave grating covered with graphene: surface plasmon-polaritons in the terahertz range *J. Phys. Condens. Matter* **25** 125303
- [39] Wong L J, Kaminer I, Ilic O, Joannopoulos J D and Soljačić M 2015 Towards graphene plasmon-based free-electron infrared to X-ray sources *Nat. Photonics* **10** 46-52
- [40] Kaminer I, Katan Y T, Buljan H, Shen Y, Ilic O, López J J, Wong L J, Joannopoulos J D and Soljačić M 2016 Efficient plasmonic emission by the quantum Čerenkov effect from hot carriers in graphene *Nat. Commun.* **7** ncomms11880
- [41] Jablan M, Buljan H and Soljačić M 2009 Plasmonics in graphene at infrared frequencies *Phys. Rev. B: Condens. Matter Mater. Phys.* **80**
- [42] Matković A V 2015 *Investigating the optical properties of graphene with spectroscopic ellipsometry* Ph.D. (University of Belgrade)

# Chapter 3

## Mechanisms

In Chapter 2, we reviewed the general background of graphene from the perspective of its properties. In this chapter, we proceed with a more detailed background specific to the thesis research. We discuss the physical mechanisms involved with the three publication chapters that follow: laser ablation and patterning, laser induced periodic surface structures, and light emission from graphene, by reviewing related literature.

### 3.1 Laser Ablation and Patterning

#### 3.1.1 Ablation Process

Laser ablation is the removal of material from the surface of a solid or liquid using a laser beam. In this process, a focused laser beam irradiates a sample providing precise surface structuring of the material in the area of irradiation [1,2]. This process is typically performed using a pulsed laser beam due to the high intensity pulses, although continuous wave lasers of high energy may also be used. The technique is applicable to a wide variety of materials such as metals, plastics, or tissue. The absorbed energy in the material breaks chemical bonds in the irradiated area, while a minimal amount of excess heat is transferred to the surrounding areas.

The laser energy is absorbed to a certain depth of the material depending

on the material properties and the laser parameters (intensity, wavelength, and pulse length). The material removal rate is used to define the amount of material removed per pulse in units of nm/pulse [2]. The laser fluence (i.e. energy per unit area) determines the mechanism of laser ablation. For example, using lower laser fluences, the material could be converted to a gas by evaporation or sublimation, while using higher laser fluences, the material could be converted to a plasma.

Laser pulses of various durations can be used for laser ablation, including femtosecond, picosecond, and nanosecond pulses. Using shorter pulses reduces the thermal damage to the surrounding area. Using a femtosecond laser has advantages including negligible heat transport, very fast creation of vapor or plasma, and the absence of a liquid phase of the material, which offers better control of the ablation process [1].

### **3.1.2 Ablation of Graphite**

Before the work in Chapter 2 on femtosecond laser damage effects on multi-layer graphene [3], the laser ablation of graphene had mainly been studied for single-layer graphene, but not for multi-layer. The laser ablation of graphite, however, has been more thoroughly studied and is applicable to multi-layer graphene [2,4]. Hence in this section we discuss the ablation of graphite, drawing from both theoretical and experimental studies [2,4].

In a theoretical study, the damage effects of a femtosecond laser on graphite were investigated [4]. Electronic theory was applied and molecular dynamics calculations were carried out using a tight binding Hamiltonian. Two different laser thresholds were found, representing two different types of graphite structural instabilities induced by the intense laser pulses.

Calculations showed that at higher fluences (adsorbed energies above 3.3 eV/atom), bond-breaking would occur within the graphite layers leading to melting followed by evaporation. At lower fluences (energies above 2 eV/atom), ablation by removal of intact graphite layers without melting would occur.

The two-threshold property was concluded to be unique to graphite, due to its layered  $sp^2$ -bonded structure [4].

In an experimental study, the damage effects of nanosecond lasers on graphite were investigated [2]. Graphite was interacted with the beam of lasers of wavelengths 532 nm and 193 nm, pulse duration of 20 ns, repetition rate of 50 Hz, and fluence of 0.25-7 J/cm<sup>2</sup> in an air environment. To put this into context, the carbon-carbon bond energy is 369 kJ/mol = 3.824 eV/atom [5], and the graphite interplanar cohesive energy is 1.927 kJ/mol = 20 meV/atom (considering electronic delocalization and van der Waals interaction) [6]. The ablation rate increased with laser fluence, and two ablation regimes were found, corresponding to physical ablation involving vaporization, or physical-chemical ablation involving heating and oxidation.

The vaporization of graphite threshold fluence is  $\sim 1$  J/cm<sup>2</sup> and vaporization typically occurs at an ablation rate of  $10^2$ - $10^5$  nm/pulse with surface temperatures above  $\sim 4000$  K [2]. Above this threshold, a deep crater can be formed in a “microhole drilling” process by the first few laser pulses due to the high ablation rates. For example, with a pulse fluence of 4 J/cm<sup>2</sup> and 10 laser pulses, a crater of over 150 nm depth with a conical shape and debris on the outside was formed in the graphite. The debris are typical of vaporization ablation in which hot atoms are expelled, condense, and redeposit near the crater.

Using a fluence below the graphite vaporization threshold, ablation with a removal rate of  $10^{-3}$  nm/pulse was observed. Since each graphene layer is  $\sim 0.3$  nm thick, this removal rate implies that on average less than a single layer of graphene is removed per pulse. It was concluded that irradiation from multiple pulses led to defect formation within the graphene layers and the removal of weakly bonded atoms due to thermal oxidation.

Heat accumulation effects were considered to be negligible in this experiment, since for the low repetition rate that was used, the absorbed laser energy spreads out to the surrounding area between pulses [2]. For example, the thermal diffusivity is  $\sim 12$  cm<sup>2</sup>/s along the graphene layers, and  $\sim 2$  cm<sup>2</sup>/s

perpendicular to the layers. The length of heat spreading between pulses was much greater than  $100\ \mu\text{m}$ , i.e. much greater than the laser spot diameter. Also, the heat penetration length ( $\sim 10^{-4}\ \text{cm}$ ) was much greater than the laser penetration length ( $\sim 10^{-6}\ \text{cm}$ ).

### 3.1.3 Laser surface structuring

By controlling the processes discussed above, it is possible to structure a material surface using laser ablation. Types of structures that can be formed include periodic and quasi-periodic structures, nanoholes, irregular nanostructures (e.g. cavities, spheres), and nanostructure-textured microstructures. In this section we discuss the mechanisms involved with this process using as an example the structuring of metals by femtosecond laser interaction [7].

Typically, surface structuring is performed using a pulsed beam focused onto a sample by a lens [7]. In this process, the morphology of the surface structures can be controlled by the laser parameters and ambient gas pressure. The energy of the laser pulses is measured by a joulemeter and the number of pulses is controlled by an electromechanical shutter. For some types of structures (e.g. periodic structures), polarized light is required, in which case a polarization controller is also used. Using a stationary sample stage, the laser beam modifies the material in one spot (the area of irradiation). Using an  $xy$ -translation stage, larger areas of the material can be structured.

As an example, we discuss the model describing the laser structuring process for metals, as shown in Figure 3.1 (top right) [7]. Upon interaction of the metal with a laser pulse, the energy from the pulse is absorbed in a skin layer of  $\sim 10\ \text{nm}$  thick by free electrons in the material through an inverse bremsstrahlung mechanism. The electron-electron interaction time is short, such that the thermalization of excited electrons can be assumed to be an instantaneous process. The resulting system is described as a non-equilibrium system consisting of two sub-equilibrium systems of hot electrons and a cold lattice. This process occurs on a femtosecond time-scale during a pulse.

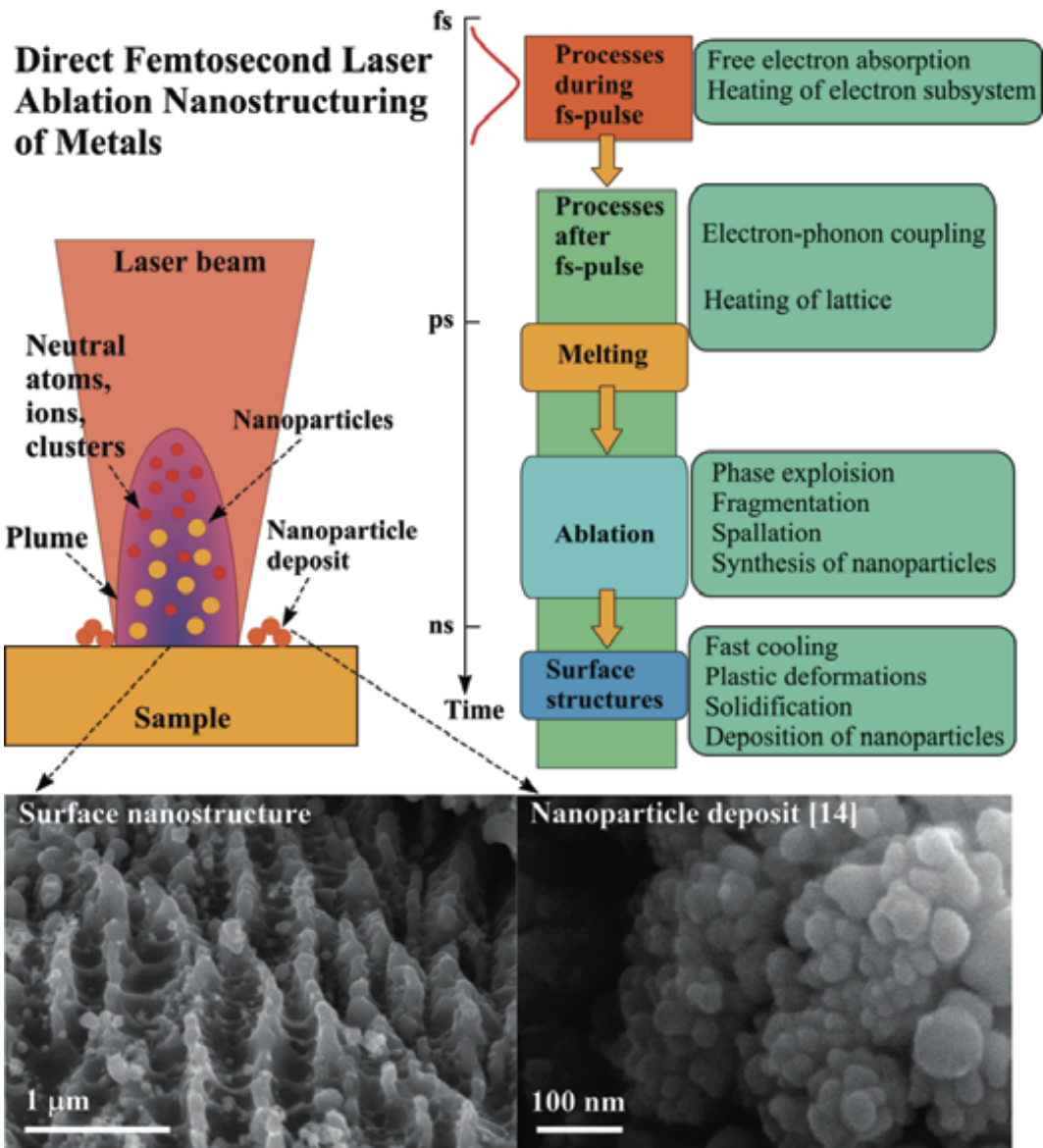


Figure 3.1: Femtosecond laser surface structuring of metals: schematics of the process (top), and images of typical nanostructures and deposits (bottom). This figure was reproduced by permission from John Wiley and Sons: Laser & Photonics Reviews, copyright (2012), <http://dx.doi.org/10.1002/lpor.201200017> [7].

After a femtosecond pulse, the system reaches equilibrium within a few picoseconds by electron-phonon interactions and electron diffusion leading to heating of the metal lattice. Following heating, melting and ablation begins on a time-scale of picoseconds, with ablation occurring from a few tens of picoseconds up to a few nanoseconds. Various mechanisms of ablation that may take place at this point include evaporation, explosive boiling (phase explosion), separation into fragments (fragmentation), or impact-induced fragment ejection (spallation). The ablation induces a plume above the metal surface that may consist of neutral atoms, ions, clusters, and/or nanoparticles (Figure 3.1 (top left)).

Finally, nanoseconds after the laser pulse, a fast cooling ( $10^{13}$ - $10^{15}$  K/s) of the metal surface occurs, leading to plastic deformations, solidification, and re-deposition of nanoparticles in the area of the interaction and its surroundings. This results in a nanostructured film in the area of laser interaction (Figure 3.1 (bottom left)) and nanoparticle deposits in the surrounding area (Figure 3.1 (bottom right)).

### 3.1.4 Patterning

Patterning of graphene is necessary for applications that require specific structures, shapes, or sizes. For example, graphene electrodes, gratings, or transistors may be fabricated by patterning methods [8,9]. Various types of samples have been investigated for their ability to be patterned, e.g. samples fabricated by CVD or mechanical exfoliation, including both single-layer and multi-layer graphene [8,9]. Desired structures include parallel periodic patterns of graphene [10-13], graphene ribbons [8,9], or holes in graphene [14-16], and patterning can be done in many ways, for example, by lithography, electron beam irradiation, or chemical, strain, or optical techniques [8,9]. Interestingly, it has been shown that graphene could even be structured in fine detail by the Japanese art of kirigami (typically used to cut paper into complex structures) using a sharp probe tip [17].

In a typical optical patterning setup, micro-cutting of graphene can be achieved by direct writing using an incident pulsed laser beam [18,19]. This technique has several advantages over lithography, including scalability and ease of fabrication without the use of additional materials (e.g. mask or photoresist). A graphene sample is irradiated by a focused pulsed laser beam to fabricate clean edged channels, ribbons, or holes on the micron scale. The energy from the incident laser quickly converts to local heat with a temperature at the irradiated spot over 500°C, causing localized burning [18,19]. The dimensions of the fabricated structures are tunable using the laser energy or a programmed laser process.

For the purpose of optical patterning and other laser applications of graphene (e.g. photoluminescence), it is important to know the laser damage effects in graphene. Several groups have studied laser damage in graphene using various laser parameters, and investigating various factors such as the damage threshold [14,15,20,21]. Laser induced damage is typically on a micron scale and assessed by Raman spectroscopy, scanning electron microscopy, and atomic force microscopy techniques.

## **3.2 Laser Induced Periodic Surface Structures**

### **3.2.1 Experimental Observations**

Another method of patterning with a laser beam that was not used before on graphene (prior to this work) produces structures known as “laser induced periodic surface structures” (LIPSS). These are parallel periodic structures (or gratings) on a material surface formed by a laser, using a power slightly above the damage threshold of the material (i.e. the threshold for a permanent change in the material, such as a defect). The LIPSS technique has several advantages such as simplicity and some degree of controllability over the structures formed. In particular, the technique can obtain much higher resolution than laser cutting, with the width and periodicity of LIPSS on the nano-scale.

With periodicities below the wavelength of light, these structures may be useful for applications in photonics. For example, anti-reflective polycarbonate films have been made with this type of structure [22].

The LIPSS effect was first explored in 1965 by M. Birnbaum using a ruby laser on semiconductors including germanium, silicon, gallium arsenide, gallium antimonide, indium antimonide, and indium arsenide [23]. Since that time, the effect has been applied to various types of materials: semiconductors, metals, and insulators [7,24-27].

### 3.2.2 Formation process

Although the LIPSS technique has been applied for over 50 years, to this day a consensus has not yet been reached as to the mechanism of LIPSS formation, and it is not completely understood. Several theories exist (e.g. self-organization of the structures [28]) with the most commonly cited theory involving the interference of the laser beam with a surface plasmon polariton [26,29-32]. In this section and the next, we discuss the surface wave mechanism in terms of the LIPSS formation process and the model that describes it.

For a metal surface with dielectric constant  $\epsilon_{metal}$  in a dielectric medium of dielectric constant  $\epsilon_d$ , the complex effective refractive index of the dielectric-metal interface for surface plasmons is given by [7,33]:

$$(3.1) \quad \eta = \frac{\epsilon_d \epsilon_{metal}}{(\epsilon_d + \epsilon_{metal})^{1/2}}.$$

When the material interacts with a linearly polarized laser of wavelength  $\lambda_{las}$  and angle of incidence  $\theta$ , the period of the induced LIPSS  $d$  is given by [7,33]:

$$(3.2) \quad d = \frac{\lambda_{las}}{Re[\eta] \mp \sin(\theta)},$$

where  $Re[\eta]$  is the real part of  $\eta$ .

LIPSS are classified by their spatial period into two regimes: low spatial frequency LIPSS (LSFL) or high spatial frequency LIPSS (HSFL). LSFL have spatial periods  $d$  on the order of the laser wavelength  $\lambda_{las}$  ( $d \sim \lambda_{las}$ ) while HSFL have spatial periods much smaller than the laser wavelength ( $d < \lambda_{las}/2$ ) [24].

As apparent from Equation 3.2, the period can be controlled by varying either the laser wavelength, the angle of incidence, or the effective refractive index of the interface. The latter is usually achieved by varying the material surroundings, e.g. by placing the material in liquid to decrease the spatial period as compared to those formed in an air environment. It has been shown experimentally that the orientation of the LIPSS can also be controlled [7]. The structures are typically found to be perpendicular to the polarization of the laser light, such that the grating vector  $\vec{g}$  is parallel to the tangential component of the electric field of the laser light  $\vec{E}$ .

Further control of the LIPSS period can be achieved by varying the number of laser shots due to the dynamic changes in surface morphology during the formation [7]. Experimentally, an increase in the number of laser shots has led to decreases in LIPSS period [29]. Also, control of the LIPSS period is offered by varying the laser fluence, although the exact effects are not completely understood. Various effects have been observed in studies of various materials (or even various studies of the same material) [7]. It has been shown that increasing the laser fluence could lead to either a decrease (e.g. [34]) or increase (e.g. [35]) in the LIPSS period.

Various types of lasers can be used in the formation process (e.g. short-pulsed or long-pulsed). LIPSS produced with femtosecond lasers have some distinct features over those produced by long-pulsed lasers [7]. In the formation of femtosecond laser induced periodic surface structures (FLIPSS), light from the laser pulse is absorbed by the surface under thermal non-equilibrium between the electron and lattice subsystems and the structures are imprinted well after the pulse has finished, as described above in Section 3.1.3.

FLIPSS are densely covered by nanostructures, whereas LIPSS formed by

long-pulsed lasers are smooth. Also, the period of the structures is substantially less than the laser wavelength in the case of FLIPSS. The smaller period is thought to be due to a change of effective refractive index of the interface when the nanostructures are formed which affects SPP propagation [29]. Specifically, on an air-metal interface irradiated by a femtosecond laser, it was found that  $Re[\eta]$  increased due to the formation of nanostructures on the metal surface. As seen by Equation 3.2, this increase in effective refractive index leads to a decrease in the LIPSS period.

As an example, Figure 3.2 shows images of the formation process of FLIPSS on titanium in air, and summarizes the process on the left panel [7]. The sample surface is shown before laser interaction in Figure 3.2 (a). After interaction of a few laser shots, random and sparse nanostructures are formed on the material surface (Figure 3.2 (b)). Because of this surface roughness, the laser light from the next few pulses are coupled to surface plasmon polaritons [36]. Interference between the laser light and the excited SPPs lead to a spatially periodic energy distribution on the sample surface. Heating of the surface is thus spatially periodically modulated and nascent periodic structures are formed (Figure 3.2 (c)). Once nascent periodic structures are formed, the laser light-to-SPP coupling becomes resonant and more efficient, deepening the grooves of the structures and leading to a positive feedback process. As the number of laser shots increases, the structures become more well defined, grow, and coalesce (Figure 3.2 (d)).

### 3.2.3 Surface Plasmon Polariton Model

The interference model of LIPSS formation has been developed specifically for FLIPSS on an air-metal surface by Makin *et al.* [32]. The model is reported to be also applicable to FLIPSS formation on semiconductors and dielectrics as they could have metallic behaviour upon irradiation with short intense laser pulses due to free carrier generation [7].

When a linearly polarized laser beam of wave vector  $\vec{k}_0$  is normally inci-

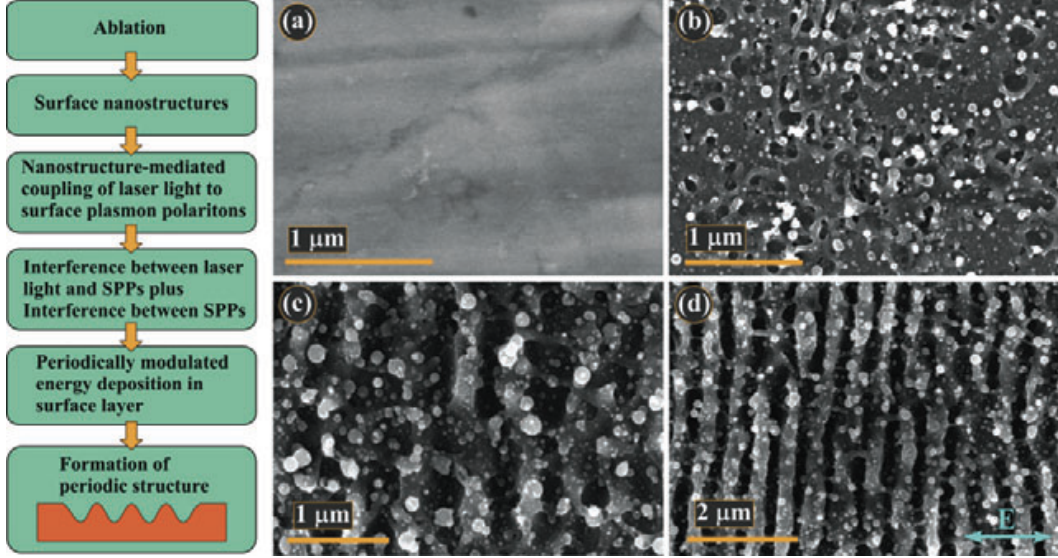


Figure 3.2: Summary of the FLIPSS formation process (left) and images of a titanium surface during the formation of FLIPSS in air: (a) before laser interaction; (b) after 2 laser shots; (c) after 10 laser shots; (d) after 40 laser shots. This figure was reproduced by permission from John Wiley and Sons: Laser & Photonics Reviews <http://dx.doi.org/10.1002/lpor.201200017> [7], copyright (2012).

dent on the surface, it excites SPPs traveling in opposite directions with wave vectors  $\vec{k}_{s1}$  and  $\vec{k}_{s2}$  as shown in Figure 3.3 (a) [32]. The SPP wavelengths  $\lambda_{s1}$  and  $\lambda_{s2}$  are given by the SPP dispersion relation [7,37] according to:

$$(3.3) \quad \lambda_{s1} = \lambda_{s2} = \frac{\lambda_{las}}{Re[\eta]},$$

where  $\lambda_{las}$  is the wavelength of the laser and  $Re[\eta]$  is the real part of  $\eta$ , as before.

Interference between the incident light wave and the excited SPPs leads to a standing wave pattern that induces two grating structures on the surface (primary and auxiliary) [32]. This is described in terms of the absorbed intensity at the metal-air surface assuming the SPPs travel along the  $x$ -direction. The total electromagnetic field intensity  $I_{\Sigma}(x)$  at the surface is given by [32]:

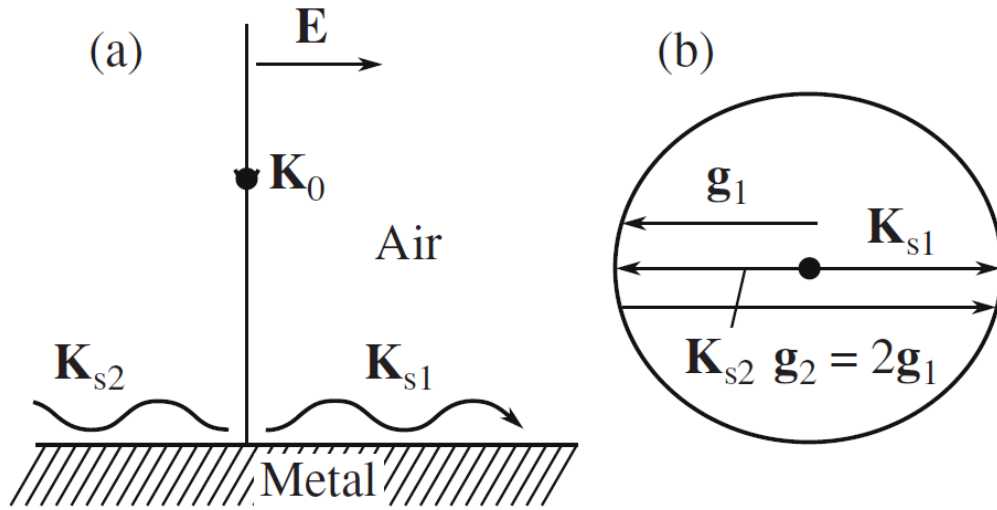


Figure 3.3: Schematic diagrams illustrating (a) the excitation of surface plasmons ( $\vec{k}_{s1}$ ,  $\vec{k}_{s2}$ ) during the interaction of normally incident linearly polarized laser radiation with a metal surface and (b) the law of quasi-momentum conservation and the formation of nanorelief lattices on the metal surface due to the interference of the incident wave with surface plasmons ( $\vec{g}_1$  lattice) and the mutual interference of the laser-excited surface plasmons ( $\vec{g}_2$  lattice). This figure and caption were reproduced by permission of Springer: Technical Physics Letters, copyright (2008), <https://doi.org/10.1134/S1063785008050088> [32].

$$(3.4) \quad I_{\Sigma}(x) = I_{las}(x) + (I_{las}I_s)^{1/2}\sin(\vec{g}_1\vec{x} + \phi) + (I_{s1}I_{s2})^{1/2}\sin(\vec{g}_2\vec{x} + \psi),$$

where  $I_{las}(x)$  is the absorbed intensity of the laser light along the surface in the  $x$ -direction,  $I_{s1}$  and  $I_{s2}$  are the absorbed intensities of the SPPs,  $I_s$  is the total absorbed intensity of the two SPPs,  $\vec{g}_1$  and  $\vec{g}_2$  are the wave vectors of the primary and auxiliary gratings, respectively, and  $\phi$  and  $\psi$  are the phase angles between the corresponding waves.

In Equation 3.4, the first term is the constant component of the total electromagnetic field intensity. The second term is due to interference effects between the incident wave and the SPPs. This leads to the formation of the primary grating with a wave vector equal to the SPP wave vectors, such that  $\vec{g}_1 = \vec{k}_{s1} = -\vec{k}_{s2}$  (Figure 3.3 (b) [32]). The third term is due to the mutual interference between the two SPPs traveling in opposite directions leading to the formation of the grating with wave vector  $\vec{g}_2 = \vec{k}_{s1} + \vec{k}_{s2}$ . The third term becomes dominant when  $I_s$  becomes larger than  $I_{las}(x)$ . This occurs due to positive feedback that enhances the intensity of the SPPs as the primary grating forms. Due to the interference between SPPs, and the interference of the second spatial harmonic of the SPP with the laser light, reduced periods of the gratings are predicted that are even fractions of the laser wavelength, i.e.  $d = \lambda_{las}, \lambda_{las}/2, \lambda_{las}/4$ , etc.. [32].

### 3.3 Light Emission from Graphene

Several different routes to graphene light emission have been experimentally demonstrated or theorized over the last several years. In this section, we review the various experiments and proposed mechanisms from recent literature.

### 3.3.1 Photoluminescence

Light emission from graphene can occur in several ways, including by optical excitation. Due to the zero band gap of graphene, photoluminescence (PL) from a conventional radiative recombination across a band gap is not expected; however, several other routes of achieving PL from graphene have been reported, including methods to open a gap.

A band gap can be induced through chemical or physical means to produce related luminescent structures such as graphene oxide or graphene quantum dots [38]. For example, broad, bright, uniform PL in the visible through infrared wavelength range has been reported from graphene oxide, attributed to band gap emission from electron-confined islands or oxygen related defect states [3943].

Secondly, PL from electronically doped graphene has been attributed to a hot luminescence (HL) mechanism [44]. This HL is described as a hot-electron process that is made possible by doping graphene so that excited-state relaxation can lead to luminescence as illustrated in Figure 3.4 (a). The luminescence is excited by a continuous-wave laser and has a broad spectrum peaking in the near infrared (NIR) wavelength range. The PL intensity depends on the doping level (i.e the Fermi energy) which is controlled electrostatically as described in Section 2.1.3. Incoming photons cause optical excitations of electrons, which relax through electron or phonon interactions, and photons are emitted when there are empty states in the valence band for radiative recombination. This condition is satisfied when the excitation energy of the incoming photon  $E_{exc}$  is greater than twice the Fermi energy  $E_F$ , i.e.  $E_{exc} > 2 | E_F |$ , and the emission energy of the outgoing photon  $E_{em}$  is less than this value, i.e.  $E_{em} < 2 | E_F |$ , as shown in Figure 3.4 (a) [44].

It is also possible to achieve nonlinear PL from pristine (i.e. untreated) graphene by ultrafast optical excitation using femtosecond [45,46] or picosecond lasers [47]. Optically-excited carriers undergo rapid scattering to produce a distribution of non-equilibrium carriers in the valence band and conduc-

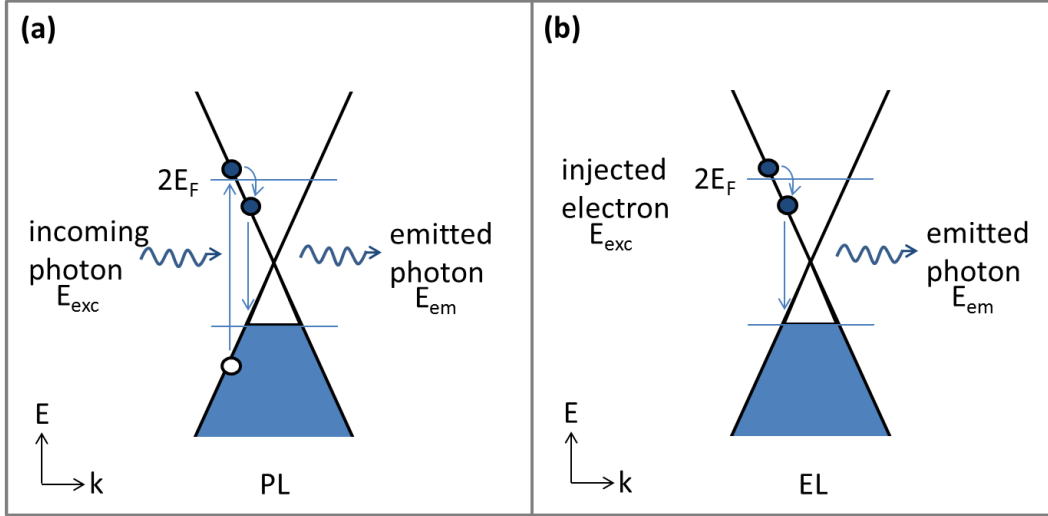


Figure 3.4: Two types of light emission from graphene, schematically represented on the dispersion relation: (a) photoluminescence (PL); (b) electroluminescence (EL). The schematic in (a) was adapted by permission from Macmillan Publishers Ltd: Nature, copyright (2011), <http://dx.doi.org/10.1038/nature09866> [44]. The schematic in (b) was adapted by permission from IOP Publishing: Nanotechnology, copyright (2014), <http://dx.doi.org/10.1088/0957-4484/25/5/055206> [48].

tion band. Upon electron-hole recombination, photons are emitted to produce both up-converted and down-converted PL, i.e. the emission energies are both higher and lower than the excitation energy of the laser. Time-resolved studies have shown that this process occurs on a femtosecond time scale [45,46].

The PL excited by pulsed lasers has a broad spectrum in the visible wavelength range, and is spatially uniform on the graphene [45,47]. The peak of the PL spectrum is located at the laser excitation wavelength [47] and the wavelength of the PL is tunable by varying the wavelength of the pump laser [45]. The intensity of the PL increases with laser power and scales with the number of graphene layers, such that PL imaging could be applied to determine the number of layers [45,47].

### 3.3.2 Electroluminescence

We saw in the previous section that several different PL processes are possible in graphene. Another way of generating light from graphene is by electrical excitation using an applied voltage in graphene-based devices. Similar methods have been applied in the past to obtain EL from related materials such as carbon nanotubes [49,50]. For graphene, EL is not expected from a conventional radiative recombination process across a band gap due to the zero band gap property, but there are other routes of achieving EL from graphene [48,49,51]. These mechanisms are distinct from the PL processes described above, and distinct from each other.

Similar to the case of PL, a band gap can be induced by modifying the graphene structure to achieve EL. For example, graphene quantum dots of 2-10 nm in diameter have band gaps that increase as the quantum dot size decreases [51]. Upon electrical excitation, they emit EL in the visible spectral range and the peak wavelength is tunable with the graphene quantum dot size (i.e. band gap size) [51]. These graphene quantum dots have been used as a dopant in light emitting diodes to generate white light. In this section we discuss the two electroluminescence mechanisms that have been proposed for unmodified graphene, i.e. electron-tunneling and phonon-assistance.

#### **Electroluminescence due to Electron-Tunneling**

Electroluminescence in the visible spectral range has been excited using electron-tunneling by Beams et al. [48]. In that experiment, a scanning tunneling microscope (STM) was used to apply a bias voltage between the tip and a graphene sample. Electron tunneling using low-energy electrons (via graphene doping of  $\sim 0.5-0.65$  eV) was used to excite EL in single-layer to few-layer graphene samples. The bias voltage was applied to inject electrons locally into the graphene using the STM in ambient conditions. The EL was measured by a wide-angle optical imaging system. Although STM-induced EL had been studied on other materials (e.g. metals [52,53]), this was the first observation

on graphene.

In metals, STM-induced light emission is due to a localized plasmon mode (“gap plasmon”) between the tip and sample that is excited by the tunneling electrons [52,54,55]. In graphene, the Fermi energy would need to be greater than the energy of the plasmon in order for the excitation to occur, but this is difficult to achieve for light emission in the visible spectral range [56].

Hence, a different process is used to explain the mechanism for STM-induced light emission from graphene, based on hot luminescence [48]. This process is analogous to the HL process described above with respect to PL, except that instead of an incoming photon exciting an electron, an electron is injected by the tip, as shown in Figure 3.4 (b). For radiative recombination to occur, there is again the condition:

$$(3.5) \quad \begin{aligned} E_{exc} &> 2 | E_F |, \\ E_{em} &< 2 | E_F |, \end{aligned}$$

where this time the excitation energy  $E_{exc}$  is related to the energy of the injected electron, which is controlled by the bias voltage.

In undoped graphene, there are no available states in the valence band for an excited electron to recombine radiatively. In order for light emission to occur, the graphene must be doped such that the Fermi energy meets the condition in Equation 3.5. In this case an excited electron-hole pair can radiatively recombine due to the available states in the valence band.

Doping was achieved in the experiment of Beams et al. using a combination of three methods [48]. First, the Fermi energy was shifted by the underlying indium-tin-oxide substrate that had a different work function than graphene, making the graphene p-doped. Second, the gold STM tip was used to dope the graphene due to the different work functions of the tip and sample, which again p-doped the sample. Third, the bias voltage between the tip and sample led to doping via a capacitive effect. Bias voltages of  $\pm 2-3$  V were used, and

in total the sample was p-doped by  $\sim 0.5\text{-}0.65$  eV.

The results of the experiment were in support of the proposed HL mechanism [48]. Because the graphene was p-doped, the HL was predicted to be excited when electrons were injected, but not holes. This effect was observed via switching the light emission on and off by inverting the voltage from positive to negative. In addition, the measured spectrum of the light emission was in agreement with previous studies of optically-excited HL, in terms of the spectral shape and wavelength range [44]. Finally, because HL is an inter-band process, the intensity of the light emission was predicted to scale with the number of graphene layers, which was confirmed by the measurements. The electron-tunneling-induced EL also had some similar properties to those of the PL discussed above; namely, the spectrum was broad and in the visible/near infrared spectral range, the emission was uniform across the area of the graphene, and the intensity scaled linearly with the number of graphene layers [48].

### **Phonon-Assisted Electroluminescence**

Electroluminescence of graphene was also claimed to be due to phonon-assisted radiative decay [49]. In a combined study of carbon nanotubes and graphene, EL was excited by applied source-drain voltages. Single-wall carbon nanotubes (SWNTs) of 0.7-1.5 nm diameter and few-layer graphene devices were fabricated on substrates of Si coated with 800-1000 nm of thermal SiO<sub>2</sub> or on substrates of (c-plane)-Al<sub>2</sub>O<sub>3</sub>. The light emission from the devices was measured through an optical microscope equipped with an optical cryostat sample chamber, held under vacuum of  $< 10^{-6}$  mbar.

The results for varying source-drain voltages between  $\sim 3 - 16$  V included light emission spectra with dual peaks in the visible/near infrared range at  $\sim 1.8$  eV and  $\sim 1.4$  eV as shown in Figure 3.5 [49]. The spectra for the various substrate-supported devices under bias did not show significant differences, whether they were graphene or nanotubes of varying diameters. The spectra were fit to two Gaussian functions, and the position of the peaks and full-width-

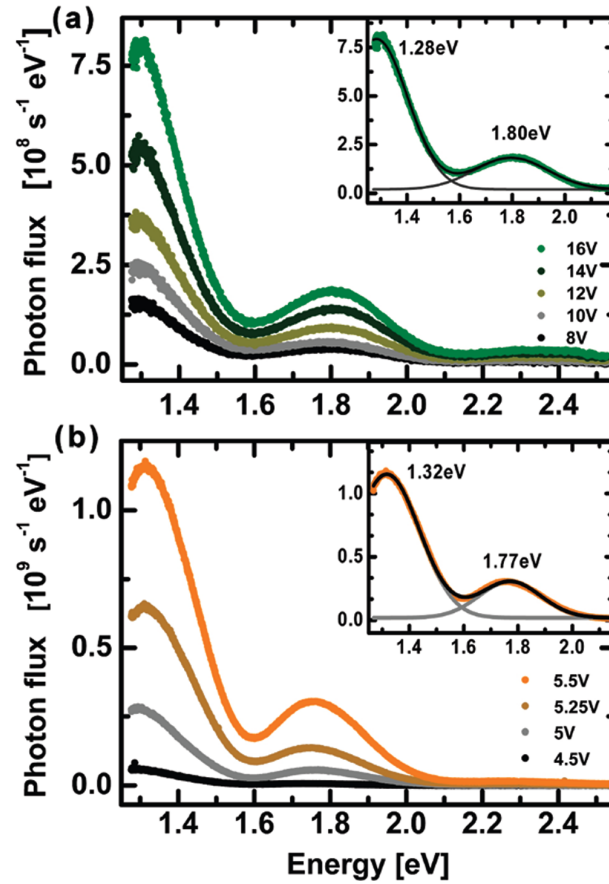


Figure 3.5: Phonon-assisted electroluminescence spectra at varying voltages for devices based on (a) single-wall carbon nanotubes, and (b) few-layer graphene. Reprinted with permission from <http://dx.doi.org/10.1021/nl9039795> [49]. Copyright (2010) American Chemical Society.

at-half-maxima were found to be weakly dependent on applied voltage. For example, for few-layer graphene devices, the peak position increased by  $\sim 0.2$  eV/mW and the peak width converged to a value of  $\sim 0.28$  eV with increasing power. The peak intensity, on the other hand, increased exponentially with voltage.

The mechanism proposed for the observed light emission was a phonon-assisted radiative decay in both the nanotubes and the graphene [49]. In this model, the relevant electronic states are the  $\pi$  and  $\pi^*$  bands at the  $\vec{M}$  point of the Brillouin zone. The  $\pi^*$  states are populated with electrons by direct carrier

injection due to the large applied bias on the device. The emission is due to the radiative decay from the  $\pi^*$  states at the  $\vec{M}$  point to  $E_F$  at the  $\vec{K}$  point. This process must involve scattering with a phonon due to the conservation of momentum. The excitation states in graphene are 1.6 eV above  $E_F$  and 2.3 eV below  $E_F$ , and in SWNTs the energies of the bottom of the conduction band and top of the valence band are similar to these values. Thus, the phonon-assisted process leads to two emission peaks at  $1.6 \pm \sim 0.2$  eV in which the phonon energy is  $\sim 0.2$  eV. Absorption of a phonon corresponds to the higher energy peak, while emission of a phonon corresponds to the lower energy peak.

The light emission was also related to the supporting substrate, as evidenced by several factors [49]. First, thermal effects were not involved since Joule heating is suppressed by substrate cooling. Second, the dual-peak behaviour displayed by the substrate-supported devices was not observed for previous work on suspended nanotube devices [57]. Finally, the substrate-supported devices had an exponential rise of light emission intensity with voltage, unlike previous work on suspended nanotubes in which there was an exponential rise with power [57]. Different types of substrates were used in the experiments with similar results, thus the substrate material was not a factor.

### 3.3.3 Thermal Emission

Another type of light emission from graphene is thermal radiation [5863]. This is also an optoelectronic process although quite distinct in its mechanism and properties from electroluminescence. This phenomenon occurs in pristine graphene without any necessary structure modification or doping. A source-drain voltage is applied to the sample to produce a current and light is generated by local heating via a blackbody or “greybody” effect. This type of emission is localized to a hot spot in the graphene corresponding to a temperature maximum of the sample or carriers [58,62,63]. The thermal emission has a broad spectrum, usually peaking in the infrared wavelength range [5862],

with one report of emission peaking in the visible wavelength range [63]. In this section, we discuss experimental works on infrared and visible thermal emission from graphene.

Experiments have shown that the infrared thermal emission spectrum of graphene on a substrate fits closely to a blackbody curve [5862] given by Planck's law [64]:

$$(3.6) \quad B(\lambda, T) = \frac{2hc^2}{\lambda^5} \frac{1}{e^{\frac{hc}{\lambda k_B T}} - 1},$$

where  $B(\lambda, T)$  is the spectral radiance of the body as a function of wavelength  $\lambda$  and temperature  $T$ ,  $k_B$  is Boltzmann's constant,  $h$  is Planck's constant, and  $c$  is the speed of light. For example, electrically-driven emission from graphene on an Si/SiO<sub>2</sub> substrate peaked in the mid-infrared range (around 4  $\mu$ m) and fit to a blackbody curve corresponding to a temperature of  $T = 673$  K [58]. While an ideal blackbody has an emissivity of 100%, this study showed that graphene behaved as a greybody with emissivity of 2-6% [58].

Thermal emission from graphene peaking in the visible range was investigated recently [63]. In this experiment, devices were fabricated from single-layer to multi-layer graphene suspended over Si/SiO<sub>2</sub> substrates with varying trench depths  $D$  from  $\sim 80$ -1100 nm [63]. Metal electrodes were attached to the graphene atop the SiO<sub>2</sub>, while the graphene bridged a gap in the SiO<sub>2</sub> layer, with Si underlying the trench, schematically represented in Figure 3.6 (a) [63]. Bright visible light emission from the suspended graphene devices was excited by source-drain voltage of a few V and measured in vacuum of  $< 10^{-4}$  torr. The emission appeared at the center of the graphene channel when the voltage surpassed a threshold, and increased in intensity and in area with increased voltage. The emission intensity also increased rapidly with the applied electric field above the threshold.

For devices of varying numbers of graphene layers with trench depths of  $D = \sim 800$ -1000 nm, the emission spectra displayed multiple (2-3) peaks in the

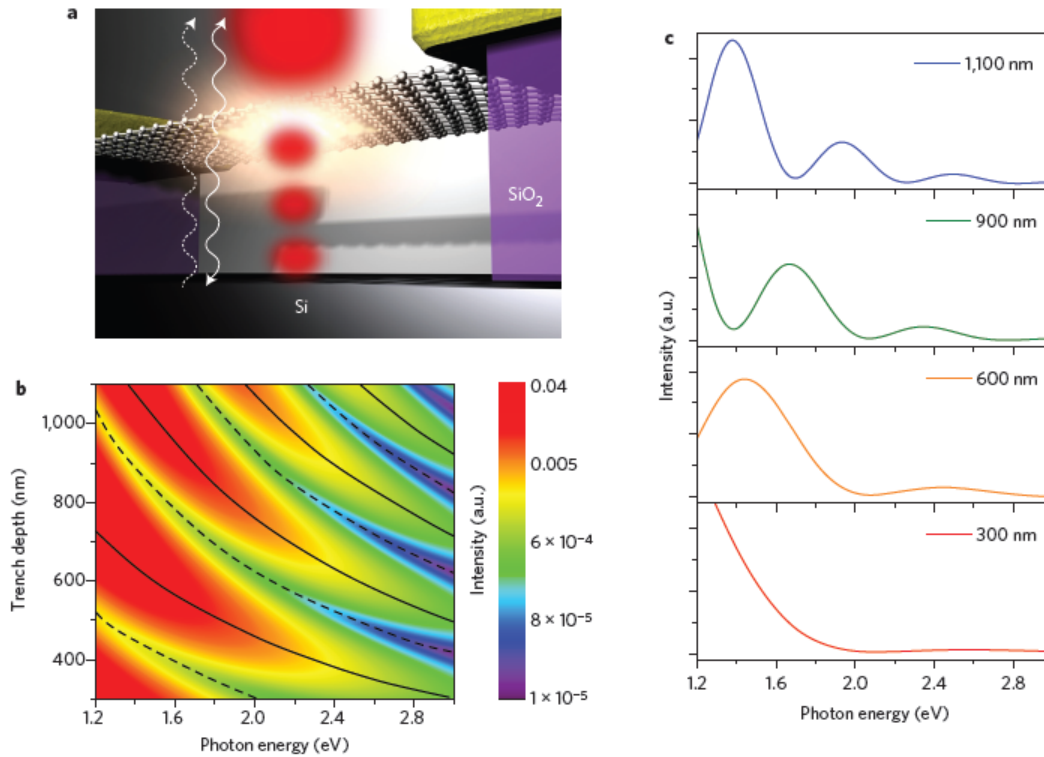


Figure 3.6: Visible thermal emission from suspended graphene devices: (a) schematic of the device structure showing interference effects between the light emission (solid arrow) and reflected light (dashed arrow) in the trench below graphene; (b) simulated emission intensity for various trench depths, showing constructive (solid curves) and destructive (dashed curves) interference conditions; (c) simulated emission spectra for various trench depths. This figure was reprinted by permission from Macmillan Publishers Ltd: Nature Nanotechnology, <http://dx.doi.org/10.1038/NNANO.2015.118> [63], copyright (2015).

visible/near infrared spectral range that did not fit simple blackbody curves. When the trench depth was reduced to  $D \approx 80\text{-}300$  nm on other devices, the emission spectra did not display multiple peaks, and instead were featureless and resembled grey body spectra. This led the authors to conclude that the peaks were strongly dependent on trench depth as opposed to the number of graphene layers or electronic band structure of the graphene devices.

Optical interference effects in the thermal emission spectrum coming from the trench was considered to be the mechanism responsible for the observations. Interference was caused by the interaction of the light from the suspended graphene with the reflected light from the air/Si interface below the trench, as shown in Figure 3.6 (a) [63]. The difference in energy between two consecutive destructive interferences  $\Delta$  was given by [63]:

$$(3.7) \quad \Delta = \frac{1239.8nm}{2D} eV.$$

Equation 3.7 was confirmed by simulating the thermal emission intensity and spectra (Figure 3.6 (b) and (c), respectively) for devices with various trench depths. The simulations showed that the trench depth controlled the peak wavelength and shape of the spectra. The simulated spectra agreed well with the experimental measurements and a comparison of the two was used to estimate the maximum electron temperature of the graphene as  $\sim 2800$  K in the hot spot at the center.

The thermal radiation efficiency was estimated as the ratio of the radiated power  $P_r$  to the applied electrical power  $P_e$ , where  $P_r$  was calculated from the Stefan-Boltzmann law with the estimated electron temperature of  $\sim 2800$  K. The obtained efficiencies were on the order of  $10^{-3}$ . Thermal emission in the infrared range on substrate-supported devices has a much lower efficiency ( $\sim 10^{-6}$ ) [62], partially due to heat dissipation through the substrate. Using suspended graphene devices overcomes this limitation by reducing vertical heat dissipation. Furthermore, lateral heat dissipation is reduced due to the strong

Umklapp phonon-phonon scattering in graphene (a scattering process in which a momentum change causes thermal resistance) [65,66]. This process reduces heat conductivity at high temperatures [65]. Hot electrons thus become localized to the center of the suspended graphene channel where the temperature is maximum [67], enhancing the efficiency of the thermal radiation by a factor of 1000 [63].

### 3.3.4 Surface plasmon-electron interaction

It has been shown theoretically that graphene light emission can result from the interaction of a free electron beam and surface plasmons [68,71]. For example, the electron beam from a transmission electron microscope normally incident on graphene could lead to radiation from the THz to optical ranges through a surface plasmon mechanism [70].

In a 2015 *Nature Photonics* work, Wong et al. showed that graphene emission from a similar mechanism could potentially be useful as a compact, tunable, highly directional, monochromatic light source, that is promising for on-chip integration [68]. In this mechanism, optically-excited surface plasmons on graphene scatter with incoming electrons to generate radiation. The high confinement and electrical tunability of graphene plasmons make them attractive for this application. The high confinement leads to high momentum plasmons, such that low-energy electrons scattering from the plasmons can produce high energy photons. Using higher-energy modestly relativistic electrons, such as from a radio frequency gun, X-ray radiation can be generated. Using lower-energy, non-relativistic electrons (such as in an on-chip device), infrared, visible, or ultraviolet radiation can be generated.

In the theoretical model, graphene on a dielectric substrate is incorporated with a grating either in the substrate, in the graphene, or on top of the graphene for the purpose of exciting graphene plasmons. Excitation of graphene plasmons is achieved using a focused laser incident on this structure. Next, incoming electrons parallel to the graphene surface interact with the

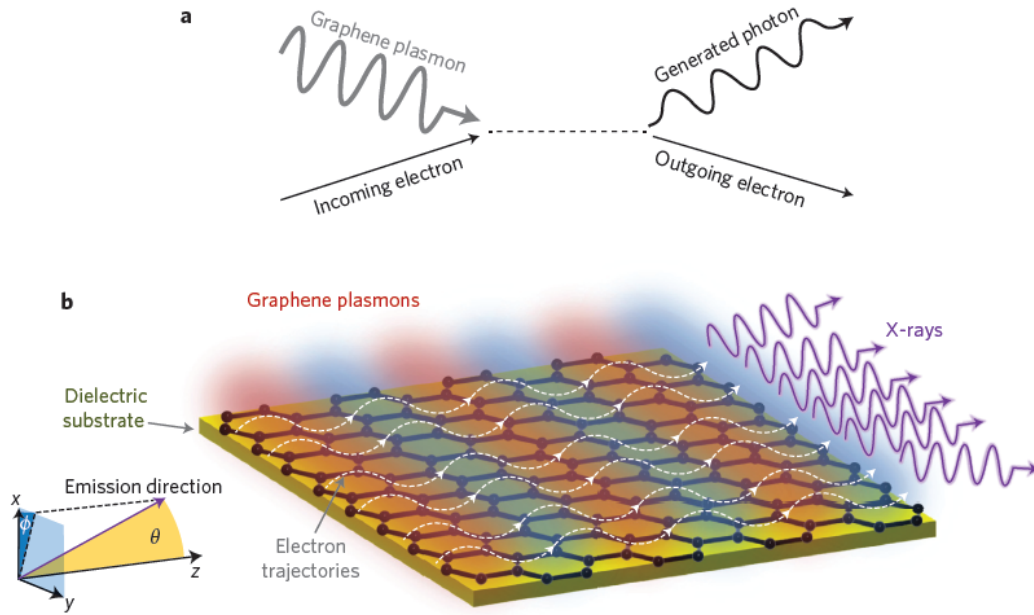


Figure 3.7: Light emission from graphene due to electron-plasmon interaction: (a) schematic diagram of the scattering process; (b) illustration of the graphene device and the emission mechanism. This figure was reprinted (adapted) by permission from Macmillan Publishers Ltd: Nature Photonics, copyright (2015), <http://dx.doi.org/10.1038/NPHOTON.2015.223> [68].

graphene plasmons in a scattering process to produce transverse electron oscillations. The electron oscillation could generate high energy, monoenergetic, highly directional photons as shown in Figure 3.7 (a) and (b) [68].

Analytical theory and *ab initio* numerical simulations for plasmon-electron interaction in graphene resulted in information about the output radiation, such as the intensity vs energy spectrum of the emitted photons [68]. First-principles calculations using conservation laws combined with classical electrodynamics derivations were used to investigate the elastic collision of an electron and plasmon to obtain equations for the intensity, frequency (or energy), and output angle of the radiation.

Calculations showed that the energy, energy spread, and directionality (angular spread) of the output photons depended on the incident electron energy [68]. For example, using 3.7 MeV electrons produces X-ray radiation of energy 20 keV with a full-width-at-half-maximum energy spread of 0.25% and angular

spread of  $<10$  mrad (highly directional). Using relatively lower energy electrons of 100 eV, on the other hand, produces visible and ultraviolet radiation of 2.16 eV and 3.85 eV with energy spreads of 0.32% and 0.2%, respectively, without directionality.

The frequency conversion regime was also calculated showing the correspondence between the electron energies to the emitted photon energies, in the energy ranges of  $\sim 10^{-1} - 10^5$  eV [68]. Both frequency up-conversion and down-conversion are possible using this surface plasmon-electron interaction technique. The frequency conversion charts are plotted for varying confinement factors (i.e. the ratio of the optical excitation free space wavelength to the graphene plasmon wavelength), demonstrating that both the electron energy and plasmon energy (or incident laser energy) can be used to tune the output photon energy. Also, the authors noted that Fermi energy of graphene can be used to control the output photon energy using this surface plasmon-electron interaction technique of light emission [68].

### 3.3.5 Čerenkov Effect

The examples above used electron beams incident on graphene, but it has also been hypothesized that using an electrical current through graphene could result in light emission from a surface plasmon mechanism [71]. This is based on the 2D quantum Čerenkov effect in graphene, which refers to the shockwave emission of surface plasmons excited by hot carriers in graphene, analogous to the conventional 3D Čerenkov radiation referring to the shockwave emission of light excited by charged particles in a 3D medium. In this section we discuss both the conventional effect and the quantum effect in graphene, and how the latter can lead to light emission.

#### Conventional Effect

The conventional Čerenkov effect was experimentally observed in 1934 by its namesake, P. A. Čerenkov [72]. In 1937, I. E. Tamm and I. M. Frank developed

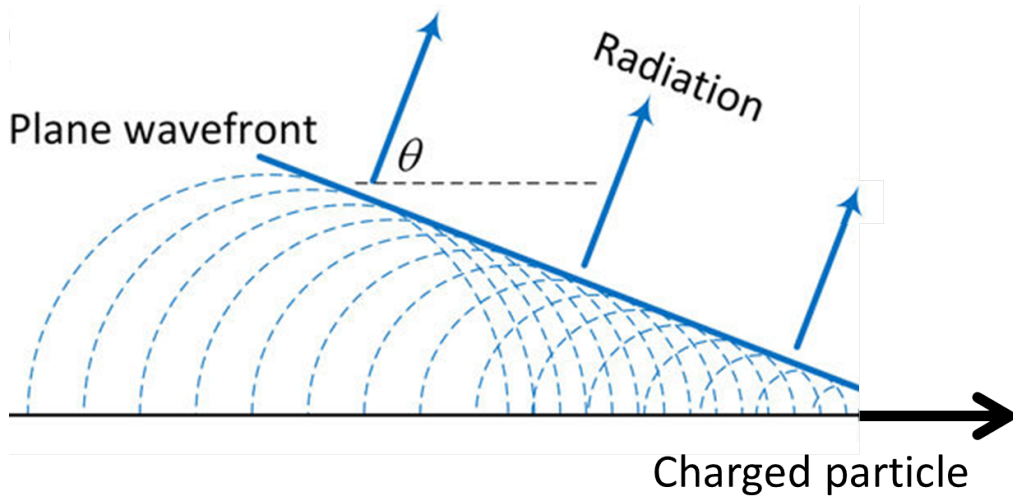


Figure 3.8: The conventional Čerenkov radiation process schematically illustrated. This figure was reprinted (with adaption) from Scientific Reports <http://dx.doi.org/10.1038/s41598-017-08705-4> [75], copyright (2017), under the Creative Commons Attribution 4.0 International License <http://creativecommons.org/licenses/by/4.0/>.

the corresponding theory to explain the observation [73]. All three scientists shared the 1958 Nobel prize in Physics “for the discovery and the interpretation of the Čerenkov effect”.

In the conventional Čerenkov effect (Figure 3.8), charged particles moving through a medium can excite light emission when the speed of the particles ( $v$ ) is larger than the phase velocity of light in the medium [74]:

$$(3.8) \quad v > v_p,$$

where  $v_p = c/n$ ,  $c$  is the speed of light in vacuum, and  $n$  is the refractive index of the medium. For this condition, the charged particles must be at relativistic speeds [74]. The emitted light intensity increases with photon energy, therefore it is often observed with a blue colour. For example, Čerenkov radiation appears as blue light in underwater nuclear reactors. The theoretical cut-off energy of the emission spectrum is the energy of the charged particle [74].

Čerenkov radiation is emitted in a cone about the axis of the moving charged particle in a forward direction (i.e. at an acute angle) as illustrated in Figure 3.8. The emission rate and spread angle are calculated using Maxwell's equations for a moving point particle and considering the far-field electric and magnetic field limit. The rate of photon emission per unit frequency  $\Gamma_\omega$  is given by [74]:

$$(3.9) \quad \Gamma_\omega = \alpha\beta\sin^2(\theta_C),$$

where  $\alpha$  is the fine structure constant,  $\beta = v/c$ , and  $\theta = \theta_C$  is the spread angle of emission. This angle is given by [74]:

$$(3.10) \quad \cos(\theta_C) = (\beta n)^{-1}.$$

The emission rate in Equation 3.9 depends on the photon frequency  $\omega$  through the refractive index  $n = n(\omega)$  due to material dispersion. In Equation 3.10,  $\theta_C = 0$  corresponds to the threshold charge velocity for Čerenkov radiation, and the maximum  $\theta_C$  corresponds to the limit as  $v$  approaches  $c$ .

### Quantum Čerenkov Effect in Graphene

In a 2016 *Nature Communications* article, Kaminer et al. showed that an analogous surface plasmon emission based on the Čerenkov effect is theoretically possible in graphene due to two main properties [70]. First, hot charge carriers in graphene travel with high velocities (up to  $10^6$  m/s), and secondly, graphene plasmons travel with relatively low phase velocities. They developed a quantum theory of the Čerenkov effect in graphene [71].

While the conventional Čerenkov effect is derived from classical physics by modeling a point charge traveling at relativistic speeds, the quantum effect is derived from quantum physics, by considering the quantum nature of the

charged particle and modeling it as a plane wave or a wave packet [74,76]. In many cases there is good agreement between the conventional and quantum effect; however, the quantum considerations in some cases could result in new phenomena [74,76]. As we shall see, there is a difference between the conventional effect and quantum effect in graphene that lies in the different charge carrier velocity threshold needed to obtain the emission in each case [71]. The modification to the threshold in graphene is due to the linearity of the dispersion relation, and the fact that the charge carriers behave as massless particles with low energies.

The quantum Čerenkov effect theory in graphene uses Fermi's golden rule to model the spontaneous emission of plasmons excited by charge carriers [71]. In this effect, an analogous threshold relation to Equation 3.8 can be satisfied by charged particles of non-relativistic speed  $v$  and surface plasmons of phase velocity  $v_p$  [71]. The process of the quantum Čerenkov effect in graphene is illustrated in Figure 3.9 (a) [71]. The graphene is in the  $y - z$  plane atop a substrate, and an incoming hot carrier flowing through the graphene in the  $z$ -direction excites graphene plasmon emission at an angle  $\theta$  with respect to the  $z$ -direction. Outgoing hot carriers are also present as shown in the diagram of the process in Figure 3.9 (b) [71].

The quantum Čerenkov effect in graphene has several attractive features for applications [71]. The process is highly efficient, ultrafast, and the plasmon output energy and direction can be tuned electrically (e.g. by tuning the Fermi energy by an applied gate voltage). Due to this tunability, the direction of plasmon emission could be both backwards and forwards (unlike conventional Čerenkov emission [77]) with low angular spread. The electron-plasmon conversion efficiency is theorized to be high (e.g. estimated at  $\sim 80\%$ ), with limitations due to competing decay processes. The predicted possible plasmon energies range from the THz to visible spectral range.

Equation 3.8 represents the conventional threshold for Čerenkov emission which would not be expected to be achievable in graphene due to the fact that the velocity of electrons  $v$  is limited by the Fermi velocity  $v_F$ , whereas

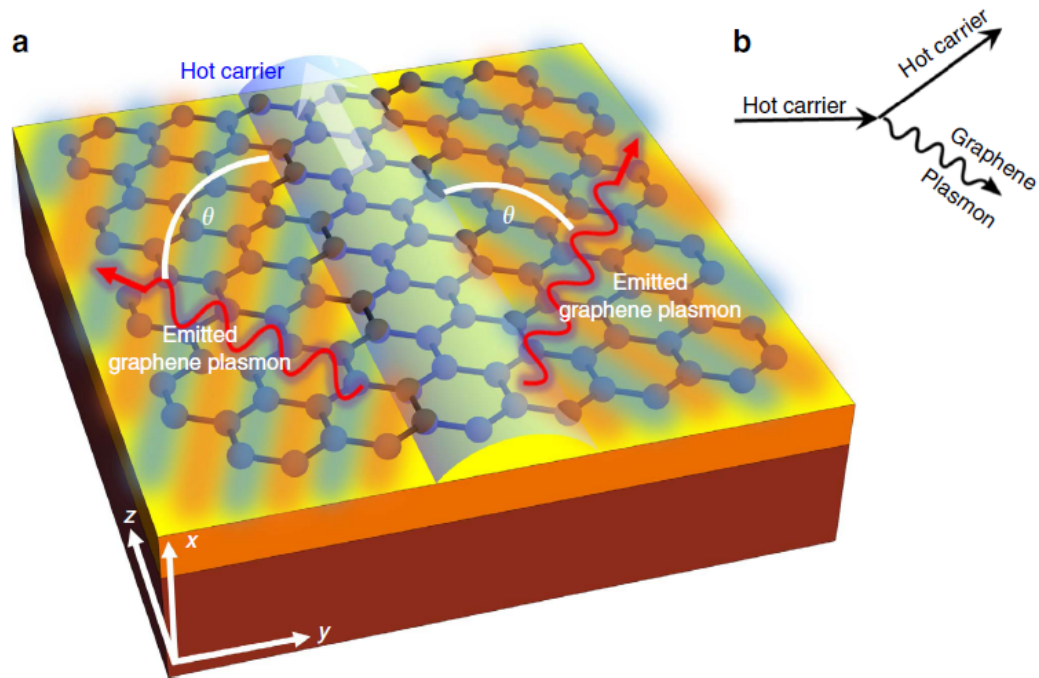


Figure 3.9: The quantum Čerenkov effect: (a) schematic of the graphene plasmon emission process from hot carrier excitation; (b) diagram of the excitation-emission process. This figure was reprinted (without adaptation) from Nature Communications, copyright (2016), <http://dx.doi.org/10.1038/ncomms11880> [71], under the Creative Commons Attribution 4.0 International License, which can be found at <https://creativecommons.org/licenses/by/4.0/>.

the phase velocity of plasmons  $v_p$  is greater than it, i.e.  $v \leq v_F < v_p$  [78]. However, due to the linearity of the energy-momentum dispersion relation in graphene, the quantum theory implies a different velocity threshold from the conventional theory. In the modified theory, an electron recoil process [74,76] causes a shift of the threshold such that the charge carriers in graphene could exceed the threshold value [71].

The theory determines the rate of graphene plasmon emission (the rate of plasmon emission per unit frequency from a single hot carrier) as [71]:

$$(3.11) \quad \Gamma_\omega = \frac{2\alpha c}{v_F \bar{\epsilon}_r} \left| \frac{\sin(\theta_C)}{1 - v_p^2/v_F^2} \right|,$$

where  $\alpha$  is the fine structure constant,  $\bar{\epsilon}_r$  is the relative permittivity of the substrate, and the plasmon emission occurs at two angles  $\theta = \pm\theta_C$ . The angle of emission is given by [71]:

$$(3.12) \quad \cos(\theta_C) = \frac{v_p}{v_F} \left[ 1 - \frac{\hbar\omega}{2E_i} \left( 1 - \frac{v_F^2}{v_p^2} \right) \right],$$

where  $\hbar\omega$  is the graphene plasmon energy and  $E_i$  is the incoming charge carrier energy.

The presence of  $\hbar$  here shifts the velocity threshold from the conventional value such that Čerenkov emission can occur for lower charge velocities [71]. If  $\hbar$  was set to zero in Equation 3.12, the classical Čerenkov emission angle (Equation 3.10) would be obtained. For example, charged particles outside of graphene usually follow a classical approximation because  $\hbar\omega \ll E_i$  in this case. However, charged particles in graphene have lower energies because they behave as massless particles such that the term  $\hbar\omega/2E_i$  becomes significant and the quantum theory applies.

Instead of the conventional threshold relation given in Equation 3.8, the quantum threshold is given by [71]:

$$(3.13) \quad v_p > v_F > v_p \left| 1 - \frac{2E_i}{\hbar\omega} \right|.$$

This modified threshold shows an important property of the graphene Čerenkov emission. The charge carriers in graphene could have velocities below the surface plasmon phase velocity for the emission to occur, unlike the conventional Čerenkov emission which would need the charge carriers to have velocities above the phase velocity of light in the medium.

By electrically controlling the hot carrier energy  $E_i$  and Fermi energy  $E_F$ , the condition in Equation 3.13 can be satisfied. There are two spectral windows of surface plasmon energies that could simultaneously satisfy the velocity inequality. The surface plasmon emission spectra are calculated for a number of specific examples of carrier energy, e.g.  $E_i = 0.2E_F$  and  $E_F = 0.639$  eV, showing the dual spectral range behaviour [71]. There is a dip in the spectrum between the two spectral ranges corresponding to the boundary between interband and intraband transitions, due to the zero density of states at the tip of the Dirac cone [71].

By letting  $\theta_C = 0$  in Equation 3.12, cut-off values for the surface plasmon spectral energies  $\hbar\omega_{cutoff}$  are determined as [71]:

$$(3.14) \quad \hbar\omega_{cutoff} = \frac{2E_i}{1 \pm v_F/v_p}.$$

The maximum plasmon energy cut-off  $\hbar\omega_{max}$  is given by [71]:

$$(3.15) \quad \hbar\omega_{max} \leq E_i \pm E_F.$$

The maximum energy can reach several eV by controlling  $E_i$  or  $E_F$  experimentally, e.g. by applying a high source-drain voltage to the graphene.

Finally, it is predicted that the quantum Čerenkov effect could lead to the

emission of photons of infrared or visible frequencies [71]. Light emission can occur from surface plasmons when they interact with an irregularity, such as a particle or roughness on the surface. The surface plasmons are inelastically scattered and part of the energy can be emitted as light. Hence, the quantum Čerenkov effect in graphene can lead to light emission through the out-coupling of the electrically-excited surface plasmons at scattering sites, thereby providing an electron-to-photon conversion mechanism. In fact, Ref. [71] suggests that light emission due to the quantum Čerenkov effect may have already been present in previous experiments involving hot carriers in graphene since the plasmons could have coupled-out at defects.

If the graphene device is incorporated with a grating or periodic structure, efficient out-coupling could be obtained for graphene plasmons emitted at particular frequencies and angles [71]. For example, the plasmon modes that could be out-coupled from this process were calculated for a grating with a period of 3.5 nm and electron energies of  $E_i = 1.9E_F$ , where  $E_F = 0.639$  eV. The calculated modes that could couple-out as light emission are of frequency  $\hbar\omega/E_F \approx 2$  (i.e. energy of  $\sim 2E_F = 1.3$  eV) at an emission angle of  $\theta = 0^\circ$  (forward direction) relative to the carrier flow direction [71]. In an ideal scenario such as this, the electron-photon energy conversion efficiency is theorized to be high because the quantum Čerenkov effect emission rate dominates over the rates associated with other scattering processes [71].

### 3.4 References

- [1] Chichkov B N, Momma C, Nolte S, Alvensleben F and Tünnermann A 1996 Femtosecond, picosecond and nanosecond laser ablation of solids *Appl. Phys. A: Mater. Sci. Process.* **63** 109-15
- [2] Frolov V D, Pivovarov P A, Zavedeev E V, Komlenok M S, Kononenko V V and Konov V I 2014 Laser nanoablation of graphite *Appl. Phys. A: Mater. Sci. Process.* **114** 51-5
- [3] Beltaos A, Kovačević A, Matković A, Ralević U, Jovanović D and Jelenković

- B 2014 Damage effects on multi-layer graphene from femtosecond laser interaction *Phys. Scr.* **T162** 014015
- [4] Jeschke H O, Garcia M E and Bennemann K H 2001 Theory for the Ultra-fast Ablation of Graphite Films *Phys. Rev. Lett.* **87**
- [5] Shabalin I L 2014 Carbon (Graphene/Graphite) *Ultra-High Temperature Materials I* (Springer) pp 7-235
- [6] Charlier J-C, Gonze X and Michenaud J-P 1994 Graphite Interplanar Bonding: Electronic Delocalization and van der Waals Interaction *Europhys. Lett.* **28** 403-8
- [7] Vorobyev A Y and Guo C 2012 Direct femtosecond laser surface nano/microstructuring and its applications *Laser Photonics Rev.* **7** 385-407
- [8] Hong J-Y and Jang J 2012 Micropatterning of graphene sheets: recent advances in techniques and applications *J. Mater. Chem.* **22** 8179
- [9] Feng J, Li W, Qian X, Qi J, Qi L and Li J 2012 Patterning of graphene *Nanoscale* **4** 4883
- [10] Kaplas T and Svirko Y 2014 Self-assembled graphene on dielectric micro- and nanostructures *Carbon* **70** 273-8
- [11] Li Y, Li Y, Shi W, Chen S, Zhang G, Liu Z, Sun Q, Tian J, Xu Y and Chen Y 2012 Periodic microstructures fabricated by multiplex interfering femtosecond laser beams on graphene sheet *Int. J. Nanomanuf.* **8** 221
- [12] Bao W, Miao F, Chen Z, Zhang H, Jang W, Dames C and Lau C N 2009 Controlled ripple texturing of suspended graphene and ultrathin graphite membranes *Nat. Nanotechnol.* **4** 562-6
- [13] Capasso A, Placidi E, Zhan H F, Perfetto E, Bell J M, Gu Y T and Motta N 2014 Graphene ripples generated by grain boundaries in highly ordered pyrolytic graphite *Carbon* **68** 330-6
- [14] Currie M, Caldwell J D, Bezares F J, Robinson J, Anderson T, Chun H and Tadjer M 2011 Quantifying pulsed laser induced damage to graphene *Appl. Phys. Lett.* **99** 211909
- [15] Kiisk V, Kahro T, Kozlova J, Matisen L and Alles H 2013 Nanosecond laser treatment of graphene *Appl. Surf. Sci.* **276** 133-7

- [16] Fischbein M D and Drndi M 2008 Electron beam nanosculpting of suspended graphene sheets *Appl. Phys. Lett.* **93** 113107
- [17] Bles M K, Barnard A W, Rose P A, Roberts S P, McGill K L, Huang P Y, Ruyack A R, Kevek J W, Kobrin B, Muller D A and McEuen P L 2015 Graphene kirigami *Nature* **524** 204-7
- [18] Zhou Y, Bao Q, Varghese B, Tang L A L, Tan C K, Sow C-H and Loh K P 2010 Microstructuring of Graphene Oxide Nanosheets Using Direct Laser Writing *Adv. Mater.* **22** 67-71
- [19] Kalita G, Qi L, Namba Y, Wakita K and Umeno M 2011 Femtosecond laser induced micropatterning of graphene film *Mater. Lett.* **65** 1569-72
- [20] Roberts A, Cormode D, Reynolds C, Newhouse-Illige T, LeRoy B J and Sandhu A S 2011 Response of graphene to femtosecond high-intensity laser irradiation *Appl. Phys. Lett.* **99** 051912
- [21] Yoo J-H, In J B, Park J B, Jeon H and Grigoropoulos C P 2012 Graphene folds by femtosecond laser ablation *Appl. Phys. Lett.* **100** 233124
- [22] Yao T-F, Wu P-H, Wu T-M, Cheng C-W and Yang S-Y 2011 Fabrication of anti-reflective structures using hot embossing with a stainless steel template irradiated by femtosecond laser *Microelectron. Eng.* **88** 2908-12
- [23] Birnbaum M 1965 Semiconductor Surface Damage Produced by Ruby Lasers *J. Appl. Phys.* **36** 3688-9
- [24] Bonse J, Krüger J, Höhm S and Rosenfeld A 2012 Femtosecond laser-induced periodic surface structures *J. Laser Appl.* **24** 042006
- [25] Dumitru G, Romano V, Weber H P, Sentis M and Marine W 2002 Femtosecond ablation of ultrahard materials *Appl. Phys. A: Mater. Sci. Process.* **74** 729-39
- [26] Huang M, Zhao F, Cheng Y, Xu N and Xu Z 2009 Origin of Laser-Induced Near-Subwavelength Ripples: Interference between Surface Plasmons and Incident Laser *ACS Nano* **3** 4062-70
- [27] Golosov E V, Ionin A A, Kolobov Y R, Kudryashov S I, Ligachev A E, Makarov S V, Novoselov Y N, Seleznev L V, Sinitsyn D V and Sharipov A R 2011 Near-threshold femtosecond laser fabrication of one-dimensional sub-

wavelength nanogratings on a graphite surface *Phys. Rev. B: Condens. Matter Mater. Phys.* **83**

[28] Reif J 2009 Basic Physics of Femtosecond Laser Ablation *Laser-Surface Interactions for New Materials Production Tailoring Structure and Properties* Springer Series in Materials Science 130 ed A Miotello and P M Ossi (Springer) pp 19-41

[29] Vorobyev A Y, Makin V S and Guo C 2007 Periodic ordering of random surface nanostructures induced by femtosecond laser pulses on metals *J. Appl. Phys.* **101** 034903

[30] Bonse J, Rosenfeld A and Krüger J 2009 On the role of surface plasmon polaritons in the formation of laser-induced periodic surface structures upon irradiation of silicon by femtosecond-laser pulses *J. Appl. Phys.* **106** 104910

[31] Sipe J E, Young J F, Preston J S and van Driel H M 1983 Laser-induced periodic surface structure. I. Theory *Phys. Rev. B: Condens. Matter Mater. Phys.* **27** 1141-54

[32] Makin V S, Makin R S, Ya. Vorobyev A and Guo C 2008 Dissipative nanostructures and Feigenbaums universality in the Metal-high-power ultrashort-pulsed polarized radiation nonequilibrium nonlinear dynamical system *Tech. Phys. Lett.* **34** 387-90

[33] Bonch-Bruевич A M 1992 Surface electromagnetic waves in optics *Opt. Eng.* **31** 718

[34] Golosov E V, Ionin A A, Kolobov Y R, Kudryashov S I, Ligachev A E, Novoselov Y N, Seleznev L V and Sinitsyn D V 2011 Ultrafast changes in the optical properties of a titanium surface and femtosecond laser writing of one-dimensional quasi-periodic nanogratings of its relief *J. Exp. Theor. Phys.* **113** 14-26

[35] Sakabe S, Hashida M, Tokita S, Namba S and Okamuro K 2009 Mechanism for self-formation of periodic grating structures on a metal surface by a femtosecond laser pulse *Phys. Rev. B: Condens. Matter Mater. Phys.* **79**

[36] Zayats A V and Smolyaninov I I 2003 Near-field photonics: surface plasmon polaritons and localized surface plasmons *J. Opt. A: Pure Appl. Opt.* **5**

- [37] Raether H 1988 *Surface Plasmons on Smooth and Rough Surfaces and on Gratings* (Springer-Verlag)
- [38] Bonaccorso F, Sun Z, Hasan T and Ferrari A C 2010 Graphene photonics and optoelectronics *Nat. Photonics* **4** 611-22
- [39] Eda G, Lin Y-Y, Mattevi C, Yamaguchi H, Chen H-A, Chen I-S, Chen C-W and Chhowalla M 2010 Blue Photoluminescence from Chemically Derived Graphene Oxide *Adv. Mater.* **22** 505-9
- [40] Sun X, Liu Z, Welsher K, Robinson J T, Goodwin A, Zaric S and Dai H 2008 Nano-graphene oxide for cellular imaging and drug delivery *Nano Res.* **1** 203-12
- [41] Luo Z, Vora P M, Mele E J, Charlie Johnson A T and Kikkawa J M 2009 Photoluminescence and band gap modulation in graphene oxide *Appl. Phys. Lett.* **94** 111909
- [42] Gokus T, Nair R R, Bonetti A, Böhmeler M, Lombardo A, Novoselov K S, Geim A K, Ferrari A C and Hartschuh A 2009 Making Graphene Luminescent by Oxygen Plasma Treatment *ACS Nano* **3** 3963-8
- [43] Lu J, Yang J-X, Wang J, Lim A, Wang S and Loh K P 2009 One-Pot Synthesis of Fluorescent Carbon Nanoribbons, Nanoparticles, and Graphene by the Exfoliation of Graphite in Ionic Liquids *ACS Nano* **3** 2367-75
- [44] Chen C-F, Park C-H, Boudouris B W, Horng J, Geng B, Girit C, Zettl A, Crommie M F, Segalman R A, Louie S G and Wang F 2011 Controlling inelastic light scattering quantum pathways in graphene *Nature* **471** 617-20
- [45] Liu W-T, Wu S W, Schuck P J, Salmeron M, Shen Y R and Wang F 2010 Nonlinear broadband photoluminescence of graphene induced by femtosecond laser irradiation *Phys. Rev. B: Condens. Matter Mater. Phys.* **82**
- [46] Lui C H, Mak K F, Shan J and Heinz T F 2010 Ultrafast Photoluminescence from Graphene *Phys. Rev. Lett.* **105**
- [47] Stöhr R J, Kolesov R, Pflaum J and Wrachtrup J 2010 Fluorescence of laser-created electron-hole plasma in graphene *Phys. Rev. B: Condens. Matter Mater. Phys.* **82**

- [48] Beams R, Bharadwaj P and Novotny L 2014 Electroluminescence from graphene excited by electron tunneling *Nanotechnology* **25** 055206
- [49] Essig S, Marquardt C W, Vijayaraghavan A, Ganzhorn M, Dehm S, Hennrich F, Ou F, Green A A, Sciascia C, Bonaccorso F, Bohnen K-P, v. Löhneysen H, Kappes M M, Ajayan P M, Hersam M C, Ferrari A C and Krupke R 2010 Phonon-Assisted Electroluminescence from Metallic Carbon Nanotubes and Graphene *Nano Lett.* **10** 1589-94
- [50] Rai P, Hartmann N, Berthelot J, Arocas J, des Francs G C, Hartschuh A and Bouhelier A 2013 Electrical Excitation of Surface Plasmons by an Individual Carbon Nanotube Transistor *Phys. Rev. Lett.* **111**
- [51] Kwon W, Kim Y-H, Lee C-L, Lee M, Choi H C, Lee T-W and Rhee S-W 2014 Electroluminescence from Graphene Quantum Dots Prepared by Amidative Cutting of Tattered Graphite *Nano Lett.* **14** 1306-11
- [52] Johansson P, Monreal R and Apell P 1990 Theory for light emission from a scanning tunneling microscope *Phys. Rev. B: Condens. Matter Mater. Phys.* **42** 9210-3
- [53] Coombs J H, Gimzewski J K, Reihl B, Sass J K and Schlittler R R 1988 Photon emission experiments with the scanning tunnelling microscope *J. Microsc.* **152** 32536
- [54] Berndt R, Gimzewski J K and Johansson P 1991 Inelastic tunneling excitation of tip-induced plasmon modes on noble-metal surfaces *Phys. Rev. Lett.* **67** 3796-9
- [55] Bharadwaj P, Bouhelier A and Novotny L 2011 Electrical Excitation of Surface Plasmons *Phys. Rev. Lett.* **106**
- [56] Koppens F H L, Chang D E and de Abajo F J G 2011 Graphene Plasmonics: A Platform for Strong Light-Matter Interactions *Nano Lett.* **11** 3370-7
- [57] Mann D, Kato Y K, Kinkhabwala A, Pop E, Cao J, Wang X, Zhang L, Wang Q, Guo J and Dai H 2007 Electrically driven thermal light emission from individual single-walled carbon nanotubes *Nat. Nanotechnol.* **2** 33-8
- [58] Lawton L M, Mahlmeister N H, Luxmoore I J and Nash G R 2014 Prospective for graphene based thermal mid-infrared light emitting devices *AIP Adv.*

- [59] Luxmoore I J, Adlem C, Poole T, Lawton L M, Mahlmeister N H and Nash G R 2013 Thermal emission from large area chemical vapor deposited graphene devices *Appl. Phys. Lett.* **103** 131906
- [60] Freitag M, Chiu H-Y, Steiner M, Perebeinos V and Avouris P 2010 Thermal infrared emission from biased graphene *Nat. Nanotechnol.* **5** 497-501
- [61] Yu D and Dai L 2010 Voltage-induced incandescent light emission from large-area graphene films *Appl. Phys. Lett.* **96** 143107
- [62] Berciaud S, Han M Y, Mak K F, Brus L E, Kim P and Heinz T F 2010 Electron and Optical Phonon Temperatures in Electrically Biased Graphene *Phys. Rev. Lett.* **104**
- [63] Kim Y D, Kim H, Cho Y, Ryoo J H, Park C-H, Kim P, Kim Y S, Lee S, Li Y, Park S-N, Yoo Y S, Yoon D, Dorgan V E, Pop E, Heinz T F, Hone J, Chun S-H, Cheong H, Lee S W, Bae M-H and Park Y D 2015 Bright visible light emission from graphene *Nat. Nanotechnol.* **10** 676-81
- [64] Fox M 2010 *Optical Properties of Solids* (Oxford University Press)
- [65] Pop E, Varshney V and Roy A K 2012 Thermal properties of graphene: Fundamentals and applications *MRS Bull.* **37** 1273-81
- [66] Maznev A A and Wright O B 2014 Demystifying umklapp vs normal scattering in lattice thermal conductivity *Am. J. Phys.* **82** 1062-6
- [67] Dorgan V E, Behnam A, Conley H J, Bolotin K I and Pop E 2013 High-Field Electrical and Thermal Transport in Suspended Graphene *Nano Lett.* **13** 4581-6
- [68] Wong L J, Kaminer I, Ilic O, Joannopoulos J D and Soljačić M 2015 Towards graphene plasmon-based free-electron infrared to X-ray sources *Nat. Photonics* **10** 46-52
- [69] Robb G 2015 Graphene plasmonics: Ultra-tunable graphene light source *Nat. Photonics* **10** 3-4
- [70] Mišković Z L, Segui S, Gervasoni J L and Arista N R 2016 Energy losses and transition radiation produced by the interaction of charged particles with a graphene sheet *Phys. Rev. B: Condens. Matter Mater. Phys.* **94**

- [71] Kaminer I, Katan Y T, Buljan H, Shen Y, Ilic O, López J J, Wong L J, Joannopoulos J D and Soljačić M 2016 Efficient plasmonic emission by the quantum Čerenkov effect from hot carriers in graphene *Nat. Commun.* **7** ncomms11880
- [72] Cherenkov P A 1934 Visible Emission of Clean Liquids by Action of  $\gamma$  Radiation *Dokl. Akad. Nauk SSSR* **2** 451
- [73] Tamm I E and Frank I M 1937 Coherent In-Medium Fast-Electron Radiation *Dokl. Akad. Nauk USSR* **14** 109
- [74] Kaminer I, Mutzafi M, Levy A, Harari G, Sheinfux H H, Skirlo S, Nemirovsky J, Joannopoulos J D, Segev M and Soljačić M 2016 Quantum Čerenkov Radiation: Spectral Cutoffs and the Role of Spin and Orbital Angular Momentum *Physical Review X* **6**
- [75] Hu Y, Li Z, Wetzell B, Morandotti R, Chen Z and Xu J 2017 Cherenkov Radiation Control via Self-accelerating Wave-packets *Sci. Rep.* **7**
- [76] Ginzburg V L 1940 Quantum theory of radiation of electron uniformly moving in medium *Zh. Eksp. Teor. Fiz* **10** 589-600
- [77] Luo, C., Ibanescu, M., Johnson, S. G. and Joannopoulos, J. D 2003 Čerenkov Radiation in Photonic Crystals *Science* **299** 368-71
- [78] Jablan M, Buljan H and Soljačić M 2009 Plasmonics in graphene at infrared frequencies *Phys. Rev. B: Condens. Matter Mater. Phys.* **80**

# Chapter 4

## Damage effects on multi-layer graphene from femtosecond laser interaction

Reprinted from Beltaos, A., Kovačević, A., Matković, A., Ralević, U., Jovanović, D., and Jelenković, B. (2014). “Damage effects on multi-layer graphene from femtosecond laser interaction”. *Physica Scripta*, 2014 (T162), 014015. The Royal Swedish Academy of Sciences. Reproduced by permission of IOP Publishing. All rights reserved.

<http://dx.doi.org/10.1088/0031-8949/2014/T162/014015>

### 4.1 Abstract

We present a study on the damage effects of femtosecond laser interaction on exfoliated multi-layer graphene using the techniques of optical microscopy, atomic force microscopy, and Raman spectroscopy. Various effects of the interaction were observed. The ablation threshold was found to be  $\sim 4 \text{ mJ cm}^{-2}$ , and was slightly higher in transmission mode than in reflection mode. This work also demonstrates the feasibility of ultrafast laser patterning of exfoliated multi-layer graphene.

## 4.2 Introduction

Since its practical realization in 2004, graphene, a two dimensional crystal made up of carbon atoms in a honeycomb lattice, has attracted much attention in the research world due to its outstanding electronic, optical, magnetic, thermal, and mechanical properties [1, 2]. It is a promising material for applications in a wide variety of fields, including optics and optoelectronics, e.g. solar cells, optical modulators, photodetectors, light emitting devices, touch screens, and mode-locked lasers [2-4].

For future applications one important aspect is the micro-cutting, patterning, or structuring of graphene, which can be achieved via interaction with an ultrafast laser [5-11] due to graphene's strong optical absorption of  $\sim 2.3\%$  [12]. Ultrafast lasers are also used in research to investigate the properties of graphene, such as its ultrafast dynamics and non-linear effects [13-17].

Therefore, it is very important for both future applications and research purposes to fully understand the damage effects of the ultrafast laser on the graphene, and to be able to control experimental parameters to achieve a specific desired effect. The laser parameters control the onset of damage in the graphene, defining the limits of graphene-based photonic devices and non-linear applications [18, 19].

So far, the damage effects of ultrafast lasers on graphene have been studied mostly for chemical vapor deposited (CVD) single-layer graphene (SLG) [6, 8, 18-20]. Much less attention has been paid to damage effects on either exfoliated [10] or multi-layer graphene, even though both are often used in ultrafast laser research [14-17] due to the fact that exfoliated graphene is of better quality than CVD [2] and multilayer graphene is important for applications [21]. Here, we present a study of damage effects on exfoliated multi-layer graphene from ultrafast laser interaction. We investigate modification of the samples as well as damage and ablation thresholds by the techniques of optical microscopy, atomic force microscopy (AFM), and Raman spectroscopy.

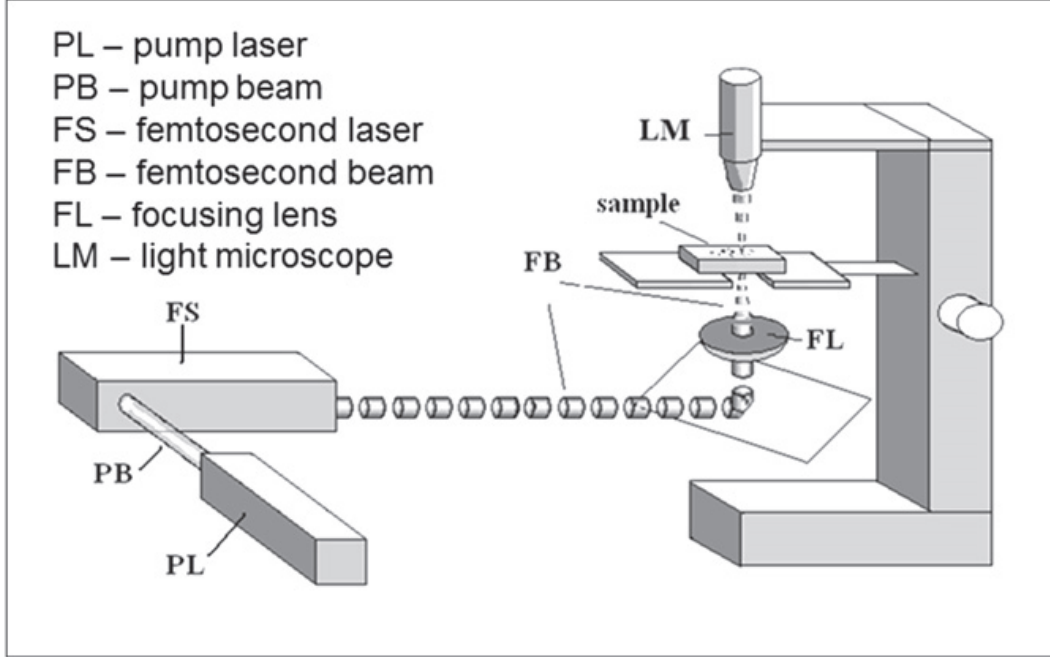


Figure 4.1: Schematic diagram of the femtosecond laser interaction setup.

### 4.3 Experiment

In this experiment, 1-15-layer graphene samples were prepared on quartz substrates by micro-mechanical exfoliation of kish graphite (NGS Naturgraphit) [1]. Optical microscopy was used for locating the samples on the quartz substrates. Sample thickness and characterization of the damage were determined by atomic force microscopy (NTEGRA prima) and Raman spectroscopy (TriVista TR557). The AFM measurements were made under ambient conditions using the tapping mode. The micro-Raman spectra were measured at room temperature using the excitation source of a  $\lambda = 532$  nm, frequency-doubled  $\text{Nd}^{3+}$ :YAG laser, and a laser power of  $\sim 2$  mW with a 50x microscope objective to prevent sample degradation. The acquisition times were 900 s and the spectral resolution was  $\sim 2.2$   $\text{cm}^{-1}$ .

The setup for the ultrafast laser interaction with the samples is shown in figure 4.1. A Ti:sapphire laser operating at 840 nm was the source of a  $\sim 150$  fs beam with 76 MHz repetition. A focusing lens was used to focus the beam onto the samples and a light microscope was used to monitor the positioning.

For the laser interaction, two configurations were used. In the first, the beam directly illuminated the front surface of the sample, which faced downward (reflection mode). In the second, the beam passed through the (transparent) substrate and then irradiated the back of the sample (transmission mode). Pulse power and exposure time were varied.

## 4.4 Results and discussion

Based on the optical microscopy, AFM, and Raman spectroscopy measurements, various damage effects of the laser interaction were found on the single- and multi-layer graphene samples. The damage was characterized mainly by two effects: either complete ablation or some damage (degradation) of the material. Figure 4.2 shows optical microscope images of the complete ablation of an entire SLG sample, as confirmed by Raman spectroscopy measurements. The laser interaction was in transmission mode at  $\sim 350$  mW for several hours of exposure. This removal of a sample represents the full extent of observed damage in all experiments. Significant damage to the nearby graphite is also seen in figure 4.2. The graphite was not ablated as was the SLG, demonstrating that a thicker sample has a higher damage threshold. Using the same laser parameters, 10-15- layer samples were examined. Figure 4.3 shows typical AFM results of the two different types of damage that were found, complete ablation (a) and degradation (b), with corresponding optical microscope images shown in (c) and (d), respectively. These two effects are consistent with previous ultrafast laser experiments done on CVD SLG [19] and theoretical predictions, which state that there exist two thresholds for the onset of damage due to two different mechanisms at work in the  $sp^2$ -bonded layered structure of graphite: removal of intact layers at low absorbed energies, and melting followed by fast evaporation at high energies due to bond breaking within layers [22].

As in figures 4.3(a) and (c), the AFM and optical microscope images showed that the ablated regions were localized, with well defined edges, thereby

demonstrating the feasibility of using ultrafast laser interaction as a way to cut or pattern exfoliated multilayer graphene (as was done by Stöhr *et al* to nanopattern exfoliated SLG [10]). Note that our findings did not identify folding at the edges of the ablated regions, as was found in [8] and [20] on CVD SLG. This was expected due to the multi-layer structure of the samples and the fact that these interactions took place in transmission mode, and the required interaction with the underlying substrate to produce folds was not present [20].

The different types of damage were also confirmed by Raman spectroscopy, which is used to characterize graphene as shown in figures 4.4(a) and (b). The shape of the 2D peak indicates the number of layers. The appearance of the D peak indicates defects (disorder) in the graphene lattice, while the area under the peak is a measure of the defects [23, 24]. In figures 4.4(a) and (b), the Raman spectra before and after 600 s of laser interaction in transmission mode at  $\sim 415$  mW showed that this was a five-layer sample with the appearance of a defect (D peak) after the interaction. The damage appeared in the optical microscope image as a crack, visible in the inset.

The sample with different damage examined in the AFM in figure 4.3(c) was also analyzed by Raman spectroscopy as shown in figure 4.4(c)-(e). The Raman spectra clearly identified the different categories of damage due to the interaction: completely ablated area (c)—the lack of peaks shows the absence of graphene; damaged area (d)—the spectrum shows graphene, and the D peak indicates damage; undamaged area (e)—the D peak (some disorder) is still present, but significantly less than in the damaged area.

Further study of 10-15-layer samples in reflection mode and transmission mode was carried out while varying laser power from  $\sim 50$  to 275 mW and exposure time from 1 to 240 s (figure 4.5). Results were comparable in the two modes. By varying the time of exposure, we observed that ablation could occur with as little as 2 s exposure time at 250 mW. We also observed that there were clear thresholds for both the onset of damage and the onset of complete ablation as laser power increased and exposure time remained constant.

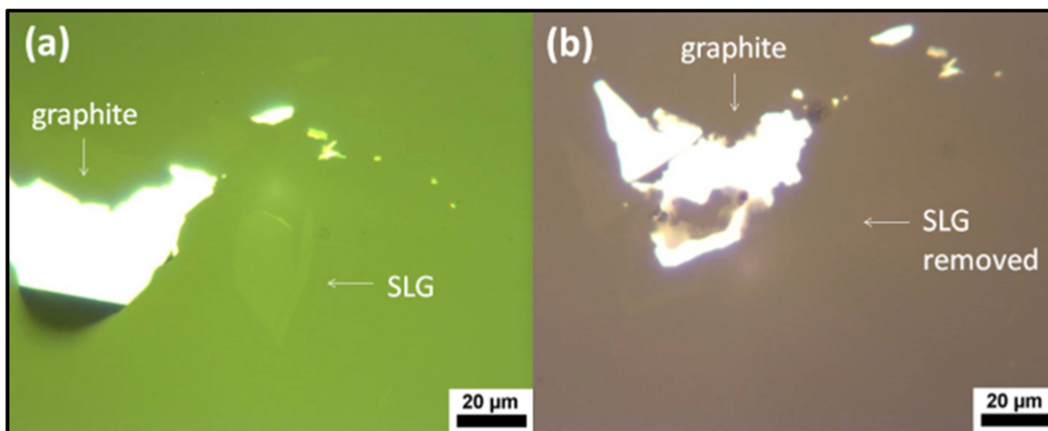


Figure 4.2: Optical microscope images of SLG with nearby graphite before (a) and after (b) laser interaction.

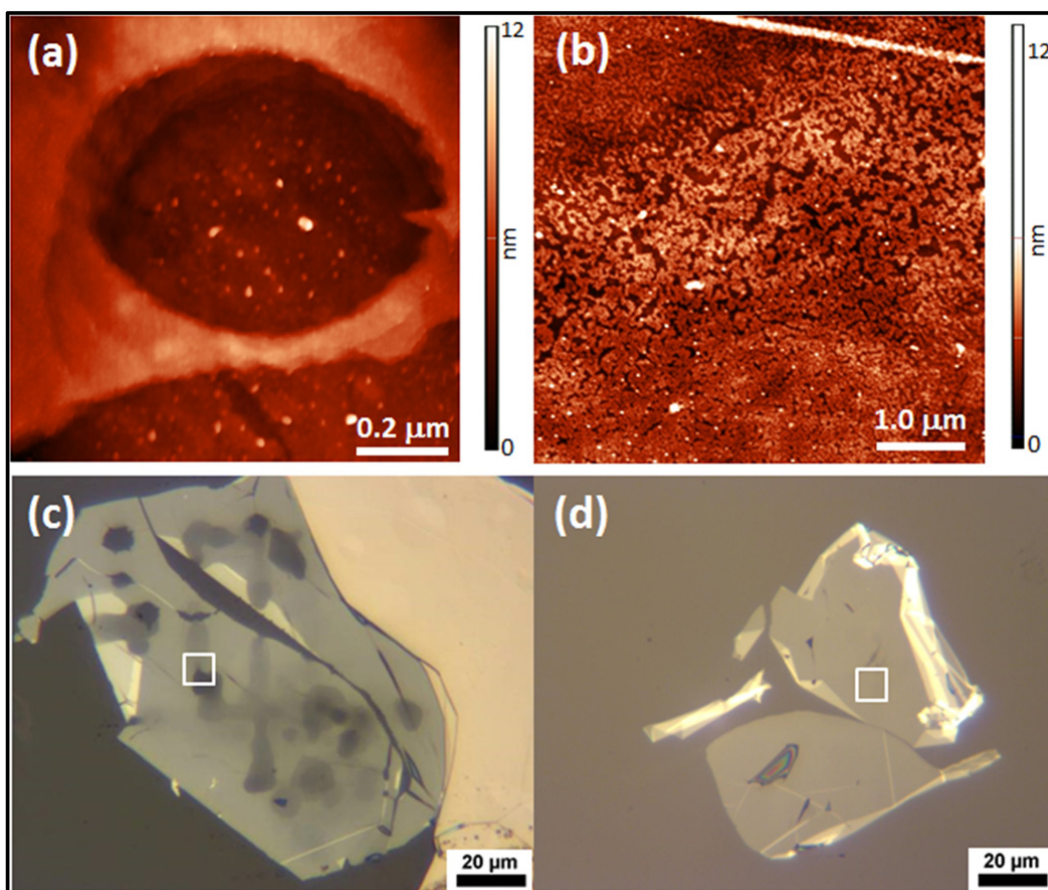


Figure 4.3: (a), (b) AFM images of the areas of laser interaction in 10-15-layer samples showing ablation and degradation, respectively; (c), (d) corresponding optical images of the samples, with white squares indicating positions of AFM measurement above.

Ablation thresholds were typically  $\sim 250$  mW in transmission mode, and were slightly lower ( $\sim 240$  mW) in reflection mode for a  $\sim 10$   $\mu\text{m}$  laser spot diameter, corresponding to fluences of  $\sim 4.2$   $\text{mJ cm}^{-2}$  and  $4.0$   $\text{mJ cm}^{-2}$ , respectively. These thresholds are comparable with that reported by Currie *et al* on CVD SLG, which was an order of magnitude lower than previously measured and theoretical thresholds [18].

The sizes of the damaged and ablated areas in figure 4.5 were analyzed. For all the regions of interaction, diameters of ablated areas were 1-10  $\mu\text{m}$ . Preliminary results showed that damaged areas were always of the same diameter as the laser spot, while ablated areas increased with exposure time up to a maximum value of the laser spot size. The ablation sizes increased faster when the laser interaction occurred on a previous crack from another interaction. The cracks observed (as in figure 4.5) stemmed radially from each of the damaged and ablated regions, which are likely due to the multi-layer structure of the samples.

## 4.5 Conclusion

In this work, the damage effects on exfoliated multi-layer graphene of femtosecond laser beam interaction were investigated. Effects varied depending on laser power, time of exposure, and number of layers of the samples. Damage ranged from complete ablation of the sample, ablated areas, and cracking to disorder of the graphene lattice, as verified by optical microscopy and AFM and Raman spectroscopy. The ablation threshold was determined to be  $\sim 4$   $\text{mJ cm}^{-2}$ , and was slightly lower in reflection mode than in transmission mode. This work also demonstrated the feasibility of ultrafast laser patterning of exfoliated multi-layer graphene.

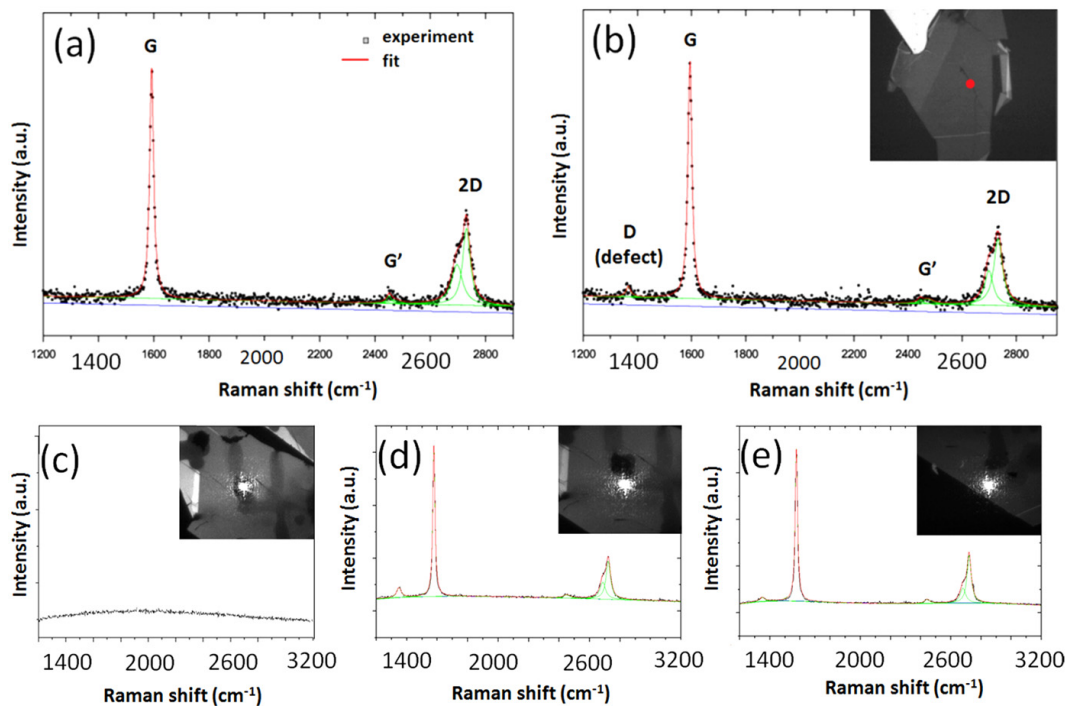


Figure 4.4: Raman spectra of top, a five-layer sample before (a) and after (b) laser interaction; bottom, the same sample from figure 4.3(c) in three different areas—completely ablated (c); damaged (d); undamaged (e); Insets: optical microscope images of the samples showing positions of measurement in the Raman spectrometer.

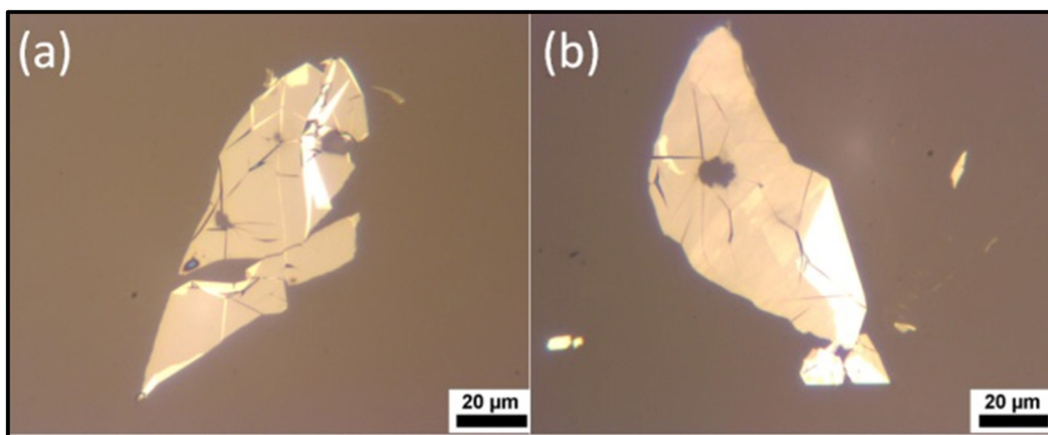


Figure 4.5: Optical microscope images of areas of interaction on 10-15-layer samples at different exposure times and laser powers in reflection mode (a) and transmission mode (b).

## 4.6 Acknowledgements

This work was supported by the Ministry of Science (Republic of Serbia) under projects OI171005, III45016, and III45018.

## 4.7 References

- [1] Novoselov K S, Geim A K, Morozov S V, Jiang D, Zhang Y, Dubonos S V, Grigorieva I V and Firsov A A 2004 *Science* **306** 666-9
- [2] Novoselov K S, Falko V I, Colombo L, Gellert P R, Schwab M G and Kim K 2012 *Nature* **490** 192-200
- [3] Bonaccorso F, Sun Z, Hasan T and Ferrari A C 2010 *Nature Photon.* **4** 611-22
- [4] Grigorenko A N, Polini M and Novoselov K S 2012 *Nature Photon.* **6** 749-58
- [5] Zhou Y, Bao Q, Varghese B, Tang L A L, Tan C K, Sow C and Loh K P 2010 *Adv. Mater.* **22** 67-71
- [6] Zhang W, Li L, Wang Z B, Pena A A, Whitehead D J, Zhong M L, Lin Z and Zhu H W 2012 *Appl. Phys. A* **109** 291-7
- [7] Hong J-Y and Jang J 2012 *J. Mater. Chem.* **22** 8179-91
- [8] Kiisk V, Kahro T, Kozlova J, Matisen L and Alles H 2013 *Appl. Surf. Sci.* **276** 133-7
- [9] Lorenzoni M, Brandi F, Dante S, Giugni A and Torre B 2013 *Sci. Rep.* **3** 1954
- [10] Stöhr R, Kolesov R, Xia K and Wrachtrup J 2011 *ACS Nano* **5** 5141-50
- [11] Kalita G, Qi L, Namba Y, Wakita K and Umeno M 2011 *Mater. Lett.* **65** 1569-72
- [12] Nair R R, Blake P, Grigorenko A N, Novoselov K S, Booth T J, Stauber T, Peres N M R and Geim A K 2008 *Science* **320** 1308-1308
- [13] Hong S-Y, Dadap J I, Petrone N, Yeh P-C, Hone J and Osgood R M 2013 *Phys. Rev. X* **3** 021014
- [14] Liu W-T, Wu S W, Schuck P J, Salmeron M, Shen Y R and Wang F 2010

*Phys. Rev. B* **82** 81408

[15] Lui C H, Mak K F, Shan J and Heinz T F 2010 *Phys. Rev. Lett.* **105** 127404

[16] Bykov A Y, Murzina T V, Rybin M G and Obraztsova E D 2012 *Phys. Rev. B* **85** 121413

[17] Dean J J and van Driel H M 2010 *Phys. Rev. B* **82** 125411

[18] Currie M, Caldwell J D, Bezares F J, Robinson J, Anderson T, Chun H and Tadjer M 2011 *Appl. Phys. Lett.* **99** 211909

[19] Roberts A, Cormode D, Reynolds C, Newhouse-Illige T and LeRoy B J 2011 *Appl. Phys. Lett.* **99** 051912

[20] Yoo J H, Bin In J, Bok Park J, Jeon H and Grigoropoulos C P 2012 *Appl. Phys. Lett.* **100** 233124

[21] Xu J L, Li X L, He J L, Hao X P, Wu Y Z, Yang Y and Yang K J 2011 *Appl. Phys. Lett.* **99** 261107

[22] Jeschke H O, Garcia M E and Bennemann K H 2001 *Phys. Rev. Lett.* **87** 015003

[23] Ferrari A C et al 2006 *Phys. Rev. Lett.* **97** 187401

[24] Graf D, Molitor F, Ensslin K, Stampfer C, Jungen A, Hierold C and Wirtz L 2007 *Nano Lett.* **7** 238-42

# Chapter 5

## Femtosecond laser induced periodic surface structures on multi-layer graphene

Reprinted from Beltaos, A., Kovačević, A. G., Matković, A., Ralević, U., Savić-Šević, S., Jovanović, D., Jelenković, B. M., and Gajić, R. (2014). “Femtosecond laser induced periodic surface structures on multi-layer graphene”. *Journal of Applied Physics*, 116(20), 204306., with the permission of AIP Publishing. <http://dx.doi.org/10.1063/1.4902950>

### 5.1 Abstract

In this work, we present an observation of laser induced periodic surface structures (LIPSS) on graphene. LIPSS on other materials have been observed for nearly 50 years, but until now, not on graphene. Our findings for LIPSS on multi-layer graphene were consistent with previous reports of LIPSS on other materials, thus classifying them as high spatial frequency LIPSS. LIPSS on multi-layer graphene were generated in an air environment by a linearly polarized femtosecond laser with excitation wavelength  $\lambda$  of 840 nm, pulse duration  $\tau$  of  $\sim 150$  fs, and a fluence  $F$  of  $\sim 4.3$ - $4.4$  mJ/cm<sup>2</sup>. The observed LIPSS

were perpendicular to the laser polarization and had dimensions of width  $w$  of  $\sim 30\text{-}40$  nm and length  $l$  of  $\sim 0.5\text{-}1.5$   $\mu\text{m}$ , and spatial periods  $\Lambda$  of  $\sim 70\text{-}100$  nm ( $\sim \lambda/8\text{-}\lambda/12$ ), amongst the smallest of spatial periods reported for LIPSS on other materials. The spatial period and width of the LIPSS were shown to decrease for an increased number of laser shots. The experimental results support the leading theory behind high spatial frequency LIPSS formation, implying the involvement of surface plasmon polaritons. This work demonstrates a new way to pattern multi-layer graphene in a controllable manner, promising for a variety of emerging graphene/LIPSS applications.

## 5.2 Introduction and background

Graphene, a two-dimensional crystal of carbon atoms in a hexagonal lattice, has been attracting much attention in the research community since its discovery in 2004<sup>1</sup> as a unique new material with outstanding electronic,<sup>2</sup> optical,<sup>3</sup> and mechanical<sup>4</sup> properties. Being an ultra-thin, strong, transparent, flexible conductor, graphene has excellent potential for a wide variety of applications, such as solar cells.<sup>5,6</sup> In addition to single-layer graphene, multi-layer graphene has also been important for fundamental studies and applications, such as investigations of its electronic and magneto-optical properties,<sup>1,7,8</sup> second harmonic generation,<sup>9</sup> Q-switching and mode-locking of lasers,<sup>10</sup> and patterning/lithography.<sup>11</sup>

For many graphene applications, the ability to pattern or structure it in a controllable manner is very important, e.g., in transparent electrodes, field effect transistors, chem/ biosensors, and energy devices.<sup>12,13</sup> So far, patterned structures have been achieved on graphene using several chemical and physical techniques mainly classified by lithography, soft lithography, and direct laser writing.<sup>12,13</sup> Parallel periodic structures have been produced on graphene by self assembly onto patterned substrates,<sup>14</sup> multi-beam interference,<sup>15</sup> and strain-based techniques,<sup>16,17</sup> and have applications in, for example, nanoscale electronic devices.<sup>16</sup> In general, various patterning techniques are required to

meet the needs of different graphene applications.<sup>12</sup>

Another patterning method, which has not yet been explored for graphene, involves laser irradiation and produces nanostructures known as “laser-induced periodic surface structures” (LIPSS). LIPSS are parallel periodic structures, also known as “surface ripples,” classified by their spatial period (centre-to-centre distance between neighbouring parallel structures), and should not be confused with nanoribbons, being ultrathin strips of material.

The occurrence of LIPSS has long been known and studied (since 1965<sup>18</sup>) on a wide variety of other materials, including metals, semiconductors, and dielectrics<sup>19–22</sup> and has many applications in fields such as photonics, plasmonics, and optoelectronics.<sup>23</sup> For example, LIPSS applications include the modification of a materials optical, electrical, or wetting properties, structural colours, absorptance enhancement, antireflective films, biomedical applications, and optofluidics applications.

The technique of producing LIPSS offers a number of advantages useful for applications:<sup>23</sup> *simplicity, wide applicability, and low cost*—neither additional materials (as in lithography) nor laser scanning (as in direct writing) are required, and patterning can be done under normal ambient conditions in a quick one-step process; *high resolution*—capable of sub-wavelength nanostructuring; and *controllability*—the LIPSS orientation depends on the beam polarization direction, while the period can be varied by the laser wavelength, incidence angle, or effective refractive index of the interface between the material and surrounding medium.<sup>23–26</sup>

LIPSS are typically formed on a material surface by a linearly polarized pulsed laser beam at normal incidence,<sup>23</sup> with orientation depending on the polarization of the incident beam.<sup>19,27,28</sup> The resulting spatial period ( $\Lambda$ ) is either on the order of the laser wavelength ( $\lambda$ ) in low spatial frequency LIPSS (LSFL) or significantly smaller than  $\lambda$  ( $\Lambda < \lambda/2$ ) in high spatial frequency LIPSS (HSFL).<sup>19</sup> For application purposes, smaller spatial periods (HSFL) are desirable, and much research is devoted to minimize the LIPSS spatial period. For example, spatial periods as little as  $\Lambda \approx 70\text{--}90$  nm ( $\lambda/10$ ) have been

reported in an air environment on titanium by Bonse *et al.*<sup>19</sup> HSFL are fabricated using femtosecond irradiation,<sup>19,23</sup> and have been observed mostly on transparent materials.<sup>27,28</sup> The underlying process of the formation of LIPSS is not completely understood, with debate in the literature and different theories proposed. Generally, the formation is described by the interference of the incident laser beam with a surface wave, such as a laser excited surface plasmon polariton (SPP), leading to a spatial periodic energy distribution on the material surface.<sup>21,29–32</sup> Second harmonic generation<sup>33</sup> and self-organization<sup>34</sup> effects have also been proposed.

Single or multi-layer graphene's high transparency and ability to be patterned or ablated with a pulsed laser in the femtosecond regime<sup>12,35</sup> make it a desirable material for HSFL formation. In addition, SPPs in graphene are in a new emerging field,<sup>36</sup> and their existence has been recently experimentally demonstrated.<sup>37</sup> SPPs in multi-layer graphene systems have also been investigated.<sup>36,38</sup> All of these properties, along with its high potential for applications, make graphene a promising candidate for the formation of LIPSS, while at the same time, the advantages of the LIPSS fabrication technique would be very useful in the applications of graphene. As an example, one potential application of graphene LIPSS could be the fabrication of graphene nanoribbons, with the advantages of mass production of nanoribbons in a quick, simple, cost-effective manner, with controllable dimensions and orientation via the laser parameters. Since LIPSS have never been observed before on graphene, the immense opportunities for new applications are apparent through the known applications of patterned graphene and the known applications of LIPSS on other materials, as mentioned above.

In this work, we present an observation of LIPSS on graphene. LIPSS on multi-layer graphene were induced by femtosecond laser irradiation. The samples and structures were analyzed using Raman spectroscopy, optical microscopy, atomic force microscopy (AFM), and scanning electron microscopy (SEM). The results were compared to previous reports on other materials.

## 5.3 Experiment

*Sample preparation and characterization:* Graphene samples of  $\sim 3$ -15 layers were prepared from kish graphite (NGS Naturgraphit GmbH) on transparent quartz substrates (Edmund Optics) by the standard micromechanical exfoliation technique,<sup>1</sup> and located on the substrates by optical microscopy. Characterization of the samples was performed by Raman Spectroscopy at room temperature using Micro Raman Chromex 2000 and TriVista TR557 Raman systems, each with a frequency doubled Nd<sup>3+</sup>: YAG laser as an excitation source at a wavelength of  $\lambda=532$  nm. In both systems, a 50x or a 40x microscope objective was used, and the laser power on the sample was  $\sim 1$ -2 mW, preventing sample degradation. Acquisition times of the micro-Raman spectra were 150-900 s with a spectral resolution of  $\sim 2$  cm<sup>-1</sup>. Sample thickness was determined by a combination of Raman spectroscopy, optical microscopy in transmission mode,<sup>39</sup> and AFM (details described below).

*Laser interaction:* Femtosecond laser beam interaction with the samples was performed in an air environment using the setup shown in Figure 5.1. The source of the beam ( $\lambda=840$  nm wavelength,  $\tau \approx 150$  fs pulse duration,  $\nu=76$  MHz repetition rate) was a Coherent Mira 900 Ti:Sapphire system. The beam power and exposure time were varied for the experiments. The beam was focused onto the samples using a focusing lens, while the position of the beam on the sample was monitored using a light microscope. The femtosecond laser experiments were performed in transmission mode, i.e., the samples were irradiated from below with the beam first passing through the transparent substrate and then irradiating the back of the sample at normal incidence. The wavelength was confirmed to be unchanged by passing through the quartz substrate and sample using an Ocean Optics HR2000CG-UV-NIR fiber-optic spectrometer.

*Characterization of laser-induced structures:* After the interaction, the samples were characterized by AFM and SEM. AFM measurements were done using an NTEGRA prima in the tapping mode under ambient conditions. The

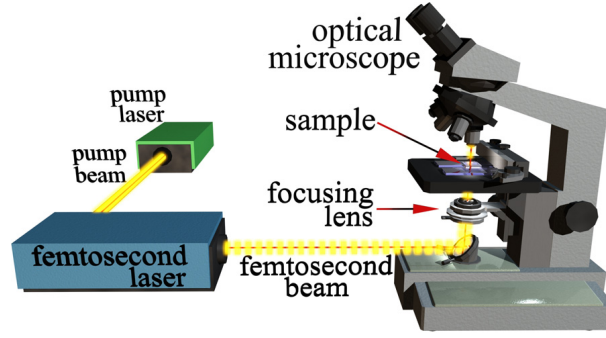


Figure 5.1: Schematic of the femtosecond laser interaction set-up.

SEM measurements were done using a Tescan MIRA3 field emission gun SEM, with electron energies of 1-2 kV. Sample preparation for the SEM measurements was performed in two different ways, coated with  $\sim 5$  nm of gold (higher resolution) and uncoated. SEM measurements were generally performed after all the other experiments, in order to avoid potential electron beam damage of the samples<sup>40,41</sup> and/or because of the gold coating on top, which restricted further experimentation.

## 5.4 Results and discussion

The experiment as described above was performed on selected graphene samples of 3-5 layers and  $\sim 10$ -15 layers. Figure 5.2 shows examples of a 15-layer graphene sample (Figs. 5.2(a) and 5.2(b)) and a 5-layer graphene sample (Figs. 5.2(c) and 5.2(d)) before (left) and after (right) femtosecond laser interaction. Raman spectroscopy and optical transmission microscopy, the methods used for sample characterization and thickness determination, are represented in Fig. 5.3(a), and Figs. 5.3(b) and 5.3(c), respectively. The occurrence of the G, G', and 2D peaks in the Raman spectrum in Fig. 5.3(a) shows the presence of graphene. The shape of the 2D peak indicates the number of layers and a relatively small (or lack of) D-peak indicates the presence of good quality (or defect-free) graphene.<sup>42,43</sup> Analysis of the optical microscope images in transmission mode (Figs. 5.3(b) and 5.3(c)) allows us to calculate the number of layers<sup>1</sup> based on the amount of absorption of transmitted light through the

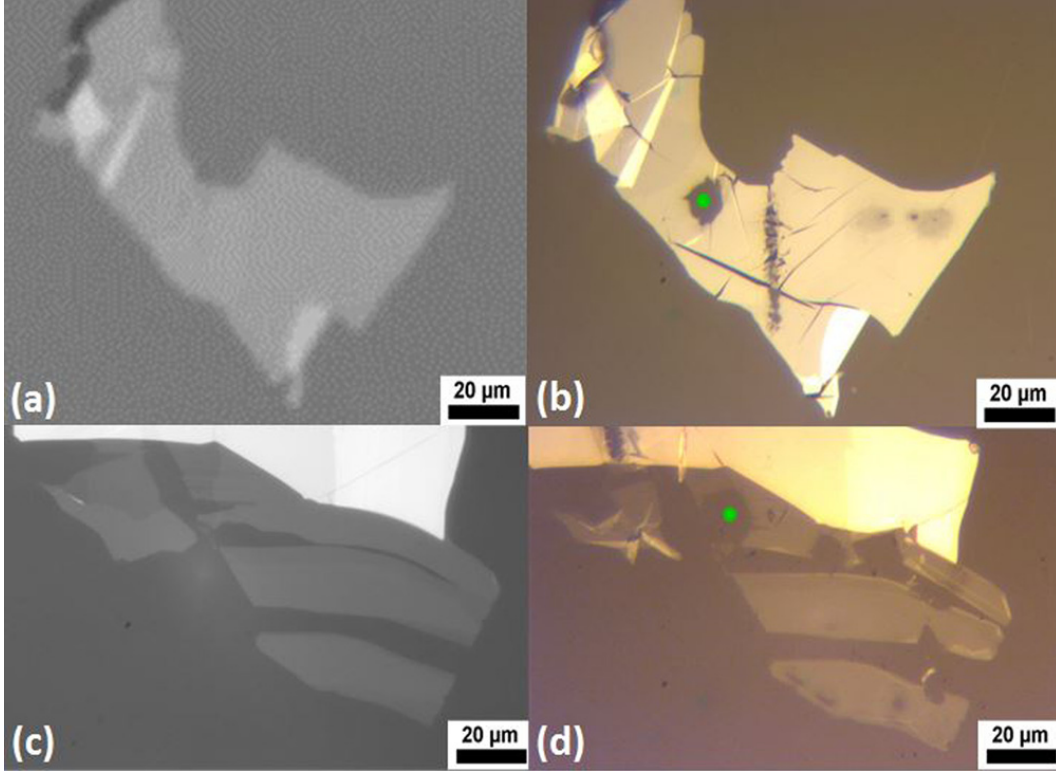


Figure 5.2: Optical microscope images of (a) and (b) 15-layer graphene, and (c) and (d) 5-layer graphene samples before (left) and after (right) laser interaction. The green dots mark regions ablated for  $t=4$  min ( $N \approx 1.8 \times 10^{10}$ ) of irradiation by a beam of  $F \approx 4.3 - 4.4$  mJ/cm<sup>2</sup>.

sample as compared to the substrate (each layer absorbing 2.3% (Ref. 39)).

In the optical microscope images of the samples after laser interaction (Figs. 5.2(b) and 5.2(d)), the areas of interaction for various fluences and exposure times are seen as dark spots on the sample, which range from disordered graphene to completely ablated regions, as shown in previous work.<sup>35</sup>

The laser fluence ( $F$ ) was varied from  $\sim 1$  to 6 mJ/cm<sup>2</sup>, while exposure time ( $t$ ) was varied from 1 s to 4 min. Analysis of the various regions of interaction in SEM showed that clearly defined parallel nanostructures (LIPSS) consistently formed in the ablated regions of the 10-15 layer samples (Figs. 5.4(a) and 5.4(b)) for laser fluences slightly above the multi-layer graphene ablation threshold of 4.2 mJ/cm<sup>2</sup> (as found in Ref. 35 using  $N$  values similar to this work of  $N = 1.5 \times 10^8 - 1.8 \times 10^{10}$ ). Incubation effects and the depen-

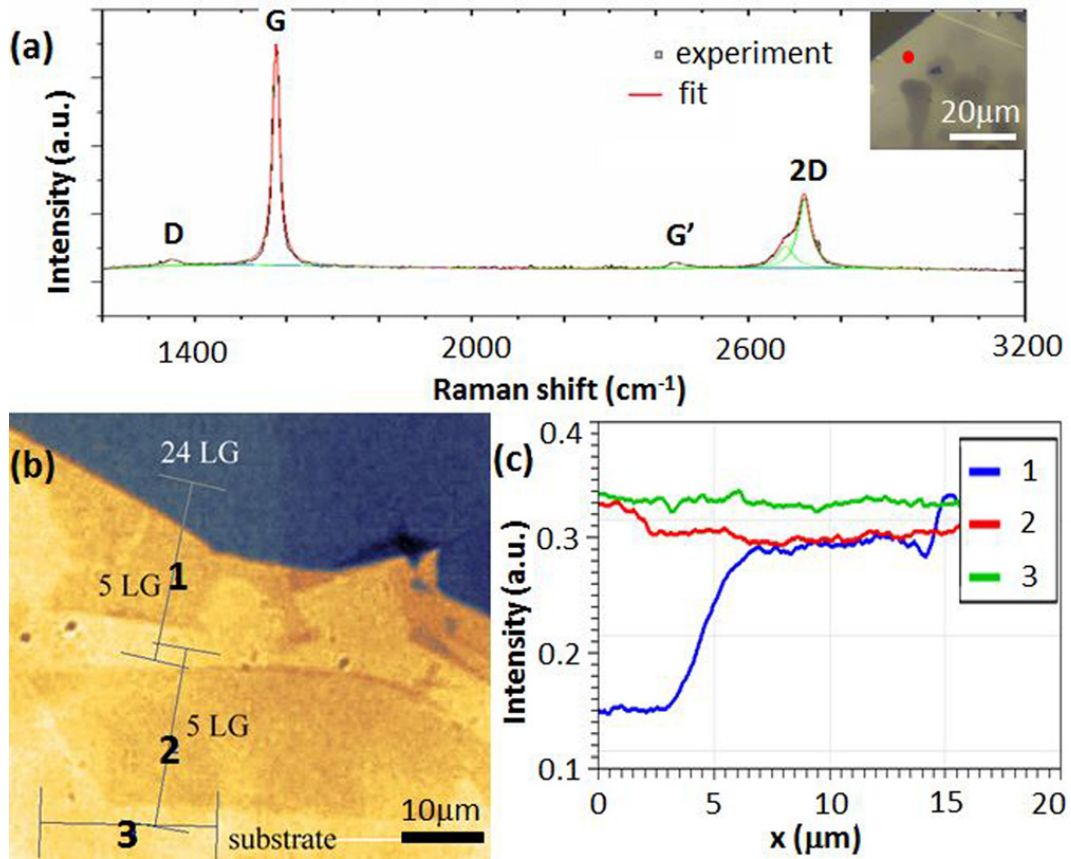


Figure 5.3: (a) Micro-Raman spectrum of a 14-layer graphene sample. Inset: Optical microscope image, where the red dot indicates the position of the Raman measurement on a non-interacted area of the sample. (b) Transmission optical image of a 5-layer graphene (5 LG) sample, adjacent to a 24-layer flake (24 LG). The intensity of transmitted light for profile lines 1, 2, and 3 is shown in (c) in blue, red, and green, respectively.

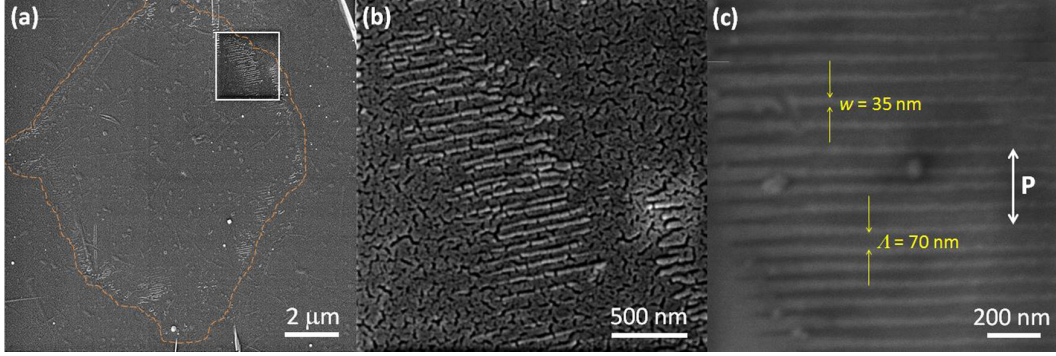


Figure 5.4: SEM images of LIPSS observed on multi-layer graphene coated with a gold layer of  $\sim 5$  nm: (a) ablated region due to laser interaction marked by orange dashed line. The white square shows where LIPSS were found, with a zoomed in image shown in part (b); (c) typical obtained LIPSS, showing width  $w$  and period  $\Lambda$  of the nanostructures and the polarization direction ( $\mathbf{P}$ ) of the laser used in the interaction.

dence of  $N$  on the threshold were not investigated.) whereas structures were not found for fluences below this threshold. The obtained structures were perpendicular to the laser polarization used in the interaction (Fig. 5.4(c)). Our results are consistent with previous observations of LIPSS on other materials, which are generally formed at fluences slightly above the damage threshold and perpendicular to the laser polarization.<sup>23,35</sup> Repeated experiments showed that the most clearly defined and intact LIPSS on multi-layer graphene were produced using the parameters  $F \approx 4.3\text{-}4.4$  mJ/cm<sup>2</sup> and  $t=4$  min (corresponding to number of laser shots ( $N$ ) of  $\sim 1.8 \times 10^{10}$ ). The green dot in Fig. 5.2(b) shows an ablated region using these parameters.

Using the same experimental parameters on the thinner samples of 3-5 layers (Fig. 5.2(d)—green dot) did not lead to the occurrence of LIPSS. Even by decreasing the fluence and exposure time to  $F=3.2$  mJ/cm<sup>2</sup> and  $t=2$  min ( $N = 9 \times 10^9$ ), LIPSS were still not observed on these samples, as shown in the comparison SEM images of Figure 5.5. Parallel structures can be clearly seen at the edge of the ablated region of a 15-layer sample (Figs. 5.5(a) and 5.5(c)) but not on a 5-layer sample (Figs. 5.5(b) and 5.5(d)) for the same SEM parameters. Further studies are required to determine the ablation threshold

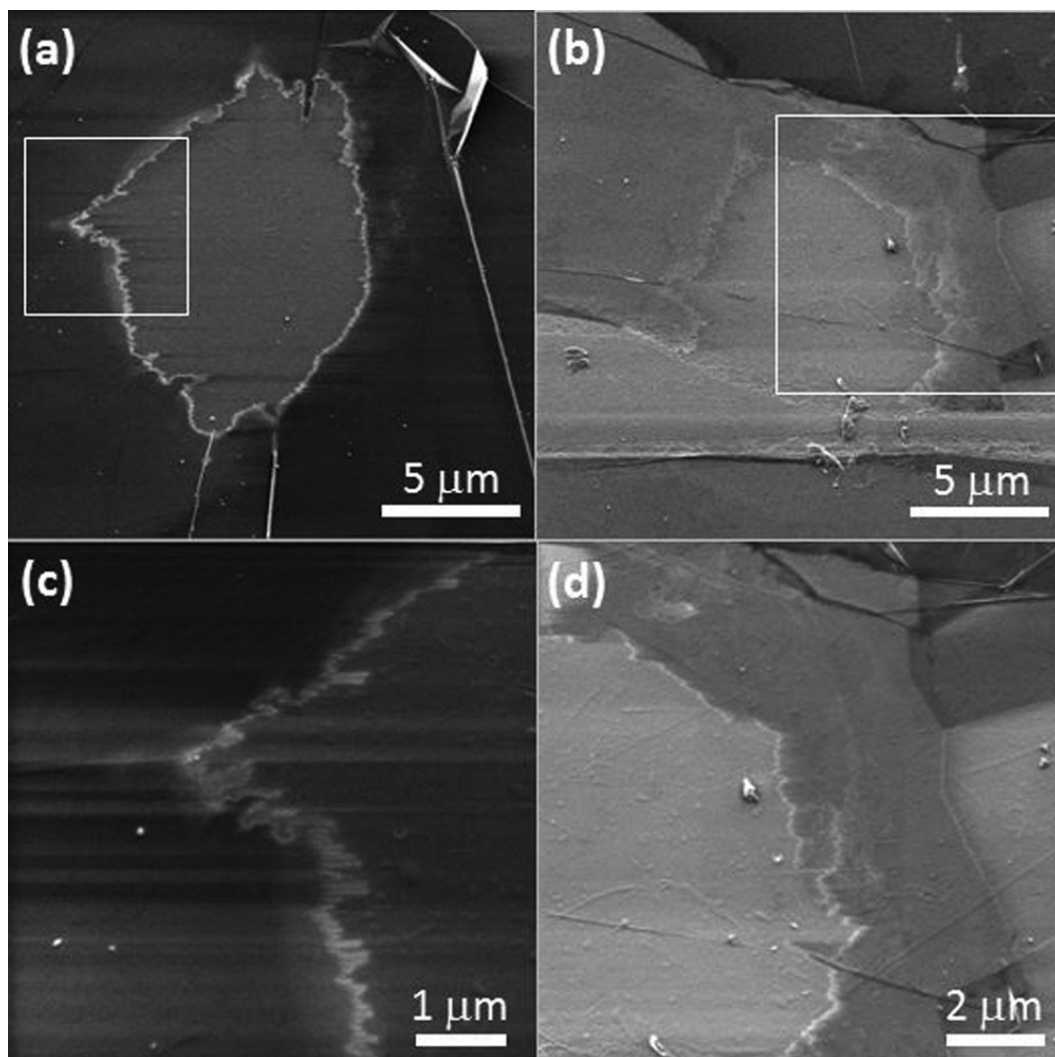


Figure 5.5: Comparison SEM images of 15-layer graphene (left panel) and 5-layer graphene (right panel) samples. Ablated regions are shown in (a) and (b), where the white squares indicate the area examined in the corresponding larger image below in (c) and (d). The SEM images were taken without gold on the sample.

of these thinner graphene samples and hence the laser interaction parameters for LIPSS formation.

The LIPSS on multi-layer graphene were further analyzed using AFM as shown in Figure 5.6. The structures were found in the ablated regions of the samples irradiated with a laser fluence of  $F \approx 4.3-4.4 \text{ mJ/cm}^2$  (Fig. 5.6(a)), usually in the peripheral area attached to the surrounding sample (Fig. 5.6(b)), and occasionally in the central area as well (Fig. 5.6(c)). A close-up phase image of the structures is shown in Fig. 5.6(d), in which it can be seen that the LIPSS were surrounded by dense nanostructures. Height profiles of the LIPSS (Fig. 5.6(e)) were obtained from which the spatial period ( $\Lambda$ ) and width ( $w$ ) of the structures were measured and found to be  $\Lambda \approx 70-100 \text{ nm}$  and  $w \approx 35 \pm 5 \text{ nm}$ . The height profiles (Fig. 5.6(e)) also showed that the LIPSS were less than or equal to the height of the surrounding sample, with some variation due to surface roughness as shown in the 3D height map of Fig. 5.6(f). Aside from these variations, the height of the structures was relatively constant along their length, with a sudden decrease where they were truncated, as represented in Fig. 5.6(f). Typical measured values of the height of the structures were  $\sim 1-2 \text{ nm}$  less than the sample height, corresponding to ablation of 3-6 layers of graphene, which indicates why structures were not observed for the thinner samples.

The width and period of the LIPSS as measured by AFM were also confirmed by SEM measurements (as in Fig. 5.4(c)). In addition, from the SEM measurements, the lateral dimensions of length ( $l$ ) and range ( $r$ ) of the structures were obtained. The structures typically spanned a range as large as the ablated region,  $r \approx 4.5-5 \mu\text{m}$ , and the length varied from  $l \approx 0.5$  to  $1.5 \mu\text{m}$  (Fig. 5.7(a)). The variation in length of structures often displayed a wave-like behaviour (Fig. 5.7(b)).

To investigate the formation of LIPSS on the 10-15 layer samples, the exposure time was significantly decreased to  $\sim 16-20 \text{ s}$  ( $N \approx 1.2 \times 10^9 - 1.5 \times 10^9$ ), while the laser fluence was kept at  $F \approx 4.4 \text{ mJ/cm}^2$ . The shorter exposure time led to a much smaller area of the ablated region,<sup>35</sup> as shown in Fig. 5.8(a).

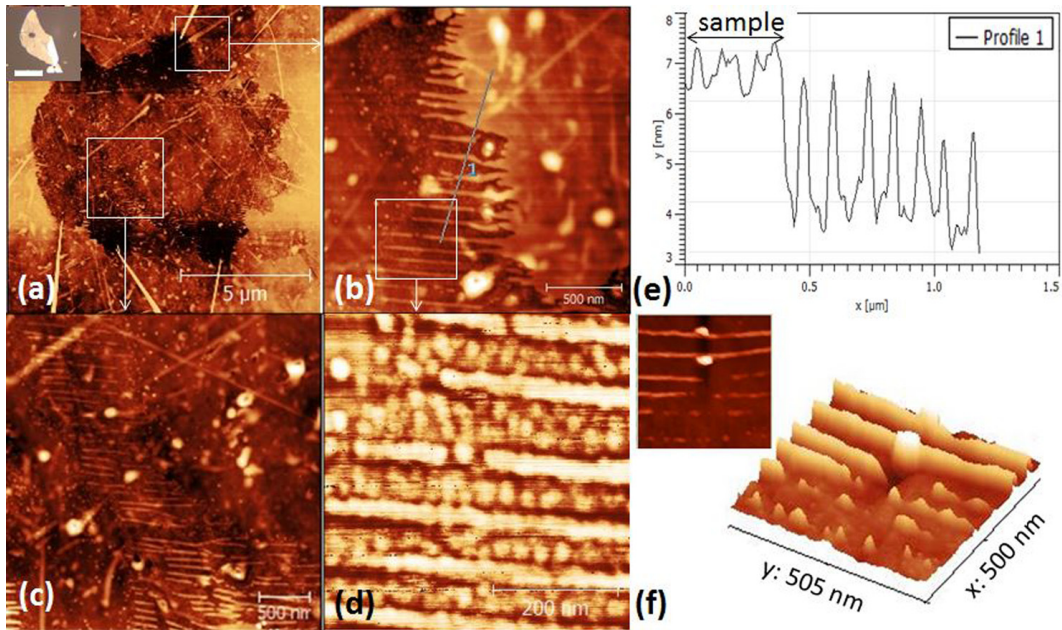


Figure 5.6: AFM analysis of LIPSS on multi-layer graphene: (a) Ablated region of the sample. Inset: optical image of the sample where the ablated region can be seen as a black dot (scale bar of inset is  $40 \mu\text{m}$ ). White squares represent areas where structures were found, corresponding to (b) and (c), respectively; (d) phase image of the structures, zoomed in from the white square in (b); (e) height profile corresponding to the profile line “1” in (b); (f) 3D height map of structures, with inset showing corresponding 2D image.

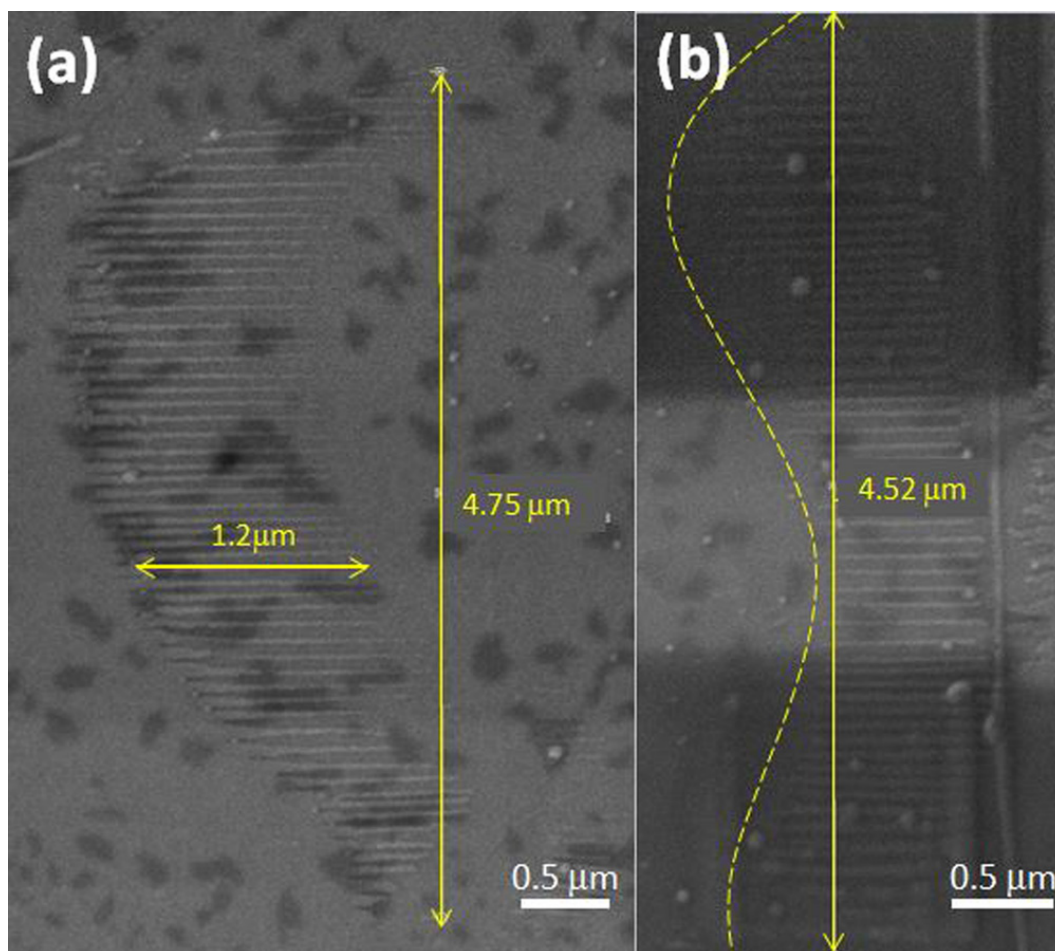


Figure 5.7: SEM images showing the lateral dimensions of the LIPSS on multilayer graphene coated with a gold layer of  $\sim 5$  nm: (a) range and length; (b) variations in length, marked by the yellow dashed curve. Black squares are due to SEM charging, while black dots are due to ambient contamination.

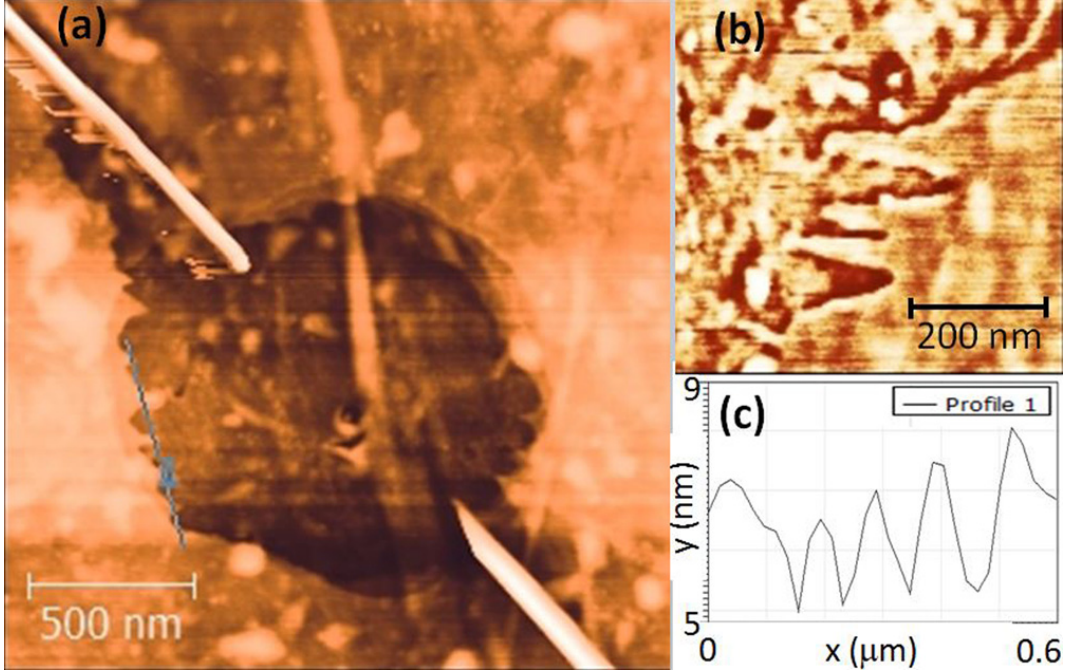


Figure 5.8: AFM analysis of LIPSS on multi-layer graphene with reduced laser exposure time: (a) ablated region; structures are seen around the peripheral area; (b) phase image of structures; (c) height profile corresponding to the profile line “1” in (a).

The existence of structures at the edges of these regions was confirmed by AFM as shown in Figures 5.8(a) and 5.8(b). The structures were much less clearly defined than those with longer exposures, and were wider ( $w \approx 55\text{-}85\text{ nm}$ ), shorter ( $l \approx 80\text{-}200\text{ nm}$ ), and farther apart ( $\Lambda \approx 115\text{-}120\text{ nm}$ ) (Fig. 5.8(c)). As before, these structures were perpendicular to the laser polarization.

*Discussion:* For our incident wavelength of  $\lambda=840\text{ nm}$ , the measured spatial periods of  $\sim 70\text{-}100\text{ nm}$  correspond to  $\sim \lambda/8\text{-}\lambda/12$ , classifying the LIPSS as HSFL with periods amongst the smallest ever reported.<sup>19</sup> For comparison, on bulk graphite, LIPSS with periods of  $110\text{-}800\text{ nm}$  were found.<sup>22</sup> The spatial period has been shown to decrease by increasing the number of laser shots  $N$ .<sup>19,21,23,44,45</sup> Our observations of LIPSS with larger periods for smaller  $N$  also agree with this phenomenon. Various effects of the laser fluence have been reported in the literature, with an increase in fluence resulting sometimes in an increase in period<sup>44</sup> and sometimes a decrease in period.<sup>24</sup> Here, we have ob-

served HSFL using orders of magnitude lower values of  $F$  and higher  $N$  than typical values on other materials,<sup>19</sup> which is possible due to the thinness of multi-layer graphene that allows for a lower ablation threshold.<sup>35</sup> Therefore, our results coincide with a decrease in period for higher  $N$  and lower  $F$  values, also suggesting a reason for the smaller observed periods. In addition, reports have shown that HSFL with wavelengths significantly smaller than the laser wavelength are found, as in our case, on transparent materials, in the femtosecond regime, and around the peripheral area of ablated regions.<sup>23,27–29</sup> The latter effect is due to the Gaussian beam profile of the laser, and studies have even shown a transition from LSFL in the high-intensity central ablated region to HSFL around the lower-intensity edges.<sup>34</sup> In our case, this effect was not observed, as the central region was mainly ablated in the higher intensity area of the laser beam.

The very small observed periods in our study as compared with other materials could be explained by following an SPP model<sup>32</sup> of LIPSS formation. While the origin of LSFL is typically described as the interference of the incident laser light with surface plasmons at the material medium interface,<sup>21,29–31</sup> the origin of HSFL has been described as two SPPs propagating in opposite directions with interference effects leading to a reduced period equal to even fractions of the laser wavelength.<sup>32</sup> This is plausible for our results, since the measured spatial periods of  $\Lambda \approx 70, 80, 90,$  and  $100$  nm are within error of  $\sim 5$  nm ( $\sim 5\%$ ) to  $\lambda/12=70$  nm,  $\lambda/10=84$  nm, and  $\lambda/8=105$  nm, and because SPPs on graphene with varying wavelengths and interference effects have also been reported.<sup>36,38</sup> Graphene is known to have SPPs with strong confinement and low loss, leading to wavelengths much smaller than that of the incident light,<sup>36</sup> and in a multi-layer system, the wavelength is predicted to be smaller as compared to single-layer graphene.<sup>38</sup>

Some studies have related the decrease in spatial period with increase in  $N$  to be due to the positive feedback of the SPP model;<sup>29</sup> a process which results in HSFL densely covered with nanostructures. A reduced period is expected by this model due to a change of effective refractive index at the air-material

interface when the nanostructures develop on the surface, affecting SPP propagation. Also, a wave-like variation in height/length of the HSFL coincides with the spatial periodic energy distribution density suggested by this model. These effects are consistent with our observations, indicating further evidence for the SPP model of the formation of LIPSS on multi-layer graphene.<sup>32</sup>

## 5.5 Conclusion

In this work, we observed laser induced periodic surface structures (LIPSS) on multi-layer graphene. Using a femtosecond laser, LIPSS perpendicular to the laser polarization with length  $\sim 0.5\text{-}1.5\ \mu\text{m}$  and width  $\sim 35 \pm 5\ \text{nm}$  were induced on 10-15-layer graphene in an air environment. The measured spatial periods were  $\sim 70\text{-}100\ \text{nm}$  ( $\sim \lambda/8\text{-}\lambda/12$ ), amongst the smallest periods ever reported for LIPSS on other materials. The spatial period and width of the LIPSS were shown to decrease for an increased number of laser shots. The incident laser beam parameters used for the fabrication of LIPSS were  $\lambda=840\ \text{nm}$ ,  $F \approx 4.3 - 4.4\ \text{mJ}/\text{cm}^2$ , and  $N \approx 1.8 \times 10^{10}$ . Using the same parameters, a comparison was made with thinner graphene samples of 3-5 layers, on which LIPSS were not observed. Our results on multi-layer graphene are consistent with previous experimental findings of LIPSS on other materials. Specifically, HSFL were observed in the femtosecond regime, on a transparent material, in the peripheral of laser-ablated regions, and with the effect of a smaller spatial period for a higher number of laser shots. The observed HSFL are also consistent with a surface plasmon polariton model of LIPSS formation.

Through this work, we have demonstrated the patterning of graphene in a new controllable way (the width, period, and orientation are controlled using the laser parameters) by using the LIPSS technique that is well-known for other materials. The discovery of graphene LIPSS displays a fundamental property of graphene, placing it into the known field of LIPSS and giving insight into the physics of this unique material and the intriguing LIPSS formation process. Thus, our results have opened up the possibility for graphene

LIPSS applications and research, laying the groundwork to build on for further studies in this direction.

## 5.6 Acknowledgements

The authors would like to thank Miloš Bokorov (Faculty of Science, University of Novi Sad, Novi Sad, Serbia) for preliminary SEM measurements, and Dejan Pantelić (Institute of Physics, University of Belgrade, Belgrade, Serbia) for helpful discussions. This work was supported by the Ministry of Science (Republic of Serbia) under the projects OI171005, III45016, and III45018.

## 5.7 References

- <sup>1</sup>K. S. Novoselov, A. K. Geim, S. V. Morozov, D. Jiang, Y. Zhang, S. V. Dubonos, I. V. Grigorieva, and A. A. Firsov, *Science* **306**, 666 (2004).
- <sup>2</sup>N. M. R. Peres, *Rev. Mod. Phys.* **82**(3), 2673 (2010).
- <sup>3</sup>K. F. Mak, L. Ju, F. Wang, and T. F. Heinz, *Solid State Commun.* **152**(15), 1341 (2012).
- <sup>4</sup>C. Lee, X. Wei, J. W. Kysar, and J. Hone, *Science* **321**(5887), 385 (2008).
- <sup>5</sup>K. S. Novoselov, V. I. Falko, L. Colombo, P. R. Gellert, M. G. Schwab, and K. Kim, *Nature* **490**, 192 (2012).
- <sup>6</sup>F. Bonaccorso, Z. Sun, T. Hasan, and A. C. Ferrari, *Nature Photon.* **4**, 611 (2010).
- <sup>7</sup>M. Koshino and T. Ando, *Phys. Rev. B* **77**(11), 115313 (2008).
- <sup>8</sup>J. Hass, W. A. De Heer, and E. H. Conrad, *J. Phys.: Condens. Matter* **20**(32), 323202 (2008).
- <sup>9</sup>A. Y. Bykov, T. V. Murzina, M. G. Rybin, and E. D. Obraztsova, *Phys. Rev. B* **85**, 121413 (2012).
- <sup>10</sup>J. L. Xu, X. L. Li, J. L. He, X. P. Hao, Y. Z. Wu, Y. Yang, and K. J. Yang, *Appl. Phys. Lett.* **99**, 261107 (2011).

- <sup>11</sup>Y. Zhou, Q. Bao, B. Varghese, L. A. L. Tang, C. K. Tan, C. Sow, and K. P. Loh, *Adv. Mater.* **22**, 67 (2010).
- <sup>12</sup>J.-Y. Hong and J. Jang, *J. Mater. Chem.* **22**, 8179 (2012).
- <sup>13</sup>J. Feng, W. Li, X. Qian, J. Qi, L. Qi, and J. Li, *Nanoscale* **4**(16), 4883 (2012).
- <sup>14</sup>T. Kaplas and Y. Svirko, *Carbon* **70**, 273 (2014).
- <sup>15</sup>Y. Li, Y. Li, W. Shi, S. Chen, G. Zhang, Z. Liu, Q. Sun, J. Tian, Y. Xu, and Y. Chen, *Int. J. Nanomanuf.* **8**(3), 221 (2012).
- <sup>16</sup>W. Bao, F. Miao, Z. Chen, H. Zhang, W. Jang, C. Dames, and C. N. Lau, *Nat. Nanotechnol.* **4**(9), 562 (2009).
- <sup>17</sup>A. Capasso, E. Placidi, H. F. Zhan, E. Perfetto, J. M. Bell, Y. Gu, and N. Motta, *Carbon* **68**, 330 (2014).
- <sup>18</sup>M. Birnbaum, *J. Appl. Phys.* **36**, 3688 (1965).
- <sup>19</sup>J. Bonse, J. Krüger, S. Höhm, and A. Rosenfeld, *J. Laser Appl.* **24**(4), 042006 (2012).
- <sup>20</sup>G. Dumitru, V. Romano, H. P. Weber, M. Sentis, and W. Marine, *Appl. Phys. A* **74**(6), 729 (2002).
- <sup>21</sup>M. Huang, F. Zhao, Y. Cheng, N. Xu, and Z. Xu, *ACS Nano* **3**(12), 4062 (2009).
- <sup>22</sup>E. V. Golosov, A. A. Ionin, Y. R. Kolobov, S. I. Kudryashov, A. E. Ligachev, S. V. Makarov, Y. N. Novoselov, L. V. Seleznev, D. V. Sinitsyn, and A. R. Sharipov, *Phys. Rev. B* **83**(11), 115426 (2011).
- <sup>23</sup>A. Y. Vorobyev and C. Guo, *Laser Photon. Rev.* **7**(3), 385 (2013).
- <sup>24</sup>E. V. Golosov, A. A. Ionin, Y. R. Kolobov, S. I. Kudryashov, A. E. Ligachev, Y. N. Novoselov, L. V. Seleznev, and D. V. Sinitsyn, *J. Exp. Theor. Phys.* **113**(1), 14 (2011).
- <sup>25</sup>T. Y. Hwang and C. Guo, *J. Appl. Phys.* **108**(7), 073523 (2010).
- <sup>26</sup>A. Y. Vorobyev and C. Guo, *J. Appl. Phys.* **104**(6), 063523 (2008).
- <sup>27</sup>M. Rohloff, S. K. Das, S. Höhm, R. Grunwald, A. Rosenfeld, J. Krüger, and J. Bonse, *J. Appl. Phys.* **110**(1), 014910 (2011).
- <sup>28</sup>Q. Wu, Y. Ma, R. Fang, Y. Liao, Q. Yu, X. Chen, and K. Wang, *Appl. Phys.*

- Lett.* **82**(11), 1703 (2003).
- <sup>29</sup>A. Y. Vorobyev, V. S. Makin, and C. Guo, *J. Appl. Phys.* **101**(3), 034903 (2007).
- <sup>30</sup>J. Bonse, A. Rosenfeld, and J. Krüger, *J. Appl. Phys.* **106**(10), 104910 (2009).
- <sup>31</sup>J. E. Sipe, J. F. Young, J. S. Preston, and H. M. Van Driel, *Phys. Rev. B* **27**(2), 1141 (1983).
- <sup>32</sup>V. S. Makin, R. S. Makin, A. Y. Vorobyev, and C. Guo, *Tech. Phys. Lett.* **34**(5), 387 (2008).
- <sup>33</sup>D. Dufft, A. Rosenfeld, S. K. Das, R. Grunwald, and J. Bonse, *J. Appl. Phys.* **105**(3), 034908 (2009).
- <sup>34</sup>J. Reif, *Laser-Surface Interactions for New Materials Production*, Springer Series in Materials Science Vol. 130, edited by A. Miotello and P. Ossi (Springer, Berlin, 2010), pp. 19-41.
- <sup>35</sup>A. Beltaos, A. Kovačević, A. Matković, U. Ralević, Dj. Jovanović, and B. Jelenković, *Phys. Scr.* **2014**(T162), 014015 (2014).
- <sup>36</sup>Y. V. Bludov, A. Ferreira, N. M. R. Peres, and M. I. Vasilevskiy, *Int. J. Mod. Phys. B* **27**(10), 1341001 (2013).
- <sup>37</sup>J. Chen, M. Badioli, P. Alonso-González, S. Thongrattanasiri, F. Huth, J. Osmond, M. Spasenović, A. Centeno, A. Pesquera, P. Godignon, A. Z. Elorza, N. Camara, F. J. García de Abajo, R. Hillenbrand, and F. H. Koppens, *Nature* **487**(7405), 77 (2012).
- <sup>38</sup>B. Wang, X. Zhang, F. J. García-Vidal, X. Yuan, and J. Teng, *Phys. Rev. Lett.* **109**(7), 073901 (2012).
- <sup>39</sup>R. R. Nair, P. Blake, A. N. Grigorenko, K. S. Novoselov, T. J. Booth, T. Stauber, N. M. R. Peres, and A. K. Geim, *Science* **320**, 1308 (2008).
- <sup>40</sup>D. Teweldebrhan and A. A. Balandin, *Appl. Phys. Lett.* **94**, 013101 (2009).
- <sup>41</sup>I. Childres, L. A. Jauregui, M. Foxe, J. Tian, R. Jalilian, I. Jovanovic, and Y. P. Chen, *Appl. Phys. Lett.* **97**, 173109 (2010).
- <sup>42</sup>A. C. Ferrari, J. C. Meyer, V. Scardaci, C. Casiraghi, M. Lazzeri, F. Mauri, S. Piscanec, D. Jiang, K. S. Novoselov, S. Roth, and A. K. Geim, *Phys. Rev.*

*Lett.* **97**, 187401 (2006).

<sup>43</sup>D. Graf, F. Molitor, K. Ensslin, C. Stampfer, A. Jungen, C. Hierold, and L. Wirtz, *Nano Lett.* **7**, 238 (2007).

<sup>44</sup>Y. Yang, J. Yang, L. Xue, and Y. Guo, *Appl. Phys. Lett.* **97**(14), 141101 (2010).

<sup>45</sup>J. Bonse and J. Krüger, *J. Appl. Phys.* **108**(3), 034903 (2010).

# Chapter 6

## Visible light emission in graphene field effect transistors

Reprinted from Beltaos, A., Bergren, A. J., Bosnick, K., Pekas, N., Lane, S., Cui, K., Matković, A., and Meldrum, A. (2017). “Visible light emission in graphene field effect transistors”. *Nano Futures*, 1(2), 025004., ©IOP Publishing. Reproduced with permission. All rights reserved. <https://doi.org/10.1088/2399-1984/aa8b04>

### 6.1 Abstract

We present an experimental study of the light-emitting properties of graphene field effect transistors in the visible and near infrared spectral range. Using spectroscopic and imaging techniques, the effects of source-drain and gate voltages on the spectrum and location of the light emission were investigated. Raman spectroscopy, electronic measurements, and scanning electron microscopy combined with energy dispersive x-ray spectroscopy were used to characterize the devices. Results show that the spectral features (peak spectral intensity and wavelength) were controllable via applied source-drain or gate voltages, while the physical location of the light emission was strongly affected by scattering sites, including defects, nanoparticles, and edges. A possible explanation

of the observed light emission is the outcoupling of surface plasmons excited by hot carriers in graphene according to the quantum Čerenkov effect. Hence, this work suggests the feasibility of all-electrical graphene devices for applications in light emission and plasmonics.

## 6.2 Introduction

In 2004, the discovery of a reliable fabrication method for graphene led to a flurry of material characterization [1]. Since then many of the theoretically predicted properties that make this two dimensional (2D) carbon material unique have been demonstrated [2]. For example, graphene has the highest known strength of any material [3], potential for extremely high carrier mobilities and current densities (up to a million times that of copper) [4,5], and the ability to support tunable surface plasmons via electrical gating [6-8]. Due to this unusual combination of mechanical, electronic, and optical properties, graphene shows promise for emerging optoelectronic applications, such as solar cells, photodetectors, and plasmonic devices [9]. Various types of light emission have been demonstrated, from graphene and graphene-related structures (e.g. graphene oxide and graphene quantum dots) including photoluminescence [10-15], electroluminescence [16-18], and thermal radiation [19-24], with promise for applications such as drug delivery, light emitting diodes, and sensors [9, 25].

Electrically-driven light emission from graphene-based devices has mainly been demonstrated in the *infrared* (IR) spectral range and attributed to grey-body or blackbody radiation due to local heating [20-24]. So far, there are just a few experimental reports of electrically-driven light emission from graphene peaking in the *visible* (VIS) range [17-19]. Using electrically-biased substrate-supported graphene, one report attributed VIS light emission to a phonon-assisted electroluminescence mechanism [18], while others attributed VIS emission from electrically-biased suspended graphene to thermal hot spots in the graphene channel [19]. These studies used an applied source-drain voltage

between two terminals to excite light emission but the effects of gate voltage on the emission spectra were not investigated. Finally, VIS emission from graphene was also excited by an electron tunneling current in a scanning tunneling microscope using a bias voltage between the tip and sample and was attributed to a hot electroluminescence mechanism [17].

In addition to these experimental reports, several recent theoretical investigations have shown that light emission at VIS or even shorter wavelengths can be achieved by the interaction of charged particles with surface plasmons in graphene [26-28]. For example, the interaction of an electron beam incident on graphene with optically-excited surface plasmons could lead to a light source that is directional, monochromatic, and tunable from IR to x-ray energies [26, 27]. The feasibility of these mechanisms is also evidenced by the first theoretical work that predicted surface plasmons in graphene, in which it was suggested that the plasmons could exist at near IR and VIS wavelengths [29].

Of particular interest, it has been predicted that due to the unique properties of graphene surface plasmons including high field confinement and low phase velocity, the 2D quantum Čerenkov effect (ČE) could be achievable in graphene [28]. The 2D quantum ČE refers to the emission of a shockwave of surface plasmons excited by hot carriers in a 2D medium, analogous to the conventional ČE for light emission in a 3D medium. This effect was predicted to lead to VIS or IR light emission from graphene devices when the surface plasmons are coupled out as free space photons through surface roughness or impurities [28]. If a specially designed grating were to be incorporated into the graphene device, a near-perfect energy conversion efficiency might be possible due to the quantum ČE dominating over other scattering processes [28]. This is particularly promising for applications given the various patterning techniques already in use with graphene [30-33].

Hence, there are several routes to achieving VIS light emission from graphene devices, but so far no consensus has been reached as to which conditions lead to which emission mechanism(s). If an understanding of how to control these properties and mechanisms can be achieved, better performance or new func-

tions of nanoelectronic devices may be enabled with exciting possibilities for graphene light sources or plasmonic devices.

In this work, we present an experimental study of electrically-driven light emission from a graphene field effect transistor (FET) in the VIS and NIR spectral range using spectroscopy and imaging techniques. By measuring the light emission and characterizing the optical and electronic properties of the device, one can obtain insights into the possible emission mechanisms. The results are compared to the mechanisms of light emission in graphene devices and the proposed quantum ĆE-based mechanism is shown to be a possible explanation [28]. We experimentally demonstrate the controllability of this type of graphene light emission, showing its promise for future graphene optoelectronics applications.

### 6.3 Methods

Single-layer to few-layer graphene samples were prepared by mechanical exfoliation on silicon/silicon dioxide substrates (Si/SiO<sub>2</sub>) [1], identified by optical microscopy [34], and characterized by Raman spectroscopy [35] using the 532 nm line of a Nicolet Almega XR Micro-Raman system with a 10x objective focused in the center region of the sample. Graphene FETs were fabricated from the exfoliated samples on Si/SiO<sub>2</sub> substrates, as shown in the device schematic of figure 6.1(a). A graphene flake was positioned atop an SiO<sub>2</sub> layer ( $\sim 300$  nm in thickness) which acts as a gate dielectric, while the underlying Si substrate ( $\sim 1$  cm<sup>2</sup> in area) acts as a back gate (G) electrode. Source (S) and drain (D) electrodes were fabricated by physical vapor deposition of 30 nm thick gold (Au) films that were contacted to the graphene flake using a wire-based shadow mask ( $\sim 10$ - $25$   $\mu$ m in diameter). Wires were then attached to the electrodes using silver epoxy to allow for the application of source-drain voltage ( $V_{sd}$ ) and gate voltage ( $V_g$ ). The dimensions of the graphene-based FETs varied depending on the sizes of the exfoliated graphene samples that were used as the conductive channels. Generally, gate (channel) lengths were

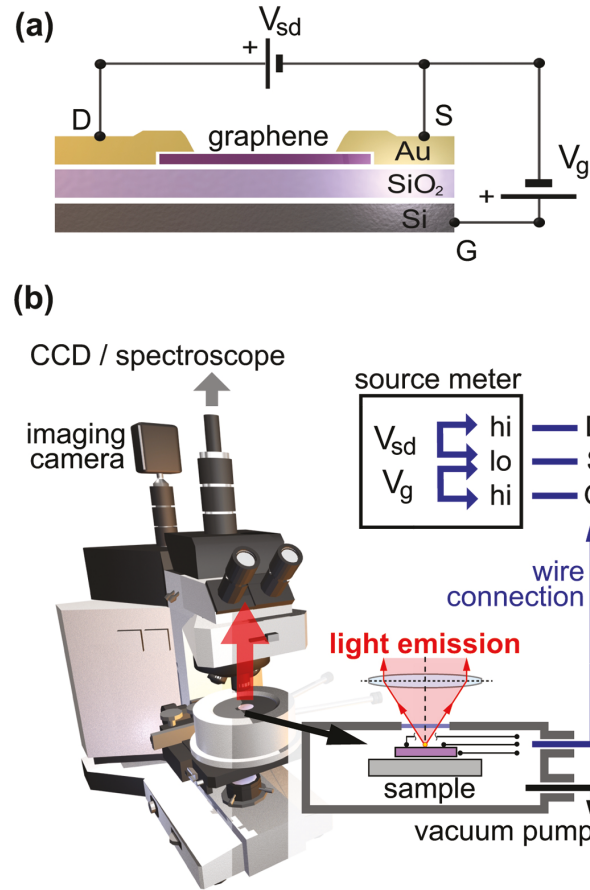


Figure 6.1: Schematics of (a) graphene FET device (NOT to scale the graphene channel length is  $\sim 15\text{-}25\ \mu\text{m}$ , and the gate dielectric thickness is  $\sim 300\ \text{nm}$ ); (b) light emission spectroscopy and imaging setup. The sample is located inside a vacuum chamber with a top window (schematically represented in the inset) and connected to a source meter for the application of voltages  $V_{sd}$  and  $V_g$ .

$\sim 15\text{-}25\ \mu\text{m}$ , channel widths were  $\sim 3\text{-}40\ \mu\text{m}$ , and active (channel) areas were  $\sim 60\text{-}1000\ \mu\text{m}^2$ . The graphene FETs were then characterized by current-voltage (I-V) and transport measurements.

Light emission from the graphene FETs was excited by applying voltages  $V_{sd}$  and  $V_g$  simultaneously using a 2-channel source-meter (Keithley 2602A). Spectroscopy and imaging were carried out using an optical microscope interfaced to a spectrograph (Andor Shamrock SR-303i-B with an Andor Newton CCD detector) and a CCD imaging color camera (SBIG STF-8300C or Lumenera Infinity 2-3C), respectively, using a 50x objective (figure 6.1(b)). The de-

vices were measured at room temperature in a low vacuum of  $10^{-3}$ - $10^{-4}$  Torr in order to minimize oxidation-related aging. Measured spectra were corrected for the wavelength-dependent sensitivity of the detector using a standard calibration process with a blackbody lamp (Ocean Optics LS-1-CAL or HL2000) to obtain the spectral intensity (i.e. the intensity per unit wavelength) [36].

Scanning electron microscopy (SEM) of the devices was performed after light emission experiments on a Hitachi S-5500 SEM or a Zeiss Sigma field emission SEM equipped with an energy dispersive x-ray spectroscopy (EDX) detector for chemical analysis. Images were collected using the secondary electron mode at an operating voltage of 15 kV. Additionally, the electron beam of the Zeiss Sigma SEM was used to pattern defect/scattering sites onto selected regions of the graphene channel by focusing a 15-20 keV beam in spot mode for several minutes per site. This technique is known to create e-beam induced deposition of amorphous nano-carbon on the graphene and localized defects in the graphene crystal lattice both of which can act as scattering sites [37-41].

## 6.4 Results

The graphene FETs exhibited stable, repeatable light emission when excited by applied voltages. Raman and electronic characterization of the graphene FETs before and after light emission experiments showed that the devices operated as expected and that light emission generally did not damage the devices. Details about the characterization results are given in the supporting information (figure 6.8 is available online at [stacks.iop.org/ NANOF/1/025004/mmedia](http://stacks.iop.org/NANOF/1/025004/mmedia)).

Examples of typical imaging results are shown in figure 6.2. Figure 6.2(a) shows the channel area of a graphene FET in an SEM image. Some particles and defects can be observed here, especially near the edges of the gold electrodes. Figure 6.2(b) shows a corresponding optical microscope real-color image of the same area under the application of high source-drain voltage. Light emission excited by the voltage appears as yellow-orange spots located

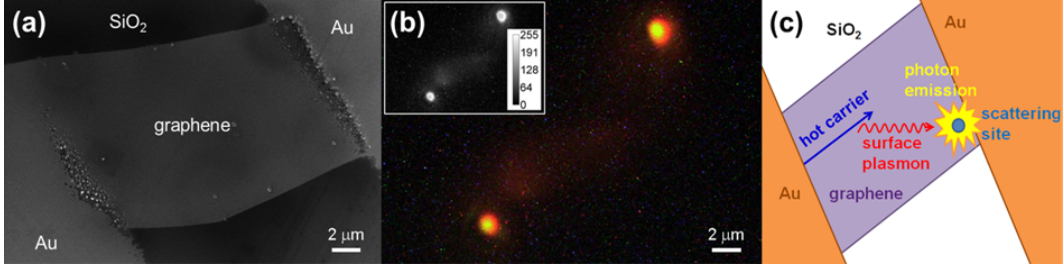


Figure 6.2: Images of a graphene FET: (a) SEM image of the graphene channel area; (b) optical microscope color image of the same area as in (a), showing light emission excited by applied voltage ( $V_g = 0$  V,  $V_{sd} = -27$  V). The inset shows the relative intensity on the corresponding black and white emission image; (c) schematic representation of light emission from a graphene FET based on the quantum CE effect.

near the edges of the graphene channel and gold electrodes. The same image in black and white shown in the inset of figure 6.2(b) demonstrates the relative intensity. As is the case for all light emission images in this work, the brighter spots correspond to more intense light.

One possible explanation of light emission localized at edges, nanoparticles, or defects could be the proposed quantum CE-based mechanism. Figure 6.2(c) shows a schematic representation of this model, in which hot carriers in a graphene FET excite surface plasmons which couple out as free space photons at scattering sites such as defects. The following results will be compared to this and other models in the discussion below.

Examples of typical light emission spectra are shown in figure 6.3 for three different graphene FET light sources (“devices A, B, and C”) excited by applied voltage. The spectra, showing the emitted spectral intensity versus wavelength, display a broad peak in the VIS range and a more intense rising tail in the NIR range that fit well to two-term Gaussian functions, as shown by the black curves. These fits were used to determine the peak spectral intensity, peak wavelength and full-width-at-half-maximum of each spectrum as shown in the supporting information (figure 6.9).

Significant variations between individual devices were observed in the spectra, with each device having its own characteristic peak wavelength, ranging

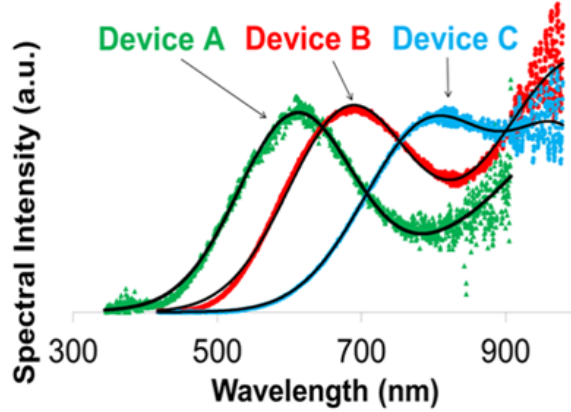


Figure 6.3: Typical light emission spectra, showing spectral intensity versus wavelength, of three different graphene FET light sources excited by applied voltage; devices A (green) ( $V_g=30$  V,  $V_{sd}=7$  V), B (red) ( $V_g=0$  V,  $V_{sd}=-30$  V), and C (blue) ( $V_g=40$  V,  $V_{sd}=18$  V), fitted to two-term Gaussian functions (black curves).

from  $\sim 600$  to  $\sim 800$  nm. Some devices displayed the long wavelength part of the spectrum only (figure 6.10), presumably due to conditions that do not support the generation of VIS light as discussed further below. As is the case with most of the spectra shown in this work, the spectral intensity in figure 6.3 is given in arbitrary units in order to compare the relative intensity from different devices excited by different voltages. Calibration of the system was performed as described in the supporting information (figure 6.11) to obtain the absolute spectral intensity in units of  $\mu\text{Wcm}^{-2} \text{nm}^{-1}$  and determine the power conversion efficiency. An order-of-magnitude estimate of the power conversion efficiency of the VIS light from graphene FETs was determined to be  $\eta = 10^{-7}$  as described in the supporting information (figure 6.11), comparable to  $10^{-8}$ - $10^{-3}$  previously reported for VIS light emission from graphene devices [17-19].

The differences in spectra observed between devices are apparently related to the different device structures. These include the different dimensions of the mechanically-exfoliated graphene channels (e.g. channel lengths were  $\sim 25$ , 20 and 15  $\mu\text{m}$  for device A, B and C, respectively) and the formation of defects. Through SEM analysis of the devices after the experiments (as will

be discussed in more detail below), these differences were correlated to the presence of features on the devices, including gold particles near the electrodes (e.g. device A), discontinuities in the graphene channel (e.g. device B), and intentionally made defects through the use of an electron beam (e.g. device C). In terms of the observed light emission, qualitative differences were observed, but the trends were similar, as demonstrated in figure 6.3.

The applied source-drain and gate voltages in a graphene FET can both be used in different ways to control the overall flow of current in the channel (e.g., see figure 6.8). Higher  $V_{sd}$  yields higher current and changes the distribution of carrier energies (with the maximum energy being  $E_{max} = eV_{sd}$  where  $e$  is the electronic charge) [36], while  $V_g$  can simultaneously modify the carrier density via the Fermi energy. By investigating the effects of varying  $V_{sd}$  and  $V_g$ , we can learn about how these electrical parameters control the light emission from the device and how the light is being generated. While this information is important for future applications, it is also significant for classifying the mechanisms of light emission. Hence, in the following, the effects of varying voltage parameters on the light emission properties were investigated with the goal of determining the light emission mechanism and controllability.

The results of changing voltage showed a marked effect on the spectral properties of the graphene FETs. Typical effects of varying  $|V_{sd}|$  and  $|V_g|$  on the emission spectra are shown in figures 6.4(a) and (b), respectively. Light emission was detectable for various combinations of  $V_{sd}$  and  $V_g$  when  $|V_{sd}|$  surpassed a threshold value which varied somewhat for each device (related to the threshold electric field  $|E|$  on the order of  $1 \times 10^6 \text{ Vm}^{-1}$  (figure 6.12)), while  $V_g$  ranged from -40 to +40 V. The light emitted by the devices was easily VIS by eye for relatively high  $|V_{sd}|$  or  $|E|$  (e.g.  $\sim 20 \text{ V}$  or  $\sim 1.2 \times 10^6 \text{ Vm}^{-1}$ ).

The emission intensity and spectral characteristics were controllable by varying  $V_{sd}$  (figure 6.4(a)), and to a lesser extent by  $V_g$  (figure 6.4(b)) (for the exact relationships see figure 6.13). The effects of varying the corresponding current  $|I_{sd}|$  via  $V_{sd}$  or  $V_g$  on the peak spectral intensity and peak wavelength showed clear, consistent trends (figures 6.4(c), (d) and figures 6.14(a), (b),

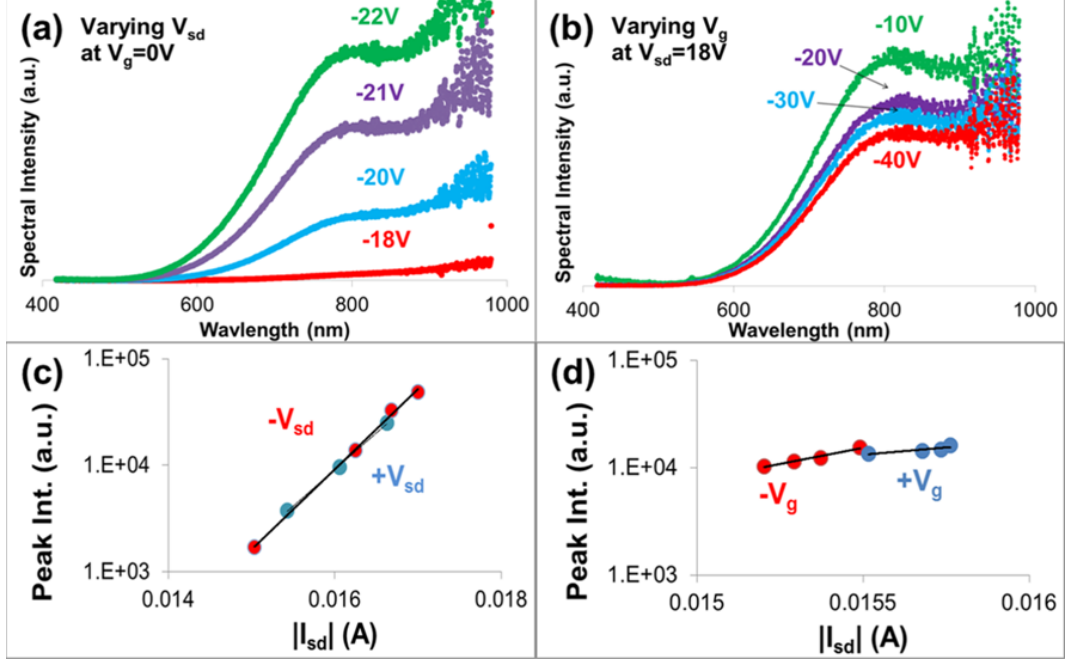


Figure 6.4: Effects of varying (a) source-drain and (b) gate voltage on light emission spectra, and corresponding effects on the spectral parameters for positive (blue) and negative (red)  $V_{sd}$  (left plot) and  $V_g$  (right plot); (c) peak spectral intensity (Int.) versus  $|I_{sd}|$  by varying  $V_{sd}$ , plotted on a log scale and fitted to exponential functions (black lines); (d) peak spectral intensity (Int.) versus  $|I_{sd}|$  by varying  $V_g$ , plotted on a log scale and fitted to exponential functions (black lines).

respectively). Varying both positive (blue) and negative (red)  $V_{sd}$  or  $V_g$  values yielded a similar behavior, implying that both current directions and majority charge carrier types could be used similarly for excitation of the light emission.

Increasing the current via  $V_{sd}$  or  $V_g$  led to an exponential increase in the spectral intensity (figures 6.4(c) and (d)), as confirmed by the straight line fits (black lines) to the data plotted on a logarithmic scale. This was accompanied by a decrease in peak wavelength (i.e. a blue-shift towards light of higher energy) (figure 6.14). The observed emitted photon energy was tunable via both  $|V_{sd}|$  or  $|V_g|$  as shown by the changes in peak light emission wavelength with current in figure 6.14.

Collectively, the plots in figure 6.4 demonstrate the controllability of the light emission spectral properties of graphene FETs through  $V_{sd}$  and  $V_g$ , in

which  $V_{sd}$  effectively modulates the emission intensity. The effects on the spectral parameters by varying the current through  $V_g$  were on a much smaller scale than those by varying  $V_{sd}$ , as could be expected given the different functions of the two voltages; however, the similarity of the trends in both cases shows that the current (as opposed to the voltage, see figure 6.13) is the main parameter related to the generation and control of light emission from the graphene FETs.

Next we discuss the effects of varying  $V_{sd}$  or  $V_g$  on the spatial light emission properties, as shown in figure 6.5. The left half of figure 6.5((a), (b), (e) and (f)) shows optical microscope color images of light emission from the same graphene FET at different voltages. The right half of figure 6.5((c), (d), (g) and (h)) shows the corresponding overlays of light emission and brightfield images which were used in order to determine the location of the emitting regions. Light emission was consistently observed to be localized and the location remained constant with either  $V_{sd}$  (figures 6.5(a)-(d)) or  $V_g$  (figures 6.5(e)-(h)), even when reversing the polarity as shown in this example.

To determine the nature of the light emission locations, further investigation was carried out on various devices by combining emission imaging and SEM. Figures 6.6(a) and (d) show typical optical microscope color light emission images (corresponding to spectral data of devices A and B in figure 6.3), and figures (b) and (e) show the corresponding overlays of light emission and brightfield images, respectively. Device A (figures 6.6(a) and (b)) represents the most frequently observed location of emission; i.e. near the edge of the graphene channel adjacent to the gold electrode. Device B (figures 6.6(d) and (e)) exhibits a second type of observed emission localized deeper within the graphene channel, confirming that the light originated from the graphene and not the gold electrodes.

The corresponding SEM results showed characteristic features in the light emission regions (white rectangles enlarged in the insets of figures 6.6(c) and (f)). In figure 6.6(c), these features included gold nanoparticles and edges, where the presence of gold was confirmed by EDX (figure 6.15). Gold nanopar-

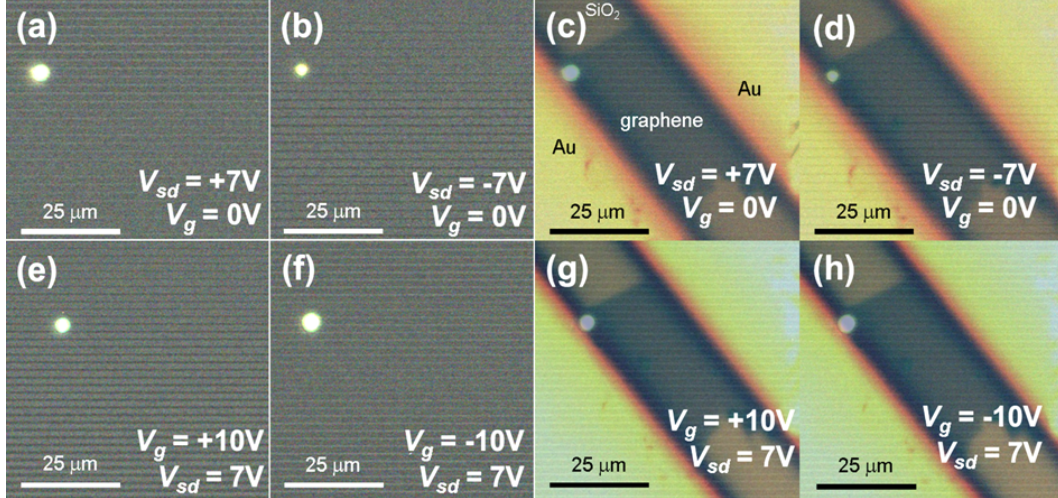


Figure 6.5: Effects of varying  $V_{sd}$  and  $V_g$  on the light emission location of a graphene FET, as observed in color light emission images (left) and corresponding overlays of light emission and brightfield images (right) for (a) positive  $V_{sd}$ ; (b) negative  $V_{sd}$ ; (c) positive  $V_{sd}$ ; (d) negative  $V_{sd}$ ; (e) positive  $V_g$ ; (f) negative  $V_g$ ; (g) positive  $V_g$ ; (h) negative  $V_g$ . The light emission appears as a bright spot in the upper left corner of the graphene channel. The horizontal scanning lines are artifacts for the particular camera/software used here.

ticles were commonly observed on the devices and were likely formed by electromigration of gold from the electrodes due to the applied voltage [42], as confirmed by SEM imaging of a device before and after light emission experiments (figure 6.16); however, the light emission itself did not cause observable damage to the graphene channel or affect the function of the device (as discussed in the supporting information (figure 6.8)). In figure 6.6(f), the emission area was localized to a discontinuity in the exfoliated graphene, which existed prior to the applied voltage, as observed in the brightfield optical image of the device before the experiment (left inset of figure 6.6(f)). This type of optical contrast difference has been correlated in past work with a change in the number of graphene layers [34].

The consistent connection of the light emission to features of the devices explains why the emission was localized at a location that could not be changed by applied voltage (e.g. reversing the current flow as in figure 6.5). From these results we hypothesized that the light emission is connected to scattering sites

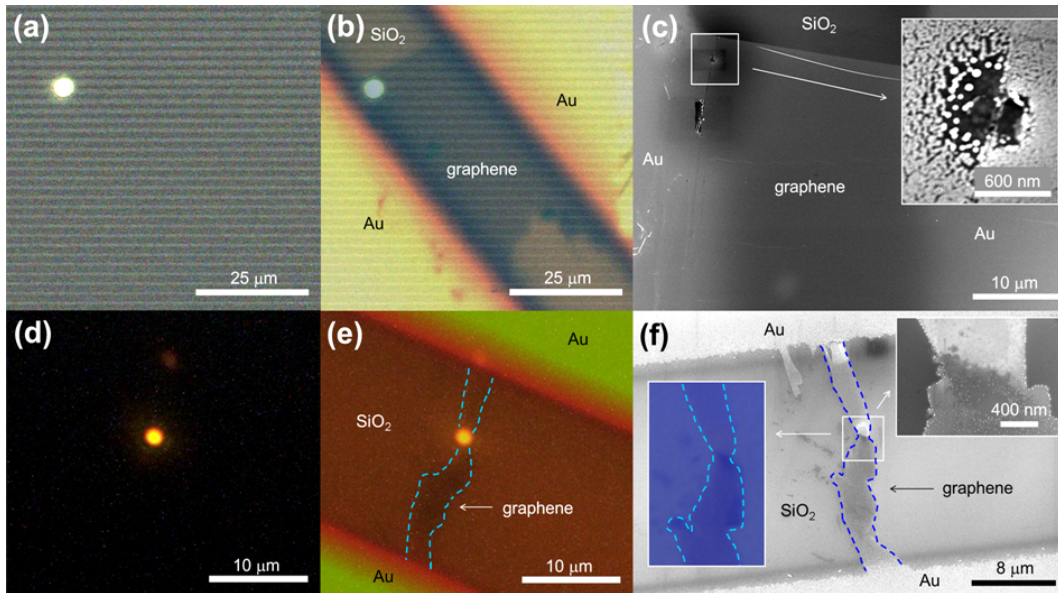


Figure 6.6: (a) and (d) typical optical microscope color images of light emission corresponding to devices A (a) ( $V_g=0$  V,  $V_{sd}=7$  V) and B (d) ( $V_g=0$  V,  $V_{sd}=-30$  V) of figure 6.3, respectively. (b) and (e) the same images of light emission overlaid with brightfield images, corresponding to (a) and (d), respectively. (c) and (f) typical SEM images of devices after light emission, corresponding to the devices in (b) and (e), respectively. White rectangles indicate selected areas of light emission enlarged in the insets. The additional left inset in (d) is a brightfield optical image of the device. The dashed blue lines in (e) and (f) mark the edges of the graphene channel.

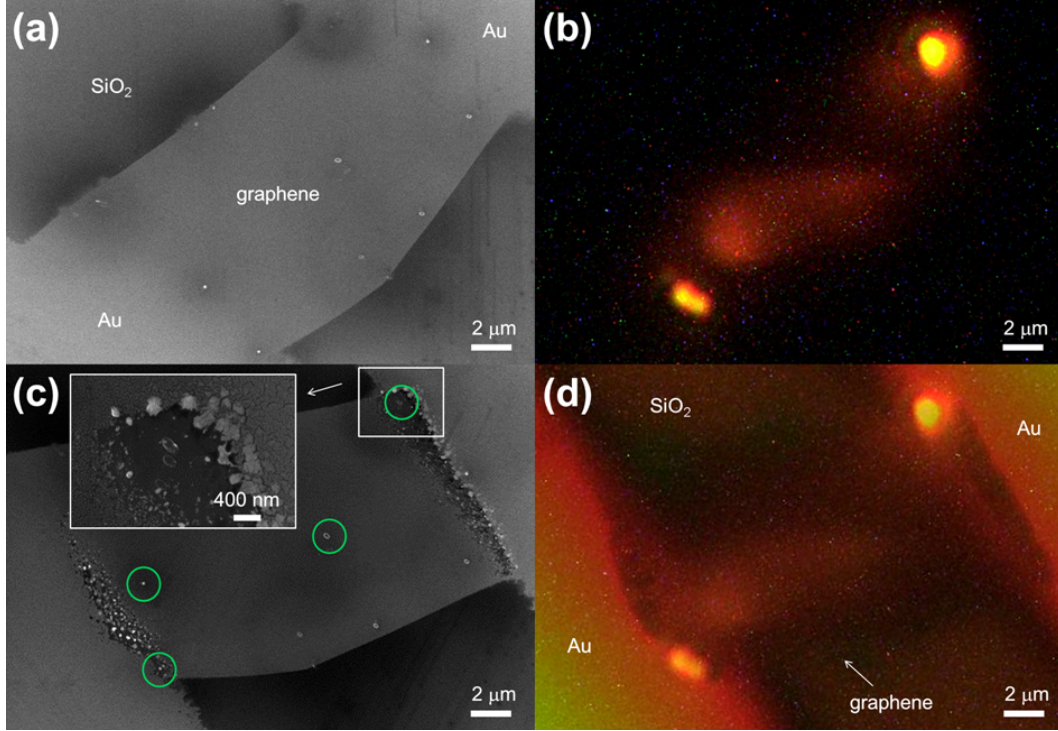


Figure 6.7: Various images showing the same channel area of a patterned device (“device C”): (a) SEM image of the device before light emission experiments; patterned defects are seen as white points; (b) color light emission image of the device ( $V_g=0$  V,  $V_{sd}= -28$  V); (c) SEM image of the device after light emission experiments; the white rectangle indicates a selected area of emission with an enlarged view in the inset; the green circles indicate defects associated with light emission locations; (d) corresponding emission and brightfield image overlay of (b).

in the channel, which would suggest a promising method for controlling the emission by intentionally patterning defects, nanoparticles, gratings, etc onto the device. We therefore patterned a new device by focusing the electron beam in the SEM (see the Experiment section) producing defects that appeared as light-contrast points (figure 7(a)). EDX and Raman spectroscopy were used to characterize the graphene after this SEM interaction and showed that the interacted regions likely consisted of amorphous carbon nano-deposits and defects in the crystal lattice of the graphene channel (figure 6.17 and table 6.1, figure 6.18) as expected by this technique [37-41].

The patterned device demonstrated similar spectral behavior (device C in

figure 6.3) as the unpatterned devices (devices A and B in figure 6.3), and displayed a combination of light near the edges of the channel and along the channel (figures 6.7(b) and (d)). A correspondence was observed between the light emission locations and some of the patterned defects, marked by green circles in the SEM image after light emission experiments (figure 6.7(c)). The strongest emission was in the vicinity of defects that were near gold nanoparticles or edges as marked by the white rectangle and enlarged view in the inset of figure 6.7(c). These results support the hypothesis that light emission occurs at scattering sites and demonstrates the feasibility of controlling the emission area.

## 6.5 Discussion

We now compare the results presented above to various theories in order to determine a possible mechanism for the observed light emission from graphene FETs. To begin with, the observed exponential rise of intensity and corresponding blue-shift of emitted photons with applied current in Si light emitting diodes has been attributed to hot carriers [43]. The contribution of high energy (hot) carriers was evidenced by the light intensity being proportional to the number density of carriers  $n(E)$  which is exponentially related to carrier energy  $E$ . Given that similar effects could also be expected for carriers in graphene [44-46], we deduce that hot carrier effects could play a role in the generation of light from the graphene FETs.

Due to this relation with hot carrier effects, the observation of an exponential rise of intensity might be explained by the quantum ĆE theory which is based on hot carrier excitation of surface plasmons [28]. There may be other light emission mechanisms that could also be relevant (e.g. hot carrier electroluminescence). To provide evidence for one explanation over another, we will compare the results (both spectral and imaging) to the quantum ĆE theory, as well as other possible mechanisms that have been proposed for electrically-driven VIS light emission from graphene.

The hot carriers for the occurrence of the quantum ČE effect can be either hot electrons or hot holes created by high  $V_{sd}$ , with a carrier energy threshold for significant emission. This is consistent with the parameters used in this work for the excitation of light, i.e. both positive and negative  $V_g$  (or  $V_g > V_d$  and  $V_g < V_d$ ) and high  $V_{sd}$ . The dual-range behavior of the observed light emission in the VIS and IR regions (e.g. figure 6.3) can be explained with this theory by the two broad spectral windows of surface plasmon energies that are predicted to occur due to both interband and intraband transitions. Also, because surface plasmon emission can occur via both types of transitions, the energies of the plasmons are predicted to be tunable via the hot carrier energy or Fermi energy [28], which can be controlled experimentally by varying  $V_{sd}$  or  $V_g$ , respectively. This is consistent with the tunability of peak emission wavelength with  $V_{sd}$  or  $V_g$  observed here (figure 6.14).

Another result to consider is the observed threshold behavior of light emission intensity with  $V_{sd}$ . The threshold for the onset of light emission was apparent with respect to applied electric field (figure 6.12). This also is consistent with the quantum ČE, in which there is a threshold hot carrier energy for surface plasmon emission [28]. Comparing this result to other experimental works, it is interesting to note that this type of threshold behavior has been previously reported with respect to both light emission [19] and current saturation in graphene devices [47], which could also be interpreted as evidence for the quantum ČE [28].

The imaging results (figures 6.6 and 6.7) show how the observed light emission corresponded to different types of scattering sites in different devices (nanoparticles, discontinuities, defects, edges, etc), while the spectral results (figure 6.3) show that all different types of scattering sites led to consistent light emission spectral features (e.g. double Gaussian shape). Therefore, given the consistent shape of spectra for various types of scatterers, effects related to any one type of scatterer alone can be ruled out. For example, nanoparticle plasmon enhanced scattering effects [48] or scatterer shape effects that could affect spectral shape seem unlikely. On the other hand, the localization of light

at various features in the device could possibly be explained by the quantum ČE theory [28], in which these features would act as scattering sites from which surface plasmon-related light emission could be observed (figure 6.2(c)). Interestingly, light emission from a carbon nanotube transistor localized at the edge of the gold electrode was also attributed to surface plasmon effects at scattering sites [49].

Although it is possible that other types of light emission (e.g. thermal) might also be enhanced near scatterers, the connection of light location to particular features has not been observed or explained in the context of other types of VIS light emission from graphene devices [17-19]. In the case of a thermal mechanism, for example, a localized source of emission in the IR or VIS spectral region has been attributed to a hot spot in previous works [19-24]. The emission was reported to be localized in a hot spot in the center of the channel on suspended graphene devices [19], or in a location that can be controlled by varying the gate voltage [22, 23] or reversing the source-drain voltage [24] on substrate-supported devices. In the present work (using substrate supported devices), neither of these were observed; the strongest emission did not occur in the center of the channel and its location could not be altered by varying  $V_g$  or reversing  $V_{sd}$ . Hence, the varied emission locations observed on different devices and the lack of dependence of voltage on the emission location implies that thermal effects were not involved here.

In addition, the thermal emission spectrum from substrate-supported graphene has been shown to follow a greybody or blackbody curve according to Planck's Law in previous works [20-24]. To investigate this possibility here, experimental emission spectra in the VIS region were compared to theoretical blackbody spectra of similar peak wavelengths (figure 6.19). The experimental spectra did not fit the theory in terms of the shape of the spectrum (Gaussian), the apparent double peak behavior, the increased intensity in the longer wavelengths, and the corresponding temperatures up to 4600 K that would be needed for blackbody emission at peak wavelengths down to  $\sim 600$  nm. Such high temperatures would likely destroy the devices on the occurrence of light emission,

but this was not the case here (figure 6.8).

Similar spectral features to those observed here (e.g. multiple peaks and threshold behavior) have been observed for VIS light emission from suspended graphene devices [19]. In that case, the emission spectra did not fit simple blackbody curves either, and a thermal-based model was proposed in which the multiple peak behavior was attributed to optical interference effects in the trench between the suspended graphene and the substrate below. Electron temperatures of  $\sim 2800$  K at the center of the graphene channel were reportedly made possible because suspended graphene samples reduce heat transport. However, this analysis does not apply to the devices in the present work which were based on substrates.

Other possible emission mechanisms such as phonon-assisted electroluminescence [18], or tunneling induced hot electroluminescence [17], also do not appear to be involved here for several reasons. In the case of phonon-assisted electroluminescence [18], two spectral peaks were predicted to occur at specific energies of  $\sim 1.4$  and  $\sim 1.8$  eV ( $\sim 900$  nm and  $\sim 700$  nm, respectively), with only a weak dependence of peak position on source-drain voltage. This is contrary to the observed spectral peaks here which varied per device, did not occur at the predicted energies, and had a significant dependence on  $V_{sd}$ . Alternatively, hot luminescence due to electron tunneling [17] has been shown to be continuous and uniform throughout the entire graphene flake; whereas in this work, the observed emission was localized to specific locations of the graphene channel. In addition, the tunneling-induced luminescence could be switched on and off by inverting the bias voltage, which was not observed here.

Hence, a possible explanation that is consistent with the spectral and imaging results in this work is the quantum  $\check{C}$ E-based mechanism [28]. To confirm that the quantum  $\check{C}$ E effect is involved in light emission from graphene FETs, further experiments/theory are necessary, and there are a number of possible routes to this end. For example, a theory describing the dependence of light emission spectral features on applied voltage could be hypothesized and tested experimentally. In addition, the design of gratings or nanoribbons incor-

porated into graphene devices for optimized outcoupling could lead to greater control of the light emission wavelength and angle, and the potential for a high electron-to-photon energy conversion efficiency [28]. The light emission measured from specially-designed devices could be compared with predictions based on the quantum ČE theory [28]. If this effect is indeed involved in graphene FET light emission, the known tunability and high confinement of graphene plasmons [6-8], combined with the controllability of the light emission demonstrated in this work offer promise for plasmonic and light emitting graphene applications.

## 6.6 Conclusion

In summary, we investigated the light emission properties of graphene FETs in order to determine the controllability and mechanism of the emission. Spectroscopy and imaging were used to measure the light emission, while Raman spectroscopy, electronic measurements, and SEM were used to characterize the graphene devices. The characteristic light emission spectrum peaked in the VIS range with a tail in the near IR. The emission spectral characteristics depended on the current in the channel via the source-drain or gate voltage, with more control offered by the source-drain voltage. The spectral intensity increased exponentially with the current, and the emission was localized to certain points on the graphene channel that were found to coincide with nanoparticles, edges, and defects. Control of the emission area was demonstrated by using an electron beam to place defects into a graphene FET. A possible explanation of the observations is a quantum ČE light emission mechanism based on hot carrier-excited surface plasmon emission in graphene that is outcoupled at scattering sites such as defects [28]. The results offer promise for controllable all-electrical light emitting graphene devices.

## 6.7 Acknowledgements

We gratefully acknowledge Richard L McCreery (National Institute for Nanotechnology and University of Alberta) for lab resources and helpful discussions, Bryan Szeto (National Institute for Nanotechnology) for technical assistance, and Frank A Hegmann (University of Alberta) for helpful discussions. This work was supported by the National Institute for Nanotechnology (projects A1-009201 and A1-004914), which is operated as a partnership between the National Research Council, Canada, the University of Alberta, and the Government of Alberta. A Matković acknowledges support from Serbian MPNTR through project ON171005.

## 6.8 References

- [1] Novoselov K S 2004 Electric Field Effect in Atomically Thin Carbon Films *Science* **306** 666-9
- [2] Novoselov K S, Fal'ko V I, Colombo L, Gellert P R, Schwab M G and Kim K 2012 A roadmap for graphene *Nature* **490** 192-200
- [3] Lee C, Wei X, Kysar J W and Hone J 2008 Measurement of the Elastic Properties and Intrinsic Strength of Monolayer Graphene *Science* **321** 385-8
- [4] Mayorov A S et al. 2011 Micrometer-Scale Ballistic Transport in Encapsulated Graphene at Room Temperature *Nano Lett.* **11** 2396-9
- [5] Moser J, Barreiro A and Bachtold A 2007 Current-induced cleaning of graphene *Appl. Phys. Lett.* **91** 163513
- [6] Robb G 2015 Graphene plasmonics: Ultra-tunable graphene light source *Nat. Photonics* **10** 3-4
- [7] Koppens F H L, Chang D E and de Abajo F J G 2011 Graphene Plasmonics: A Platform for Strong Light-Matter Interactions *Nano Lett.* **11** 3370-7
- [8] Bao Q and Loh K P 2012 Graphene Photonics, Plasmonics, and Broadband Optoelectronic Devices *ACS Nano* **6** 3677-94
- [9] Bonaccorso F, Sun Z, Hasan T and Ferrari A C 2010 Graphene photonics

- and optoelectronics *Nat. Photonics* **4** 611-22
- [10] Wang J and Qiu J 2015 Luminescent Graphene Quantum Dots: As Emerging Fluorescent Materials for Biological Application *Sci. Technol. Adv. Mater.* **7** 1979-89
- [11] Gokus T, Nair R R, Bonetti A, Böhmeler M, Lombardo A, Novoselov K S, Geim A K, Ferrari AC and Hartschuh A 2009 Making Graphene Luminescent by Oxygen Plasma Treatment *ACS Nano* **3** 3963-8
- [12] Cao L, Meziani M J, Sahu S and Sun Y-P 2013 Photoluminescence Properties of Graphene versus Other Carbon Nanomaterials *Acc. Chem. Res.* **46** 171-80
- [13] Lui C H, Mak K F, Shan J and Heinz T F 2010 Ultrafast Photoluminescence from Graphene *Phys. Rev. Lett.* **105**
- [14] Liu W-T, Wu S W, Schuck P J, Salmeron M, Shen Y R and Wang F 2010 Nonlinear broadband photoluminescence of graphene induced by femtosecond laser irradiation *Phys. Rev. B: Condens. Matter Mater. Phys.* **82**
- [15] Stöhr R J, Kolesov R, Pflaum J and Wrachtrup J 2010 Fluorescence of laser-created electron-hole plasma in graphene *Phys. Rev. B: Condens. Matter Mater. Phys.* **82**
- [16] Kwon W, Kim Y-H, Lee C-L, Lee M, Choi H C, Lee T-W and Rhee S-W 2014 Electroluminescence from Graphene Quantum Dots Prepared by Amidative Cutting of Tattered Graphite *Nano Lett.* **14** 1306-11
- [17] Beams R, Bharadwaj P and Novotny L 2014 Electroluminescence from graphene excited by electron tunneling *Nanotechnology* **25** 055206
- [18] Essig S et al. 2010 Phonon-Assisted Electroluminescence from Metallic Carbon Nanotubes and Graphene *Nano Lett.* **10** 1589-94
- [19] Kim Y D et al. 2015 Bright visible light emission from graphene *Nat. Nanotechnol.* **10** 676-81
- [20] Berciaud S, Han M Y, Mak K F, Brus L E, Kim P and Heinz T F 2010 Electron and Optical Phonon Temperatures in Electrically Biased Graphene *Phys. Rev. Lett.* **104**
- [21] Yu D and Dai L 2010 Voltage-induced incandescent light emission from

- large-area graphene films *Appl. Phys. Lett.* **96** 143107
- [22] Freitag M, Chiu H-Y, Steiner M, Perebeinos V and Avouris P 2010 Thermal infrared emission from biased graphene *Nat. Nanotechnol.* **5** 497-501
- [23] Lawton L M, Mahlmeister N H, Luxmoore I J and Nash G R 2014 Prospective for graphene based thermal mid-infrared light emitting devices *AIP Adv.* **4** 087139
- [24] Luxmoore I J, Adlem C, Poole T, Lawton L M, Mahlmeister N H and Nash G R 2013 Thermal emission from large area chemical vapor deposited graphene devices *Appl. Phys. Lett.* **103** 131906
- [25] Shen J, Zhu Y, Yang X and Li C 2012 Graphene quantum dots: emergent nanolights for bioimaging, sensors, catalysis and photovoltaic devices *Chem. Commun.* **48** 3686
- [26] Mišković Z L, Segui S, Gervasoni J L and Arista N R 2016 Energy losses and transition radiation produced by the interaction of charged particles with a graphene sheet *Phys. Rev. B: Condens. Matter Mater. Phys.* **94**
- [27] Wong L J, Kaminer I, Ilic O, Joannopoulos J D and Soljačić M 2015 Towards graphene plasmon-based free-electron infrared to X-ray sources *Nat. Photonics* **10** 46-52
- [28] Kaminer I, Katan Y T, Buljan H, Shen Y, Ilic O, López J J, Wong L J, Joannopoulos J D and Soljačić M 2016 Efficient plasmonic emission by the quantum Čerenkov effect from hot carriers in graphene *Nat. Commun.* **7** ncomms11880
- [29] Jablan M, Buljan H and Soljačić M 2009 Plasmonics in graphene at infrared frequencies *Phys. Rev. B: Condens. Matter Mater. Phys.* **80**
- [30] Hong J-Y and Jang J 2012 Micropatterning of graphene sheets: recent advances in techniques and applications *J. Mater. Chem.* **22** 8179
- [31] Feng J, Li W, Qian X, Qi J, Qi L and Li J 2012 Patterning of graphene *Nanoscale* **4** 4883
- [32] Bao W, Miao F, Chen Z, Zhang H, Jang W, Dames C and Lau C N 2009 Controlled ripple texturing of suspended graphene and ultrathin graphite membranes *Nat. Nanotechnol.* **4** 562-6

- [33] Beltaos A, Kovačević A G, Matković A, Ralević U, Savić-Šević S, Jovanović D, Jelenković B M and Gajić R 2014 Femtosecond laser induced periodic surface structures on multi-layer graphene *J. Appl. Phys.* **116** 204306
- [34] Nair R R, Blake P, Grigorenko A N, Novoselov K S, Booth T J, Stauber T, Peres N M R and Geim A K 2008 Fine Structure Constant Defines Visual Transparency of Graphene *Science* **320** 1308-1308
- [35] Ferrari A C et al. 2006 Raman Spectrum of Graphene and Graphene Layers *Phys. Rev. Lett.* **97**
- [36] Ivashenko O, Bergren A J and McCreery R L 2016 Light Emission as a Probe of Energy Losses in Molecular Junctions *J. Am. Chem. Soc.* **138** 722-5
- [37] Iqbal M Z, Singh A K, Iqbal M W, Seo S and Eom J 2012 Effect of e-beam irradiation on graphene layer grown by chemical vapor deposition *J. Appl. Phys.* **111** 084307
- [38] Xu Z, Chen L, Li J, Wang R, Qian X, Song X, Liu L and Chen G 2011 Oxidation and disorder in few-layered graphene induced by the electron-beam irradiation *Appl. Phys. Lett.* **98** 183112
- [39] Meyer J C, Girit C O, Crommie M F and Zettl A 2008 Hydrocarbon lithography on graphene membranes *Appl. Phys. Lett.* **92** 123110
- [40] Teweldebrhan D and Balandin A A 2009 Modification of graphene properties due to electron-beam irradiation *Appl. Phys. Lett.* **94** 013101
- [41] van Dorp W F, van Someren B, Hagen C W, Kruit P and Crozier P A 2005 Approaching the Resolution Limit of Nanometer-Scale Electron Beam-Induced Deposition *Nano Lett.* **5** 1303-7
- [42] Besold J 1994 Electromigration kinetics of gold on a carbon thin film surface studied by scanning tunneling microscopy and scanning tunneling potentiometry *J. Vac. Sci. Technol. B Microelectron. Nanometer Struct. Process. Meas. Phenom.* **12** 1764
- [43] Ohtsu M 2016 *Silicon Light-Emitting Diodes and Lasers: Photon Breeding Devices using Dressed Photons* (Springer)
- [44] Ruzicka B A, Wang S, Werake L K, Weintrub B, Loh K P and Zhao H 2010 Hot carrier diffusion in graphene *Phys. Rev. B: Condens. Matter Mater.*

*Phys.* **82**

[45] Johannsen J C et al. 2013 Direct View of Hot Carrier Dynamics in Graphene *Phys. Rev. Lett.* **111**

[46] Brida D et al. 2013 Ultrafast collinear scattering and carrier multiplication in graphene *Nat. Commun.* **4**

[47] Meric I, Han MY, Young A F, Ozyilmaz B, Kim P and Shepard KL 2008 Current saturation in zero-bandgap, top-gated graphene field effect transistors *Nat. Nanotechnol.* **3** 654-9

[48] Amendola V 2016 Surface plasmon resonance of silver and gold nanoparticles in the proximity of graphene studied using the discrete dipole approximation method *Phys. Chem. Chem. Phys.* **18** 2230-41

[49] Rai P, Hartmann N, Berthelot J, Arocas J, Colas des Francs G, Hartschuh A and Bouhelier A 2013 Electrical excitation of surface plasmons by an individual carbon nanotube transistor *Phys. Rev. Lett.* **111** 026804-1 - 026804-5

## 6.9 Supporting information

### Supporting Information:

Characterization of graphene FETs (Figure 6.8),

Gaussian fitting to spectra (Figure 6.9),

Light emission spectrum in the NIR range only (Figure 6.10),

Efficiency Calculation (Figure 6.11),

Threshold behavior of the peak spectral intensity (Figure 6.12),

Voltage effects on spectral parameters (Figure 6.13),

Effects of current on spectral peak wavelength (Figure 6.14),

SEM and EDX data showing gold nanoparticles (Figure 6.15),

SEM images before and after experiments (Figure 6.16),

SEM and EDX data showing defect characterization (Figure 6.17 and Table 6.1),

Raman spectra before and after SEM interaction (Figure 6.18),

Blackbody theory comparison to light emission spectra (Figure 6.19).

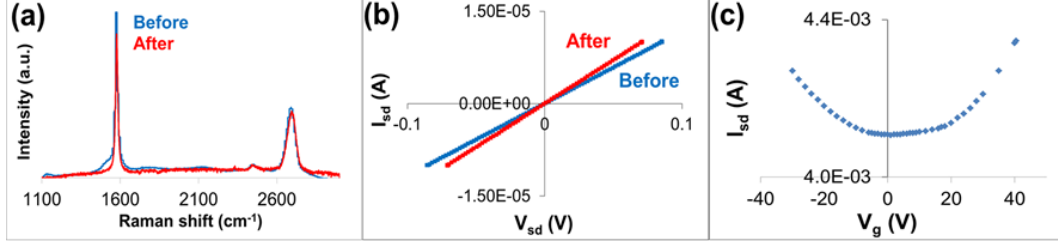


Figure 6.8: Typical Characterization of graphene FETs: (a) Raman spectra before (blue) and after (red) light emission, (b)  $I - V$  curves ( $I_{sd}$  vs  $V_{sd}$ ) before (blue) and after (red) light emission, (c) transfer characteristics ( $I_{sd}$  vs  $V_g$ ) during a light emission experiment at a fixed  $V_{sd}$ .

Graphene FETs were characterized by Raman spectroscopy and electronic measurements (Figure 6.8) in order to determine if the devices behaved as expected and if they were damaged by light emission. As discussed below, this data showed that generally the devices were not damaged by light emission experiments, in terms of the graphene itself (as characterized by Raman spectra), and in terms of the device functionality (as characterized by  $I - V$  curves). However, as discussed in the main text, in some experiments there was particle migration occurring from the gold electrodes due to the applied voltage (electro-migration), and intentionally-placed defects in the graphene channel using an SEM e-beam. This characterization is important in comparing the results to theories of light emission mechanisms as discussed in the main text.

Raman spectra were obtained to characterize the graphene before and after light emission experiments and to determine whether any detectable damage occurred in the process. Typical Raman spectra (Figure 6.8 (a)) were characteristic of single-layer to few-layer graphene [1]. The similarity of the Raman spectra before and after light emission show that there were no detectable large-scale damages to the graphene in the experiments. However, due to the resolution limit of the objective lens, this method was unable to characterize localized defects in a region smaller than  $\sim 10\%$  of the channel area.

The electrical properties of the graphene devices were characterized by

current-voltage ( $I - V$ ) curves before and after light emission. Typical  $I - V$  curves (Figure 6.8 (b)) showed the characteristic behavior of graphene FETs [2], in which the source-drain voltage controls the source-drain current  $I_{sd}$  linearly by Ohm's law ( $V_{sd} = I_{sd}R$ ), and the resistance  $R$  is determined from the inverse slope. The curves were linear both before and after the experiments, confirming that the source-drain electrodes were functioning Ohmic contacts and the light emission experiments did not significantly damage the devices. Small changes in the slope of the  $I - V$  curve were consistent with small changes in the measured resistance in experiments.

Transfer characteristics of the graphene FETs were simultaneously measured with spectroscopy to relate the optical data to the doping level and resistance of the graphene. Typical transfer characteristics (Figure 6.8 (c)) showed the characteristic behavior in agreement with other graphene FET work [2], in which the gate voltage can be used to modulate the current  $I_{sd}$  (or equivalently the resistance of the graphene) by shifting the Fermi energy such that the carrier density is directly proportional to  $V_g$ . The minimum of the current at the Dirac voltage  $V_d$  represents the charge neutrality point (*CNP*). Large positive  $V_g$  (or  $V_g > V_d$ ) is associated with *n*-type graphene, large negative  $V_g$  (or  $V_g < V_d$ ) is associated with *p*-type graphene, and the residual doping is given by the sign of  $V_d$  [3,4]. These samples were typically *p*-doped (positive value of  $V_d$ ) but exhibited hysteresis of the *CNP* (*CNP* shift upon reversal of the sweep direction of  $V_g$ ) such that some measured samples were also *n*-doped. The electrical hysteresis of a graphene FET that has been exposed to ambient conditions is probably due to adsorbed water which can persist in vacuum at room temperature [3,5].

An example of how the experimental spectra were fitted to Gaussian functions is shown in Figure 6.9. The Gaussian functions were fitted to the experimental spectral data using an automatic fitting tool in Matlab. The fitting functions were two-term Gaussians based on the equation:

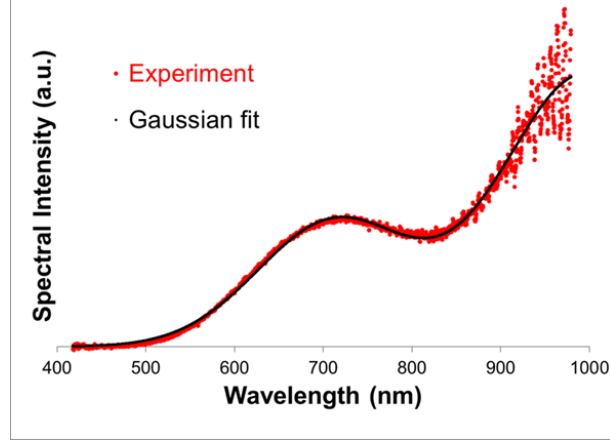


Figure 6.9: Experimental spectrum (red) of a graphene FET ( $V_g = 0$  V,  $V_{sd} = -25$  V) with a two-term Gaussian fit (black) using coefficients:  $a1 = 10200$ ,  $b1 = 997.2$ ,  $c1 = 135$ ,  $a2 = 4701$ ,  $b2 = 713.7$ ,  $c2 = 123.8$  as defined below.

$$(6.1) \quad f(x) = a1 \times \exp[-((x - b1)/c1)^2] + a2 \times \exp[-((x - b2)/c2)^2]$$

where:

$a1$  = height of peak 1

$b1$  = center of peak 1

$c1 = FWHM/\sqrt{2 \times \ln 2}$  of peak 1

$a2$  = height of peak 2

$b2$  = center of peak 2

$c2 = FWHM/\sqrt{2 \times \ln 2}$  of peak 2

and

$FWHM$  = full-width-at-half-maximum

These coefficients, as given by the fitting tool in Matlab, were used to find the peak spectral intensity ( $a2$ ), peak wavelength ( $b2$ ), and  $FWHM$  ( $c2 \times \sqrt{2 \times \ln 2}$ ) for each measured spectral peak in the visible range.

An example calculation of the power conversion efficiency of the light emission from graphene FETs was calculated from the spectrum shown in Figure 6.11. The measured spectrum was calibrated by an absolute intensity calibra-

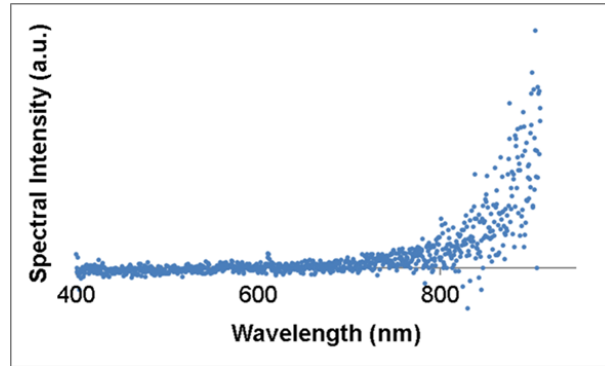


Figure 6.10: Light emission spectrum from a graphene FET ( $V_g = -40$  V,  $V_{sd} = 12$  V) displaying light in the NIR range only, without the characteristic peak in the VIS range as observed on other devices.

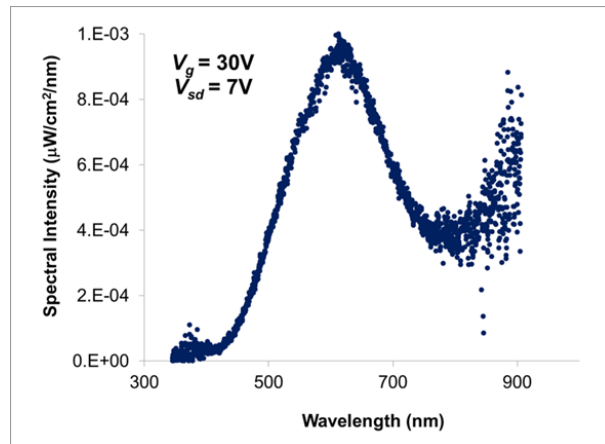


Figure 6.11: Light emission spectrum of a graphene FET ( $V_g = 30$  V,  $V_{sd} = 7$  V,  $R = 2.49 \times 10^4 \Omega$ ) used to calculate an order-of-magnitude estimate of the power conversion efficiency  $\eta = 10^{-7}$ .

tion lamp (Ocean Optics LS1-CAL) to obtain the spectral intensity in units of  $[\mu\text{W}/\text{cm}^2/\text{nm}]$ .

The efficiency  $\eta$  is given by:

$$(6.2) \quad \eta = P_{out}/P_{in}$$

where  $P_{out}$  is the optical radiated (output) power and  $P_{in}$  is the applied electrical (input) power.

The output and input power are calculated by:

$$(6.3) \quad P_{out}[W] = P_{out}[W/cm^2/nm] \times \lambda[nm] \times A_{fiber}[cm^2] = A_{curve}[W/cm^2] \times A_{fiber}[cm^2]$$

$$(6.4) \quad P_{in}[W] = (V_{sd}[V])^2/R[\Omega]$$

where  $A_{curve}$  is the area under the spectral curve, which was determined by a Gaussian fit to the spectral peak in the visible range, and  $A_{fiber} = 0.002827 \text{ cm}^2$  is the area of the collection fiber in the spectroscopy setup.

The spectrum shown in Figure 6.11 was used to obtain an order-of-magnitude estimate of  $\eta = 10^{-7}$ , representing typical results.

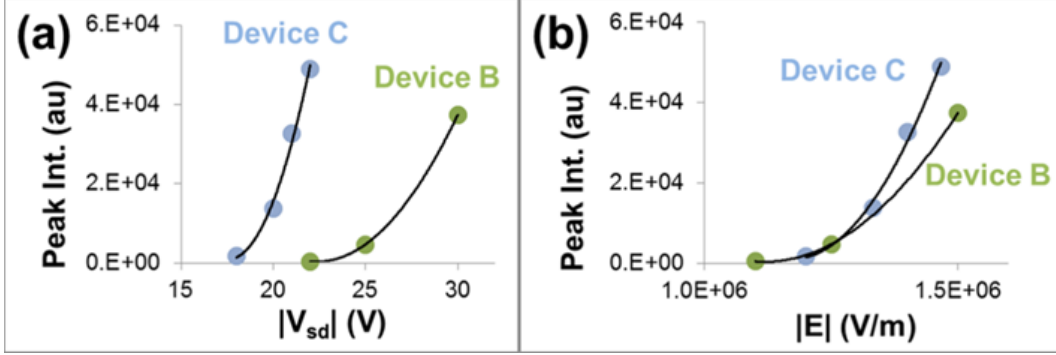


Figure 6.12: Threshold behaviour of the peak spectral intensity ( $Int.$ ) of the VIS light emission for two different graphene FETs: device C (blue) and device B (green). The peak spectral intensity is plotted in terms of (a) the source-drain voltage  $|V_{sd}|$  and (b) the electric field  $|E| = |V_{sd}|/L$ , where  $L$  is the channel length. The threshold for observable light emission in terms of source-drain voltage is different for each device as seen in (a), but becomes apparent as a single value in (b) as the minimum of the curves for the two devices converge at a value on the order of  $1 \times 10^6$  V/m (i.e. the threshold electric field for observable light emission). All fits (black curves) are polynomials of a second order.

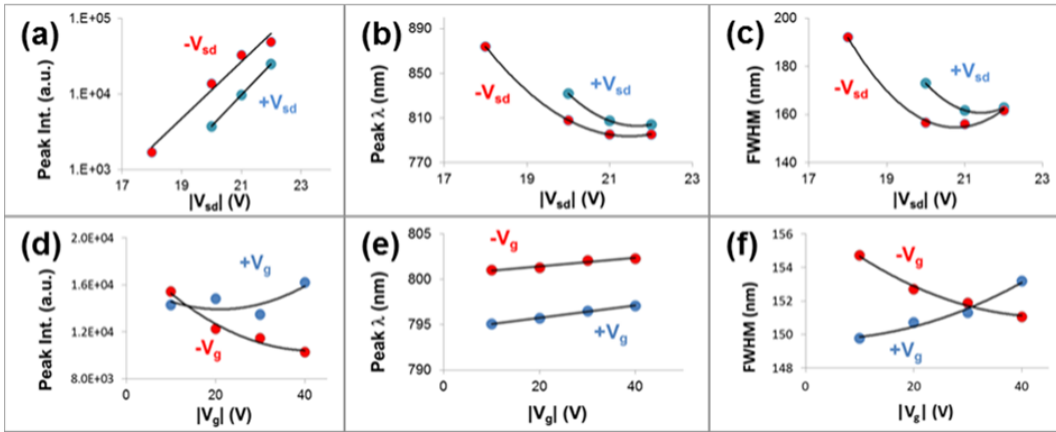


Figure 6.13: Effects of varying source-drain (top row) and gate voltage (bottom row) on light emission spectral parameters for positive (blue) and negative (red)  $V_{sd}$  and  $V_g$ , corresponding to the spectra shown in Figure 6.3 of the main text: (a) peak spectral intensity ( $Int.$ ) vs  $|V_{sd}|$ , plotted on a logarithmic scale and fitted to exponential functions (black lines); (b) peak wavelength ( $\lambda$ ) vs  $|V_{sd}|$ ; (c) full-width-at-half-maximum ( $FWHM$ ) vs  $|V_{sd}|$ ; (d)  $Int.$  vs  $|V_g|$ ; (e) peak  $\lambda$  vs  $|V_g|$ , fitted to linear functions (black lines); (f)  $FWHM$  vs  $|V_g|$ . All fits (black curves) except in (a) and (e) are polynomials of a second order.

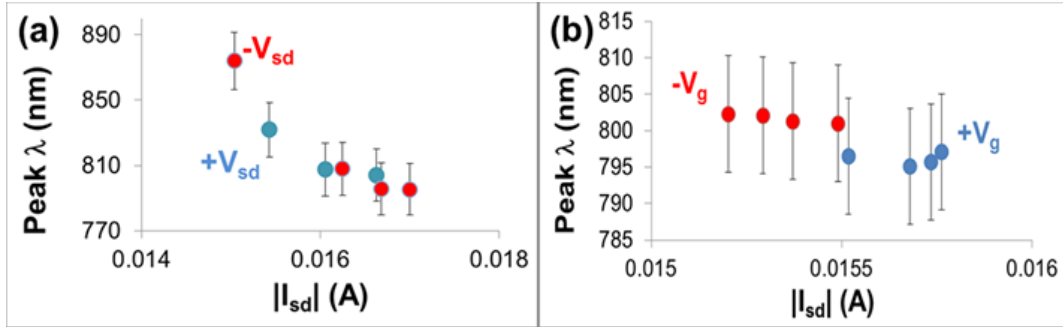


Figure 6.14: Effects of current on spectral peak wavelength corresponding to the spectra in Figure 6.4 (a) and (b): (a) peak wavelength ( $\lambda$ ) vs  $|I_{sd}|$  by varying  $V_{sd}$  and (b) peak wavelength ( $\lambda$ ) vs  $|I_{sd}|$  by varying  $V_g$ . Error bars representing 2% (a) and 1% (b) were determined from the 95% confidence bounds of the Matlab Gaussian fits to the data. In (a) and (b) a downward trend was observed corresponding to a blue-shift in emitted light with increasing current.

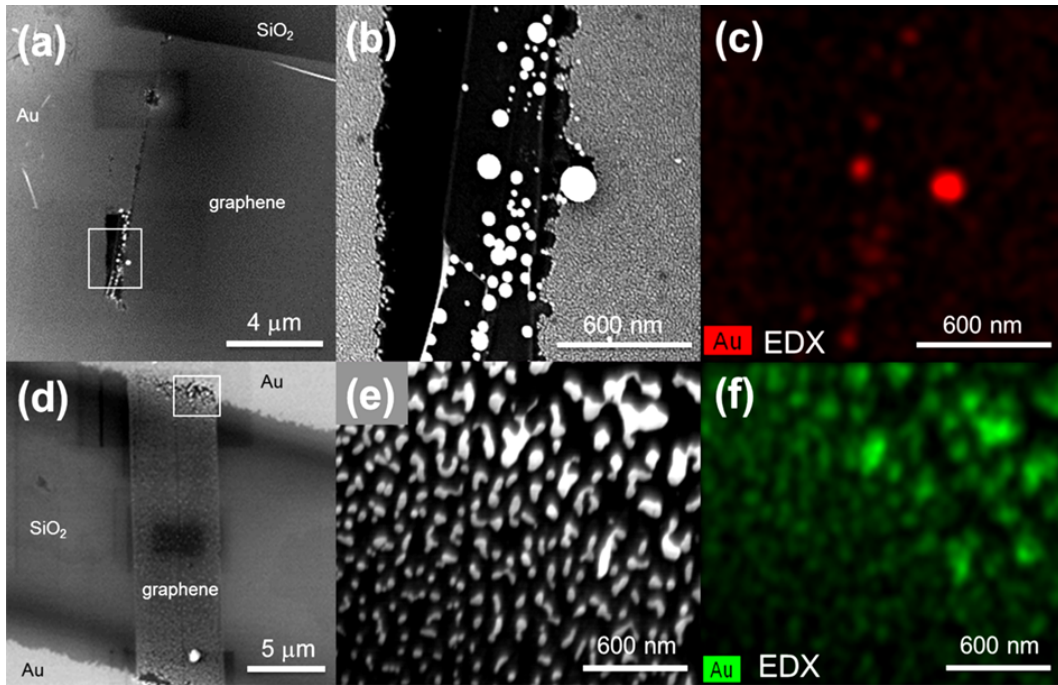


Figure 6.15: SEM and EDX characterization of graphene FETs after applying voltage in light emission experiments showing gold nanoparticles. (a) and (d): SEM images of two different graphene FETs in which nanoparticles were observed near the gold electrodes (white rectangles); (b) and (e) corresponding enlarged SEM images from the white rectangles in (a) and (d), respectively; (c) and (f) corresponding EDX maps of gold (Au) from the SEM images in (b) and (e), respectively showing that the nanoparticles consisted of gold.

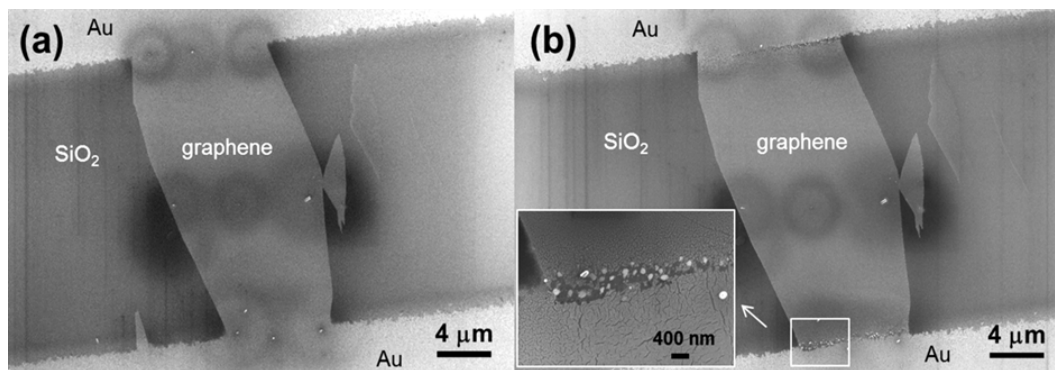


Figure 6.16: SEM images of a graphene FET before (a) and after (b) applying voltage in light emission experiments. Nanoparticles were observed after experiments (b) near the gold electrode (white rectangle and corresponding enlarged view in inset). Before experiments (a), no such nanoparticles were observed, confirming that the nanoparticles formed due to applied voltage, likely by electromigration of gold. The dark shaded circles centered by light-contrast points in (a) and (b) are due to focused e-beam interaction for patterning defects on the graphene channel as described in the main text.

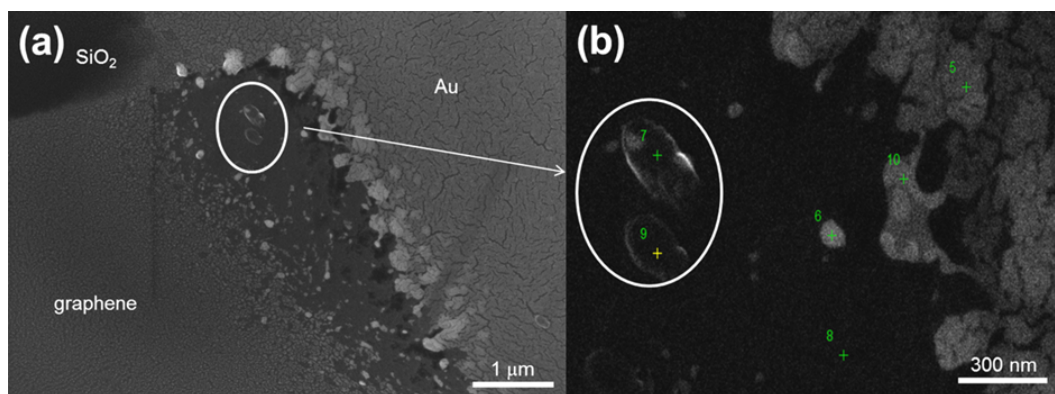


Figure 6.17: SEM and EDX characterization of defects patterned onto a graphene FET by e-beam interaction: (a) SEM image of a graphene channel where the e-beam was used to pattern defects (white oval); (b) Enlarged view of the area, showing points of EDX analysis (green numbered crosses) given in Table 6.1 below. Points 7 and 9 (white oval) are the e-beam interacted spots, while the others are used as reference points.

Atomic percent (%)				
Spectrum	C	O	Si	Au
5	22.88	25.08	49.45	2.60
6	20.44	31.10	45.93	2.54
7	37.95	22.95	39.10	-
8	24.81	26.40	48.79	-
9	34.83	24.51	40.66	-
10	22.21	27.82	47.78	2.19
Mean value	27.19	26.31	45.28	2.44

Table 6.1: Atomic percent (%) of the EDX spectra for the points indicated in Figure 6.17 (b). All points show the presence of C, O, and Si due to the graphene and backing Si/SiO<sub>2</sub> substrate, while points 7 and 9 (interacted by the e-beam) show increased values of C due to the EBID C nano-deposits, as well as a lack of Au distinguishing them from the gold nanoparticles known to form near the electrodes (eg. point 6).

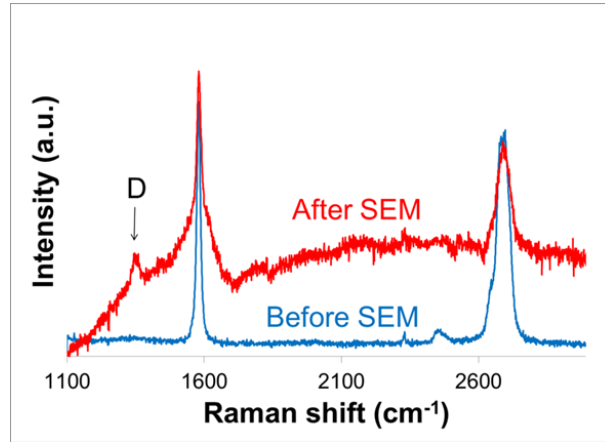


Figure 6.18: Raman spectra of a graphene FET channel before (blue) and after (red) focused e-beam interaction in an SEM for the purpose of patterning defects as described in the main text. The D-peak (marked “D”) in the spectrum after SEM e-beam interaction indicates the presence of defects in the crystal lattice of the graphene channel.

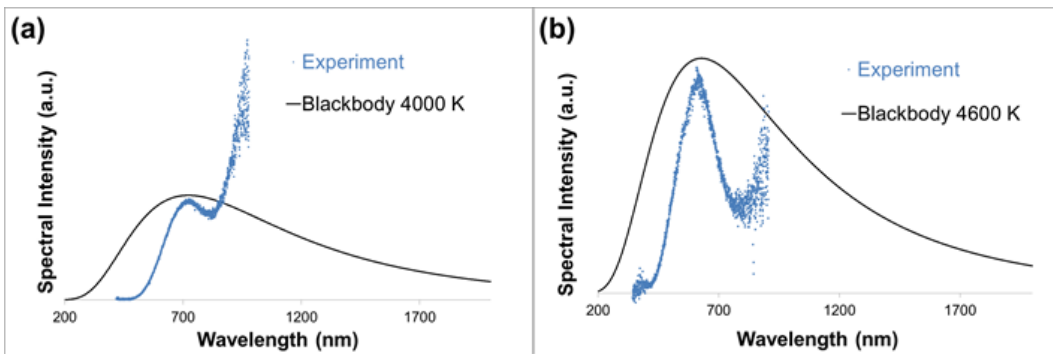


Figure 6.19: Blackbody spectra based on Plancks law (black) compared to experimental light emission spectra (blue) of two different graphene FETs excited by applied voltage: (a) graphene FET at  $V_g = 0$  V,  $V_{sd} = -25$  V with peak emission of  $\sim 700$  nm compared to a blackbody at 4000K ; (b) graphene FET at  $V_g = 30$  V,  $V_{sd} = 7$  V with peak emission at  $\sim 600$  nm compared to a blackbody at 4600 K.

## 6.10 References for Supporting Information

- [1] Ferrari A C et al. 2006 Raman Spectrum of Graphene and Graphene Layers *Phys. Rev. Lett.* **97**
- [2] Schwierz F 2010 Graphene transistors *Nat. Nanotechnol.* **5** 487-96
- [3] Joshi P, Romero H E, Neal A T, Toutam V K and Tadigadapa S A 2010 Intrinsic doping and gate hysteresis in graphene field effect devices fabricated on SiO<sub>2</sub> substrates *J. Phys. Condens. Matter* **22** 334214
- [4] Peres N M R 2010 Colloquium: The transport properties of graphene: An introduction *Rev. Mod. Phys.* **82** 2673-700
- [5] Lafkioti M, Krauss B, Lohmann T, Zschieschang U, Klauk H, Klitzing K v. and Smet J H 2010 Graphene on a Hydrophobic Substrate: Doping Reduction and Hysteresis Suppression under Ambient Conditions *Nano Lett.* **10** 1149-53

# Chapter 7

## Conclusions

### 7.1 Summary

In summary, this thesis has presented an experimental investigation of the optoelectronic properties of graphene, focusing on light interaction with graphene and light emission from graphene. In particular, the structural effects that occur in graphene under pulsed laser irradiation and the electrically-driven light emission characteristics of graphene devices were studied. The main objective in investigating the optoelectronic properties of graphene was to further the development of future graphene-based applications.

The thesis begins with three preliminary chapters to the research studies: “Introduction” (Chapter 1), “Background” (Chapter 2), and “Mechanisms” (Chapter 3). These chapters outline the history, applications, and properties of graphene as well as the physical mechanisms and theories behind the experimental studies that follow. The next three publications/chapters consist of the thesis research: “Damage effects on multi-layer graphene from femtosecond laser interaction” (Chapter 4), “Femtosecond laser induced periodic surface structures on multi-layer graphene” (Chapter 5), and “Visible light emission in graphene field effect transistors” (Chapter 6).

The main experimental methods used in the studies were femtosecond laser beam interaction and optical spectroscopy and imaging. Fabrication

of graphene samples was done by mechanical exfoliation, and graphene devices were completed by electron beam vapour deposition of patterned electrodes (detailed methods are provided in Appendix A). Several techniques were used to characterize the graphene samples and devices, including Raman spectroscopy, optical microscopy, scanning electron microscopy, atomic force microscopy, and electronic measurements.

The main results of this work were the demonstration of patterning multilayer graphene by ultrafast laser interaction, the determination of the femtosecond laser ablation threshold of exfoliated multilayer graphene, the first observation of laser induced periodic surface structures (LIPSS) on graphene (a phenomenon which was known for nearly 50 years on other materials), and the determination of visible light emitting properties of graphene field effect transistors (FETs).

The experimental results also provided evidence to support or rule out previous theories outlined in Chapter 3. In the case of femtosecond LIPSS observed on graphene, the results supported a well known surface plasmon model of LIPSS formation. In this model, the interference of the incident laser beam with two surface plasmons propagating in opposite directions causes a periodic energy distribution at the material surface leading to the formation of parallel periodic structures. This model was consistent with the observed small spatial periods of the LIPSS that were nearly even fractions of the laser wavelength, as well as previous observations of surface plasmons on graphene as outlined in Chapter 5.

In the case of light emission from graphene FETs, the results were consistent with a recently proposed theory of light emission based on the quantum Čerenkov effect. In this model, hot carriers in graphene lead to the emission of surface plasmons, which couple-out as light at scattering sites. This model was evidenced by a combination of several of the observed light emission properties: the generation of light by either hot electrons or holes under the application of high source-drain voltage, a threshold behavior of the emission intensity with source-drain voltage, an exponential relationship of the intensity with current,

a tunable peak energy with source-drain or gate voltages, spatially localized emission at various types of scattering sites, and emission locations that were unaffected by varying voltages. Other possible theories, such as blackbody radiation, were ruled out due to inconsistencies with the results as outlined in Chapter 6.

From this thesis work, several new insights into the optoelectronic properties of graphene are added to the growing body of knowledge of this interesting 2D material, demonstrating new functionality and promise for graphene in the field of optoelectronics. With graphene being a relatively new material, there is yet much to discover about it, and it continues to be an exciting material to study with the promise of novel future applications.

## 7.2 Future Work

The conclusions of this thesis naturally lead to further questions and hence continued research and suggested topics of study. In terms of the works in Chapters 4 and 5 on light interaction with graphene, this research is completed; however, it also suggests several interesting avenues for further research. For example, interesting studies would include the effects of the number of graphene layers on the structures fabricated by laser induction, the controllability of laser induced periodic surface structures on graphene, and the synthesis of controlled laser induced structures on graphene for specific purposes. The latter study could be useful, for example, to fabricate graphene nanogratings for surface plasmon applications, such as enhancing the efficiency of light emission from graphene devices as described in Chapter 6.

Future study evolving from the third paper (Chapter 6) on encapsulated light emitting graphene devices is planned. The electronic properties of graphene are affected by their environment, and this is why graphene-based devices are typically protected from air by a vacuum chamber. Electrically-driven light emission from graphene devices could also be affected, as suggested by preliminary spectroscopy experiments that were carried out in air. Thus it is

important for applications to protect light emitting graphene devices from air, but a vacuum chamber is not a practical solution. Ideally, devices would be in a protected, compact, portable format that is easily integrable in current technology. In a future study, the light emitting properties of encapsulated graphene field effect transistors sealed by ceramic “quad flat packages” (QFPs) could be investigated. This type of package is designed for use in optoelectronics and includes electrical access and an optical window, and is compatible with on-chip technology. Light emission properties could be measured over timescales of days to weeks, in order to determine the quality of the protected device.

Encapsulated light emitting graphene devices could also be useful for research in terms of a convenient and practical experimental setup that does not require a vacuum chamber. In particular, time resolved spectroscopy measurements of light emission from graphene could be enabled using the encapsulated devices with a typical microscope/spectrograph set-up. This experiment would measure the dynamics of the light emission from encapsulated graphene devices. A pulsed electrical source could be used to excite light emission, and the time-resolved spectra could be measured in order to obtain the timescale of the light emission processes. These results would likely provide further insight into the physical mechanism of light emission and the optoelectronic properties of graphene.

The future topics of study in this section are in keeping with the main goal of this thesis: investigating the optoelectronic properties of graphene in order to further the development of its emerging applications.

## 7.3 Outlook

We began this thesis with a historical introduction to graphene and discussed some of the reasons why it has created so much excitement. Now, decades after the theoretical research began and seven years after the Nobel prize was awarded for this “miracle material”, much hype remains and research on the

properties of graphene is constantly leading to new developments. We conclude this thesis with a discussion of the outlook for graphene in the future.

From this author's perspective, graphene is indeed an outstanding and promising material for the future. Through the ongoing research of many groups around the world, new properties are being continuously discovered, unlocking increasing potential for graphene in science and applications. With experimental research on this material being still relatively new, the main challenges that remain include the need for simple and low cost production techniques and the development of methods to integrate graphene devices into current technologies that are designed for other materials. Additional experiments and theory would lead to a more thorough knowledge of the properties and capabilities of graphene and an understanding of the controllable processes for the optimal design of graphene-based technology.

With this in mind, the majority of reported graphene applications (e.g. solar cells or touch screens) so far are in a developmental or emerging stage. Even so, a broad variety of applications have been experimentally demonstrated and an increasing number of graphene products are reaching the market. These products make use of the outstanding properties of graphene as discussed in this thesis, such as its high strength and light-weight for use in vehicle bodywork, or extremely high conductivity for electronics. Of particular promise are the quite material properties of graphene that could be useful where there is a need for new materials in developing technologies or where theoretical predictions have surpassed current capabilities. For example, it is due to its two-dimensionality that the quantum Čerenkov effect has been theorized so far only for graphene. The prediction of an electrically-controllable 2D plasmonic shockwave that can also lead to visible light emission is interesting in itself in terms of newly discovered physics. Put into practice, the effect could open up a realm of new photonic and plasmonic possibilities such as on-chip transmission of optoelectronic signals. As can be seen by the work presented in this thesis, such possibilities could potentially be realized in the next few years.

Only time will tell how the story of graphene unfolds, and whether it is indeed the material of the future, or just the material of present interest. However, given that much of the previously predicted theory on graphene that make it so exciting has now been experimentally verified, the potential for this material has been proven to be real indeed. This author believes that graphene will be present in many future products and enable novel technologies, especially in optoelectronics where it may make a large contribution to the emerging field.

# Bibliography

## Chapter 1 References

- 1-[1] Novoselov K S, Fal'ko V I, Colombo L, Gellert P R, Schwab M G and Kim K 2012 A roadmap for graphene *Nature* **490** 192-200
- 1-[2] Cahangirov S, Topsakal M, Aktürk E, Şahin H and Ciraci S 2009 Two- and One-Dimensional Honeycomb Structures of Silicon and Germanium *Phys. Rev. Lett.* **102**
- 1-[3] Lin Y and Connell J W 2012 Advances in 2D boron nitride nanostructures: nanosheets, nanoribbons, nanomeshes, and hybrids with graphene *Nanoscale* **4** 6908
- 1-[4] Wallace P R 1947 The Band Theory of Graphite *Physical Review* **71** 622-34
- 1-[5] Andrei E Y, Li G and Du X 2012 Electronic properties of graphene: a perspective from scanning tunneling microscopy and magnetotransport *Rep. Prog. Phys.* **75** 056501
- 1-[6] Geim A K and Novoselov K S 2007 The rise of graphene *Nat. Mater.* **6** 183-91
- 1-[7] Novoselov K S, Geim A K, Morozov S V, Jiang D, Zhang Y, Dubonos S V, Grigorieva I V and Firsov A A 2004 Electric Field Effect in Atomically Thin Carbon Films *Science* **306** 666-9
- 1-[8] Nair R R, Blake P, Grigorenko A N, Novoselov K S, Booth T J, Stauber T, Peres N M R and Geim A K 2008 Fine Structure Constant Defines Visual Transparency of Graphene *Science* **320** 1308-1308
- 1-[9] Ferrari A C, Meyer J C, Scardaci V, Casiraghi C, Lazzeri M, Mauri F, Piscanec S, Jiang D, Novoselov K S, Roth S and Geim A K 2006 Raman Spectrum of Graphene and Graphene Layers *Phys. Rev. Lett.* **97**

- 1-[10] Wang J, Chen Y, Li R, Dong H, Zhang L, Lotya M, Jonathan N and Werner J 2011 Nonlinear Optical Properties of Graphene and Carbon Nanotube Composites *Carbon Nanotubes - Synthesis, Characterization, Applications*
- 1-[11] Pei S, Zhao J, Du J, Ren W and Cheng H-M 2010 Direct reduction of graphene oxide films into highly conductive and flexible graphene films by hydrohalic acids *Carbon N. Y.* **48** 4466-74
- 1-[12] Lee C, Wei X, Kysar J W and Hone J 2008 Measurement of the Elastic Properties and Intrinsic Strength of Monolayer Graphene *Science* **321** 385-8
- 1-[13] Shen J, Zhu Y, Yang X and Li C 2012 Graphene quantum dots: emergent nanolights for bioimaging, sensors, catalysis and photovoltaic devices *Chem. Commun.* **48** 3686
- 1-[14] Mayorov A S, Gorbachev R V, Morozov S V, Britnell L, Jalil R, Ponomarenko L A, Blake P, Novoselov K S, Watanabe K, Taniguchi T and Geim A K 2011 Micrometer-Scale Ballistic Transport in Encapsulated Graphene at Room Temperature *Nano Lett.* **11** 2396-9
- 1-[15] Moser J, Barreiro A and Bachtold A 2007 Current-induced cleaning of graphene *Appl. Phys. Lett.* **91** 163513
- 1-[16] Bonaccorso F, Sun Z, Hasan T and Ferrari A C 2010 Graphene photonics and optoelectronics *Nat. Photonics* **4** 611-22
- 1-[17] Grigorenko A N, Polini M and Novoselov K S 2012 Graphene plasmonics *Nat. Photonics* **6** 749-58
- 1-[18] News B 2016 The worlds first graphene car is unveiled in Manchester - BBC News *BBC News*
- 1-[19] Anon 2015 Vittorias 2016 Graphene tire range - Vittoria.com *Vittoria.com*
- 1-[20] Anon 2017 ORA introduce the worlds first graphene headphones - News *soundonsound.com*
- 1-[21] Anon 2017 Graphene products: introduction and market status - The graphene experts *graphene-info.com*
- 1-[22] Wu Y, Lin Y-M, Bol A A, Jenkins K A, Xia F, Farmer D B, Zhu Y and

- Avouris P 2011 High-frequency, scaled graphene transistors on diamond-like carbon *Nature* **472** 74-8
- 1-[23] Anon World premiere of the new HEAD Graphene<sup>TM</sup> Speed racquet — Novak Djokovic *Novak Djokovic*
- 1-[24] Hong J-Y and Jang J 2012 Micropatterning of graphene sheets: recent advances in techniques and applications *J. Mater. Chem.* **22** 8179
- 1-[25] Feng J, Li W, Qian X, Qi J, Qi L and Li J 2012 Patterning of graphene *Nanoscale* **4** 4883
- 1-[26] Bao Q and Loh K P 2012 Graphene Photonics, Plasmonics, and Broadband Optoelectronic Devices *ACS Nano* **6** 3677-94
- 1-[27] Maier S A 2012 Graphene plasmonics: All eyes on flatland *Nat. Phys.* **8** 581-2
- 1-[28] Wong L J, Kaminer I, Ilic O, Joannopoulos J D and Soljačić M 2015 Towards graphene plasmon-based free-electron infrared to X-ray sources *Nat. Photonics* **10** 46-52
- 1-[29] Beltaos A, Kovačević A, Matković A, Ralević U, Jovanović D and Jelenković B 2014 Damage effects on multi-layer graphene from femtosecond laser interaction *Phys. Scr.* **T162** 014015
- 1-[30] Beltaos A, Kovačević A G, Matković A, Ralević U, Savić-Šević S, Jovanović D, Jelenković B M and Gajić R 2014 Femtosecond laser induced periodic surface structures on multi-layer graphene *J. Appl. Phys.* **116** 204306
- 1-[31] Beltaos A, Bergren A J, Bosnick K, Pekas N, Lane S, Cui K, Matković A and Meldrum A 2017 Visible light emission in graphene field effect transistors *Nano Futures* **1** 025004

## Chapter 2 References

- 2-[1] Fox M 2010 *Optical Properties of Solids* (Oxford University Press)
- 2-[2] Bonaccorso F, Sun Z, Hasan T and Ferrari A C 2010 Graphene photonics and optoelectronics *Nat. Photonics* **4** 611-22
- 2-[3] Andrei E Y, Li G and Du X 2012 Electronic properties of graphene: a perspective from scanning tunneling microscopy and magnetotransport *Rep. Prog. Phys.* **75** 056501
- 2-[4] Castro Neto A H, Guinea F, Peres N M R, Novoselov K S and Geim A K 2009 The electronic properties of graphene *Rev. Mod. Phys.* **81** 109-62
- 2-[5] Reddy D, Register L F, Carpenter G D and Banerjee S K 2011 Graphene field-effect transistors *J. Phys. D Appl. Phys.* **44** 313001
- 2-[6] Peres N M R 2010 Colloquium: The transport properties of graphene: An introduction *Rev. Mod. Phys.* **82** 2673-700
- 2-[7] Gonçalves P A D and Peres N M R 2015 *An Introduction to Graphene Plasmonics* (World Scientific)
- 2-[8] Wallace P R 1947 The Band Theory of Graphite *Physical Review* **71** 622-34
- 2-[9] Ashcroft N W and David Mermin N 1976 *Solid state physics* (Harcourt School)
- 2-[10] Yang L, Deslippe J, Park C-H, Cohen M L and Louie S G 2009 Excitonic Effects on the Optical Response of Graphene and Bilayer Graphene *Phys. Rev. Lett.* **103**
- 2-[11] Novoselov K S, Geim A K, Morozov S V, Jiang D, Zhang Y, Dubonos S V, Grigorieva I V and Firsov A A 2004 Electric Field Effect in Atomically Thin Carbon Films *Science* **306** 666-9
- 2-[12] Schwierz F 2010 Graphene transistors *Nat. Nanotechnol.* **5** 487-96
- 2-[13] Joshi P, Romero H E, Neal A T, Toutam V K and Tadigadapa S A 2010 Intrinsic doping and gate hysteresis in graphene field effect devices fabricated on SiO<sub>2</sub> substrates *J. Phys. Condens. Matter* **22** 334214
- 2-[14] Novoselov K S, Falko V I, Colombo L, Gellert P R, Schwab M G and Kim K 2012 A roadmap for graphene *Nature* **490** 192-200
- 2-[15] Ponomarenko L A, Belle B D, Jalil R, Britnell L, Gorbachev R V, Geim

- A K, Novoselov K S, Castro Neto A H, Eaves L and Katsnelson M I 2013 Field-effect control of tunneling barrier height by exploiting graphenes low density of states *J. Appl. Phys.* **113** 136502
- 2-[16] Nair R R, Blake P, Grigorenko A N, Novoselov K S, Booth T J, Stauber T, Peres N M R and Geim A K 2008 Fine Structure Constant Defines Visual Transparency of Graphene *Science* **320** 1308-1308
- 2-[17] Casiraghi C, Hartschuh A, Lidorikis E, Qian H, Harutyunyan H, Gokus T, Novoselov K S and Ferrari A C 2007 Rayleigh Imaging of Graphene and Graphene Layers *Nano Lett.* **7** 2711-7
- 2-[18] Zhu S-E, Yuan S and G C A 2014 Optical transmittance of multilayer graphene *EPL* **108** 17007
- 2-[19] Wall M 2011 *The Raman spectroscopy of graphene and the determination of layer thickness* ( Madison, WI Thermo Fisher Scientific)
- 2-[20] Ferrari A C, Meyer J C, Scardaci V, Casiraghi C, Lazzeri M, Mauri F, Piscanec S, Jiang D, Novoselov K S, Roth S and Geim A K 2006 Raman Spectrum of Graphene and Graphene Layers *Phys. Rev. Lett.* **97**
- 2-[21] Malard L M, Pimenta M A, Dresselhaus G and Dresselhaus M S 2009 Raman spectroscopy in graphene *Phys. Rep.* **473** 51-87
- 2-[22] Childres I, Jauregui L A, Park W, Cao H and Chen Y P 2013 Raman spectroscopy of graphene and related materials *New developments in photon and materials research*
- 2-[23] Graf D, Molitor F, Ensslin K, Stampfer C, Jungen A, Hierold C and Wirtz L 2007 Spatially Resolved Raman Spectroscopy of Single- and Few-Layer Graphene *Nano Lett.* **7** 238-42
- 2-[24] Grigorenko A N, Polini M and Novoselov K S 2012 Graphene plasmonics *Nat. Photonics* **6** 749-58
- 2-[25] Shalaev V M and Kawata S 2007 *Nanophotonics with surface plasmons* (Elsevier)
- 2-[26] Solymar L, Walsh D and Syms R R A 2014 *Electrical Properties of Materials* (OUP Oxford)
- 2-[27] Heinrichs J 1973 Surface plasmons at metal-vacuum and metal-dielectric

- interfaces *Solid State Commun.* **12** 167-70
- 2-[28] Pitarke J M, Silkin V M, Chulkov E V and Echenique P M 2007 Theory of surface plasmons and surface-plasmon polaritons *Rep. Prog. Phys.* **70** 1-87
- 2-[29] Raether H 1988 *Surface Plasmons on Smooth and Rough Surfaces and on Gratings* (Springer-Verlag)
- 2-[30] Bludov Y U V, Ferreira A, Peres N M R and Vasilevskiy M I 2013 A primer on surface plasmon-polaritons in graphene *Int. J. Mod. Phys. B* **27** 1341001
- 2-[31] Zayats A V and Smolyaninov I I 2003 Near-field photonics: surface plasmon polaritons and localized surface plasmons *J. Opt. A: Pure Appl. Opt.* **5** S16-50
- 2-[32] Bao Q and Loh K P 2012 Graphene Photonics, Plasmonics, and Broadband Optoelectronic Devices *ACS Nano* **6** 3677-94
- 2-[33] Koppens F H L, Chang D E and de Abajo F J G 2011 Graphene Plasmonics: A Platform for Strong Light-Matter Interactions *Nano Lett.* **11** 3370-7
- 2-[34] Kretschmann E and Raether H 1968 Notizen: Radiative Decay of Non Radiative Surface Plasmons Excited by Light *Zeitschrift für Naturforschung A* **23**
- 2-[35] Maier S A 2012 Graphene plasmonics: All eyes on flatland *Nat. Phys.* **8** 581-2
- 2-[36] Brambring J and Raether H 1965 Plasma Radiation from Thin Silver Foils Excited by Light *Phys. Rev. Lett.* **15** 882-3
- 2-[37] Kretschmann E 1972 The angular dependence and the polarisation of light emitted by surface plasmons on metals due to roughness *Opt. Commun.* **5** 331-6
- 2-[38] Peres N M R, Bludov Y V, Ferreira A and Vasilevskiy M I 2013 Exact solution for square-wave grating covered with graphene: surface plasmon-polaritons in the terahertz range *J. Phys. Condens. Matter* **25** 125303
- 2-[39] Wong L J, Kaminer I, Ilic O, Joannopoulos J D and Soljačić M 2015 Towards graphene plasmon-based free-electron infrared to X-ray sources *Nat. Photonics* **10** 46-52

- 2-[40] Kaminer I, Katan Y T, Buljan H, Shen Y, Ilic O, López J J, Wong L J, Joannopoulos J D and Soljačić M 2016 Efficient plasmonic emission by the quantum Čerenkov effect from hot carriers in graphene *Nat. Commun.* **7** ncomms11880
- 2-[41] Jablan M, Buljan H and Soljačić M 2009 Plasmonics in graphene at infrared frequencies *Phys. Rev. B: Condens. Matter Mater. Phys.* **80**
- 2-[42] Matković A V 2015 *Investigating the optical properties of graphene with spectroscopic ellipsometry* Ph.D. (University of Belgrade)

## Chapter 3 References

- 3-[1] Chichkov B N, Momma C, Nolte S, Alvensleben F and Tünnermann A 1996 Femtosecond, picosecond and nanosecond laser ablation of solids *Appl. Phys. A: Mater. Sci. Process.* **63** 109-15
- 3-[2] Frolov V D, Pivovarov P A, Zavedeev E V, Komlenok M S, Kononenko V V and Konov V I 2014 Laser nanoablation of graphite *Appl. Phys. A: Mater. Sci. Process.* **114** 51-5
- 3-[3] Beltaos A, Kovačević A, Matković A, Ralević U, Jovanović D and Jelenković B 2014 Damage effects on multi-layer graphene from femtosecond laser interaction *Phys. Scr.* **T162** 014015
- 3-[4] Jeschke H O, Garcia M E and Bennemann K H 2001 Theory for the Ultrafast Ablation of Graphite Films *Phys. Rev. Lett.* **87**
- 3-[5] Shabalín I L 2014 Carbon (Graphene/Graphite) *Ultra-High Temperature Materials I* (Springer) pp 7-235
- 3-[6] Charlier J-C, Gonze X and Michenaud J-P 1994 Graphite Interplanar Bonding: Electronic Delocalization and van der Waals Interaction *Europhys. Lett.* **28** 403-8

- 3-[7] Vorobyev A Y and Guo C 2012 Direct femtosecond laser surface nano/microstructuring and its applications *Laser Photonics Rev.* **7** 385-407
- 3-[8] Hong J-Y and Jang J 2012 Micropatterning of graphene sheets: recent advances in techniques and applications *J. Mater. Chem.* **22** 8179
- 3-[9] Feng J, Li W, Qian X, Qi J, Qi L and Li J 2012 Patterning of graphene *Nanoscale* **4** 4883
- 3-[10] Kaplas T and Svirko Y 2014 Self-assembled graphene on dielectric micro- and nanostructures *Carbon* **70** 273-8
- 3-[11] Li Y, Li Y, Shi W, Chen S, Zhang G, Liu Z, Sun Q, Tian J, Xu Y and Chen Y 2012 Periodic microstructures fabricated by multiplex interfering femtosecond laser beams on graphene sheet *Int. J. Nanomanuf.* **8** 221
- 3-[12] Bao W, Miao F, Chen Z, Zhang H, Jang W, Dames C and Lau C N 2009 Controlled ripple texturing of suspended graphene and ultrathin graphite membranes *Nat. Nanotechnol.* **4** 562-6
- 3-[13] Capasso A, Placidi E, Zhan H F, Perfetto E, Bell J M, Gu Y T and Motta N 2014 Graphene ripples generated by grain boundaries in highly ordered pyrolytic graphite *Carbon* **68** 330-6
- 3-[14] Currie M, Caldwell J D, Bezares F J, Robinson J, Anderson T, Chun H and Tadjer M 2011 Quantifying pulsed laser induced damage to graphene *Appl. Phys. Lett.* **99** 211909
- 3-[15] Kiisk V, Kahro T, Kozlova J, Matisen L and Alles H 2013 Nanosecond laser treatment of graphene *Appl. Surf. Sci.* **276** 133-7
- 3-[16] Fischbein M D and Drndi M 2008 Electron beam nanosculpting of suspended graphene sheets *Appl. Phys. Lett.* **93** 113107
- 3-[17] Blees M K, Barnard A W, Rose P A, Roberts S P, McGill K L, Huang P Y, Ruyack A R, Kevek J W, Kobrin B, Muller D A and McEuen P L 2015 Graphene kirigami *Nature* **524** 204-7
- 3-[18] Zhou Y, Bao Q, Varghese B, Tang L A L, Tan C K, Sow C-H and Loh K P 2010 Microstructuring of Graphene Oxide Nanosheets Using Direct Laser Writing *Adv. Mater.* **22** 67-71
- 3-[19] Kalita G, Qi L, Namba Y, Wakita K and Umeno M 2011 Femtosecond

- laser induced micropatterning of graphene film *Mater. Lett.* **65** 1569-72
- 3-[20] Roberts A, Cormode D, Reynolds C, Newhouse-Illige T, LeRoy B J and Sandhu A S 2011 Response of graphene to femtosecond high-intensity laser irradiation *Appl. Phys. Lett.* **99** 051912
- 3-[21] Yoo J-H, In J B, Park J B, Jeon H and Grigoropoulos C P 2012 Graphene folds by femtosecond laser ablation *Appl. Phys. Lett.* **100** 233124
- 3-[22] Yao T-F, Wu P-H, Wu T-M, Cheng C-W and Yang S-Y 2011 Fabrication of anti-reflective structures using hot embossing with a stainless steel template irradiated by femtosecond laser *Microelectron. Eng.* **88** 2908-12
- 3-[23] Birnbaum M 1965 Semiconductor Surface Damage Produced by Ruby Lasers *J. Appl. Phys.* **36** 3688-9
- 3-[24] Bonse J, Krüger J, Höhm S and Rosenfeld A 2012 Femtosecond laser-induced periodic surface structures *J. Laser Appl.* **24** 042006
- 3-[25] Dumitru G, Romano V, Weber H P, Sentis M and Marine W 2002 Femtosecond ablation of ultrahard materials *Appl. Phys. A: Mater. Sci. Process.* **74** 729-39
- 3-[26] Huang M, Zhao F, Cheng Y, Xu N and Xu Z 2009 Origin of Laser-Induced Near-Subwavelength Ripples: Interference between Surface Plasmons and Incident Laser *ACS Nano* **3** 4062-70
- 3-[27] Golosov E V, Ionin A A, Kolobov Y R, Kudryashov S I, Ligachev A E, Makarov S V, Novoselov Y N, Seleznev L V, Sinitsyn D V and Sharipov A R 2011 Near-threshold femtosecond laser fabrication of one-dimensional sub-wavelength nanogratings on a graphite surface *Phys. Rev. B: Condens. Matter Mater. Phys.* **83**
- 3-[28] Reif J 2009 Basic Physics of Femtosecond Laser Ablation *Laser-Surface Interactions for New Materials Production Tailoring Structure and Properties* Springer Series in Materials Science 130 ed A Miotello and P M Ossi (Springer) pp 19-41
- 3-[29] Vorobyev A Y, Makin V S and Guo C 2007 Periodic ordering of random surface nanostructures induced by femtosecond laser pulses on metals *J. Appl. Phys.* **101** 034903

- 3-[30] Bonse J, Rosenfeld A and Krüger J 2009 On the role of surface plasmon polaritons in the formation of laser-induced periodic surface structures upon irradiation of silicon by femtosecond-laser pulses *J. Appl. Phys.* **106** 104910
- 3-[31] Sipe J E, Young J F, Preston J S and van Driel H M 1983 Laser-induced periodic surface structure. I. Theory *Phys. Rev. B: Condens. Matter Mater. Phys.* **27** 1141-54
- 3-[32] Makin V S, Makin R S, Ya. Vorobyev A and Guo C 2008 Dissipative nanostructures and Feigenbaums universality in the Metal-high-power ultrashort-pulsed polarized radiation nonequilibrium nonlinear dynamical system *Tech. Phys. Lett.* **34** 387-90
- 3-[33] Bonch-Bruевич A M 1992 Surface electromagnetic waves in optics *Opt. Eng.* **31** 718
- 3-[34] Golosov E V, Ionin A A, Kolobov Y R, Kudryashov S I, Ligachev A E, Novoselov Y N, Seleznev L V and Sinitsyn D V 2011 Ultrafast changes in the optical properties of a titanium surface and femtosecond laser writing of one-dimensional quasi-periodic nanogratings of its relief *J. Exp. Theor. Phys.* **113** 14-26
- 3-[35] Sakabe S, Hashida M, Tokita S, Namba S and Okamuro K 2009 Mechanism for self-formation of periodic grating structures on a metal surface by a femtosecond laser pulse *Phys. Rev. B: Condens. Matter Mater. Phys.* **79**
- 3-[36] Zayats A V and Smolyaninov I I 2003 Near-field photonics: surface plasmon polaritons and localized surface plasmons *J. Opt. A: Pure Appl. Opt.* **5** S16-50
- 3-[37] Raether H 1988 *Surface Plasmons on Smooth and Rough Surfaces and on Gratings* (Springer-Verlag)
- 3-[38] Bonaccorso F, Sun Z, Hasan T and Ferrari A C 2010 Graphene photonics and optoelectronics *Nat. Photonics* **4** 611-22
- 3-[39] Eda G, Lin Y-Y, Mattevi C, Yamaguchi H, Chen H-A, Chen I-S, Chen C-W and Chhowalla M 2010 Blue Photoluminescence from Chemically Derived Graphene Oxide *Adv. Mater.* **22** 505-9
- 3-[40] Sun X, Liu Z, Welsher K, Robinson J T, Goodwin A, Zaric S and Dai

- H 2008 Nano-graphene oxide for cellular imaging and drug delivery *Nano Res.* **1** 203-12
- 3-[41] Luo Z, Vora P M, Mele E J, Charlie Johnson A T and Kikkawa J M 2009 Photoluminescence and band gap modulation in graphene oxide *Appl. Phys. Lett.* **94** 111909
- 3-[42] Gokus T, Nair R R, Bonetti A, Böhmler M, Lombardo A, Novoselov K S, Geim A K, Ferrari A C and Hartschuh A 2009 Making Graphene Luminescent by Oxygen Plasma Treatment *ACS Nano* **3** 3963-8
- 3-[43] Lu J, Yang J-X, Wang J, Lim A, Wang S and Loh K P 2009 One-Pot Synthesis of Fluorescent Carbon Nanoribbons, Nanoparticles, and Graphene by the Exfoliation of Graphite in Ionic Liquids *ACS Nano* **3** 2367-75
- 3-[44] Chen C-F, Park C-H, Boudouris B W, Horng J, Geng B, Girit C, Zettl A, Crommie M F, Segalman R A, Louie S G and Wang F 2011 Controlling inelastic light scattering quantum pathways in graphene *Nature* **471** 617-20
- 3-[45] Liu W-T, Wu S W, Schuck P J, Salmeron M, Shen Y R and Wang F 2010 Nonlinear broadband photoluminescence of graphene induced by femtosecond laser irradiation *Phys. Rev. B: Condens. Matter Mater. Phys.* **82**
- 3-[46] Lui C H, Mak K F, Shan J and Heinz T F 2010 Ultrafast Photoluminescence from Graphene *Phys. Rev. Lett.* **105**
- 3-[47] Stöhr R J, Kolesov R, Pflaum J and Wrachtrup J 2010 Fluorescence of laser-created electron-hole plasma in graphene *Phys. Rev. B: Condens. Matter Mater. Phys.* **82**
- 3-[48] Beams R, Bharadwaj P and Novotny L 2014 Electroluminescence from graphene excited by electron tunneling *Nanotechnology* **25** 055206
- 3-[49] Essig S, Marquardt C W, Vijayaraghavan A, Ganzhorn M, Dehm S, Hennrich F, Ou F, Green A A, Sciascia C, Bonaccorso F, Bohnen K-P, v. Löhneysen H, Kappes M M, Ajayan P M, Hersam M C, Ferrari A C and Krupke R 2010 Phonon-Assisted Electroluminescence from Metallic Carbon Nanotubes and Graphene *Nano Lett.* **10** 1589-94
- 3-[50] Rai P, Hartmann N, Berthelot J, Arocas J, des Francs G C, Hartschuh A and Bouhelier A 2013 Electrical Excitation of Surface Plasmons by an In-

- dividual Carbon Nanotube Transistor *Phys. Rev. Lett.* **111**
- 3-[51] Kwon W, Kim Y-H, Lee C-L, Lee M, Choi H C, Lee T-W and Rhee S-W 2014 Electroluminescence from Graphene Quantum Dots Prepared by Amidative Cutting of Tattered Graphite *Nano Lett.* **14** 1306-11
- 3-[52] Johansson P, Monreal R and Apell P 1990 Theory for light emission from a scanning tunneling microscope *Phys. Rev. B: Condens. Matter Mater. Phys.* **42** 9210-3
- 3-[53] Coombs J H, Gimzewski J K, Reihl B, Sass J K and Schlittler R R 1988 Photon emission experiments with the scanning tunnelling microscope *J. Microsc.* **152** 32536
- 3-[54] Berndt R, Gimzewski J K and Johansson P 1991 Inelastic tunneling excitation of tip-induced plasmon modes on noble-metal surfaces *Phys. Rev. Lett.* **67** 3796-9
- 3-[55] Bharadwaj P, Bouhelier A and Novotny L 2011 Electrical Excitation of Surface Plasmons *Phys. Rev. Lett.* **106**
- 3-[56] Koppens F H L, Chang D E and de Abajo F J G 2011 Graphene Plasmonics: A Platform for Strong Light-Matter Interactions *Nano Lett.* **11** 3370-7
- 3-[57] Mann D, Kato Y K, Kinkhabwala A, Pop E, Cao J, Wang X, Zhang L, Wang Q, Guo J and Dai H 2007 Electrically driven thermal light emission from individual single-walled carbon nanotubes *Nat. Nanotechnol.* **2** 33-8
- 3-[58] Lawton L M, Mahlmeister N H, Luxmoore I J and Nash G R 2014 Prospective for graphene based thermal mid-infrared light emitting devices *AIP Adv.* **4** 087139
- 3-[59] Luxmoore I J, Adlem C, Poole T, Lawton L M, Mahlmeister N H and Nash G R 2013 Thermal emission from large area chemical vapor deposited graphene devices *Appl. Phys. Lett.* **103** 131906
- 3-[60] Freitag M, Chiu H-Y, Steiner M, Perebeinos V and Avouris P 2010 Thermal infrared emission from biased graphene *Nat. Nanotechnol.* **5** 497-501
- 3-[61] Yu D and Dai L 2010 Voltage-induced incandescent light emission from large-area graphene films *Appl. Phys. Lett.* **96** 143107
- 3-[62] Berciaud S, Han M Y, Mak K F, Brus L E, Kim P and Heinz T F 2010

Electron and Optical Phonon Temperatures in Electrically Biased Graphene  
*Phys. Rev. Lett.* **104**

3-[63] Kim Y D, Kim H, Cho Y, Ryoo J H, Park C-H, Kim P, Kim Y S, Lee S, Li Y, Park S-N, Yoo Y S, Yoon D, Dorgan V E, Pop E, Heinz T F, Hone J, Chun S-H, Cheong H, Lee S W, Bae M-H and Park Y D 2015 Bright visible light emission from graphene *Nat. Nanotechnol.* **10** 676-81

3-[64] Fox M 2010 *Optical Properties of Solids* (Oxford University Press)

3-[65] Pop E, Varshney V and Roy A K 2012 Thermal properties of graphene: Fundamentals and applications *MRS Bull.* **37** 1273-81

3-[66] Maznev A A and Wright O B 2014 Demystifying umklapp vs normal scattering in lattice thermal conductivity *Am. J. Phys.* **82** 1062-6

3-[67] Dorgan V E, Behnam A, Conley H J, Bolotin K I and Pop E 2013 High-Field Electrical and Thermal Transport in Suspended Graphene *Nano Lett.* **13** 4581-6

3-[68] Wong L J, Kaminer I, Ilic O, Joannopoulos J D and Soljačić M 2015 Towards graphene plasmon-based free-electron infrared to X-ray sources *Nat. Photonics* **10** 46-52

3-[69] Robb G 2015 Graphene plasmonics: Ultra-tunable graphene light source *Nat. Photonics* **10** 3-4

3-[70] Mišković Z L, Segui S, Gervasoni J L and Arista N R 2016 Energy losses and transition radiation produced by the interaction of charged particles with a graphene sheet *Phys. Rev. B: Condens. Matter Mater. Phys.* **94**

3-[71] Kaminer I, Katan Y T, Buljan H, Shen Y, Ilic O, López J J, Wong L J, Joannopoulos J D and Soljačić M 2016 Efficient plasmonic emission by the quantum Čerenkov effect from hot carriers in graphene *Nat. Commun.* **7** ncomms11880

3-[72] Cherenkov P A 1934 Visible Emission of Clean Liquids by Action of  $\gamma$  Radiation *Dokl. Akad. Nauk SSSR* **2** 451

3-[73] Tamm I E and Frank I M 1937 Coherent In-Medium Fast-Electron Radiation *Dokl. Akad. Nauk USSR* **14** 109

3-[74] Kaminer I, Mutzafi M, Levy A, Harari G, Sheinfux H H, Skirlo S,

- Nemirovsky J, Joannopoulos J D, Segev M and Soljačić M 2016 Quantum Čerenkov Radiation: Spectral Cutoffs and the Role of Spin and Orbital Angular Momentum *Physical Review X* **6**
- 3-[75] Hu Y, Li Z, Wetzel B, Morandotti R, Chen Z and Xu J 2017 Cherenkov Radiation Control via Self-accelerating Wave-packets *Sci. Rep.* **7**
- 3-[76] Ginzburg V L 1940 Quantum theory of radiation of electron uniformly moving in medium *Zh. Eksp. Teor. Fiz* **10** 589-600
- 3-[77] Luo, C., Ibanescu, M., Johnson, S. G. and Joannopoulos, J. D 2003 Čerenkov Radiation in Photonic Crystals *Science* **299** 368-71
- 3-[78] Jablan M, Buljan H and Soljačić M 2009 Plasmonics in graphene at infrared frequencies *Phys. Rev. B: Condens. Matter Mater. Phys.* **80**

## Chapter 4 References

- 4-[1] Novoselov K S, Geim A K, Morozov S V, Jiang D, Zhang Y, Dubonos S V, Grigorieva I V and Firsov A A 2004 *Science* **306** 666-9
- 4-[2] Novoselov K S, Falko V I, Colombo L, Gellert P R, Schwab M G and Kim K 2012 *Nature* **490** 192-200
- 4-[3] Bonaccorso F, Sun Z, Hasan T and Ferrari A C 2010 *Nature Photon.* **4** 611-22
- 4-[4] Grigorenko A N, Polini M and Novoselov K S 2012 *Nature Photon.* **6** 749-58
- 4-[5] Zhou Y, Bao Q, Varghese B, Tang L A L, Tan C K, Sow C and Loh K P 2010 *Adv. Mater.* **22** 67-71
- 4-[6] Zhang W, Li L, Wang Z B, Pena A A, Whitehead D J, Zhong M L, Lin Z and Zhu H W 2012 *Appl. Phys. A* **109** 291-7
- 4-[7] Hong J-Y and Jang J 2012 *J. Mater. Chem.* **22** 8179-91

- 4-[8] Kiisk V, Kahro T, Kozlova J, Matisen L and Alles H 2013 *Appl. Surf. Sci.* **276** 133-7
- 4-[9] Lorenzoni M, Brandi F, Dante S, Giugni A and Torre B 2013 *Sci. Rep.* **3** 1954
- 4-[10] Stöhr R, Kolesov R, Xia K and Wrachtrup J 2011 *ACS Nano* **5** 5141-50
- 4-[11] Kalita G, Qi L, Namba Y, Wakita K and Umeno M 2011 *Mater. Lett.* **65** 1569-72
- 4-[12] Nair R R, Blake P, Grigorenko A N, Novoselov K S, Booth T J, Stauber T, Peres N M R and Geim A K 2008 *Science* **320** 1308-1308
- 4-[13] Hong S-Y, Dadap J I, Petrone N, Yeh P-C, Hone J and Osgood R M 2013 *Phys. Rev. X* **3** 021014
- 4-[14] Liu W-T, Wu S W, Schuck P J, Salmeron M, Shen Y R and Wang F 2010 *Phys. Rev. B* **82** 81408
- 4-[15] Lui C H, Mak K F, Shan J and Heinz T F 2010 *Phys. Rev. Lett.* **105** 127404
- 4-[16] Bykov A Y, Murzina T V, Rybin M G and Obraztsova E D 2012 *Phys. Rev. B* **85** 121413
- 4-[17] Dean J J and van Driel H M 2010 *Phys. Rev. B* **82** 125411
- 4-[18] Currie M, Caldwell J D, Bezares F J, Robinson J, Anderson T, Chun H and Tadjer M 2011 *Appl. Phys. Lett.* **99** 211909
- 4-[19] Roberts A, Cormode D, Reynolds C, Newhouse-Illige T and LeRoy B J 2011 *Appl. Phys. Lett.* **99** 051912
- 4-[20] Yoo J H, Bin In J, Bok Park J, Jeon H and Grigoropoulos C P 2012 *Appl. Phys. Lett.* **100** 233124
- 4-[21] Xu J L, Li X L, He J L, Hao X P, Wu Y Z, Yang Y and Yang K J 2011 *Appl. Phys. Lett.* **99** 261107
- 4-[22] Jeschke H O, Garcia M E and Bennemann K H 2001 *Phys. Rev. Lett.* **87** 015003
- 4-[23] Ferrari A C et al 2006 *Phys. Rev. Lett.* **97** 187401
- 4-[24] Graf D, Molitor F, Ensslin K, Stampfer C, Jungen A, Hierold C and Wirtz L 2007 *Nano Lett.* **7** 238-42

# Chapter 5 References

- 5-[1] K. S. Novoselov, A. K. Geim, S. V. Morozov, D. Jiang, Y. Zhang, S. V. Dubonos, I. V. Grigorieva, and A. A. Firsov, *Science* **306**, 666 (2004).
- 5-[2] N. M. R. Peres, *Rev. Mod. Phys.* **82**(3), 2673 (2010).
- 5-[3] K. F. Mak, L. Ju, F. Wang, and T. F. Heinz, *Solid State Commun.* **152**(15), 1341 (2012).
- 5-[4] C. Lee, X. Wei, J. W. Kysar, and J. Hone, *Science* **321**(5887), 385 (2008).
- 5-[5] K. S. Novoselov, V. I. Falko, L. Colombo, P. R. Gellert, M. G. Schwab, and K. Kim, *Nature* **490**, 192 (2012).
- 5-[6] F. Bonaccorso, Z. Sun, T. Hasan, and A. C. Ferrari, *Nature Photon.* **4**, 611 (2010).
- 5-[7] M. Koshino and T. Ando, *Phys. Rev. B* **77**(11), 115313 (2008).
- 4-[8] J. Hass, W. A. De Heer, and E. H. Conrad, *J. Phys.: Condens. Matter* **20**(32), 323202 (2008).
- 5-[9] A. Y. Bykov, T. V. Murzina, M. G. Rybin, and E. D. Obraztsova, *Phys. Rev. B* **85**, 121413 (2012).
- 5-[10] J. L. Xu, X. L. Li, J. L. He, X. P. Hao, Y. Z. Wu, Y. Yang, and K. J. Yang, *Appl. Phys. Lett.* **99**, 261107 (2011).
- 5-[11] Y. Zhou, Q. Bao, B. Varghese, L. A. L. Tang, C. K. Tan, C. Sow, and K. P. Loh, *Adv. Mater.* **22**, 67 (2010).
- 5-[12] J.-Y. Hong and J. Jang, *J. Mater. Chem.* **22**, 8179 (2012).
- 5-[13] J. Feng, W. Li, X. Qian, J. Qi, L. Qi, and J. Li, *Nanoscale* **4**(16), 4883 (2012).
- 5-[14] T. Kaplas and Y. Svirko, *Carbon* **70**, 273 (2014).
- 5-[15] Y. Li, Y. Li, W. Shi, S. Chen, G. Zhang, Z. Liu, Q. Sun, J. Tian, Y.

- Xu, and Y. Chen, *Int. J. Nanomanuf.* **8**(3), 221 (2012).
- 5-[16] W. Bao, F. Miao, Z. Chen, H. Zhang, W. Jang, C. Dames, and C. N. Lau, *Nat. Nanotechnol.* **4**(9), 562 (2009).
- 5-[17] A. Capasso, E. Placidi, H. F. Zhan, E. Perfetto, J. M. Bell, Y. Gu, and N. Motta, *Carbon* **68**, 330 (2014).
- 5-[18] M. Birnbaum, *J. Appl. Phys.* **36**, 3688 (1965).
- 5-[19] J. Bonse, J. Krüger, S. Höhm, and A. Rosenfeld, *J. Laser Appl.* **24**(4), 042006 (2012).
- 5-[20] G. Dumitru, V. Romano, H. P. Weber, M. Sentis, and W. Marine, *Appl. Phys. A* **74**(6), 729 (2002).
- 5-[21] M. Huang, F. Zhao, Y. Cheng, N. Xu, and Z. Xu, *ACS Nano* **3**(12), 4062 (2009).
- 5-[22] E. V. Golosov, A. A. Ionin, Y. R. Kolobov, S. I. Kudryashov, A. E. Ligachev, S. V. Makarov, Y. N. Novoselov, L. V. Seleznev, D. V. Sinitsyn, and A. R. Sharipov, *Phys. Rev. B* **83**(11), 115426 (2011).
- 5-[23] A. Y. Vorobyev and C. Guo, *Laser Photon. Rev.* **7**(3), 385 (2013).
- 5-[24] E. V. Golosov, A. A. Ionin, Y. R. Kolobov, S. I. Kudryashov, A. E. Ligachev, Y. N. Novoselov, L. V. Seleznev, and D. V. Sinitsyn, *J. Exp. Theor. Phys.* **113**(1), 14 (2011).
- 5-[25] T. Y. Hwang and C. Guo, *J. Appl. Phys.* **108**(7), 073523 (2010).
- 5-[26] A. Y. Vorobyev and C. Guo, *J. Appl. Phys.* **104**(6), 063523 (2008).
- 5-[27] M. Rohloff, S. K. Das, S. Höhm, R. Grunwald, A. Rosenfeld, J. Krüger, and J. Bonse, *J. Appl. Phys.* **110**(1), 014910 (2011).
- 5-[28] Q. Wu, Y. Ma, R. Fang, Y. Liao, Q. Yu, X. Chen, and K. Wang, *Appl. Phys. Lett.* **82**(11), 1703 (2003).
- 5-[29] A. Y. Vorobyev, V. S. Makin, and C. Guo, *J. Appl. Phys.* **101**(3), 034903 (2007).
- 5-[30] J. Bonse, A. Rosenfeld, and J. Krüger, *J. Appl. Phys.* **106**(10), 104910 (2009).
- 5-[31] J. E. Sipe, J. F. Young, J. S. Preston, and H. M. Van Driel, *Phys. Rev. B* **27**(2), 1141 (1983).

- 5-[32] V. S. Makin, R. S. Makin, A. Y. Vorobyev, and C. Guo, *Tech. Phys. Lett.* **34**(5), 387 (2008).
- 5-[33] D. Dufft, A. Rosenfeld, S. K. Das, R. Grunwald, and J. Bonse, *J. Appl. Phys.* **105**(3), 034908 (2009).
- 5-[34] J. Reif, *Laser-Surface Interactions for New Materials Production*, Springer Series in Materials Science Vol. 130, edited by A. Miotello and P. Ossi (Springer, Berlin, 2010), pp. 19-41.
- 5-[35] A. Beltaos, A. Kovačević, A. Matković, U. Ralević, Dj. Jovanović, and B. Jelenković, *Phys. Scr.* **2014**(T162), 014015 (2014).
- 5-[36] Y. V. Bludov, A. Ferreira, N. M. R. Peres, and M. I. Vasilevskiy, *Int. J. Mod. Phys. B* **27**(10), 1341001 (2013).
- 5-[37] J. Chen, M. Badioli, P. Alonso-González, S. Thongrattanasiri, F. Huth, J. Osmond, M. Spasenović, A. Centeno, A. Pesquera, P. Godignon, A. Z. Elorza, N. Camara, F. J. García de Abajo, R. Hillenbrand, and F. H. Koppens, *Nature* **487**(7405), 77 (2012).
- 5-[38] B. Wang, X. Zhang, F. J. García-Vidal, X. Yuan, and J. Teng, *Phys. Rev. Lett.* **109**(7), 073901 (2012).
- 5-[39] R. R. Nair, P. Blake, A. N. Grigorenko, K. S. Novoselov, T. J. Booth, T. Stauber, N. M. R. Peres, and A. K. Geim, *Science* **320**, 1308 (2008).
- 5-[40] D. Teweldebrhan and A. A. Balandin, *Appl. Phys. Lett.* **94**, 013101 (2009).
- 5-[41] I. Childres, L. A. Jauregui, M. Foxe, J. Tian, R. Jalilian, I. Jovanovic, and Y. P. Chen, *Appl. Phys. Lett.* **97**, 173109 (2010).
- 5-[42] A. C. Ferrari, J. C. Meyer, V. Scardaci, C. Casiraghi, M. Lazzeri, F. Mauri, S. Piscanec, D. Jiang, K. S. Novoselov, S. Roth, and A. K. Geim, *Phys. Rev. Lett.* **97**, 187401 (2006).
- 5-[43] D. Graf, F. Molitor, K. Ensslin, C. Stampfer, A. Jungen, C. Hierold, and L. Wirtz, *Nano Lett.* **7**, 238 (2007).
- 5-[44] Y. Yang, J. Yang, L. Xue, and Y. Guo, *Appl. Phys. Lett.* **97**(14), 141101 (2010).
- 5-[45] J. Bonse and J. Krüger, *J. Appl. Phys.* **108**(3), 034903 (2010).

## Chapter 6 References

- 6-[1] Novoselov K S 2004 Electric Field Effect in Atomically Thin Carbon Films *Science* **306** 666-9
- 6-[2] Novoselov K S, Fal'ko V I, Colombo L, Gellert P R, Schwab M G and Kim K 2012 A roadmap for graphene *Nature* **490** 192-200
- 6-[3] Lee C, Wei X, Kysar J W and Hone J 2008 Measurement of the Elastic Properties and Intrinsic Strength of Monolayer Graphene *Science* **321** 385-8
- 6-[4] Mayorov A S et al. 2011 Micrometer-Scale Ballistic Transport in Encapsulated Graphene at Room Temperature *Nano Lett.* **11** 2396-9
- 6-[5] Moser J, Barreiro A and Bachtold A 2007 Current-induced cleaning of graphene *Appl. Phys. Lett.* **91** 163513
- 6-[6] Robb G 2015 Graphene plasmonics: Ultra-tunable graphene light source *Nat. Photonics* **10** 3-4
- 6-[7] Koppens F H L, Chang D E and de Abajo F J G 2011 Graphene Plasmonics: A Platform for Strong Light-Matter Interactions *Nano Lett.* **11** 3370-7
- 6-[8] Bao Q and Loh K P 2012 Graphene Photonics, Plasmonics, and Broadband Optoelectronic Devices *ACS Nano* **6** 3677-94
- 6-[9] Bonaccorso F, Sun Z, Hasan T and Ferrari A C 2010 Graphene photonics and optoelectronics *Nat. Photonics* **4** 611-22
- 6-[10] Wang J and Qiu J 2015 Luminescent Graphene Quantum Dots: As Emerging Fluorescent Materials for Biological Application *Sci. Technol. Adv. Mater.* **7** 1979-89
- 6-[11] Gokus T, Nair R R, Bonetti A, Böhmeler M, Lombardo A, Novoselov K S, Geim A K, Ferrari AC and Hartschuh A 2009 Making Graphene Luminescent by Oxygen Plasma Treatment *ACS Nano* **3** 3963-8

- 6-[12] Cao L, Meziani M J, Sahu S and Sun Y-P 2013 Photoluminescence Properties of Graphene versus Other Carbon Nanomaterials *Acc. Chem. Res.* **46** 171-80
- 6-[13] Lui C H, Mak K F, Shan J and Heinz T F 2010 Ultrafast Photoluminescence from Graphene *Phys. Rev. Lett.* **105**
- 6-[14] Liu W-T, Wu S W, Schuck P J, Salmeron M, Shen Y R and Wang F 2010 Nonlinear broadband photoluminescence of graphene induced by femtosecond laser irradiation *Phys. Rev. B: Condens. Matter Mater. Phys.* **82**
- 6-[15] Stöhr R J, Kolesov R, Pflaum J and Wrachtrup J 2010 Fluorescence of laser-created electron-hole plasma in graphene *Phys. Rev. B: Condens. Matter Mater. Phys.* **82**
- 6-[16] Kwon W, Kim Y-H, Lee C-L, Lee M, Choi H C, Lee T-W and Rhee S-W 2014 Electroluminescence from Graphene Quantum Dots Prepared by Amidative Cutting of Tattered Graphite *Nano Lett.* **14** 1306-11
- 6-[17] Beams R, Bharadwaj P and Novotny L 2014 Electroluminescence from graphene excited by electron tunneling *Nanotechnology* **25** 055206
- 6-[18] Essig S et al. 2010 Phonon-Assisted Electroluminescence from Metallic Carbon Nanotubes and Graphene *Nano Lett.* **10** 1589-94
- 6-[19] Kim Y D et al. 2015 Bright visible light emission from graphene *Nat. Nanotechnol.* **10** 676-81
- 6-[20] Berciaud S, Han M Y, Mak K F, Brus L E, Kim P and Heinz T F 2010 Electron and Optical Phonon Temperatures in Electrically Biased Graphene *Phys. Rev. Lett.* **104**
- 6-[21] Yu D and Dai L 2010 Voltage-induced incandescent light emission from large-area graphene films *Appl. Phys. Lett.* **96** 143107
- 6-[22] Freitag M, Chiu H-Y, Steiner M, Perebeinos V and Avouris P 2010 Thermal infrared emission from biased graphene *Nat. Nanotechnol.* **5** 497-501
- 6-[23] Lawton L M, Mahlmeister N H, Luxmoore I J and Nash G R 2014 Prospective for graphene based thermal mid-infrared light emitting devices *AIP Adv.* **4** 087139
- 6-[24] Luxmoore I J, Adlem C, Poole T, Lawton L M, Mahlmeister N H and

- Nash G R 2013 Thermal emission from large area chemical vapor deposited graphene devices *Appl. Phys. Lett.* **103** 131906
- 6-[25] Shen J, Zhu Y, Yang X and Li C 2012 Graphene quantum dots: emergent nanolights for bioimaging, sensors, catalysis and photovoltaic devices *Chem. Commun.* **48** 3686
- 6-[26] Mišković Z L, Segui S, Gervasoni J L and Arista N R 2016 Energy losses and transition radiation produced by the interaction of charged particles with a graphene sheet *Phys. Rev. B: Condens. Matter Mater. Phys.* **94**
- 6-[27] Wong L J, Kaminer I, Ilic O, Joannopoulos J D and Soljačić M 2015 Towards graphene plasmon-based free-electron infrared to X-ray sources *Nat. Photonics* **10** 46-52
- 6-[28] Kaminer I, Katan Y T, Buljan H, Shen Y, Ilic O, López J J, Wong L J, Joannopoulos J D and Soljačić M 2016 Efficient plasmonic emission by the quantum Čerenkov effect from hot carriers in graphene *Nat. Commun.* **7** ncomms11880
- 6-[29] Jablan M, Buljan H and Soljačić M 2009 Plasmonics in graphene at infrared frequencies *Phys. Rev. B: Condens. Matter Mater. Phys.* **80**
- 6-[30] Hong J-Y and Jang J 2012 Micropatterning of graphene sheets: recent advances in techniques and applications *J. Mater. Chem.* **22** 8179
- 6-[31] Feng J, Li W, Qian X, Qi J, Qi L and Li J 2012 Patterning of graphene *Nanoscale* **4** 4883
- 6-[32] Bao W, Miao F, Chen Z, Zhang H, Jang W, Dames C and Lau C N 2009 Controlled ripple texturing of suspended graphene and ultrathin graphite membranes *Nat. Nanotechnol.* **4** 562-6
- 6-[33] Beltaos A, Kovačević A G, Matković A, Ralević U, Savić-Šević S, Jovanović D, Jelenković B M and Gajić R 2014 Femtosecond laser induced periodic surface structures on multi-layer graphene *J. Appl. Phys.* **116** 204306
- 6-[34] Nair R R, Blake P, Grigorenko A N, Novoselov K S, Booth T J, Stauber T, Peres N M R and Geim A K 2008 Fine Structure Constant Defines Visual Transparency of Graphene *Science* **320** 1308-1308
- 6-[35] Ferrari A C et al. 2006 Raman Spectrum of Graphene and Graphene

Layers *Phys. Rev. Lett.* **97**

- 6-[36] Ivashenko O, Bergren A J and McCreery R L 2016 Light Emission as a Probe of Energy Losses in Molecular Junctions *J. Am. Chem. Soc.* **138** 722-5
- 6-[37] Iqbal M Z, Singh A K, Iqbal M W, Seo S and Eom J 2012 Effect of e-beam irradiation on graphene layer grown by chemical vapor deposition *J. Appl. Phys.* **111** 084307
- 6-[38] Xu Z, Chen L, Li J, Wang R, Qian X, Song X, Liu L and Chen G 2011 Oxidation and disorder in few-layered graphene induced by the electron-beam irradiation *Appl. Phys. Lett.* **98** 183112
- 6-[39] Meyer J C, Girit C O, Crommie M F and Zettl A 2008 Hydrocarbon lithography on graphene membranes *Appl. Phys. Lett.* **92** 123110
- 6-[40] Teweldebrhan D and Balandin A A 2009 Modification of graphene properties due to electron-beam irradiation *Appl. Phys. Lett.* **94** 013101
- 6-[41] van Dorp W F, van Someren B, Hagen C W, Kruit P and Crozier P A 2005 Approaching the Resolution Limit of Nanometer-Scale Electron Beam-Induced Deposition *Nano Lett.* **5** 1303-7
- 6-[42] Besold J 1994 Electromigration kinetics of gold on a carbon thin film surface studied by scanning tunneling microscopy and scanning tunneling potentiometry *J. Vac. Sci. Technol. B Microelectron. Nanometer Struct. Process. Meas. Phenom.* **12** 1764
- 6-[43] Ohtsu M 2016 *Silicon Light-Emitting Diodes and Lasers: Photon Breeding Devices using Dressed Photons* (Springer)
- 6-[44] Ruzicka B A, Wang S, Werake L K, Weintrub B, Loh K P and Zhao H 2010 Hot carrier diffusion in graphene *Phys. Rev. B: Condens. Matter Mater. Phys.* **82**
- 6-[45] Johannsen J C et al. 2013 Direct View of Hot Carrier Dynamics in Graphene *Phys. Rev. Lett.* **111**
- 6-[46] Brida D et al. 2013 Ultrafast collinear scattering and carrier multiplication in graphene *Nat. Commun.* **4**
- 6-[47] Meric I, Han MY, Young A F, Ozyilmaz B, Kim P and Shepard KL 2008 Current saturation in zero-bandgap, top-gated graphene field effect transistors

*Nat. Nanotechnol.* **3** 654-9

6-[48] Amendola V 2016 Surface plasmon resonance of silver and gold nanoparticles in the proximity of graphene studied using the discrete dipole approximation method *Phys. Chem. Chem. Phys.* **18** 2230-41

6-[49] Rai P, Hartmann N, Berthelot J, Arocas J, Colas des Francs G, Hartschuh A and Bouhelier A 2013 Electrical excitation of surface plasmons by an individual carbon nanotube transistor *Phys. Rev. Lett.* **111** 026804-1 - 026804-5

### **References for Supporting Information:**

6S-[1] Ferrari A C et al. 2006 Raman Spectrum of Graphene and Graphene Layers *Phys. Rev. Lett.* **97**

6S-[2] Schwierz F 2010 Graphene transistors *Nat. Nanotechnol.* **5** 487-96

6S-[3] Joshi P, Romero H E, Neal A T, Toutam V K and Tadigadapa S A 2010 Intrinsic doping and gate hysteresis in graphene field effect devices fabricated on SiO<sub>2</sub> substrates *J. Phys. Condens. Matter* **22** 334214

6S-[4] Peres N M R 2010 Colloquium: The transport properties of graphene: An introduction *Rev. Mod. Phys.* **82** 2673-700

6S-[5] Lafkioti M, Krauss B, Lohmann T, Zschieschang U, Klauk H, Klitzing K v. and Smet J H 2010 Graphene on a Hydrophobic Substrate: Doping Reduction and Hysteresis Suppression under Ambient Conditions *Nano Lett.* **10** 1149-53

# Appendix A

## Fabrication Methods

In this appendix, we discuss fabrication methods used in this thesis. Details about the fabrication procedures, materials, equipment, challenges, and so on is provided, with the aim of the methods being repeatable by the interested reader. The interested reader may also refer to the methods sections of the publication chapters for detailed descriptions of the experimental methods used in the research.

### A.1 Sample Fabrication

In this research, all graphene samples were fabricated by mechanical exfoliation (i.e. the separation of bulk graphite into atomic layers using tape). This technique was first published in Novoselov and Geim's original work on graphene [1], with details of the methods given in the supporting information. The exact detailed recipe for graphene exfoliation which was used in this thesis research was published in reference [2] (please see Appendix B). Here we provide a summary of the materials, equipment and step-by-step techniques that were used.

## Materials and Equipment

The materials used for graphene exfoliation included: kish graphite flakes from NGS Naturgraphit GmbH, wafer tape from NITTO Denko (product number BT-150E-CM), Si/SiO<sub>2</sub> wafers from IDB Technologies and quartz substrates from Edmund Optics. The Si/SiO<sub>2</sub> substrates were p-doped, and the SiO<sub>2</sub> layer was  $\sim 300$  nm. Common lab items which were also used included lab beakers, distilled water, acetone, isopropyl alcohol (IPA), methyl isobutyl ketone (MIBK), a small rubber/cork cylinder used as a roller (e.g. top of lab beaker), a small knife/blade and scissors for tape-cutting and a diamond knife for wafer-dicing.

Equipment that was needed for the process included an optical microscope, ultrasonic cleaner, hot plate, argon or nitrogen gun, an ultraviolet (UV) lamp, and wafer dicer. Cleanliness is very important for the fabrication process to be successful. In particular, any kind of contamination on the substrate surface could lead to poor adhesion with graphite and a lack of deposited graphene. Hence, the materials and surfaces used should be kept as clean as possible, and ideally, sample fabrication should be done in a clean room.

The fabrication process involved a number of main steps and typically took about a day or two to complete a “batch” of graphene samples (5-10 substrates). The main steps were wafer-dicing, substrate-cleaning (mechanical/chemical), tape preparation, substrate-cleaning (ozone), first exfoliation, second exfoliation, and sample identification. The steps are described below in the order that they were performed.

### Wafer-Dicing

First, dicing of Si/SiO<sub>2</sub> wafers was performed to prepare substrates of  $\sim 1$  cm  $\times$  1 cm in area (quartz substrates were ordered with areas of  $\sim 1$  cm  $\times$  1 cm, and did not need dicing). Dicing was done in one of two ways: using a diamond pen or a wafer-dicing machine.

The first method involved scribing the bottom of the wafer along the crystal

planes with a diamond pen. The wafer was snapped along the cracks to make substrates of the desired area. The second method used a Disco-DAD 321 Si dicing saw to precisely dice the wafer into substrates of the desired area. The bottom surfaces of the diced wafers were cleaned using acetone with a cotton swab or vacuum wipes to remove dust created in the process.

### **Substrate-Cleaning (Mechanical/Chemical)**

Next, the substrates were prepared for exfoliation by thorough cleaning processes. Substrate cleaning was done either by mechanical or chemical means, or a combination, depending on the need. The substrates were checked for cleanliness throughout the process by viewing them in an optical microscope in darkfield mode (in which dirt is highly visible).

Mechanical cleaning involved a combination of methods depending on the need, including: using cotton swabs dipped in acetone, using an argon or nitrogen gun, and using NITTO tape to clean the top surface of the substrates. In the latter process, tape was pressed onto each substrate surface and removed.

In preparation for chemical cleaning, lab beakers were rinsed with distilled water and left to dry. Before use of a beaker with any chemical, the bottom of the beaker (up to  $\sim 1$  cm in height) was rinsed with that chemical. The beaker was then emptied and ready for use with the same chemical. Chemical cleaning involved placing the substrates in a beaker of acetone, and in the ultrasonic cleaner for several minutes ( $\sim 5$  min) and then repeating the process with IPA. The substrates were then removed from the chemical, and dried with an argon or nitrogen gun.

After substrate-cleaning, the substrates (5-10 per batch) were placed on a hot plate at  $250^{\circ}$  C in air for at least 30 min. Substrates were left on the hot plate until the first exfoliation to avoid water accumulation on the surface. Tape preparation was done during this time of substrate heating.

## **Tape Preparation**

While the substrates were heated on the hot plate, tape preparation was carried out. Tape was cut into pieces of  $\sim 2 \text{ cm} \times 2 \text{ cm}$  and a flake of graphite (of mm-scale area) was selected from the ordered supply. Two pieces of tape were pressed onto the graphite flake on both sides and rolled over with the rubber or cork roller to remove air bubbles. The pieces of tape were separated from each other leaving one piece of tape with the original graphite flake attached and the other piece of tape with small thin separated flakes attached.

Using the tape with thinner flakes, another piece of tape was pressed on top and again rolled over to remove air bubbles. Then the two pieces were separated leaving thinner flakes on each piece of tape. This process was repeated many times with new pieces of tape each time to thin down the flakes on the tape until some areas appeared grey (as opposed to black). Multiple pieces of tape were prepared in this way for each substrate in the batch.

## **Substrate-Cleaning (Ozone)**

Once the tape pieces were prepared, the next step was ozone-cleaning, which was performed just before first exfoliation. The temperature of the hot plate holding the substrates was reduced to  $150^{\circ} \text{C}$  and the substrates were further cleaned by exposure to ozone using a short wavelength UV lamp. The lamp was hand-held above the substrates on the hot plate for  $\sim 5$  min. The substrates were then ready for first exfoliation.

## **First Exfoliation**

With both the substrates and tape prepared as described above, first exfoliation was performed. A substrate was removed from the hot plate and left to cool for  $\sim 30$  seconds. A tape piece with grey flakes was pressed over the substrate surface and rolled over to remove air bubbles. Excess tape was cut off around the perimeter of the substrate with a knife/blade. For each substrate in the batch, the process was repeated. The tape-covered substrates were then

placed in a beaker of MIBK and left on a hot plate at 40<sup>0</sup> C, which served to slowly and gently remove the tape from the surfaces of the substrates. This process usually takes 1-2 hours.

Once the tape had been removed by the MIBK, the substrates were rinsed by placing them in a beaker of acetone for several seconds followed by a beaker of IPA for several seconds. Then they were dried at grazing incidence with an argon or nitrogen gun, and placed on a hot plate. They were gradually (during a span of  $\sim 10$  min) heated from room temperature to 150<sup>0</sup> C and left at this temperature for at least 30 min. Then they were gradually (during a span of  $\sim 30$  min) cooled down to less than 50<sup>0</sup> C. This process served to enhance the contact between the graphite flakes and substrate.

### **Second Exfoliation**

Second exfoliation was then carried out. A substrate was removed from the hot plate and left to cool for  $\sim 30$  seconds. A new (empty) piece of tape was pressed and rolled over the substrate surface. The tape was then gently and slowly (several minutes per substrate) removed from the substrate surface by hand (using tweezers or gloved fingers). This step marks the end of the fabrication process.

### **Sample Identification**

Finally, the samples were ready for identification. This was carried out by viewing the substrates in an optical microscope and scanning the area for graphene flakes. Maps of the sample locations on each substrate were sketched out for reference to easily find the samples again.

The exfoliation process leaves flakes of varying thicknesses, shapes, and areas randomly deposited on the substrate surface. The thickness could be determined by colour/intensity contrast in the microscope so that graphene samples of single-layer to multi-layer were identified and located on the substrate. On Si/SiO<sub>2</sub> substrates, thicker exfoliated graphite flakes appear as

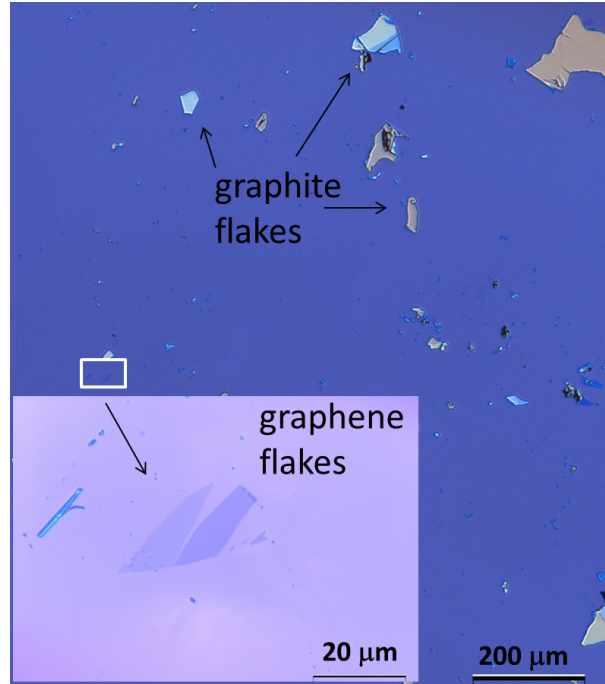


Figure A.1: Optical microscope image of an Si/SiO<sub>2</sub> substrate with exfoliated graphite flakes and graphene flakes (enlarged in inset).

white or yellow, thinner flakes appear blue, and the thinnest (graphene or few layer graphene) appear purple (as does the surrounding substrate). An example optical microscope image of exfoliated flakes on an Si/SiO<sub>2</sub> substrate is shown in Figure A.1. On quartz substrates, the contrast is also apparent when viewing the samples with transmitted light due to the increased absorption per added layer. The thinnest samples appear the lightest in colour.

## A.2 Device Fabrication

For the light emission experiments, graphene field effect transistor devices were fabricated. Exfoliated graphene samples on Si/SiO<sub>2</sub> substrates were used as the basis of the devices. The device structure is schematically illustrated in Figure A.2 (a), outlining the placement of the source (S), drain (D), and gate (G) electrodes. The fabrication process involved a number of main steps: sample selection, shadow mask design and fabrication, mask alignment, deposition

of electrodes, and wire attachment.

### **Sample Selection**

First, samples were selected for device fabrication based on appropriate size and position on the substrate. The samples needed to have lengths of more than  $\sim 50 \mu\text{m}$  and be located significantly far from the substrate edges (ideally near the center) to be useful as the channel of the device. The size requirement was due to the dimensions of the shadow masks that were used. The distance requirement was to allow sufficient amount of space to deposit gold (Au) as source and drain contacts without the gold touching the edge of the substrate. If the gold connected to the Si substrate along the cut side edge or chips within the top surface it could cause a short circuit; hence this situation was avoided.

### **Shadow Mask Design and Fabrication**

The next step was to fabricate a shadow mask for the purpose of depositing gold electrodes on the device. Because of the individuality of exfoliated graphene samples, a new shadow mask was fabricated for each device specific to the sample size and position. A wire-based mask design was used to allow for the necessary resolution and flexibility needed for various samples.

A schematic illustration of the wire-based mask design is shown in Figure A.2 (b). The base of the shadow masks was a thin layer of stainless steel ( $140 \mu\text{m}$  thick) with a slit that was machine-cut out of the center of  $\sim 2 \text{mm}$  width. A thin wire of gold or platinum of diameter 10, 25, or  $50 \mu\text{m}$  was placed across the center of the slit (held in place by vacuum tape), separating the slit area into two parts for the source and drain electrodes. The wire provided the mask for the graphene channel area.

The diameter of the wire was chosen according to the size of the graphene sample. The shadow-mask deposition process usually resulted in a thinner channel than the wire diameter due to factors such as distance between the sample and the mask, the cylindrical wire shape, and the angle of deposition.

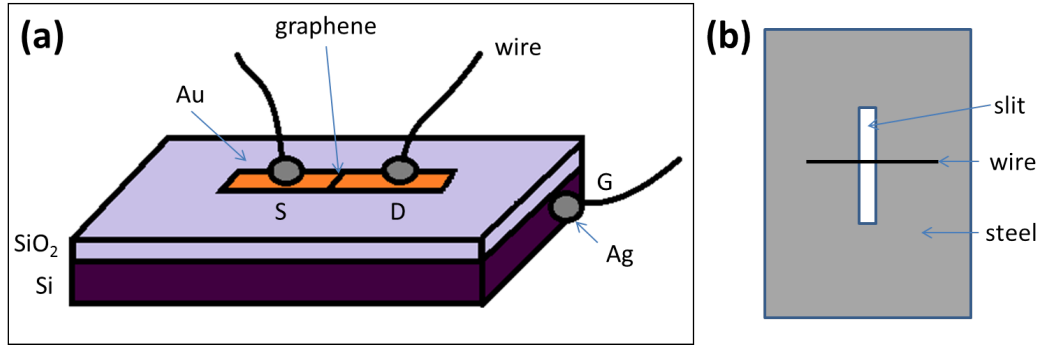


Figure A.2: Schematic illustrations of (a) device structure; (b) shadow mask (not to scale).

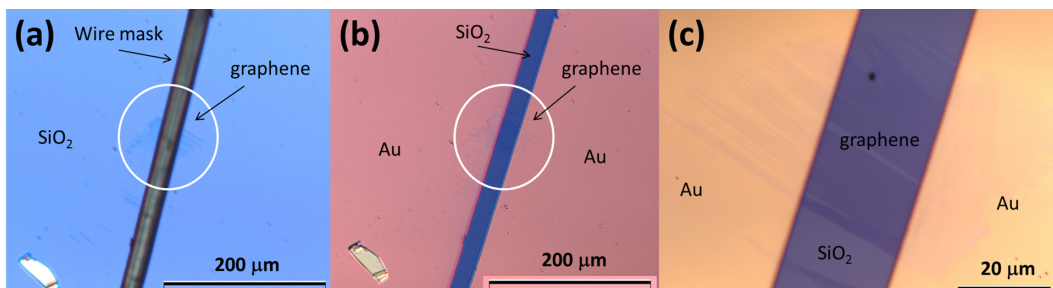


Figure A.3: Optical microscope images of (a) graphene sample aligned with wire mask above; (b) the same sample with gold deposited; (c) an enlarged view of (b).

For example, using a 25 μm wire mask typically resulted in a channel length of ~15 μm.

### Mask Alignment

The substrate and mask were placed in a sample holder with a built-in mask aligner specially designed for shadow mask deposition. The mask was held in a separate frame, and positioned atop the substrate according to the geometry of the sample on the substrate. The mask was placed with the wire side facing down, and held in place to the frame by vacuum tape. This way, the wire was as close to the substrate as possible for the most accurate deposition. The vacuum tape acted as a spacer so that the wire did not come in contact with the sample. Direct contact was avoided as this could damage the sample.

The mask aligner allowed x-y translation of the mask using attached screws

so that the wire mask could be positioned directly atop the graphene sample. Fine positioning was achieved by using an optical microscope to view the sample during alignment (see Figure A.3 (a)). Once positioned in the desired alignment, the mask frame was secured to the aligner using vacuum tape. This step and all subsequent handling of the aligner needed to be done with extreme care, as any micrometer-scale movement of the mask position could misplace the position of the deposited electrodes. A final check of the position was done in the microscope before each deposition.

### **Deposition of Electrodes**

Gold was chosen as the contact material for the source and drain electrodes due to its frequent use with graphene and other devices. As discussed in Chapter 6, electro-migration of gold from the contacts led to some interesting results in the light emission from the devices. Hence, an additional adhesion layer (such as chrome) was avoided to allow for this process to be consistent between experiments.

The gold source and drain electrodes were deposited onto the sample as shown in Figure A.3 (b) and (c). The deposition was performed in a clean room on a Lesker AXXIS electron beam evaporation system. A layer of  $\sim 30$  nm of gold was deposited onto the mask-covered substrate. The deposition was done in ultrahigh vacuum with a base pressure of  $2 \times 10^{-6}$  torr (deposition pressure between  $1 - 2 \times 10^{-6}$  torr), and deposition rate of  $0.2-0.6 \text{ \AA/s}$ .

### **Wire Attachment**

The next step in device fabrication was the attachment of wires to the electrodes to allow for the application of voltage. This was done by applying silver (Ag) epoxy (EPO-TEK Epoxy Technology) to the device using a Westbond epoxy die bonder machine in a clean room. The wires were first placed in the desired positions on the substrate: atop the source and drain electrodes and on the side of the substrate to attach to the back gate through the exposed Si

on the diced edge. The substrate and wires were held in place to a metal base by vacuum tape.

The epoxy was mixed according to the epoxy instructions and then applied to the device using the die bonder machine. This machine allowed for precise application of epoxy from a controlled dispenser while viewing through a microscope. A flow time of 15 ms was used to dispense small amounts of epoxy at a time, thus avoiding unwanted extra epoxy on the substrate.

The device on the metal base was then placed in an oven for 3 hours at 80<sup>o</sup> C in air to cure the epoxy. The devices were cooled down gradually to ~50<sup>o</sup> C, as sudden temperature changes could cause stress or strain to the graphene. Once cooled, the devices were taken out of the oven, marking the last step in the device fabrication process, and completing the device structure shown in Figure A.2 (a).

Raman characterization of the graphene samples and electrical characterization of the devices and was performed as described in Chapter 6 (supporting information). The fabrication methods described here produced a good yield of high quality graphene samples and functional devices.

### A.3 References

- [1] Novoselov K S, Geim A K, Morozov S V, Jiang D, Zhang Y, Dubonos S V, Grigorieva I V and Firsov A A 2004 Electric Field Effect in Atomically Thin Carbon Films *Science* **306** 666-9
- [2] Matković A V 2015 *Investigating the optical properties of graphene with spectroscopic ellipsometry* Ph.D. (University of Belgrade)